Experimental and numerical study of vibro-impact systems with two-sided constraints

Scuola di Dottorato in Ingegneria Civile e Architettura

Dottorato di Ricerca in Ingegneria Strutturale e Geotecnica – XXXIII Ciclo

Candidate
Giulia Stefani
ID number 1342305

Thesis Advisor
Prof. Maurizio De Angelis

May 2021

Thesis defended on May 14, 2021
in front of a Board of Examiners composed by:

Prof. Carlo G. Lai
Prof. Gabriele Milani
Prof. Mauro Sassu

This thesis has been typeset by LaTeX and the Sapthesis class.

Author's email: giulia.stefani@uniroma1.it

To Chiara

Abstract

Vibro-impact dynamics has been, and still is, the subject of growing interest for its practical and theoretical significance. Many practical engineering problems involve mechanical components or structures repeatedly colliding with one another or with obstacles during their motion. From a theoretical point of view, impact dynamics is highly interesting for the complex nonlinear behaviors and phenomena exhibited by vibro-impact systems, even the simplest. Despite the vibro-impact dynamics has been the subject of intense study, few works deal with the topic resorting to both experimental and numerical analyses. Furthermore, there are still some aspects that, to date, have been little deepened and deserve more attention.

The aim of this Ph.D. thesis is to characterize, in a systematic and transversal way, the nonlinear non-smooth response of vibro-impact systems with two-sided constraints. The study was inspired by the practical problem of large horizontal seismic-induced displacements in base-isolated structures. These displacements can damage the isolation system itself or can lead to pounding with surrounding moat walls or adjacent structures if the available seismic gap is not sufficient.

The problem was studied considering a Single-Degree-Of-Freedom (SDOF) system with two-sided deformable and dissipative constraints (bumpers) under harmonic base excitation and resorting to extensive parametric analyses, of both experimental and numerical nature, continuously interacting and feeding each other throughout the doctoral course. Shaking table tests were carried out on a small-scale physical model, using a rich sensor apparatus, and considering different values of gap amplitude, peak table acceleration and different bumpers. The numerical simulations were performed considering a relatively simple model, in which the impact phenomenon was modeled by a viscoelastic law, and using a Matlab code, specifically created for this purpose. This made it possible to carry out extensive parametric investigations. The adoption of a soft impact model allowed to describe the deformation and the recovery of the bumpers, otherwise not observable by resorting to the coefficient of restitution.

The influence of the fundamental parameters which characterize the problem on the system's response was first investigated. The numerical model, despite its relative simplicity, satisfactorily reproduced the experimental results and allowed to extend the range of investigation, compared to the experimental tests. A wide variety of behaviors and phenomena was observed. Different types of primary resonance (without hysteresis, with right or left hysteresis), secondary resonances (without hysteresis, with right or left hysteresis or of non-regular type), non-symmetric responses, multiple impacts, periodic, quasi-periodic and chaotic motion, were highlighted and investigated resorting to different types of representations. The occurrence of the (primary and secondary) grazing phenomenon, and its relationship with some of the observed scenarios, was also highlighted. The transition from a hardening-like to a softening-like behavior was experimentally observed passing from positive to small negative gaps, through the zero-gap configuration.

The study of the scenarios, besides being interesting from a theoretical point of view, highlighted possible issues associated with the occurrence of impact. This enabled to make interesting considerations on vibration control. By properly selecting

the bumpers' parameters (gap and mechanical properties), it is possible to guide the system's response to reach specific objectives, avoiding some undesirable scenarios and encouraging others, and thus exploiting the occurrence of impact with beneficial effects. Some indications of optimal design of the bumpers are provided to reduce both the displacement and the acceleration of the mass, compared to the case without obstacles, without possibly reducing the vibration isolation frequency range.

Sommario

Da diversi anni ormai, la dinamica con impatto è oggetto di crescente interesse da parte della comunità scientifica per la sua rilevanza teorica ed applicativa. In molti problemi concreti tipici dell'ingegneria, e non solo, si verificano impatti ripetuti tra componenti meccaniche o strutture. D'altra parte, i sistemi che impattano, anche i più semplici, mostrano una grande varietà di comportamenti dinamici estremamente interessanti dal punto di vista teorico. Nonostante l'attenzione rivolta alla tematica della dinamica con impatto, sono pochi gli studi che affrontano il problema sia dal punto di vista sperimentale che teorico. Inoltre, ci sono alcuni aspetti che, ad oggi, sono stati poco approfonditi e che quindi meritano maggiore attenzione.

L'obiettivo di questa tesi di dottorato è caratterizzare, in una maniera sistematica e trasversale, la risposta non lineare di sistemi soggetti ad impatto. Lo studio è stato ispirato dal problema concreto ed attuale dei grandi spostamenti nelle strutture isolate alla base. Tali spostamenti possono, da un lato, deformare eccessivamente, o addirittura danneggiare, il sistema di isolamento. Dall'altro lato, se il gap sismico disponibile non è sufficiente, possono provocare l'urto tra il sistema isolato ed eventuali strutture adiacenti.

Il problema è stato studiato considerando un sistema ad un grado di libertà (SDOF) soggetto ad un'azione armonica applicata alla base, il cui moto è limitato da due ostacoli deformabili e dissipativi (bumpers). Lo studio è stato condotto attraverso estese indagini parametriche, di carattere sia numerico che sperimentale, che hanno interagito e si sono alimentate a vicenda durante tutta la durata del dottorato. Le prove sperimentali sono state condotte su un modello fisico in scala ridotta del sistema ed utilizzando la tavola vibrante. Sono state utilizzate diverse tipologie di sensori e sono stati investigati diversi valori del gap, del valore di picco dell'accelerazione e diversi bumpers. Le analisi numeriche sono state condotte considerando un modello relativamente semplice, nel quale l'impatto è stato modellato con un legame visco-elastico, ed utilizzando un codice Matlab appositamente creato per lo scopo. L'adozione del modello visco-elastico per la forza di contatto ha permesso di descrivere la deformazione ed il recupero dei bumpers, cosa non possibile utilizzando il coefficiente di restituzione.

Nella prima parte dello studio condotto durante il dottorato, è stata investigata l'influenza dei principali parametri coinvolti sulla risposta del sistema. Il modello numerico, nonostante la sua relativa semplicità, si è dimostrato in grado di riprodurre i risultati sperimentali in maniera soddisfacente. Per questo motivo è stato sfruttato per estendere il campo di indagine, considerando altri valori dei parametri non testati in laboratorio. Le indagini numeriche hanno permesso di evidenziare una grande varietà di comportamenti e fenomeni. Sono stati osservati: diversi tipi di risonanze primarie (senza isteresi, con isteresi a destra o a sinistra) e secondarie (senza isteresi, con isteresi a destra o a sinistra, oppure non regolari), risposte non simmetriche, impatti multipli, risposte periodiche, quasi-periodiche e caotiche. Questi aspetti sono stati successivamente investigati ricorrendo a diversi tipi di rappresentazione. Il fenomeno del grazing, distinto in primario e secondario, è stato inoltre evidenziato e messo in relazione con alcuni degli scenari osservati. Il passaggio da un comportamento di tipo hardening ad un comportamento di tipo softening è

stato osservato sperimentalmente passando da gaps positivi a piccoli gaps negativi, attraverso la configurazione con gap nullo.

Lo studio parametrico degli scenari, oltre ad essere interessante dal punto di vista teorico, ha permesso di evidenziare possibili problemi legati al verificarsi dell'impatto e di fare degli interessanti ragionamenti sul controllo delle vibrazioni. Scegliendo opportunamente le caratteristiche geometriche e meccaniche dei bumpers è possibile guidare la risposta del sistema in modo tale da evitare alcuni scenari e favorirne altri, sfruttando in questo modo il verificarsi dell'impatto con effetti benefici. Sono state fornite anche delle indicazioni preliminari sulla progettazione ottimale dei bumpers al fine di ridurre sia lo spostamento che l'accelerazione della massa rispetto al caso senza bumpers.

Acknowledgments

I would first like to thank my tutor, Prof. Maurizio De Angelis, for his guidance and encouragement during the doctoral course. I wish also to express my gratitude to Prof. Ugo Andreaus, with whom I had the pleasure of working in these years. I would like to express my deep gratitude to them both. Thank you for the valuable advice and teachings and for the pleasant and stimulating moments of discussion, constant source of inspiration and enriching opportunity.

Thanks to all the friends, colleagues and to all those who have contributed to the achievement of this important goal.

Finally, a special thanks goes to my parents and to Andrea. Thank you for your support, encouragement and patience.

Giulia Stefani

Ringraziamenti

Desidero innanzitutto ringraziare il mio tutor, il Prof. Maurizio De Angelis, per avermi guidato ed incoraggiato nel mio percorso di ricerca. Vorrei ringraziare anche il Prof. Ugo Andreaus, con il quale ho avuto il piacere di lavorare durante questi anni. Ad entrambi va la mia gratitudine. Grazie per i preziosi consigli ed insegnamenti e per i piacevoli momenti di confronto e discussione, fonte costante di ispirazione ed occasione di arricchimento.

Un grazie a tutti gli amici, i colleghi e a tutti coloro che hanno contribuito al raggiungimento di questo importante traguardo.

Infine, un ringraziamento speciale va ai miei genitori e ad Andrea per il loro supporto, incoraggiamento e soprattutto per la loro pazienza.

Giulia Stefani

Contents

List of Symbols

The principal symbols used in this thesis are listed below, together with their meaning. All symbols are defined, within the text, where they first appear. It can happen that the same symbol may denote more than one quantity, but the meaning should be clear when read in context.

Dimensional symbols

Ω	Base acceleration circular frequency
$a(t)$	Absolute acceleration of the mass
A_{G}	Base acceleration amplitude
$A_{\mathrm{t}}(t)$	Base acceleration
C	Viscous damping coefficient of the damper
C_j	Viscous damping coefficient of the bumpers ($j = $ R, L)
$E_{\mathrm{a}0}$	Maximum excursion of the absolute acceleration of the mass in free flight condition
E_{a}	Excursion of the absolute acceleration of the mass
$E_{\mathrm{d}0}$	Maximum excursion of the relative displacement of the mass in free flight condition
E_{d}	Excursion of the relative displacement of the mass
f	Frequency
F^*	Maximum force acting on the SDOF system in free flight condition
F_{I}	Inertia force
$F_j(t)$	Contact force ($j = $ R, L)
$G_j(t)$	Clearance function ($j = $ R, L)
G_{0j}	Initial gap ($j = $ R, L)
K	Elastic stiffness of the damper

K_j	Elastic stiffness of the bumpers (j = R, L)
M	Mass of the SDOF system
$u(t)$	Relative displacement of the mass with respect to the ground
u^*	Maximum value of the relative displacement in free flight condition
$u_j(t)$	Relative displacement of the bumpers (j = R, L) with respect to the ground
$v_j(t)$	Position of the bumpers (j = R, L)
G	Total initial gap

Dimensionless symbols

$\alpha(\tau)$	Dimensionless absolute acceleration of the mass
β	Frequency ratio
β_1	Value of the frequency ratio corresponding to the lower limit of the geometric impact range
β_2	Value of the frequency ratio corresponding to the upper limit of the geometric impact range
β_3	Downward jump frequency ratio
β_c	Value of the frequency ratio, over which, when impact occurs, the transmitted absolute acceleration is lower than the ground acceleration
$\beta_{Ra}(\xi)$	Absolute acceleration resonant frequency ratio in the linear case
$\beta_{Rd}(\xi)$	Relative displacement resonant frequency ratio in the linear case
β_R	Absolute acceleration resonant frequency ratio when impact occurs
$\Delta\alpha$	Excursion of the absolute acceleration of the mass
$\Delta\alpha_0$	Maximum value of the excursion of the absolute acceleration of the mass in free flight condition
Δf_B	Excursion of the contact force
Δq	Excursion of the relative displacement of the mass
Δq_0	Maximum value of the excursion of the relative displacement of the mass in free flight condition
Δq_B	Excursion of the deformation of the bumpers
δ	Dimensionless total initial gap

$\delta_0^*(\xi)$ Characteristic value of the dimensionless gap

δ_{0c} Value of the dimensionless gap at which $\beta_2 = \sqrt{2}$

$\delta_j(\tau)$ Dimensionless clearance function ($j = $ R, L)

δ_{0j} Dimensionless initial gap ($j = $ R, L)

η_a Normalized excursion of the absolute acceleration of the mass

η_a^* Value of the normalized excursion of the absolute acceleration of the mass in resonance condition

η_B Normalized excursion of the deformation of the bumpers

η_B^* Value of the normalized excursion of the deformation of the bumpers in resonance condition

$\eta_{d,st}$ Normalized excursion of the static displacement of the mass

η_d Normalized excursion of the relative displacement of the mass

η_d^* Value of the normalized excursion of relative displacement of the mass in resonance condition

η_F Normalized excursion of the contact force

η_F^* Value of the normalized excursion of the contact force in resonance condition

η_j Normalized maximum deformation of the bumper ($j = $ R, L)

γ_j Damping ratio ($j = $ R, L)

λ_c Value of the stiffness ratio exceeded which the occurrence of impact modifies the response of the system, compared to the free flight condition, also for $\beta > \sqrt{2}$

λ_H Value of the stiffness ratio, exceeded which, a primary hysteresis region is observed in the Pseudo-Resonance Curves

λ_{opt} Value of the stiffness ratio corresponding to the optimal condition (minimum value of η_a^*)

λ_j Stiffness ratio ($j = $ R, L)

ω Natural circular frequency of the SDOF system

$\overline{\alpha}$ Eccentricity of the absolute acceleration of the mass

$\overline{q}$ Eccentricity of the relative displacement of the mass

τ Dimensionless time

ξ Damping ratio of the SDOF system

a_G	Dimensionless base acceleration amplitude
$a_\mathrm{t}(\tau)$	Dimensionless base acceleration
$d_j(\tau)$	Dimensionless position of the bumpers ($j = \mathrm{R},\ \mathrm{L}$)
e_a	Normalized eccentricity of the absolute acceleration of the mass
e_d	Normalized eccentricity of the relative displacement of the mass
f_I	Dimensionless inertia force
$f_j(\tau)$	Dimensionless contact force ($j = \mathrm{R},\ \mathrm{L}$)
n	Subharmonic oscillation order
$q(\tau)$	Dimensionless relative displacement of the mass with respect to the ground
$q_j(\tau)$	Dimensionless relative displacement of the bumpers ($j = \mathrm{R},\ \mathrm{L}$) with respect to the ground
$R(\xi, \beta)$	Dynamic amplification factor (normalization with respect to the maximum displacement in resonance condition)
$R_\mathrm{d,max}(\xi)$	Maximum value of the dynamic amplification factor $R_\mathrm{d}(\xi, \beta)$
$R_\mathrm{d}(\xi, \beta)$	Dynamic amplification factor (normalization with respect to the static displacement)
r_j	Normalized maximum contact force ($j = \mathrm{R},\ \mathrm{L}$)
$\mathrm{TR}(\xi, \beta)$	Transmissibility (normalization with respect to the maximum absolute acceleration in resonance condition)
$\mathrm{TR}_\mathrm{a,max}(\xi)$	Maximum value of the transmissibility $\mathrm{TR}_\mathrm{a}(\xi, \beta)$
$\mathrm{TR}_\mathrm{a}(\xi, \beta)$	Transmissibility (normalization with respect to the amplitude of ground acceleration)

Other symbols

ψ_k	Heaviside functions ($k = 1,\ 2$)
$(\dot{\ })$	Differentiation with respect to time t
$(')$	Differentiation with respect to the dimensionless time τ

List of Abbreviations

EPDM   Ethylene Propylene Diene Monomer.

HDRB   High Damping Rubber Bearing.

MDOF   Multi-Degree-Of-Freedom.

NB   No Bumpers.

NF   near-fault.

PADJS   Pounding of ADJacent Structures.

PBIS   Pounding of Base-Isolated Structures.

PRCs   Pseudo-Resonance Curves.

SBR   Styrene Butadiene Rubber Copolymer.

SDOF   Single-Degree-Of-Freedom.

SNM   Simplified Nonlinear Model.

YB   Yes Bumpers.

Chapter 1

Introduction

1.1 Dynamics with impact

Vibro-impact dynamics has been, and still is, a subject of growing interest in the engineering literature for its practical and theoretical significance. First of all, mechanical collisions are ubiquitous in manufacturing, engineering, sports and everyday life. Many practical (biomedical, mechanical, civil, ...) systems possess mechanical components repeatedly colliding with one another or with obstacles during their motion [27, 110, 203, 218]. Almost any mechanical device must have space between its components, to allow for variability in the manufacture of the components, for the effects of thermal expansion, or for the movement of components. Potential collisions between components can cause noise, disturbing vibrations, wear and fatigue, leading to reduced efficiency or even failure of the device. On the other hand, the occurrence of impacts can be suitably exploited to reduce structural vibrations with beneficial effects. Another widespread problem is the study of the effects of earthquakes, of sea waves or of other forms of excitation causing two or more structures to repeatedly collide. From a theoretical point of view, impact dynamics is highly interesting, because vibro-impact systems, even the simplest, exhibit complex nonlinear nonsmooth dynamics and a wide variety of phenomena, characterized by different types of resonances, instabilities, bifurcations, periodic and quasi-periodic trajectories and chaotic regimes, that need to be carefully investigated [205, 206, 257].

1.2 Practical applications of vibro-impact dynamics

The recent scientific literature has shown a growing interest in the practical applications of the vibro-impact dynamics. In this section and in the following one (Sect. 1.3), an overview of some of well-known applications is provided. Greater emphasis is given to some of these applications, close to the study presented in this thesis with regard to the methodological approach (formulations, modeling, analysis and control techniques), namely the endoscopic vibro-impact capsule systems (Sect. 1.2.1), the drill string vibrations (Sect. 1.2.2). An entire section is finally dedicated to structural pounding (Sect. 1.3), in the context of which this research work is framed.

1.2.1   Endoscopic capsule

Impacts occur in the capsule systems used in clinic endoscopy to inspect the surface lining of the intestine in the human body, an anatomical site previously considered to be inaccessible to clinicians. The dynamics of this system has been the subject of several works, of both numerical and experimental nature [87, 160, 163–166, 293, 294]. In these studies the endoscopy capsule is typically modeled by a two-degree-of-freedom system, consisting of rigid capsule and a movable internal mass, the latter driven by a harmonic force, with one-sided or two-sided soft constraints (Fig. 1.1). The impact occurs when the relative displacement of the internal mass and the capsule exceeds the gap between them. The studies focused on exploring the dynamics of the system (bifurcation phenomena, co-existing attractors, . . .) and its performance (progression speed, energy efficiency, . . .) under various system and control parameters, such as the frequency and the magnitude of excitation, the natural frequency of the inner mass, the gap between the inner mass and the constraint, the capsule's geometry, the constraints' properties and the friction models.
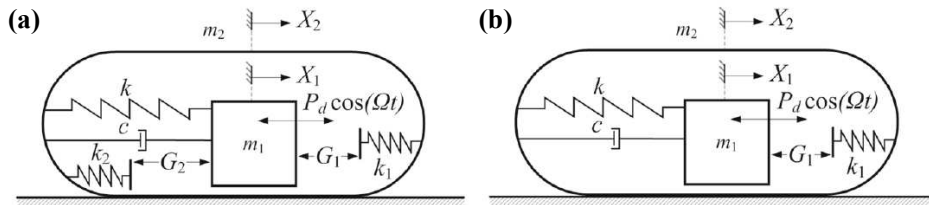

Figure 1.1. Models of the vibro-impact capsule systems, with: **a** double-sided constraints; **b** one-sided constraint [293].

1.2.2   Drill string vibrations

Non-smooth dynamics is observed also in the drilling rig used in the oil and gas industry for creation of the wellbore [53, 57, 65, 131, 132, 141, 155, 156, 158, 159, 161, 198, 267]. A typical drill string system, which is the fundamental part of the rig, consists of a drill bit, the drill collars, and the drill pipes (Fig. 1.1). The drill bit, which is located at the bottom of the wellbore, is used to break up rock formations, while the drill collars are used to apply weight to the drill bit [159]. During drilling, the interaction between the drill-string and the rock causes alternating contact and noncontact phases, leading to detrimental axial, torsional and flexural vibrations. These vibrations may cause catastrophic failures in drill strings or could lead to the wear of expensive equipment. The behavior of the system, typically studied resorting to reduced order models, is highly nonlinear, due to dry friction, loss of contact, and collisions, and shows rich and complex dynamics, characterized by the occurrence of bifurcations, multistability phenomena, aperiodic dynamics and chaotic motion.

1.2.3   Other applications

There are many other practical applications of vibro–impact dynamics including inertial shakers [282, 283], pile drivers [178], vibration hammers [290], forming machines [175], geared systems [58, 169, 170, 219, 233] (Fig. 1.3a), ground moling
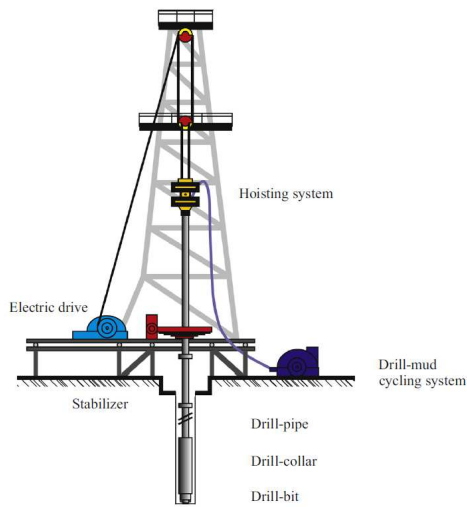
Figure 1.2. Schematic view of a typical drilling rig [132].

[214], fuel rods [107], sloshing impact [70, 220, 303], impact of ships with fenders, barriers or floating ice [83, 84, 111] (Fig. 1.3b), woodpecker toy [149, 218] (Fig. 1.3c), collision of human vocal folds [88, 104, 110, 128, 145] to mention a few.
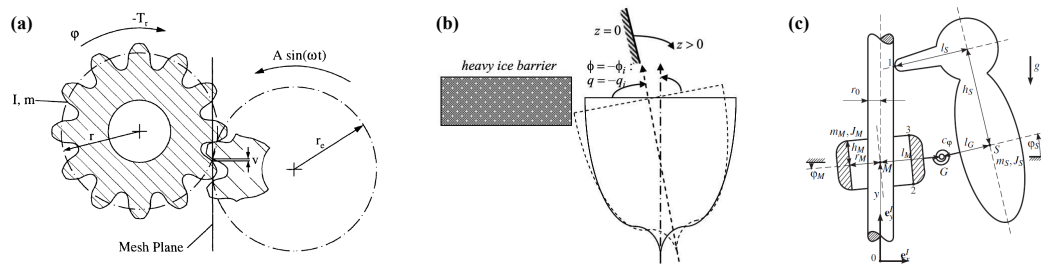
Figure 1.3. a One-stage gear rattling model [218]; **b** ship in roll motion with one-sided ice barrier impact [83, 84]; **c** woodpecker toy model [149].

1.3   Structural pounding

In earthquake-prone areas, civil structures can experience exceptional loading conditions that may result in wide undesirable losses, significant damage or even total collapse of the structures. In metropolitan areas, due to limited separation distance between adjacent structures, the large horizontal displacements resulting from the seismic excitation, may cause the collision between adjacent structures. Such collisions, known as seismic-induced pounding, may occur between adjacent conventional buildings, base-isolated highway bridges, base-isolated building and the surrounding moat wall, base-isolated building and adjacent structures, isolated equipment confined by physical constrains. The consequences of pounding can range from local slight nonstructural to serious structural damage or even collapse. A sufficiently extensive and in-depth review can be found in [14], where distinction is made between Pounding of ADJacent Structures (PADJS) and Pounding of Base-Isolated Structures (PBIS).

1.3.1   Adjacent structures

The pounding between adjacent buildings usually generate large impact forces, displacements and short duration acceleration pulses which may result in significant damage to the colliding buildings [196]. Furthermore, it may be unfavorable to the response of equipment due to the considerable influence on acceleration and, thus, on floor response spectra [51]. The effects of pounding depend on the vibration characteristic of the adjacent buildings, the input excitation characteristic, the gap size, coefficient of restitution, impact velocity, and stiffness of impact spring element [201]. In particular, pounding can cause high overstresses mainly when the colliding buildings have significantly different heights, periods or masses [7]. The parametric investigation presented in [6] shows that in a block of several adjacent structures, the end structures experience almost always substantial increases in their response while for interior structures the opposite often happens. When the colliding buildings have the same floor heights usually a slab-to-slab collision occurs (Fig. 1.4a), while when the colliding buildings have different floor heights a slab-to-column collisions take place (Fig. 1.4b) causing high shear forces developed at the mid-height of the impacted column [196].
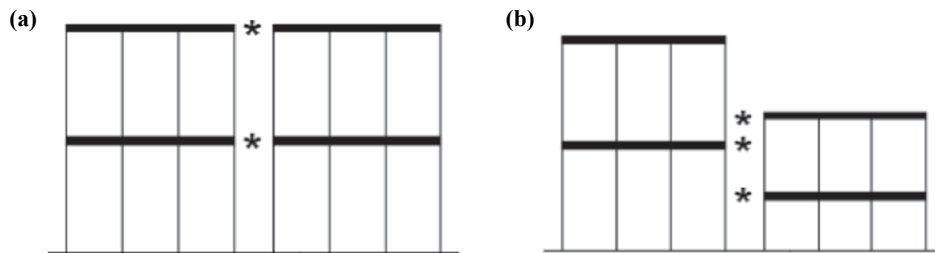
Figure 1.4. Pounding between adjacent structures: **a** slab-to-slab collision; **b** slab-to-column collision [196].

1.3.2   Base-isolated systems

In the context of civil engineering, seismic isolation represents one of the most applied, reliable and effective, passive control strategies to mitigate the dynamic response of both new and existing structures [35, 106, 121, 130, 133–136, 244, 246, 253], bridges [36, 62, 120, 143, 167, 193, 212, 287], strategic facilities [38, 284], nonstructural components and equipment [5, 44, 73, 80, 92, 116, 168, 228, 229, 255], works of art [37, 49, 245]. The aim of base isolation is to uncouple the motion of the structure from that of the ground by introducing some type of support that isolates it from the shaking ground, thus limiting the energy input into the system and protecting it from damaging. By means of its flexibility and energy absorption capability, the isolation system partially reflects and partially absorbs some of the earthquake input energy before this energy can be transmitted to the structure. Furthermore, isolation systems possess re-centering capability to bring back the structure to its original position at the end of the earthquake. The flexibility introduced by base isolation increases the fundamental vibration period of the structure. Consequently, seismically isolated structures are expected to experience

large horizontal displacements relative to the ground especially under near-fault (NF) earthquakes, which are characterized by one or more intense long-period velocity and displacement pulses. Such large displacements, concentrated in the isolation system, are accommodated by providing a sufficient seismic gap around the isolated structure. During severe seismic excitations, these displacements, if excessive, can permanently deform or seriously damage the isolation system itself or can lead to pounding with the surrounding moat walls or adjacent structures, if the available seismic gap is not sufficient because of practical constraints. Pounding may result in local structural damage, excitation of higher modes and substantial increase of storey accelerations, which can be detrimental, not only for the structure itself, but also for any sensitive equipment housed in it. Typically, the isolation system is placed on top of piers and abutments, for what concerns the bridges, and at the foundation level, for what concerns the buildings. However, also different configurations can be encountered, such as roof isolation [260, 268, 269] that utilizes the tuned mass damper concept, inter-story isolations, in which the isolation systems is placed at intermediate locations along the height of the building [230, 234, 276–278, 313] and floor isolation [8, 124], which can be an efficient and cost-effective mean for providing seismic protection for precision equipment or delicate works of art.

Bridges

The seismic performance of highway and railway bridges can be significantly improved by employing base-isolation devices, placed on top of piers and abutments. The augmented system deformability, provided by the isolation system leads to an increase of displacements under earthquake loading. This may be detrimental for railway structures because the lateral displacements of the ground can lead to displacements between the decks and between the decks and abutments along the transversal direction, which can permanently deform the rail tracks, impairing the serviceability of the bridge [62] (Fig. 1.5a). Typical earthquake-induced damages in bridges structures include: span collapses due to unseating at expansion joints, shear key failure, and damage of the expansion joint due to the slide-induced large relative displacement between the bottom of the girder and the top of the laminated-rubber bearing [153] (Figs. 1.5b,c). Furthermore, during strong earthquakes pounding may occur in bridge structures with conventional expansion joints, due to the small amplitude of the separation gap of an expansion joint [64, 93, 197]. Pounding has been identified as one of the primary causes of damage in many major earthquakes[90, 153, 197]. It takes place because the closing or opening relative displacement between adjacent structures is larger than the provided structural gap between adjacent decks or between the deck and abutment [25, 151, 197]. The influence of pounding on the structural response is significant in the longitudinal direction of the bridge and significantly depends on the gap size between superstructure segments [123]. The smallest response can be obtained for very small gap sizes and for gap sizes large enough to prevent pounding. In addition to damage along longitudinal direction, lateral displacement and rotation of bridge girders caused by pounding to adjacent girders can also lead to unseating [312]. Li et al. [151] experimentally studied the influence of spatial variation of ground motions on the pounding behaviour of three adjacent bridge segments and found that the spatially non-uniform ground motions

increase the relative displacement of adjacent bridge girders and pounding forces.
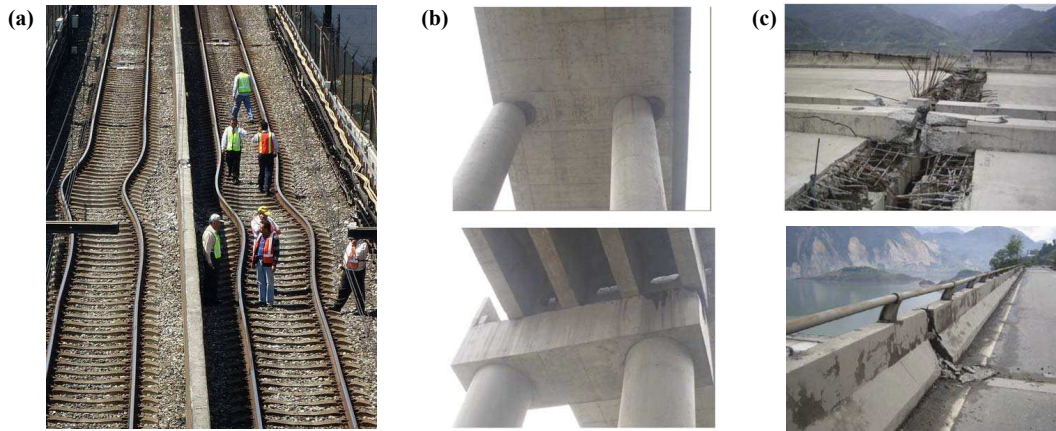
Figure 1.5. Typical earthquake-induced damage in bridges: **a** deformation of rail tracks [62]; **b** relative displacement between the bottom of the girder and the top of the laminated-rubber bearing [153]; **c** expansion joint damage [153].

Spatially varying transverse ground motions at multiple bridge supports or asymmetric decks may result in torsional response of the adjacent decks and thus eccentric pounding between adjacent bridge decks [25]. The experimental and numerical results shown in [100] show that non-uniform excitations and foundation rocking can affect the relative displacements and pounding responses significantly.

Strategic facilities

Seismic isolation can be an effective strategy for the protection of strategic facilities, such as seismically isolated nuclear power plants [142, 235, 284, 285] (Fig. 1.6a), liquid-storage tanks [41, 42, 119, 188, 189, 240] (Fig. 1.6b), to mention a few, from the damaging effects of horizontal earthquake ground shaking.
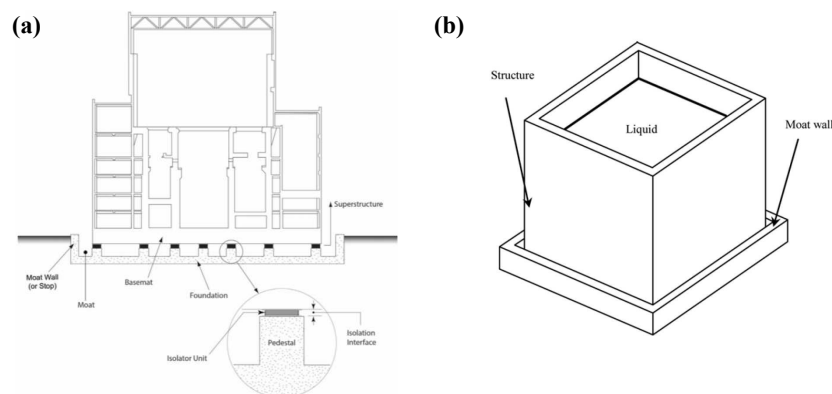
Figure 1.6. Schematic representations of **a** an isolated nuclear facility [285]; **b** a sliding base-isolated concrete rectangular liquid-storage structure with a moat wall [41, 42].

A simplified model for impact simulation that captures the impact forces and the effects of impact on the response of is presented in [142, 235]. In order to identify

the parameters that influence the response of the system, different values of the clearance to the stop and a range of properties for the moat wall and isolation system were considered by the authors. The dynamic response of a concrete rectangular liquid-storage structure and the effects of pounding with the surrounding moat wall, due to large amounts of slippage during strong earthquakes, were studied in [42]. The dynamic responses and the liquid sloshing height were found to increase after pounding. Furthermore, a parametric analysis showed that impact stiffness, initial gap, peak ground velocity, isolation period, liquid height and length-width ratio of the structure are the main factors affecting the pounding response. The effect of soil-structure interaction (SSI), initial gap, and friction coefficient, on the pounding response of the rectangular liquid-storage structure was considered in [41]. The results of the analysis showed that when soil-structure interaction is considered, the liquid sloshing height increases, whereas the friction energy dissipation and pounding energy dissipation of the system are reduced.

Buildings

The consequences of impact between base-isolated buildings and the surrounding moat walls, which exclusively occurs in correspondence of the base level where the isolator is located (Figs. 1.7a,c), has been the subject of several scientific works of both numerical and experimental nature. The effects of pounding on the seismic response of base-isolated structures, modeled as elastic or inelastic shear beams impacting against elastic or inelastic stops, was numerically studied in [263]. The results showed that impact can induces high accelerations if the beam remain elastic, whereas if the beam yields, the impact waves cannot propagate through the shear beam and low accelerations were observed except for the base of the beam. Furthermore, the acceleration response can be reduced considering nonlinear elastic stops. Similar studies were carried out by Malhotra [187], showing that the base shear forces increase with the stiffness of the isolated structure or the surrounding retaining wall and with the mass of the base mat. The seismic response of base-isolated multi-story building, supported on various base isolation systems, during impact with adjacent walls was investigated, through numerical analyses, in [192] under different real earthquake ground motions. The results of the simulations indicated that as the gap increases, the superstructure acceleration increases until a certain gap value is reached and then the decreases with further increase of gap, whereas the displacement decreases. Furthermore, the consequences of impact are found to be more serious for the system with flexible superstructure, increased number of story and greater stiffness of the adjacent structure. The effects of potential pounding of seismically isolated building with the surrounding moat wall on the effectiveness of seismic isolation were investigated by Komodromos et al. [139, 140] through parametric analyses conducted. Parametric numerical simulations under strong near-fault ground motions, and considering different contact force models, were carried out by Ye et al. [298] to investigate the behavior of a base-isolated multi-story building pounding with adjacent retaining walls. The results showed that the occurrence of pounding with the moat walls increases floor accelerations, especially at the ground level where impacts occur and excites higher modes of vibration, thus increasing the inter-story drifts. Furthermore, both inter-story drifts

and floor absolute accelerations increase with the impact stiffness Masroor and Mosqueda conducted a series of shake table tests [190] and numerical simulations [191] in order to investigate the response of a three-story frame impacting against the surrounding moat wall. Different moat wall types and gap amplitudes were considered. The test results highlighted the influence of the gap distance, impact velocity and wall flexibility on the contact forces. The effects of impact modeling characteristics on the response of a base-isolated building that experiences structural pounding were investigated in [194].
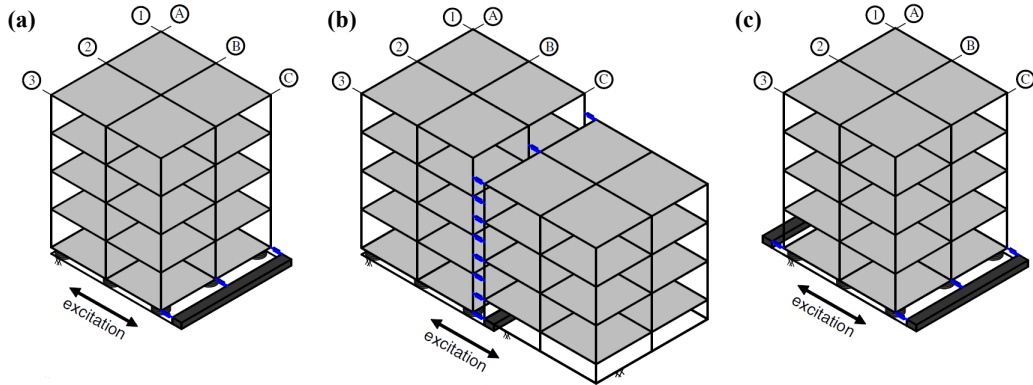

Figure 1.7. Schematic configurations of a seismically isolated multi-story building with **a** a retaining wall on one side; **b** a retaining wall and a conventional fixed-base building on one side; **c** two retaining walls on both sides [210].

In addition to the impact against the surrounding moat walls, another situation that may occur, when there are other buildings nearby the base-isolated one, is the risk of pounding also in correspondence of the upper floors, due to the deformation of the superstructures during strong earthquakes (Fig. 1.7b). The effect on the structural performance of a four-story base-isolated reinforced concrete building, of pounding against retaining walls at the base and with a four-story fixed-base reinforced concrete building, was studied in [210], through three-dimensional finite element analyses, including material and geometric nonlinearities and considering different earthquake ground motions. Three different configurations were analyzed, namely: one-sided and two-sided pounding of the building with a retaining wall, pounding with the retaining wall and a fixed-base building on one side (Fig. 1.7). The effects of potential earthquake-induced pounding between a seismically isolated building and adjacent fixed-supported buildings, subjected to various earthquake excitations, were investigated through numerical simulations by Polycarpou and Komodromos [221, 222]. Different configurations of neighboring structures and earthquake excitations were considered. The results of the numerical simulations showed that the impact at the upper floor levels, due to the deformation of the superstructures, may occur even if the provided gap is sufficient to avoid pounding with the surrounding moat wall at the base of the building. Polycarpou et al. [225] proposed a numerical approach for the dynamic analyses of 3D multistory buildings, considering the possibility of pounding and taking into account the geometry of the overlapping region during contact and without limitations regarding the geometry of the simulated structures and their position in plan. Nonlinear time-history analyses

were carried out in [195] to numerically investigate the conditions that lead to pounding between base-isolated buildings (BIB) and adjacent conventionally fixed-supported buildings and/or the surrounding moat walls, and considering the effect of the directionality of the imposed seismic excitations, the clearance, the structural characteristics of the neighboring structures and the torsional vibrations due to potential mass eccentricities.

1.4   Nonlinear response of vibro-impact systems

The study of practical problems involving collisions has been the subject of several scientific works. It allowed to highlight a wide variety of complex behaviors and non-smooth dynamical phenomena exhibited by vibro-impact systems, even the simplest. Most studies on this topic are numerical [12, 29, 31, 47, 72, 152, 172–174, 176, 177, 179–182, 184, 204, 217, 237, 238, 254, 256, 273, 274, 291, 295], whereas few works address the subject resorting to both numerical and experimental investigations [9, 10, 13, 14, 50, 61, 102, 112, 113, 162, 185, 216, 232].

Parametric investigations   The nonlinear response of vibro-impact systems is influenced by several factors, including the mechanical properties of the obstacles, the distance between them and the system (gap) and the excitation frequency and amplitude. There are few works in which extensive parametric, numerical and/or experimental, investigations are carried out. Typically, the variation of one or few parameters is considered and the results of the investigations are presented in the form of bifurcations diagrams, phase portraits, basins of attraction and Poincaré maps. Andreaus et al. [9, 10, 13] carried out experimental and numerical analyses on a Single-Degree-Of-Freedom (SDOF) oscillator with two-sided deformable and dissipative constraints (bumpers) considering different bumpers, gaps amplitudes, and table accelerations. Christopher et al. [47], considering a Multi-Degree-Of-Freedom (MDOF) structure impacting a rigid stop, found that as the contact-to-structure stiffness ratio reduces, also the complexity of the bifurcation parameter space decreases, whereas as the contact-to-structure stiffness ratio increases, very complex and rich bifurcation structures are encountered. de Souza Rebouças et al. [61] investigated the experimental response of a cantilever beam with unilateral constraint, considering different gap configurations and levels of excitation. Ing et al. investigated, both experimentally and numerically, the influence of the excitation frequency, for a number of values of the excitation amplitude, on the bifurcation scenarios in a SDOF system with two-sided [112] and one-sided [113] elastic constraints. The influence of the exciting frequency and of the clearance on the dynamics of a two-degree-of-freedom system with a two symmetric rigid stops was investigated by Luo et al. [176]. The correlation between the dynamics of a two-degree-of-freedom periodically-forced system with symmetric motion limiting constraints and the constraint parameters, clearance and stiffness ratio, was studied by Luo and Wang [182]. Masroor and Mosqueda [190] experimentally investigated the effect of various moat wall properties, including stiffness and gap distance, on the response of a quarter scale three-story frame isolated at base.

Small, null and negative gaps   As concerns the influence of the gap size, few works can be found in Literature, usually dealing with positive gaps. In these works the response is found to decrease as the gap increases [6, 139, 140, 221, 222]. Very small seismic gaps, in combination with strong ground excitation, can lead to relatively milder consequences from pounding, not allowing the structure to develop high velocities before the impact [221, 222]. Considering a harmonically excited Duffing-type suspension system, with a pair of symmetric viscoelastic buffers under primary resonance conditions, Sun et al. [254] observed that as the free travel decreases, the amplitude of the displacement response decreases for a hardening primary system, while it increases for a stronger softening primary system. However, if there is enough damping of the end-stop in the stronger softening primary system, the response amplitude decreases for a smaller free travel. Furthermore, the decrease of the free travel results in the amplification of the acceleration response for the softening primary system. According to Jankowski et al. [123] the optimal gap size to reduce the response is either a very small one or large enough to avoid collisions. The zero-gap configuration was recommended by Aguiar and Weber [4], since it allows to maximize the impact force in a vibro-impact system without the occurrence of nonlinear jumps. Even less are the works that deal with negative gaps, which cause an initial pre-stress/pre-strain state in the bumpers. Relatively simpler dynamic responses of a two-degree-of-freedom periodically-forced system are found in [182] if the constraints are initially prepressed. The effect of the introduction of a prepressing constraint in a capsule system was highlighted in [293].

Primary resonance   Some of studies available in literature focus the attention mainly on the response of vibro-impact systems in primary resonance conditions. The primary resonance was theoretically and experimentally investigated by Rigaud and Perret-Liaudet [232], considering a preloaded Hertzian contact subjected to harmonic normal forces. Sun et al. [254] studied the primary resonance response of a harmonically excited duffing-type suspension system with a pair of symmetric viscoelastic buffers, considering the effect of the end-stops parameters (stiffness ratio, damping ratio and free travel).

Secondary resonances   The motion of vibro-impact systems under harmonic excitation may include also superharmonic and subharmonic resonances [48, 236, 238]. Impact oscillators can exhibit, to the right of the mean resonance, family of subharmonic resonant peaks between which cascades of period-doubling bifurcations leading to chaotic regimes are observed, and, to the left, irregular resonances [257]. There are not many studies dealing with this topic. Andreaus et al. [12], studying the dynamic response of a SDOF oscillator, exited by a base acceleration and constrained by two unilateral constraints (bumpers), highlighted the existence of peaks and dwells in the low frequency range, at which multiperiodicities of orbits were observed and the existence of super-harmonics detected.

Types of impact motions   Most of the works deal with the types of motion, bifurcations and phenomena that can occur in the dynamics of such non-smooth dynamical systems. Many different types of periodic and chaotic impact motions

exist even for simple systems with external periodic excitation forces [217]. Each type of periodic motion is characterized by a number of impacts in one motion period and has a region in the space of system parameters in which the solution can exist and is stable. Harmonic, subharmonic, and chaotic motions are found to exist in the response of a periodically forced SDOF system with one-sided elastic constraint studied in [238]. For some parameter values, infinitely many unstable periodic and nonperiodic orbits coexist with a stable orbit [237]. These unstable orbits can have a dramatic effect on the transient motion of the system, and cause sensitive dependence on initial conditions. Wagg and Bishop [271] investigated the dynamics of a two-degree-of-freedom impact oscillator with motion limiting constraint, and highlighted a range of periodic and nonperiodic impact motions. They studied the bifurcations which occur between differing regimes of impacting motion, in particular those which occur due to a grazing bifurcation, the periodic and chaotic chatter motions and the regions of sticking. Luo et al. [176], considering a two-degree-of-freedom system with two-sided rigid stops subjected to harmonic excitation, defined the fundamental group of impact motions and studied the transitions from one motion to the other, which basically goes through different types of bifurcations, and the occurrence of chattering-impact vibration. A similar system was studied in [173], where stability and local bifurcations of the period-one double-impact symmetrical motions, with special attention to Neimark–Sacker bifurcations, were analyzed by using the Poincaré maps. Poincaré maps were used also to analyze the nonlinear dynamics of a MDOF system having placed a single rigid stop and subjected to periodic excitation [177]. The observed properties of the map have been shown to exhibit particular types of sliding and grazing bifurcations of periodic-impact motions under parameter variation. The generation mechanism of complete and incomplete chattering-impact vibration in a SDOF with one-sided rigid constraint was investigated in [181]. In the theoretical-numerical work by Andreaus and De Angelis in [12], the study of the dynamic response of SDOF oscillator with two-sided deformable and dissipative constraints (bumpers) allowed the authors to highlight the presence of hysteresis ranges, jumps between multi-periodic orbits, and super-harmonics and to observe how unilateral constraints modify the response of the system with respect to the absence of bumpers. The study of the dynamics of a two-degree-of-freedom periodically-forced system with symmetric motion limiting constraints, with emphasis on the transition between fundamental impact motions, together with the design and implementation of an electronic circuit, describing the dynamic characteristics of the non-smooth system, were presented in [182]. Gritli and Belghith [86] illustrated, through time-traces, phase portraits and Poincaré sections, the occurrence of several behaviors in the nonlinear dynamic behavior of a one-degree-of-freedom impact oscillator with a single rigid constraint, including the period-doubling route to chaos, the period-adding cascade, interior and boundary crisis, the complete and incomplete chaotic chattering, the cyclic-fold bifurcation, the saddle-saddle bifurcation, the Neimark–Sacker bifurcation, the sub-critical period-doubling bifurcation, the grazing bifurcation and the border-collision bifurcation. Extremely rich and complex behaviour were observed by Christopher et al. [47], exploring, through parametric investigations, the nonlinear dynamics of a MDOF structure impacting a rigid stop, particularly in the cases where at least two-floor degrees of freedom impact the stop and when the contact-to-storey stiffness ratio

is large. In [50] Costa et al. explored, both experimentally and numerically, the complex dynamics of a SDOF oscillator with one-sided elastic constraint [286] and proposed a new technique for processing of the experimental data to improve quality of the recorded phase portraits. In [183], pattern types, stability domains and bifurcation characteristics of periodic motions for a two-degree-of-freedom oscillator with a clearance are investigated and attracting domains and Poincaré mapping diagrams of coexisting motions in the neighborhood of grazing bifurcations are discussed. Phenomena of coexisting attractors and chaotic transitions, including crisis, are discussed in [299], considering single and two degree-of-freedom impact oscillators. Focusing on the switching behaviors on the boundary between two adjacent domains, in a periodically forced modified Duffing-Rayleigh system, the coexistence of attractors, under different initial conditions, is illustrated through basins of attraction and phase planes in [304].

Grazing   In studying vibro-impact systems different types of bifurcations may be encountered. Among these, of particular interest is the grazing impact bifurcation. Grazing bifurcation occurs when an orbit just touches the constraint, or stop, with a zero (or very low) velocity impact. It thus represent the bordering state between impacting and nonimpacting motion. When the driving frequency is continuously varied, the vibro-impact system can undergo complicated motions, with several impacts or chaotic behavior, close to the value of frequency at which impact may first occur, due to this type of bifurcation [28, 105, 207, 270]. A sudden loss of stability and either a jump to a distant attracting solution or an immediate jump to long period, apparently chaotic behaviour can result from the system undergoing a grazing bifurcations [79]. Three major types of grazing bifurcations that can occur in a simple sinusoidally forced oscillator system in the presence of friction and with one-sided rigid stop were analyzed by Chin et al. [43]. Different transition scenarios associated with grazing conditions for a periodic response of an impact microactuator were presented by Dankowicz and Zhao [56]. Banerjee et al. [17] experimentally demonstrated that simple soft impact oscillator may exhibit a peculiar dynamical behavior where the orbit abruptly jumps to a large-amplitude chaotic motion close to a grazing condition, which lasts for a very narrow range of the parameter. This abrupt onset to chaos is caused by a dangerous bifurcation in which two unstable periodic orbits, created at "invisible" grazings, take part. The rich dynamics of an impact oscillator with a one-sided elastic constraint close to grazing is demonstrated in [213], paying particular attention to the chaotic oscillations recorded near grazing frequency when a nonimpacting orbit becomes an impacting one under increasing excitation frequency. The differences between the grazing-induced bifurcations in impact oscillators with one-sided elastic and rigid constraints by a path-following (continuation) method were investigated by Jiang et al. [126].

Coexisting attractors   Vibro-impact systems can be characterized by the coexistence of different final stable states (attractors), depending on the considered set of parameters (*multistability*). In this case, which of the attractors is eventually reached depends strongly on the initial conditions [32]. Multistability is significant in suggesting the possibility of multiple operating conditions for the physical systems

under consideration [306]. The set of initial conditions leading to a certain attractor is called basin of attraction. The shape of the basin reflects the nature of the behavior of the system. A basin with a smooth shape indicates periodic dynamics while a basin with fractal boundaries suggests either a complex mixture of different dynamical patterns or a coexistence of periodic solutions [144]. The results obtained by Błażejczyk-Okolewska and Kapitaniak [32] showed that some attractors cannot be reached if their basins of attraction are too small and the noise forces the trajectories out of them towards other attractors with larger basins. Depending on the specific system requirements and objectives, switching between co-existing attractors should either be avoided to increase operational lifetime or desired to rapidly bring the system from one stable state to another [50].

1.5   Control strategies for vibro-impact systems

Potential collisions between mechanical components can cause noise, disturbing vibrations, wear and fatigue, leading to reduced efficiency or even failure of the device. As concerns seismically isolated civil structures, the consequences of potential pounding can range from local slight nonstructural to serious structural damage or even collapse. Therefore, in general, impact is seen as a negative aspect to avoid, as far as possible.

Damage because of large displacements   In the context of civil engineering, seismically isolated structures, due to the greater flexibility offered by the isolators at the base, are expected to experience large horizontal displacements relative to the ground, especially under near-fault (NF) earthquakes, characterized by long-period pulses. These large displacements, on the one hand, can seriously damaged the isolation system by exceeding its limit deformation, on the other, can lead to pounding with surrounding moat walls or adjacent structures if the available seismic gap size is not sufficient.

Seismic gap   A first possibility to reduce the risk of pounding consists in providing an adequate clearance at expansion joints in bridges, around base-isolated structures and between adjacent structures [26, 103, 125, 157, 215, 289]. When a sufficient gap is provided, however, the possible permanent deformation, or rupture, of the isolation system must be taken into account.

Inner and outer pounding   In order to prevent the damage of the isolation system, the displacements should be limited. This objective could be achieved, for example, by inserting suitable obstacles, which can be placed at a certain distance (gap) from the structure to be protected (*outer pounding*, [14]) or can be incorporated into the isolation system (*inner pounding*, [14]). In this latter case, the built-in buffer (self-braking) mechanism prevents pounding of the isolated structure with the surrounding structures and limits the possible pounding (if any) to be only within the own body of the isolator. Some isolation systems include self-braking mechanisms which serve as end-stops, limiting their displacement. Sliding isolator bearings, for example, have a restraining rim along the perimeter of the sliding

plate to prevent the slider from exceeding the displacement capacity and dropping off the sliding surface [18, 75]. Also the High Damping Rubber Bearing (HDRB) devices are inside self-braking seismic isolators (by constitutive law), due to their strong nonlinearities and stiffening characteristics at large shear strains, because of a strain crystallization process in the rubber [262, 288, 302]. Alternatively, the maximum stroke of rubber bearings can be limited using supplemental spring and damping devices [309]. In the Rolling Isolation System (RIS), proposed by Harvey et al. [98] and Harvey and Gavin [96, 97], the displacement of the steel spheres encapsulated between convex surfaces is limited by means of a lip, located at the edge of each rolling surface, which acts as stiff end-stop. The roll-n-cage (RNC) isolator [114, 115, 117, 118] has a built-in buffer (braking) mechanism that limits the isolator displacement under extreme earthquakes and prevents adjacent structural pounding.

Other types of control strategies   Alternatively to the introduction of obstacles, which may lead to possible pounding, or when it is not possible to guarantee a sufficient seismic gap, such as in densely built metropolitan areas, the seismic-induced displacements can be limited including other types of (passive, active, semi-active, hybrid) control strategies. The control devices can be installed on the single building or between adjacent structures, in order to reduce the vibrational response of the main individual structure and avoid undesirable interactions with adjacent structures (pounding) [2, 21, 23, 24, 46, 122, 138, 209, 227, 231, 297, 301, 305, 310, 311].

Damage because of large accelerations   Very often, especially when base-isolation is used as retrofitting strategy for existing structures in metropolitan zones, the width of the provided seismic gap is limited due to practical constraints. Consequently, the possibility of impact against the surrounding moat walls or adjacent structures during severe earthquakes, and its likely consequences, must be taken into account. Potential pounding can produce detrimental effects on the effectiveness of seismic isolation [140, 222]. In particular, the occurrence of impact, either with the surrounding moat wall or with adjacent buildings, causes an increase in both floor accelerations and interstory deflections. The increase in both accelerations at floor levels and displacements between stories can impair not only the operation of the structure itself, but also the functionality of any equipment housed in the structure [6, 140, 190, 211]. In particular, the existence of high spikes in the acceleration response, in correspondence of the floors where pounding occurs, and whose amplitude is influenced by impact rigidity, may affect floor response spectra and thus the response of vulnerable equipment housed in the buildings [52, 224].

Deformable shock absorbers   When it is not possible to avoid the occurrence of impact, the side effects induced by the collisions against rigid obstacles can be mitigated reducing the impact stiffness, by interposing deformable shock absorbers. Anagnostopoulos [6] investigated the effects of pounding in several adjacent buildings due to strong earthquakes and found that the interposition of soft viscoelastic materials between two adjacent structures can reduce the effects of pounding significantly. The effectiveness of rubber bumpers as mitigation measure for pounding of

seismically isolated buildings was numerically investigated in [223, 224]. The use of polymer bumpers in the suppression of pounding forces between colliding buildings, considering different types of pounding force models, was studied by He et al. [99]. The results showed that polymer bumpers can reduce maximum values of pounding force but increase pounding times and the viscoelasticity of bumper materials has a certain range of influences on pounding force responses. The application of polymer elements placed between the colliding members so as to mitigate earthquake-induced pounding between adjacent steel structures in series was studied experimentally in [242], considering different dynamic characteristics of the structures and various in-between distances. The effectiveness of rubber shock-absorber model in reducing pounding response in the adjacent planar structures due to the earthquake, was demonstrated by Trung et al. [261]. The mitigation of impact effects between bridge segments or at the restrainers' ends using shock absorbers was investigated by Abdel Raheem [1]. The natural rubber shock absorber can smooths the sudden changes of stiffness during poundings, and prevents to some extent, the acceleration peaks due to impact. Furthermore, the reaction forces at the pier bases and the pounding forces exerted on the superstructure can be satisfactorily reduced. The study carried out by Jankowski at al. [123] showed that the bridge behaviour, in the presence of collisions between adjacent superstructure segments, can be effectively improved by placing hard rubber bumpers between segments and by stiff linking the segments one with another. An extensive investigation on the effectiveness of combining rubber bumpers as a shock absorbing device along with Shape Memory Alloy (SMA) or steel cable restrainers to mitigate pounding and unseating damages on multiple-span bridges subjected to spatially varying ground motions is presented in [239]. The results indicated that the SMA restrainers combined with rubber bumpers could lead to better performance in terms of reduction of joint opening and mitigation of large pounding forces. In [296] an experimental study on the transverse pounding reduction of a high-speed railway (HSR) simply-supported girder bridge using rubber dampers was presented. The experimental results showed that the rubber bumpers are effective on mitigating the adverse seismic responses caused by the pounding. The structural acceleration response and pounding forces due to collisions between adjacent segments of a highway bridges with base-isolated rubber bearings in severe seismic events can be effectively reduced also using magnetorheological (MR) dampers [89]. A pair of symmetric linear viscoelastic end-stops was used by Sun et al. [254] to improve the performance of a SDOF nonlinear suspension system under primary resonance conditions, which has cubic nonlinearity.

Response scenarios and control   The study of the behavior of vibro-impact systems, allowing to highlight possible issues associated with the occurrence of impact, is necessary to identify suitable strategies to mitigate and control the response of such systems. There is therefore a close link between the study of the nonlinear dynamics and the control of vibro-impact systems. Several authors proposed different strategies for the control of unstable orbits, bifurcation, co-existing orbits and chaos on the basis of the study of practical problem involving collisions. By properly selecting the parameters which characterize the vibro-impact problem, it is possible to guide the behavior of the system, in order to avoid certain scenarios and encourage others,

and thus exploit the occurrence of impact with beneficial effects. Bolotnik and Melikyan [33] proposed a time-optimal feedback control, for a simple vibro-impact system consisting of a particle moving on a line segment between two rigid stops and undergoing elastic impacts against these stops, by driving the particle from an arbitrary initial state to a prescribed terminal position is constructed. Considering two periodically forced oscillators that can interact via soft impacts, Brzeski et al. [34] showed that with properly selection of the systems' parameters, such as the gap between the systems or/and the phase shift of external excitation, it is possible to decrease the number of coexisting solutions via discontinuous coupling. A method for controlling the persistence of a local attractor in the near-grazing dynamics of an impact oscillator was presented in [54, 55]. The Ott–Grebogi–Yorke (OGY) method was used by de Souza and Caldas [59] to stabilize a desired unstable periodic orbit embedded in the chaotic invariant sets of mechanical vibro-impact systems by applying a small perturbation on an available control parameter. Gritli and Belghith [86] proposed a state-feedback control law designed based on the OGY approach in order to control chaos exhibited in the impulsive hybrid non-autonomous linear dynamics of a SDOF impact mechanical oscillator with a single rigid obstacle. Considering the same system, Gritli [85] adopted a state-feedback controller for the robust stabilization of the master-slave synchronization error and the Linear Matrix Inequality (LMI) approach for the design of stability conditions. A similar control strategy was proposed by Turki et al. [264, 265] for a periodically forced SDOF impact oscillator with two asymmetric rigid end-stops. Gutiérrez and Arrowsmith [91] considered a representative model of the doubly constrained impacting system and studied the control strategies, based on the OGY scheme and applied to both numerical and experimental models, for preservation and annihilation of experimental and analytical resonant periodic orbits. A two-sided damping constraint control strategy was proposed by Hao et al. [95] to improve the performance of the quasi-zero stiffness (QZS) isolator. The proposed control approach can largely lower the isolation frequency while enhancing the effectiveness of isolation in high frequencies and preventing the severity of end-stop impacts. Based on the analysis of two-parameter bifurcations and basins of attraction, the authors found that the key issue to realize such control objective, is the suppression of period-3 solutions that coexist with the desired period-1 orbits. Lee and Yan [148] proposed a position control method for an impact oscillator under asymmetric double-side end stops, which can control and keep the stable or unstable (chaotic) impact oscillators in a desired position. Lenci and Rega [150] studied the problem of reducing the chaotic response of an inverted pendulum with rigid unilateral constraints. They showed that a significative reduction of the region of chaotic response can be obtained by suitably adjusting the shape of the excitation. In particular, this can be obtained by applying two equal and opposite impulses plus a regular excitation. An impulsive control method was developed in [275] to stabilize the chaotic motions in a class of vibro-impact systems, by implementing the pulses just when the impact occurs. In [171] Luo et al. studied the dynamics of a two-degree-of-freedom impact oscillator in which the maximum displacement of one of the masses is limited to a threshold value by the symmetrical rigid stops, with special attention to periodic-impact motions and bifurcations. Chaotic-impact motions are suppressed to minimize their adverse effects by using external driving force, delay feedback and feedback-based

method of period pulse. The results of the analysis carried out by Sun et al. [254] showed that by properly designing the dynamic parameters of viscoelastic end-stops, the relative displacement response of a SDOF nonlinear suspension system can be effectively suppressed and the jump can be eliminated for both hardening and softening primary isolators. Suitable choices of pairs of bumpers and gaps, that allows to reach a trade-off between two conflicting objectives, namely, control of excessive displacements and control of excessive accelerations in a base-isolated SDOF with two-sided deformable constraints, were suggested in [14].

Vibro-impact as passive control strategy   The occurrence of impact can also be used as control strategy to mitigate the structural response. Vibro-impact systems can be used as absorbing sources of undesirable vibrations of structures, machines, and multi-storey buildings [110]. Some well-known examples are represented by the impact dampers and the Pounding Tuned Mass Dampers (PTMDs), whose behavior has been the subject of experimental, analytical and numerical investigations.

An impact damper is a freely moving mass, constrained by stops, located on a dynamic structural system to be controlled [154]. As the main system is excited, the impact mass moves relative to the structure resulting in impacts between the mass and the stops, transferring momentum from the structure to the impact mass, and dissipating energy as heat, noise and high frequency vibrations. On the other hand, the occurrence of collisions gives rise to discontinuity and strong nonlinearity [39]. In order to reduce the acceleration spikes imparted to the structures, a buffer region can be incorporated between the mass and the stop at the point of impact [154]. Compared to a rigid impact damper, the buffered impact damper not only significantly reduces the accelerations, contact force and the associated noise generated by a collision but also enhances the level of vibration control. Application of the impact dampers for suppressing forced vibrations was studied in [3] with changing the mass ratio and restitution coefficient.

Pounding Tuned Mass Damper (PTMD) is a control system obtained by combining a traditional Tuned Mass Damper (TMD) with the impact damper. It thus exploits the occurrence of collisions or impacts with viscoelastic materials to efficiently absorb and dissipate the vibration energy of the primary structures to be controlled. An experimental study on the use of a PTMD system to suppress the undesired vibrations of a submerged cylindrical pipe was carried out by Jiang et al. [127]. The results showed that the PTMD system is effective and efficient to suppress the forced vibrations of the submerged cylindrical pipe at the tuned frequency and is also robust over a range of detuning frequencies. The effectiveness of PTMDs as control strategies to reduce the response of pipeline structures, was also investigated, both numerically and experimentally, by Song et al. [243]. The use of PTMDs to control the wind-induced vibrations of power transmission tower was studied in [258]. Results showed that the PTMD is very effective in reducing the wind-induced vibration and the vibration control performance improves as the external wind load increases. The PTMD was found to be very effective in reducing also the vibrations of power transmission tower under multi-component seismic excitations [259]. The non-smooth dynamics of a Tuned Mass Damper system with stiff lateral stops was studied by van Til et al. [266], using an alternating

frequency/time harmonic balancing (AFT-HB) method. The control performance of pounding tuned mass damper (PTMD) in reducing the dynamic responses of SDOF structures was investigated in [292], taking into account the influence of material properties and contact geometries for PTMD, as well as the robustness of the device. In [280] Wang et al. proposed a single-side PTMD in which the pounding boundary covered by viscoelastic materials is simply added to one side of the tuned mass. Unlike the conventional PTMD, the gap between the tuned mass and the viscoelastic pounding boundary is zero. They verified the control performance of the proposed PTMD through both experimental and numerical investigations. The same control system was proposed to mitigate vortex-induced vibrations of a bridge deck [281]. Yin et al. [300] studied, through numerical simulations, the effectiveness of a new pounding tuned mass damper (PTMD), compared to a traditional TMD, to reduce the traffic-induced bridges vibrations, considering the road surface conditions. Comprehensive numerical simulations of the wind/traffic/bridge coupled system with multiple PTMDs (MPTMDs) were performed by Yin et al. [300], considering different numbers and locations, mass ratio, and pounding stiffness of MPTMDs. A PTMD was also proposed by Zhao et al. [308] to reduce the wind-induced vibrations in cantilevered traffic signal structures. Semi-active vibration absorbers (SAVAs), including rubberized stops that limit the absorber mass motion, were proposed by Arena et al. [15] to suppress large amplitude oscillations in container cranes during maneuvers and wind forcing.

Vibro-Impact Nonlinear Energy Sinks (VI NESs) were used by Nucera et al. [208] to control the seismic-induced vibrations of a two degree-of-freedom primary linear system. The VI NESs can passively absorb, at a fast time scale, and locally dissipate a significant portion of the seismic energy of the primary structures to which they are attached. Furthermore, vibro-impacts cause a redistribution of seismic energy from lower to higher structural modes of the integrated system, resulting in a reduced response of the primary structures, since higher structural modes generally possess lower amplitudes of vibration, and, in addition, dissipate energy more efficiently than lower structural modes.

Wang et al. [279] studied, numerically and experimentally, the effectiveness of a Pendulum-Pounding Tuned Mass Damper (PPTMD), consisting of a tuned pendulum mass and a pounding boundary next to the equilibrium position of the pendulum mass, to mitigate the response of a single degree-of-freedom structure under various excitations. A layer of viscoelastic materials is attached on the pounding boundary to dissipate the vibration energy through impacts. They found that the PPTMD still achieves considerable control performance even if the frequency of the controlled structure is varied in a wide range.

1.6   Modeling of vibro-impact systems

The modeling of vibro-impact systems is a crucial aspect in order to study and predict their behavior.

Experimental vs. Numerical modeling   The problem can be studied resorting to physical (or experimental) and numerical models. Actually, these two types of

modeling, equally important, are intimately linked to each other, interact and feed each other. On the one hand, the experimental investigations are used to validate the numerical predictions and modeling and can also highlight behaviors which can guide subsequent numerical studies. On the other hand, the numerical simulations, once proven the ability of the model to reproduce the experimental results, are useful tools which allow to interpret the experimental outcomes and to extend the range of investigation, considering values of the parameters not investigated experimentally. Furthermore, the results of the numerical simulation are essential to guide the design of experimental setup and tests.

SDOF vs. MDOF models The study of vibro-impact systems can be carried out resorting to more or less complex models, depending on the particular problem studied, ranging from continuous [11, 71, 74, 191, 199, 272] to lumped systems with one [9, 10, 13, 14, 50, 112, 113, 152, 162, 173, 184, 185, 204, 216, 217, 232, 237, 238, 254, 274, 295] or more [29, 47, 172, 174, 176, 177, 179–182, 256, 273, 291] degrees of freedom. The use of simple Single-Degree-Of-Freedom (SDOF) model allows to identify, in a simple manner, the fundamental and general aspects which characterize the nonlinear non-smooth vibro-impact dynamics and to provide conceptual insights which are fundamental for the study of more complicated systems, such as Multi-Degree-Of-Freedom (MDOF) systems. It is worth noting that the use of complex models entails the risk of making less visible the influence of the various parameters of the model on the response in general and on the parameters of the impact in particular.

Hard vs. soft impact modeling When dealing with vibro-impact dynamics, resorting to numerical simulations, one of the crucial problems is represented by the selection of appropriate impact models [30]. The classical approach, assumes infinitely small time of the contact between non-deformable colliding bodies (*hard impact*) [30]. The impact is modeled using the momentum conservation principle and the energy loss during impact is represented by a constant value of the coefficient of restitution s, defined as the ratio between the post- ($\dot{\delta}^+$) and the pre-impact ($\dot{\delta}^-$) velocities [77, 82, 252]:

$$s = -\frac{\dot{\delta}^+}{\dot{\delta}^-} \tag{1.1}$$

The coefficient of restitution, thus defined, attains values between 0 and 1. In particular, for a fully elastic contact is equal to unity, while for a fully plastic contact is null; in this last case the kinetic energy is entirely converted to heat by work done in deforming the objects.

Impact can be modeled also by resorting to a force-based approach [129], assuming the finite nonzero contact time and considering the deformation of the colliding bodies (*soft impact*) [30]. In this approach, which more accurately describes the process of collision, the contact phenomenon is simulated through suitable more or less sophisticated force-penetration laws. A comprehensive literature survey on the contact modeling techniques is presented in [16, 77, 78, 81, 186, 200, 241]. The simplest model is represented by the linear spring element, which assumes a linear relation between the contact force F_N and the penetration δ (Fig. 1.8a), not taking

into account the energy loss during the impact:

$$F_N = K\delta \tag{1.2}$$

Another well-known contact force model, which, in turn, does not account for energy dissipation, is the Hertz contact model [101, 226], represented by a nonlinear spring element, in which the normal contact force F_N is expressed as a nonlinear power function of the penetration δ (Fig. 1.8b):

$$F_N = K\delta^n \tag{1.3}$$

In Eq. 1.3, K and n are the contact stiffness parameter and the nonlinear power exponent determined from material and geometric of the contact surfaces. One advantage of the Hertz contact law, compared to the Hooke law, is that it considers the geometric and material characteristics of the contacting surfaces, which are of particular importance in the contact dynamic responses [186]. The power exponent n is typically equal to $3/2$ for the case where there is a parabolic distribution of contact stresses [76]. For two spheres in contact, the generalized stiffness parameter is a function of radii of the spheres i and j and the material properties as [82]:

$$K = \frac{4}{3(\sigma_i + \sigma_j)} \left[\frac{R_i R_j}{R_i + R_j} \right]^{\frac{1}{2}} \tag{1.4}$$

where the material parameters σ_l $(l = i, j)$ are given by:

$$\sigma_l = \frac{1 - \nu_l^2}{E_l} \tag{1.5}$$

and the quantities ν_l and E_l are, respectively, the Poisson's ratio and Young's modulus associated with each sphere. For contact between a sphere i and a plane surface body j, the generalized stiffness parameter K depends on the radius of the sphere and the material properties of the contacting surfaces, and is expressed as [76]:

$$K = \frac{4}{3(\sigma_i + \sigma_j)} \sqrt{R_i} \tag{1.6}$$

By definition, the radius R_i is negative for concave surfaces and positive for convex surfaces [101].
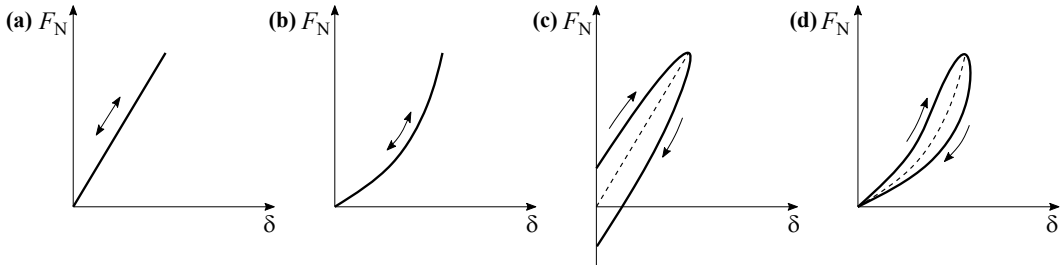

Figure 1.8. Normal contact force vs. penetration laws for: **a** linear spring element; **b** Hertz non-linear spring element; **c** Kevin-Voigt model; **d** Hertzdamp model.

In order to overcome the limitations of the pure elastic contact force models, dissipative contact force models were proposed to take into account the energy loss during the contact process. Among these, one of the first proposed was the linear Kelvin-Voigt model which combines a linear spring with a linear damper, arranged in parallel [82] (Fig. 1.8c). The normal contact force is expressed as:

$$F_\mathrm{N} = K\delta + D\dot{\delta} \tag{1.7}$$

where D is the damping coefficient of the damper, and $\dot{\delta}$ represents the relative normal contact velocity [77,81]. The existence of the damping component causes that, at the beginning of the contact process, the damping force is not null. Furthermore, at the end of the restitution phase, the relative velocity, and thus the contact force, is negative meaning that the colliding bodies attract each other, but this does not make sense from a physical point of view. Another limitation of the model, not fully consistent with reality, is that the assumption of a constant damping coefficient results in a uniform dissipation during the impact time interval. Despite these weaknesses, the Kelvin-Voigt model has been used by a several researchers [66–69, 137].

To overcome the drawbacks of the Kelvin-Voigt model, modified versions have been proposed by several authors [60, 108, 146, 147, 186, 307]. Hunt and Crossley [108] proposed a compliant contact force model in which the nonlinear elastic Hertz's element is combined with a nonlinear viscoelastic element:

$$F_\mathrm{N} = K\delta^n + \chi\delta^n\dot{\delta} \tag{1.8}$$

where the hysteresis damping factor χ, which depends on the generalized stiffness parameter K, the coefficient of restitution s (Eq. 1.1) and the initial contact velocity $\dot{\delta}^-$, is given by:

$$\chi = \frac{3K(1 - s)}{2\dot{\delta}^-} \tag{1.9}$$

Since the damping term is expressed as a function of indentation, the contact force is null both at the beginning and at the end of the contact process (Fig. 1.8d).

The applicability of *soft* and *hard impact* models in modeling of the vibro-impact systems was discussed by Błażejczyk-Okolewska et al. [30], deriving the conditions under which both methods are equivalent in the sense of the same rate of energy dissipation and discussing the advantages and disadvantages of both models. They showed that both methods give the same results when considering a stiff base, whereas in the case of an elastic base, the hard impact model leads to wrong results.

One-sided vs. Two-sided constraints   Some of the existing studies on vibro-impact dynamics deal with the problem of the impact against a single rigid or soft obstacle (one-sided constraints) [29, 47, 50, 113, 174, 177, 181, 184, 185, 216, 217, 232, 237, 238, 272]. Others consider the presence of two rigid or soft obstacles (two-sided constraints) [9, 10, 13, 14, 112, 152, 162, 173, 176, 180, 182, 204, 254, 256, 274, 291, 295]. It is worth noting that the literature on the vibro-impact systems with two-sided soft constraints has developed in more recent years.

1.7   Motivations

Despite, as illustrated in the previous sections, vibro-impact dynamics has been the subject of intense study and broad interest, this topic still deserves attention. Some of the existing studies available in literature are only numerical, others experimental and only a few deals with the subject resorting both to experimental and numerical investigations [9, 10, 13, 14, 17, 50, 112, 113, 162, 163, 165, 185, 213, 216, 232]. As concerns the dynamics of base-excited Single-Degree-Of-Freedom (SDOF) vibro-impact systems with two-sided constraints, some, but not all, phenomena that may occur have been highlighted and studied, in more or less depth, and some control strategies have been proposed, but there are still many things to explore. Furthermore, as concerns the modeling, in many cases, the impact phenomenon is still modeled resorting to the coefficient of restitution, without taking into account the deformability of impacting bodies at the interaction zones.

1.8   Objectives and original contributions

The main objective of this Ph.D. thesis is to characterize, in a systematic and transversal way, the nonlinear non-smooth response of a SDOF vibro-impact system with two-sided deformable and dissipative constraints under base excitation. Furthermore, based on the results obtained studying the behavior of such vibro-impact system, another aim of this study is to give some preliminary control-oriented indications. Extensive parametric analyses, of both experimental and numerical nature, are used for these purposes.

The nature, both experimental and numerical, of the study represents the first original contribution of this Ph.D. thesis. The numerical and experimental modeling are two instruments, equally important, used in parallel, that interact and feed each other. On the one hand, the experimental investigations are used to validate the numerical predictions and modeling. Furthermore, they can also highlight behaviors which can guide subsequent numerical studies. On the other hand, the numerical simulations, once proven the ability of the model to reproduce the experimental results, are useful tools which allow to interpret the experimental outcomes and to extend the range of investigation. Furthermore, the results of the numerical analyses are essential to guide the design of experimental setup and tests.

Another important aspect that characterizes this Ph.D. thesis is the intimate link between the study of the response scenarios and control problem. The study was inspired by the practical problem of large displacement in base-isolated systems. With the aim of mitigating the system response (displacements and accelerations), the first step was that of studying, through numerical and experimental parametric analyses, the influence of the fundamental parameters that characterize the problem on the system response. This allowed to identify different response scenarios that can occur varying the involved parameters. The study of the scenarios enabled to highlight interesting aspects related to the nonlinear non-smooth response of the system, but also to make considerations about vibration control. On the other hand, reasoning about the control problem, brought out interesting considerations about the response scenarios.

As concerns the modeling, the study is carried out considering a simple system (SDOF), in which both the damper and the bumpers are modeled by a viscoelastic model (Kelvin-Voigt model). The adoption of an elementary system allows to identify and study, in a simple manner, the fundamental aspects which characterize the nonlinear non-smooth vibro-impact dynamics without resorting to complex models. Simple systems can provide conceptual insights which are fundamental for the study of more complicated systems. The SDOF model is considered adequate to simulate the behavior of equipment devices, bridge decks, and buildings representing a very stiff superstructure, where the maximum acceleration spikes are observed at the base level, closest to the point of impact. The use of this model, however, does not allow to include the effects of the excitation of higher modes, which is a major consequence of impact in base-isolated buildings. Despite its relative simplicity, the SDOF vibro-impact model with linear components (damper and bumpers) exhibited complex nonlinear dynamics and allowed to highlight a wide variety of behaviors and phenomena, with different types of primary and secondary resonances and periodic, quasi-periodic and chaotic motion.

The adoption of a soft impact model (Kelvin-Voigt model), although quite simple, allowed to take into account the dynamics of the bumpers and to more accurately describes some phenomena related to the process of collision, such as the deformation of the obstacles, otherwise not observable by resorting to the hard impact model. Furthermore, this modeling is more suitable to simulate the bahavior of real shock absorbers, which are more or less deformable [30], and when dealing with the control problem. The inclusion of other sources of nonlinearity, such as those associated with the behavior of the damper, probably will change something or will allow to highlight other features. The adopted simple model, however, has proven to be satisfactory for the purposes of this study, being able to highlight the peculiarities of the problem.

Similar models have been studied in literature, but not in a such a systematic way, resorting to extensive parametric analyses, of both experimental and numerical nature, and different types of representations. Some of the phenomena and scenarios that can occur in the response of SDOF vibro-impact systems with two-sided constraints have already been highlighted. However, there are other aspects, investigated in this thesis, that, to date, have been little deepened and which deserve more attention, such as the types of secondary resonances in the low frequency range (with right or left hysteresis or of non-regular type) which can occur, the existence of eccentric solutions, the occurrence of primary and secondary grazing and the effect null and negative gaps on the system response.

1.9   Structure of the thesis

Chapter 2. The numerical and experimental modelization of the studied Single-Degree-Of-Freedom (SDOF) vibro-impact system is described. In the first part of the chapter, the numerical model is introduced, together with the governing equations, written in terms of both physical and dimensionless parameters. The adopted contact force model, including the modeling of the bumpers' relaxation, is described. The main dimensionless parameters which influence the system response are defined and the nonlinearities sources taken into account are stated. In the second part of the chapter, the experimental apparatus is introduced, describing its main components, the considered inputs, the used sensors and acquisition system. Finally, a summary of the tests carried out, with the corresponding sensors configurations, is provided.

Chapter 3. Possible scenarios within the experimental dynamic response of the vibro-impact SDOF system are identified and described. The different scenarios were experimentally realized varying the peak table acceleration, the amplitude of the total gap between mass and bumpers and the bumper's stiffness. A comparison with the results obtained with the numerical model is performed. The existence of other scenarios, that can be obtained for values of the parameters not considered in the experimental laboratory campaign, is highlighted with further numerical analyses.

Chapter 4. The results of a more extensive and detailed numerical analysis on the scenarios that can occur in the nonlinear non-smooth response of the vibro-impact SDOF system, varying selected dimensionless parameters, are presented. The scenarios are described in a systematic way, identifying homogeneous frequency intervals, characterized by similar features in terms of number and types of limit cycles, and resorting to phase portraits, basins of attraction and Fourier spectra.

Chapter 5. The influence of the gap amplitude on the response of the SDOF vibro-impact oscillator is investigated through experimental tests, considering both positive, null and negative gaps. Particular attention is paid to the study of the effect, on the system's response, of the transition from positive to small negative gaps and of excessive negative gaps. Finally, a comparison with the results obtained with the numerical model is performed.

Chapter 6. The effect of the presence of (existing or newly added) obstacles on the response of the SDOF system is investigated through numerical parametric analyses. The aim is to understand if, by properly selecting the obstacles' parameters, it is possible to guide the system's response to achieve specific objectives, avoiding some scenarios and favouring others, and thus exploiting the occurrence of impact with beneficial effects.

Chapter 7. The main conclusions are drawn and possible future developments of this Ph.D. thesis are illustrated.

Chapters 3-6 were structured as journal papers, with their own introduction, motivations and aims, model description, results and conclusions. I am aware that this choice inevitably involves some repetitions. However, I believe that this structure, with self-supporting chapters, represents a valuable element of this thesis. The individual chapters, in fact, can be read both in the context of the thesis and independently of each other. This can help the reader, who has at hand all the necessary elements to read each chapter, without needing to look for them in the thesis.

Chapter 2

Theoretical and experimental modelization

Chapter outline In this chapter the numerical and experimental modeling of the studied vibro-impact system is described. First, the numerical model is introduced, together with the governing equations, written in terms of both physical and dimensionless parameters. The adopted contact force model, including the modelling of the bumpers' relaxation, is described. The main dimensionless parameters, which influence the system response, are defined and the nonlinearities sources are stated. In the second part of this chapter, the experimental apparatus is introduced, describing its main components, the considered inputs, the used sensors and acquisition system. Finally, a summary of the tests carried out, with the corresponding sensors configurations, is provided.

2.1 Introduction

The modeling of vibro-impact systems is a crucial aspect in order to study and predict their behavior. The problem can be studied resorting to physical (or experimental) and numerical models. Actually, these two types of modeling, equally important, are intimately linked, interacting and feeding each other constantly. On the one hand, the experimental investigations are used to validate the numerical predictions and modeling and can also highlight behaviors which can guide subsequent numerical studies. On the other hand, the numerical simulations, once proven the ability of the model to reproduce the experimental results, are useful tools which allow to interpret the experimental outcomes and to extend the range of investigation, considering values of the parameters not investigated experimentally. Furthermore, the results of the numerical simulation are essential to guide the design of experimental setup and tests.

The numerical model considered in this thesis is quite simple, with regards to the constituent elements and the number of degrees of freedom. However, despite its relative simplicity, it shows strong nonlinearities, due to the presence of clearance, the unilateral constrains and the occurrence of impact that causes abrupt changes of stiffness and damping during the contact phase.

2.2   Numerical modeling

The numerical model consists of a Single-Degree-Of-Freedom (SDOF) system, composed of a mass M and a damper D, that is constrained by two deformable and dissipative obstacles (bumpers), symmetrically located on either side of the mass (Fig. 2.1). In the following, the two bumpers will be denoted as right (B_R) and left (B_L) bumper respectively. The system is excited by a harmonic base acceleration $A_t(t) = A_G \sin \Omega t$, with amplitude A_G and circular frequency Ω. The damper D is modeled by a linear elastic element, with stiffness K, and a linear viscous dashpot, with damping coefficient C, arranged in parallel (Kelvin-Voigt model) and connects the mass with the vibrating base.
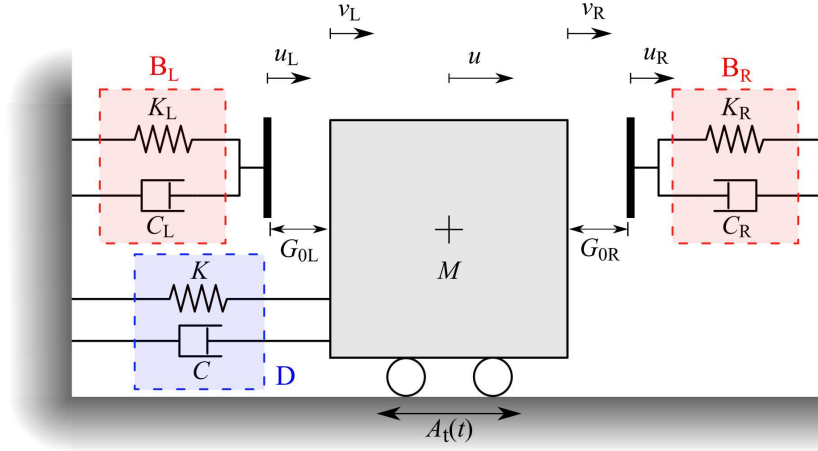
Figure 2.1. Model of the system: dimensional parameters.

2.2.1   Governing equations

During its motion, the mass can be or not in contact with the bumpers. The two conditions will be referred to as *contact* and *flight* phases respectively. The equations that govern the motion of the system can be written in the following form:

$$\begin{cases} M\ddot{u}(t) + C\dot{u}(t) + Ku(t) + F_j(t) \cdot \psi_1\left[G_j(t)\right] \cdot \psi_2\left[F_j(t)\right] = -MA_t(t) \\ F_i(t) = 0 \end{cases} \tag{2.1}$$

In Eq. 2.1, it is assumed that whether $j = L$ then $i = R$, or whether $j = R$ then $i = L$. $u(t)$ and $u_j(t)$ ($j = R, L$) are the relative displacements of the mass and of the bumpers respectively with respect to the ground and the dot ($\cdot$) denotes differentiation with respect to the time t. The absolute acceleration of the mass is therefore given by $a(t) = \ddot{u}(t) + A_t(t)$. $G_j(t)$ ($j = R, L$) is the clearance function which represents the distance, at all times, between the mass and the j-th bumper:

$$G_j(t) = G_{0j} + \Delta u_j(t) \quad (j = R, L) \tag{2.2}$$

where:

$$\Delta u_R(t) = u_R(t) - u(t); \quad \Delta u_L(t) = u(t) - u_L(t) \tag{2.3}$$

and G_{0j} $(j = R, L)$ is the j-th initial gap, that is the initial distance between the mass and the j-th bumper. When the mass is in contact with the j-th bumper $G_j(t) = 0$, otherwise $G_j(t) > 0$.

In Eq. 2.1, ψ_1 and ψ_2 represent the Heaviside functions, defined as follows:

$$\text{Contact} \quad \psi_1 [G_j(t)] = \begin{cases} 0, & G_j(t) > 0 \\ 1, & G_j(t) = 0 \end{cases} \tag{2.4a}$$

$$\text{Separation} \quad \psi_2 [F_j(t)] = \begin{cases} 0, & F_j(t) \leq 0 \ (j = R) \text{ or } F_j(t) \geq 0 \ (j = L) \\ 1, & F_j(t) > 0 \ (j = R) \text{ or } F_j(t) < 0 \ (j = L) \end{cases} \tag{2.4b}$$

where $F_j(t)$ is the contact force occurring during the contact period with the j-th bumper (Sect. 2.2.2).

Nondimensionalization

The equations of motion can be written in dimensionless form, by introducing the following characteristic quantities:

$$\omega = \sqrt{\frac{K}{M}}, \quad u^* = \frac{M A_G}{K} R_{d,max}, \quad F^* = K u^* = M \omega^2 u^* = M A_G R_{d,max} \tag{2.5}$$

namely the natural circular frequency of the SDOF system ω, the maximum relative displacement u^* and the maximum force F^* in the SDOF system in free flight (that is without obstacles) resonance condition. In Eq. 2.5, $R_{d,max}$ represents the maximum value of the dynamic amplification factor R_d [45], defined as the ratio between the amplitude of the dynamic displacement u_0 to the static displacement $u_{st,0} = M A_G / K$:

$$R_d(\xi, \beta) = \frac{u_0}{u_{st,0}} = \frac{1}{\sqrt{(1 - \beta^2)^2 + (2\xi\beta)^2}} \tag{2.6}$$

In Eq. 2.6, $\beta = \Omega/\omega$ represents the ratio between the circular frequency of the base excitation Ω and the natural circular frequency of the SDOF system ω and $\xi = C/(2M\omega)$ is the damping ratio of the SDOF system. At the resonant frequency, $\beta_R = \sqrt{1 - 2\xi^2}$ (for $\xi < \sqrt{2}/2$), from Eq. 2.6, it follows that:

$$R_{d,max}(\xi) = \frac{1}{2\xi\sqrt{1 - \xi^2}} \tag{2.7}$$

By dividing both members of Eq. 2.1 by F^*, the equations of motion can be written in the following dimensionless form:

$$\begin{cases} q''(\tau) + 2\xi q'(\tau) + q(\tau) + f_j(\tau) \cdot \psi_1 [\delta_j(\tau)] \cdot \psi_2 [f_j(\tau)] = -a_G \sin \beta\tau \\ f_i(\tau) = 0 \end{cases} \tag{2.8}$$

In Eq. 2.8, it is assumed that whether $j = L$ then $i = R$, or whether $j = R$ then $i = L$. The dimensionless relative displacements of the mass and of the right and left bumper are denoted as $q = u/u^*$ and $q_j = u_j/u^*$ $(j = R, L)$ respectively (Fig. 2.2), and the apex $(')$ indicates differentiation with respect to the dimensionless time
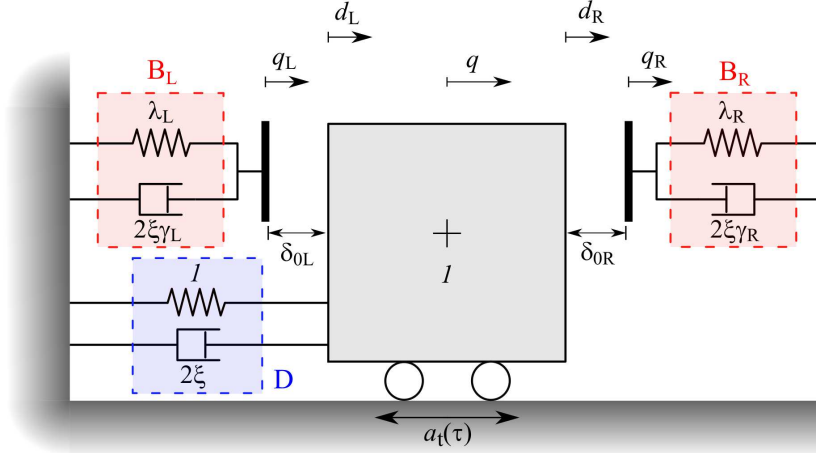
Figure 2.2. Model of the system: dimensionless parameters.

$\tau = \omega t$. $a_{\mathrm{G}} = 2\xi\sqrt{1-\xi^2}$ is the dimensionless amplitude of the base acceleration $a_{\mathrm{t}}(\tau)$. The normalized absolute acceleration of the mass is therefore given by $\alpha(\tau) = q''(\tau) + a_{\mathrm{t}}(\tau)$. The dimensionless clearance function is denoted by $\delta_j(\tau)$ and it is given by:

$$\delta_j(\tau) = \delta_{0j} + \Delta q_j(\tau) \quad (j = \mathrm{R, L}) \tag{2.9}$$

where:

$$\Delta q_{\mathrm{R}}(\tau) = q_{\mathrm{R}}(\tau) - q(\tau), \quad \Delta q_{\mathrm{L}}(\tau) = q(\tau) - q_{\mathrm{L}}(\tau) \tag{2.10}$$

When the mass is in contact with the j-th bumper $\delta_j(\tau) = 0$ (j = R, L), otherwise $\delta_j(\tau) > 0$. In Eq. 2.9 $\delta_{0j} = G_{0j}/u^*$ (j = R, L) denotes the initial dimensionless gap between the mass and the j-th bumper. Based on the adopted normalization, $\delta_{0j} = 0$ if the j-th bumper is initially in contact with the mass; for $0 < \delta_{0j} < 1$ the mass beats and deforms the j-th bumper; whereas the mass will be in free flight condition for $\delta_{0j} \geq 1$.

The Heaviside functions ψ_1 and ψ_2 assume the following expression:

$$\text{Contact} \quad \psi_1\left[\delta_j(\tau)\right] = \begin{cases} 0, & \delta_j(\tau) > 0 \\ 1, & \delta_j(\tau) = 0 \end{cases} \tag{2.11a}$$

$$\text{Separation} \quad \psi_2\left[f_j(\tau)\right] = \begin{cases} 0, & f_j(\tau) \leq 0 \ (j = \mathrm{R}) \text{ or } f_j(\tau) \geq 0 \ (j = \mathrm{L}) \\ 1, & f_j(\tau) > 0 \ (j = \mathrm{R}) \text{ or } f_j(\tau) < 0 \ (j = \mathrm{L}) \end{cases} \tag{2.11b}$$

where $f_j(\tau)$ is the normalized contact force occurring during the contact period with the j-th bumper (Sect. 2.2.2).

2.2.2   Contact force model

The two bumpers are massless and, as the damper, are modeled by a linear elastic element, with stiffness K_j (j = R, L), and a linear viscous dashpot, with damping coefficient C_j (j = R, L), arranged in parallel (Kelvin-Voigt model). The contact

force, occurring during the contact phase with the j-th bumper, is therefore given by:

$$F_j(t) = C_j \dot{u}_j(t) + K_j u_j(t) \quad (j = \text{R}, \text{L}) \tag{2.12}$$

When the mass is in contact with the j-bumper $G_j(t) = 0$ (Eq. 2.2). Consequently, from Eq. 2.3 it follows that:

$$\begin{cases} u_\text{R}(t) = u(t) - G_{0\text{R}} \\ u_\text{L}(t) = u(t) + G_{0\text{L}} \end{cases} \tag{2.13}$$

Since G_{0j} ($j = \text{R, L}$) is constant, from Eq. 2.13 it follows that, during the contact phase, the velocity of the bumper is equal to that of the mass $\dot{u}_j(t) = \dot{u}(t)$ ($j = \text{R}$, L). In terms of dimensionless parameters, Eq. 2.12 can be rewritten as follows:

$$f_j(\tau) = 2\xi\gamma_j q'_j(\tau) + \lambda_j q_j(\tau) \quad (j = \text{R}, \text{L}) \tag{2.14}$$

where $\gamma_j = C_j/C$ ($j = \text{R, L}$) is the ratio between the viscous damping coefficient of the j-th bumper and that of the damper and $\lambda_j = K_j/K$ ($j = \text{R, L}$) represents the ratio between the stiffness of the j-th bumper and that of the damper. During the contact phase $q'_j(\tau) = q'(\tau)$ ($j = \text{R, L}$) and:

$$\begin{cases} q_\text{R}(\tau) = q(\tau) - \delta_{0\text{R}} \\ q_\text{L}(\tau) = q(\tau) + \delta_{0\text{L}} \end{cases} \tag{2.15}$$

The Kelvin-Voigt model has some weaknesses [77, 78, 186, 241]. In particular, the existence of the damping component causes that, at the beginning of the contact process, the contact force is not continuous This is not realistic, because, when impact begins, both the components of the contact force must be null. Furthermore, at the end of the restitution phase, while the deformation of the bumper is null (and thus also the elastic component of the contact force), the relative velocity, and thus the contact force, is negative meaning that the colliding bodies attract each other, but this does not make sense from a physical point of view. Another limitation of the model, not fully consistent with reality, is that the assumption of a constant damping coefficient results in a uniform dissipation during the impact time interval. Despite these weaknesses, the model has been used by several researchers [66–69, 137].

Based on these considerations, in this study the change of sign of the contact force was assumed as indicator of the end of the contact phase (Eqs. 2.4b, 2.11b). The beginning of the contact was instead identified based on the value of the clearance function (Eqs. 2.4a, 2.11a).

Bumper relaxation

At the time of detachment, the bumper has a residual deformation that it will recover by dissipating energy. The dissipative component of the contact force means that the bumper recovers this deformation more slowly than a fully elastic material, for which the recovery is instantaneous. The time required to recover the residual deformation, which depends on the dissipative capabilities of the bumpers, is defined as relaxation time:

$$t_{\text{r}j} = \frac{C_j}{K_j} \quad (j = \text{R}, \text{L}) \tag{2.16}$$
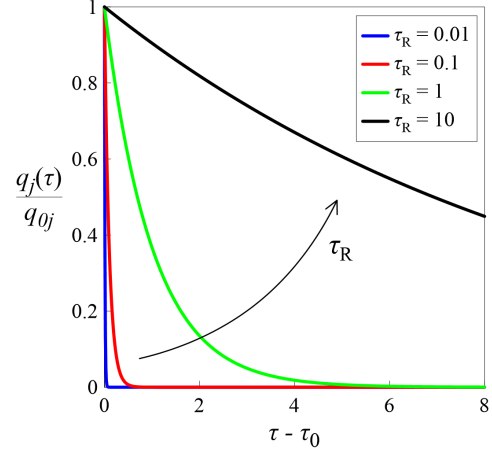
Figure 2.3. Viscoelastic recovery of the bumper deformation for different values of the relaxation time τ_{r} (Eq. 2.19a).

In dimensionless terms, Eq. 2.16 becomes:

$$\tau_{\mathrm{r}j} = \omega \ t_{\mathrm{r}j} = 2\xi \frac{\gamma_j}{\lambda_j} \quad (j = \mathrm{R}, \mathrm{L}) \tag{2.17}$$

Form Eq. 2.17 it follows that, for a fully elastic material, that is when $C_j = 0$, $\tau_{\mathrm{r}j} = 0$ ($j = \mathrm{R}, \mathrm{L}$), whereas for a fully viscous material, that is when $K_j = 0$, $\tau_{\mathrm{r}j} \to \infty$ ($j = \mathrm{R}, \mathrm{L}$).

In the proposed model, the viscoelastic recovery of the deformation of the bumper was modeled. After the detachment, the dynamics of the bumper is governed, in dimensionless terms, by the equation:

$$2\xi \gamma_j q_j'(\tau) + \lambda_j q_j(\tau) = 0 \quad (j = \mathrm{R}, \mathrm{L}) \tag{2.18}$$

which admits the following closed-form solution:

$$q_j(\tau) = q_{0j} \ e^{-\frac{\tau - \tau_0}{\tau_{\mathrm{r}j}}} \quad (j = \mathrm{R}, \mathrm{L}) \tag{2.19a}$$

$$q_j'(\tau) = q_{0j}' \ e^{-\frac{\tau - \tau_0}{\tau_{\mathrm{r}j}}} \quad (j = \mathrm{R}, \mathrm{L}) \tag{2.19b}$$

where τ_0 represents the time instant at the beginning of the relaxation phase (when the detachment from the mass occurs) and $q_{0j} = q_j(\tau_0)$ ($j = \mathrm{R}, \mathrm{L}$) denotes the corresponding residual deformation of the bumper. The bumper's velocity in the same instant is given by $q_{0j}' = -q_{0j}/\tau_{\mathrm{r}j}$ ($j = \mathrm{R}, \mathrm{L}$). From Eqs. 2.19 it can be observed that, after the detachment from the mass, which occurs when the velocity of the mass exceeds that of the bumper, the latter recovers its deformation according to an exponential law (Fig. 2.3).

For a fully elastic material ($\tau_{\mathrm{r}j} = 0$) the recovery is instantaneous, whereas a fully viscous material ($\tau_{\mathrm{r}j} \to \infty$) never recovers the deformation but it remains deformed after the detachment. In presence of both elastic and viscous components, the relaxation time is finite and, depending on the ratio of bumper relaxation time to time interval between two consecutive contacts, it may happen that the mass can impact again the same bumper when it has not yet recover all its deformation, causing a gradually increment of the gap, compared to the initial one (G_{0j}).

2.2.3 Parameters

Based on what was said in the previous sections, the dimensionless parameters that influence the response of the system are:

- Frequency ratio $\quad \beta = \dfrac{\Omega}{\omega}$

- Damping ratio $\quad \xi = \dfrac{C}{C_{\text{cr}}} = \dfrac{C}{2M\omega}$

- Dimensionless initial gap $\quad \delta_{0j} = \dfrac{G_{0j}}{u^*} \quad (j = \text{R, L})$

- Stiffness ratio $\quad \lambda_j = \dfrac{K_j}{K} \quad (j = \text{R, L})$

- Damping ratio $\quad \gamma_j = \dfrac{C_j}{C} \quad (j = \text{R, L})$

As an alternative to the damping ratio γ_j, the dissipative capabilities of the bumpers can be represented through the relaxation time $\tau_{\text{r}j}$ $(j = \text{R, L})$.

The study carried out during the doctoral course was conducted considering two equal bumpers symmetrically arranged on the two sides of the mass. It follows that $\delta_{0\text{R}} = \delta_{0\text{L}} = \delta_0$, $\lambda_\text{R} = \lambda_\text{L} = \lambda$ and $\gamma_\text{R} = \gamma_\text{L} = \gamma$ (or alternatively $\tau_{\text{rR}} = \tau_{\text{rL}} = \tau_\text{r}$).

2.2.4 Nonlinearities of the numerical model

The proposed numerical model, although both the bumpers and the damper have been modeled by a linear elastic spring in parallel with a linear viscous dashpot (Kelvin-Voigt model), is strongly nonlinear. In particular, the nonlinearities are due to the presence of clearance, the unilateral constrains and the occurrence of impact that causes abrupt changes of stiffness and damping during the contact phase. In the following this model will be referred to as Simplified Nonlinear Model (SNM).

2.2.5 Procedure for numerical simulations

In the numerical simulations, the equations of motion (Eqs. 2.8) were numerically solved using the central difference method [22], implemented with a numerical code written in Matlab. As concerns the identification of the time period in which impact occurs, this was done as follows. The beginning of the contact phase between the mass and the j-th bumper was identified based on the value of the clearance function $\delta_j(\tau)$ $(j = \text{R, L})$, as illustrated in Eq. 2.11a. In particular, impact occurs when $\delta_j(\tau) = 0$. Regarding instead the evaluation of the time instant of detachment, this was made based on the value of the contact force $f_j(\tau)$ $(j = \text{R, L})$, as illustrated in Eq. 2.11b. This choice was motivated by the necessity to overcome one of the drawbacks of the Kelvin-Voigt model, when used to model the contact, that is the existence of attracting forces after the restitution phase [77, 78, 186, 241]. Since this does not make sense from a physical point of view, in this study the change of sign of the contact force was assumed as indicator of the end of the contact phase. Furthermore, using Eqs. 2.19, also the viscoelastic recovery of the bumpers after the detachment was implemented.

2.3   Experimental modeling

Based on the results of preliminary numerical investigations, an experimental setup was designed in order to validate the numerical model through shaking table tests. In particular, as it will be shown in more detail in Sect. 2.3.5, three experimental laboratory campaigns were carried out, in 2016, 2017 and 2020 respectively. The characteristics of the physical model were designed taking into account the performances of the shaking table and considering the potential impact forces and relative displacement of the mass with respect to the table. Furthermore, the selection of the system was conditioned also by the availability of the required components for the scaled model.

2.3.1   System

The physical model of the Single-Degree-Of-Freedom (SDOF) vibro-impact system is shown in Fig. 2.4. It consists of a rigid body that can be treated as a lumped mass, an elastomeric High Damping Rubber Bearing (HDRB) isolator (damper) and two elastomeric shock absorbers (bumpers) symmetrically arranged on the two sides of the mass. The mass ($M = 550$ kg), composed of eight plates of mild steel ($68 \times 78 \times 1.6$ cm) jointed by bolts, is supported by four spherical bearings, rotating within unidirectional guides. The unidirectionality of the motion is guaranteed by a system composed by welded steel sections, bolted onto the base plate, with spherical bearings, just touching the steel angular sections bolted to the mass. The bumpers are mounted on steel plates, which are connected, by means of screws, to steel moat walls bolted onto the base plate of the shaking table.

Isolator

The High Damping Rubber Bearing (HDRB) isolator (denoted also as damper), whose dimensions are shown Fig. 2.6, consists of 27 2 mm-thick layers of rubber and 26 1 mm-thick steel shims. The height of the isolator, excluding the end plates, is 80 mm and its total diameter is 58 mm. The two end plates, with plan dimensions 100×100 mm and thickness 10 mm, permit the connection of the isolator with adjacent structures. In particular, the lower end plate is bolted onto the shaking table, while the upper end plate is centrally bolted to the lower plate of the mass (Fig. 2.4).

Bumpers

In the experimental tests, four elastomeric bumpers were considered, in the following denoted as Bk ($k = 1, 2, 3, 4$). The four bumpers were obtained from three types of elastomeric shock absorbers, with D-shape hollow section (Fig. 2.7):

- type 1: width 60 mm and height 52 mm (Fig. 2.7a);

- type 2: width 40 mm and height 22 mm (Fig. 2.7b);

- type 3: width 65 mm and height 52 mm (Fig. 2.7c).

(a)

(b)

SECTION A-A

(c)

SECTION B-B

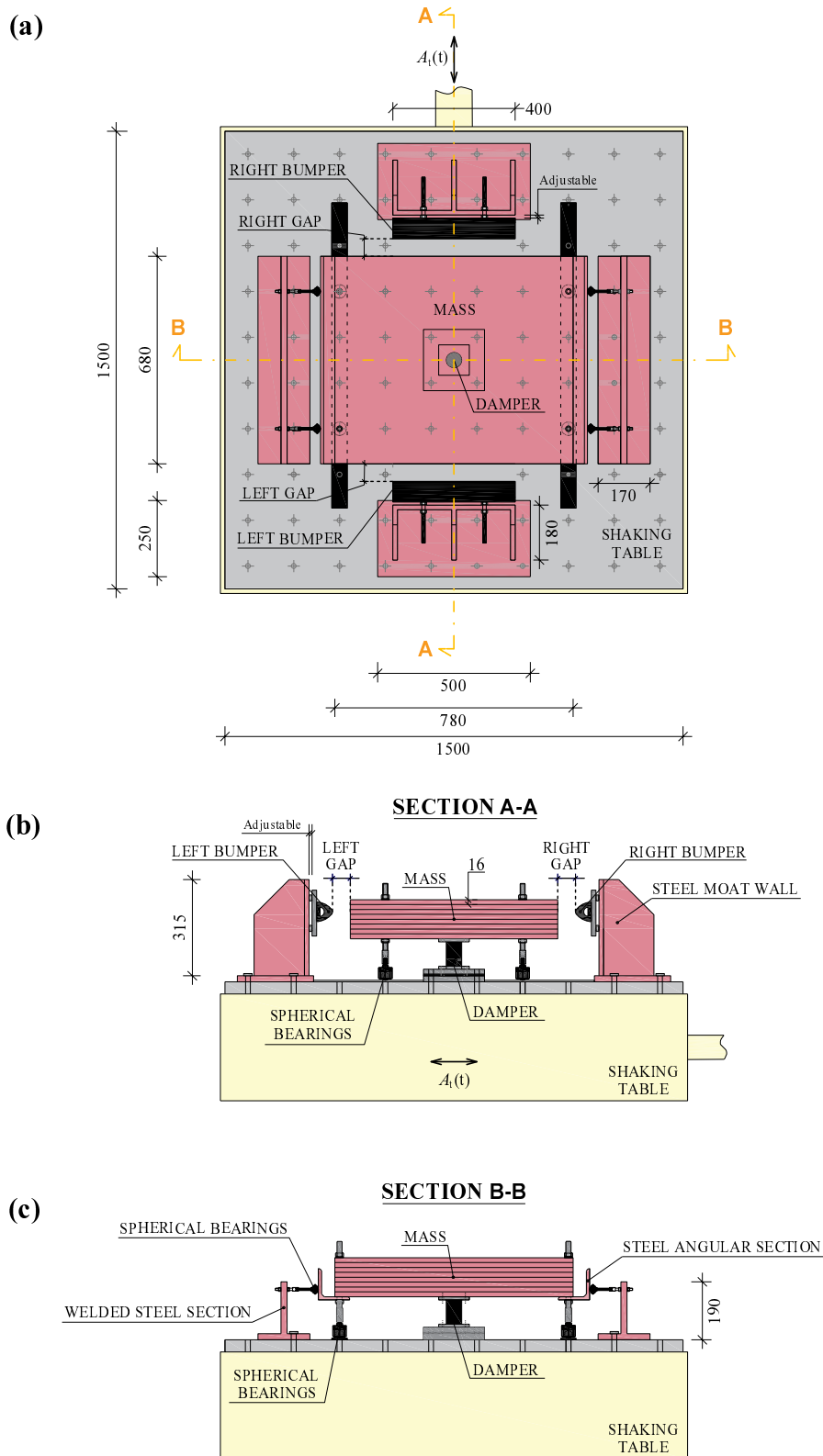**Figure 2.4.** Experimental setup: **a** plan view; **b** lateral view (Section A-A); **c** lateral view (Section B-B).
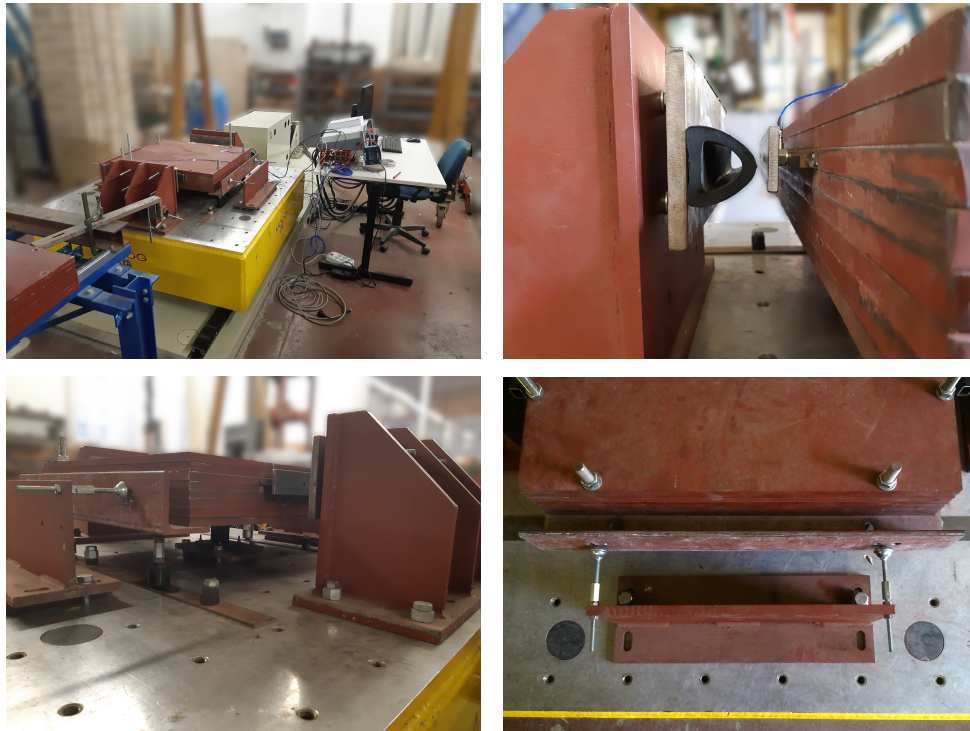
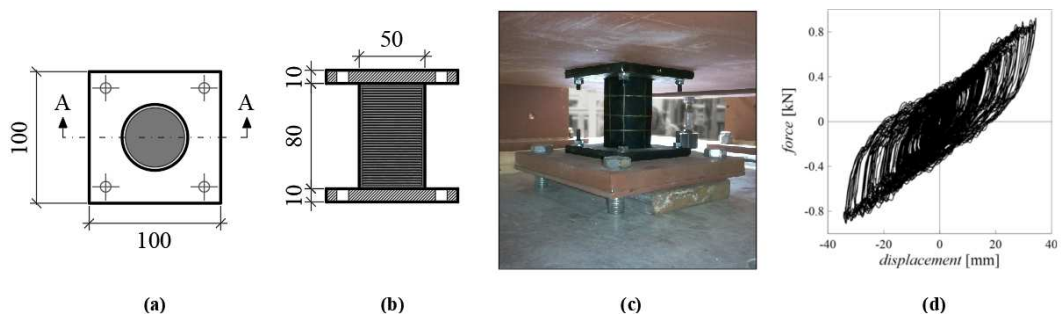**Figure 2.5.** Photos of the experimental setup.

Figure 2.6. HDRB isolator: **a** plan view; **b** side view (Section A-A); **c** photo; **d** force-displacement cycle (step-wise sine sweep signal).
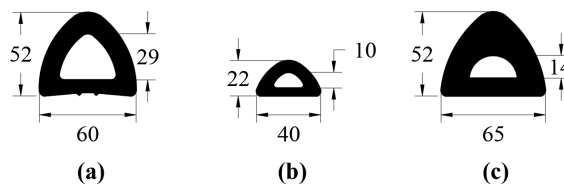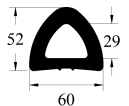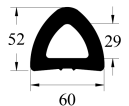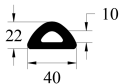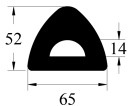

Figure 2.7. Cross sections of bumpers: **a** type 1; **b** type 2; **c** type 3.

As regards the material, the bumpers type 1 and 2 are constituted by a Styrene Butadiene Rubber Copolymer (SBR) having a hardness of 70 Shore A, while the bumper type 3 is constituted by an Ethylene Propylene Diene Monomer (EPDM) having a hardness of 75 Shore A. The bumpers B1 and B2 were obtained from bumper type 1; consequently, they have the same cross section but different contact length: $L = 100$ mm for B1 and $L = 400$ mm for B2. The bumper B3 was obtained from bumper type 2 and has contact length $L = 400$ mm. Finally, the bumper B4 was obtained from bumper type 3 and has contact length $L = 400$ mm. Table 2.1 summarizes the main features of the bumpers used in the experimental tests.

The mechanical (stiffness and damping) properties of the bumpers increase passing from B1 to B4. In particular the bumper B1 can be assumed as representative of soft (not very rigid) shock absorbers, whereas bumper B4 can be assimilated to a hard (very rigid) obstacle. The remaining two bumpers, B2 and B3, are characterized by intermediate mechanical properties.

Table 2.1. Main features of the bumpers

Bumper	B1	B2	B3	B4
Cross section				
Type	type 1	type 1	type 2	type 3
Material	SBR[a]	SBR	SBR	EPDM[b]
Hardness	70 Shore A	70 Shore A	70 Shore A	75 Shore A
Contact length L	100 mm	400 mm	400 mm	400 mm

[a] Styrene Butadiene Rubber Copolymer.
[b] Ethylene Propylene Diene Monomer.

The mechanical characterization of the bumpers was carried out in the Materials and Structures Testing Laboratory of the Department of Structural and Geotechnical Engineering of "Sapienza" University of Rome, through static and dynamic cyclic tests, using the Universal testing machine MTS 810 (Material Test System). Fig. 2.8 shows the hysteresis loops obtained in both the static and dynamic cyclic tests, considering 400 mm long samples of bumpers type 1 (Fig. 2.8a), type 2 (Fig. 2.8b) and type 3 (Fig. 2.8c) respectively. Before starting the tests, in order to obtain the contact between the actuator and the sample, alternative initial conditions were imposed of approaching equal to 3 mm or of compressive force of 200 N. As concerns the static tests, they were performed by increasing the compressive force, until a prefix value, with a specific loading and unloading velocity. The dynamic tests were performed assigning an initial compressive displacement and then subjecting the sample to programs of imposed displacement variable with sinusoidal law, at different frequencies and with a specific amplitude, for a certain number of cycles.

As concerns the bumper type 1 (Fig. 2.8a), in the dynamic tests an initial compressive displacement of about 15 mm was assigned to the specimen; subsequently,
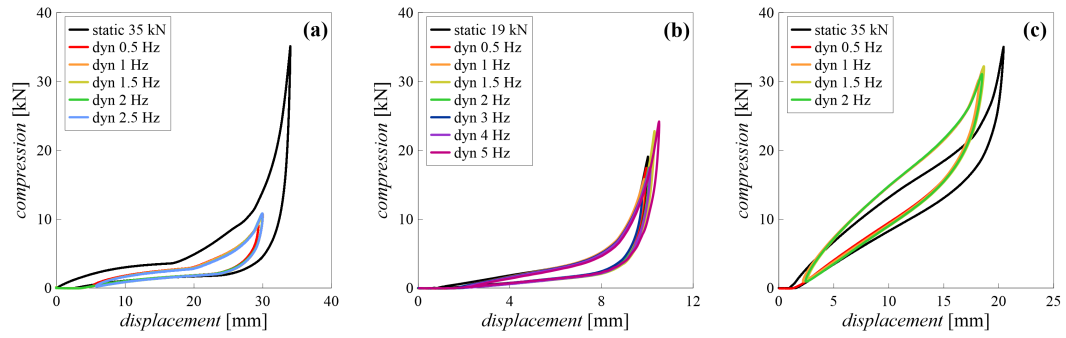
Figure 2.8. Results of static and dynamic cyclic tests (400 mm samples length): **a** bumper type 1; **b** bumper type 2; **c** bumper type 3.

an excursion in displacement, with amplitude of about ±12 mm, was imposed, in a frequency range between 0.5 and 2.5 Hz, with a step of 0.5 Hz. The "static" loop (black curve) was obtained by increasing the compressive force until 35 kN with a 8 mm/min speed. From Fig. 2.8a an initial softening behavior, followed by a hardening behavior was observed, in both "static" and "dynamic" loops. The initial softening behavior is due to both slenderness and large dimension of the internal hole and upward curvature of the contact surface of the sample (Fig. 2.7a). The "dynamic" are substantially superimposed, with only small differences at the extremes, whereas a significant difference is observed between the "dynamic" and the "static" loops. In particular, in the loading phase, the "dynamic" curves coincide with each other but not with the static cycle, whereas both the "static" and the "dynamic" curves coincide in the unloading path in the displacement range between 0 and 20 mm.

As concerns the bumper type 2 (Fig. 2.8b), in the dynamic tests an initial compressive displacement of about 5 mm was assigned to the specimen; subsequently, an excursion in displacement, with amplitude of about ±5 mm, was imposed, in a frequency range between 0.5 and 5 Hz, with a step of 0.5 Hz between 0.5 and 2 Hz, and of 1 Hz between 2 and 5 Hz. The "static" loop (black curve) was obtained by increasing the compressive force until 19 kN with a 8 mm/min speed. From Fig. 2.8b it can be observed that there are no significant variations in stiffness between the static and dynamic tests. When the displacement grows from 0 to 8 mm, the "static" and "dynamic" curves have the same slope, but do not exactly coincide in the loading path, whereas they coincide in the unloading path within the same displacement range. Some differences were observed for displacements between 8 and 10 mm.

As concerns the bumper type 3 (Fig. 2.8c), in the dynamic tests an initial compressive displacement of about 10 mm was assigned to the specimen; subsequently, an excursion in displacement, with amplitude of about ±10 mm, was imposed, in a frequency range between 0.5 and 2 Hz, with a step of 0.5 Hz. The "static" loop (black curve) was obtained by increasing the compressive force until 35 kN with a 2 mm/min speed. From Fig. 2.8c it can be observed that in the phase of initial load, the stiffness corresponding to the dynamic tests is larger than that of the static test. Furthermore, the "dynamic" cycles are substantially superimposed, with only small differences at the extremes.

The three types of bumpers globally show similar behavior. In particular, a significant increase of stiffness is observed for high values of compression load. This is due to an important change in the form of bumpers, which leads to the almost total closure of the internal hole and thus to the contact between the inner contours.

Gap

Different values of the total gap G, defined as the sum of right G_{0R} and left G_{0L} gaps respectively were considered. The distance between bumpers and mass was experimentally varied by adjusting the screws behind the plates on which the bumpers are mounted (Fig. 2.4). In the following the considered gaps will be indicated as Gj, where $j = 1, 2, 3, 4$ in the first laboratory campaigns (in particular G1 = 15 mm, G2 = 20 mm, G3 = 25 mm, G4 = 30 mm), whereas j denotes the amplitude, expressed in mm, of the total gap in the last campaign of tests. Furthermore, G∞ will be used to denote both the condition without bumpers (free flight condition) and all the situations in which the gap is large enough not to have the impact between the mass and the bumpers.

In the experimental tests both positive (G > 0), approximately null (G $\simeq$ 0) and negative gaps (G < 0) were tested. The negative gaps were realized by initially compressing the bumpers against the mass, leading to an initial pre-stress/pre-strain state in the bumpers.

2.3.2 Input

Shaking table

The experimental tests were performed using the uni-axial shaking table Moog (L081-324-011), managed by *Moog Replication Software*, at the Materials and Structures Testing Laboratory of the Department of Structural and Geotechnical Engineering of "Sapienza" University of Rome (Fig. 2.9). The table, with dimensions 1.5×1.5 m, is characterized by a maximum payload capacity of 1000 kg and a maximum excitation frequency of 100 Hz. Powered by a hydraulic cylinder controlled by servo-valves, it is equipped with horizontal guides that allow the movement along only one direction, with a maximum stroke of ± 200 mm.

Figure 2.9. The uni-axial shaking table Moog.

Input signals

The system was excited by a step-wise forward and backward sine sweep signal, that is a harmonic signal in which the forcing frequency is increased (forward sweep) and then decreased (backward sweep) over time, after a certain number of cycles n_c, within a specific frequency range and with an appropriate frequency increment Δf. In particular, using the shaking table, a signal in displacement control was applied at the base of the system, in order to impose a given constant value of peak table acceleration Ai (i = 1, 2, 3) and with a number of cycles n_c, in each sub-frequency range, sufficient to reach the steady state response. The attainment of the steady state condition was checked by verifying the convergence to the limit cycle in both hysteresis loops and phase portraits planes. In particular, three values of peak table acceleration were considered, namely: A1 = 0.03 g, A2 = 0.04 g, A3 = 0.05 g, where g is the acceleration due to gravity. For illustrative purposes, in Fig. 2.10 the time histories of the step-wise forward and backward sine sweep signal are shown for A3 in terms of both displacement (Fig. 2.10a) and acceleration (Fig. 2.10b).
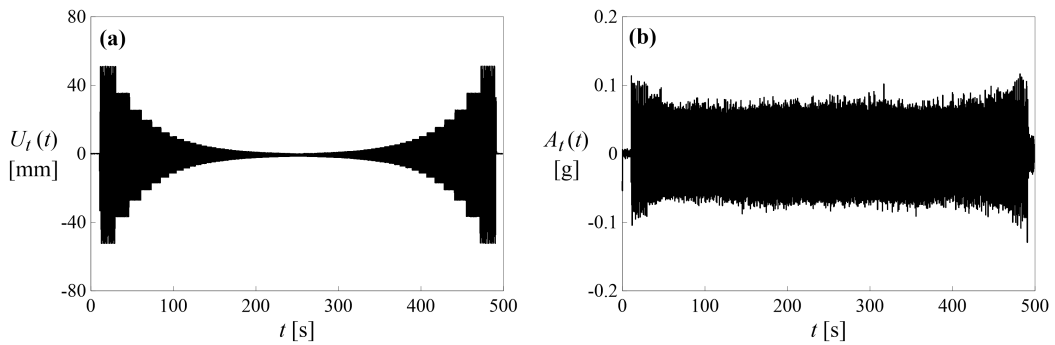
Figure 2.10. Step-wise forward and backward sine sweep signal for A3: **a** displacement; **b** acceleration.

In most tests, the sweep frequency range was between 0.5 Hz and 5 Hz, with frequency step $\Delta f = 0.1$ Hz and a number of cycles per step $n_c = 10$. In some cases, in particular for very small and negative gaps, the sweep range, the frequency step and the number of cycles were varied in order to better capture the response of the system, especially in the low frequency range (Chap. 5).

2.3.3   Sensors

The measured response quantities are the absolute accelerations and the absolute displacements of the mass, and of the table and the contact forces.

Accelerometers

The accelerations were measured by seismic ICP® accelerometers Model 393A03 by the PCB Piezotronics company (Fig. 2.11). The accelerometers have measuring range ±5 g and frequency range from 0.5 Hz to 2000 Hz.

Figure 2.11. Accelerometers: **a** mass; **b** table.

Displacement transducers

The displacements were measured by:

- SLS190 linear displacement sensors (inductive transducers) by Penny&Giles company with stroke length of 200 mm;

- optoNCDT Model ILD1402-600 laser displacement sensor by Micro-Epsilon company, with measuring range of 600 mm;

- optoNCDT Model ILD1420-500 laser displacement sensor by Micro-Epsilon company, with measuring range of 500 mm.

In particular, in the first two laboratory campaigns, the inductive transducer SLS190/200 was used to measure the table absolute displacement (Fig. 2.12a), whereas the optoNCDT ILD1402-600 laser sensor was used to measure the absolute displacement of the mass (Fig. 2.12b). In the last campaign of tests, the absolute displacements of both the table and the mass were measured by the optoNCDT ILD1420-500 and the ILD1402-600 laser sensors respectively.
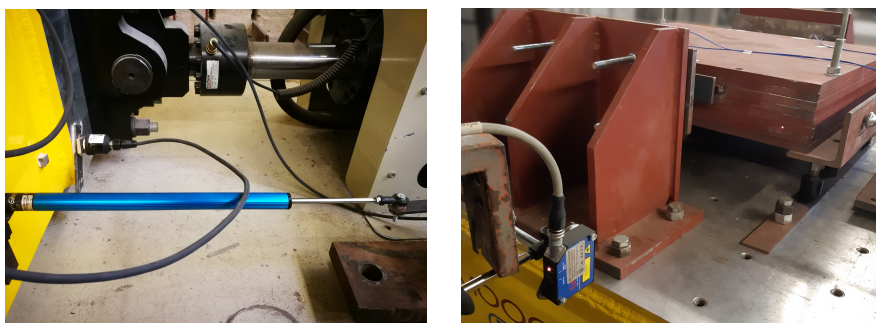
Figure 2.12. Displacement transducers: **a** SLS190/200; **b** optoNCDT ILD1402-600.

Impact load cells

The contact forces exchanged, at the moment of the impact, between mass and bumpers were measured by the ICP® Force sensor Model 208C05 by the PCB

Piezotronics company (Fig. 2.13). These force sensors are able to measure a maximum dynamic force of 22.24 kN in compression and of 2.224 kN in tension and a maximum static force of 35.59 kN in compression and of 2.224 kN in tension. Four impact load cells were used, symmetrically mounted on the mass, two on each side (Fig. 2.13b). Between the impact load cells and the bumpers, steel plates were mounted to distribute the impact force (Fig. 2.5). In the first laboratory campaign, only accelerometers and displacement transducers were employed. In subsequent campaigns of tests, the impact load cells were added.

Figure 2.13. Impact load cells.

2.3.4   Data acquisition system

Data acquisition and synchronization was performed by means of the KRYPTON-3xSTG and KRYPTON-4xACC systems by Dewesoft company. The KRYPTON acquisition data systems, to which the sensors are connected, are combined in a single measurement chain. At one end, the chain is connected to the power supply network, at the other to the Ethernet port of the computer (Fig. 2.14). The real time visualization of the recorded signals was managed by Dewesoft X3 software, which allows also to analyze and process the data. Once the data acquisition systems are connected to the computers, the Dewesoft software automatically recognizes and setups the devices.

Figure 2.14. Data acquisition system

The signals were acquired with a sampling rate of 2000 Hz and, subsequently, a 2nd order low-pass Butterworth filter, with 30 Hz cut-off frequency, was applied to all data.

2.3.5 Experimental tests summary

During the doctoral course three experimental laboratory campaigns were carried out: in 2016, 2017 and 2020 respectively. These campaigns have constantly intersected with the numerical analyses. Each campaign, which differs from the previous for what concerns the objectives, the range of investigation and t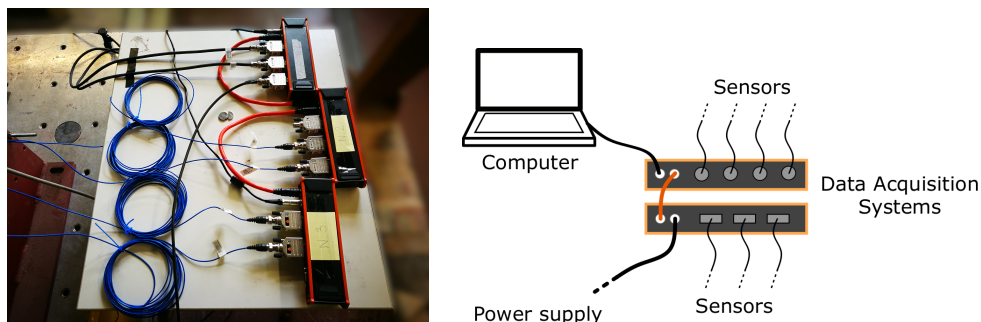he sensors setup, was motivated and designed based on the results obtained processing the data recorded in the previous tests, together with the results of the numerical investigations. The aim of each campaign was to cover the gaps left by the previous, extend the range of investigation and validate numerical results.

The series of experimental investigations considered two distinct configurations: the absence (No Bumpers, NB) and the presence (Yes Bumpers, YB) of bumpers, under the same type of excitation. Each performed test corresponds to a combination of peak table acceleration Ai, total gap amplitude Gj and bumper Bk. Table 2.2 reports the summary of the tested cases in the three campaigns. In particular, the green square, the red triangle and the blue circle denote the tests performed in 2016, 2017 and 2020 respectively.

Table 2.2. Summary of the experimental tests.

		G∞	G40	G30[a]	G25[b]	G20[c]	G16	G15[d]	G10	G4	G0	G-1	G-2	G-10
	A1	🟩🔺🔵												
B0	A2	🟩🔺🔵												
	A3	🟩🔺🔵												
	A1			🟩	🟩	🟩		🟩						
B1	A2			🟩	🟩	🟩		🟩						
	A3			🟩	🟩	🟩		🟩						
	A1			🟩	🟩	🟩		🟩						
B2	A2			🟩	🟩	🟩		🟩						
	A3		🔵	🟩🔵	🟩	🟩	🔵	🟩	🔵	🔵	🔵	🔵	🔵	🔵
	A1			🟩	🟩	🟩🔺		🟩🔺						
B3	A2			🟩	🔺	🟩		🟩						
	A3			🟩🔺		🟩		🟩						
	A1			🟩	🟩	🟩		🟩						
B4	A2			🟩	🟩	🟩		🟩						
	A3			🟩	🟩	🟩		🟩						

[a] Gap denoted as G4 in 2016 and 2017 tests
[b] Gap denoted as G3 in 2016 and 2017 tests
[c] Gap denoted as G2 in 2016 and 2017 tests
[d] Gap denoted as G1 in 2016 and 2017 tests
(🟩): 2016 tests; (🔺): 2017 tests; (🔵): 2020 tests.

In Table 2.2 the NB configuration is referred to as a B0 bumper configuration, indicating conventionally with B0 a bumper placed at an infinite distance from the mass (G∞) or, equivalently, a bumper of stiffness tending to zero, and thus representing the extreme case of absence of bumpers.

It can be observed that, in each campaign, some of the tests carried out in the previous were repeated. In particular the configuration without bumpers (B0) was tested in all experimental laboratory campaigns with the three values of peak table acceleration. As concerns the configuration with bumpers, the first experimental laboratory campaign (green square) has been relatively extended. All four bumpers were tested, considering four gap amplitudes and three values of peak table acceleration. In the second campaign (red triangle), only some of the tests carried out in 2016 with bumper B3 have been repeated. The main difference with the previous experimentation, is the addition of the impact load cells to directly measure the contact forces. Finally, based on the results of the numerical investigations, the third campaign of tests (blue circle), was designed primarily to investigate the effect of the gap, considering both large and small positive, null and negative gaps. Only one value of peak table acceleration (A3) and one bumper (B2) were considered.

Sensors configurations

Experimental campaign 1 (2016)   The absolute accelerations of the mass and the table were measured by accelerometers (Sect. 2.3.3). In particular, the acceleration of the mass was measured by two accelerometers (Fig. 2.15) and the average value of the two measurements has been taken into account. The absolute displacements were measured by a laser transducer, for what concerns the mass, and by an inductive transducer, for what concerns the shaking table.

Experimental campaign 2 (2017)   Compared to the previous experimental laboratory campaign, four impact load cells were installed on the mass, two on each side, to directly measure the contact force during the impact phases (Fig. 2.16). Between the impact load cells and the bumpers, steel plates were mounted to distribute the impact force.

Experimental campaign 3 (2020)   The main difference with the previous campaign of tests is the use of laser transducers to measure the absolute displacements of both the mass and the table (Fig. 2.17). Furthermore, the absolute acceleration of the mass was measured by a single accelerometer placed in a central position on the mass.

(a)

SECTION A-A

(b)

Figure 2.15. Sensors configuration - experimental laboratory campaign 1 (2016).
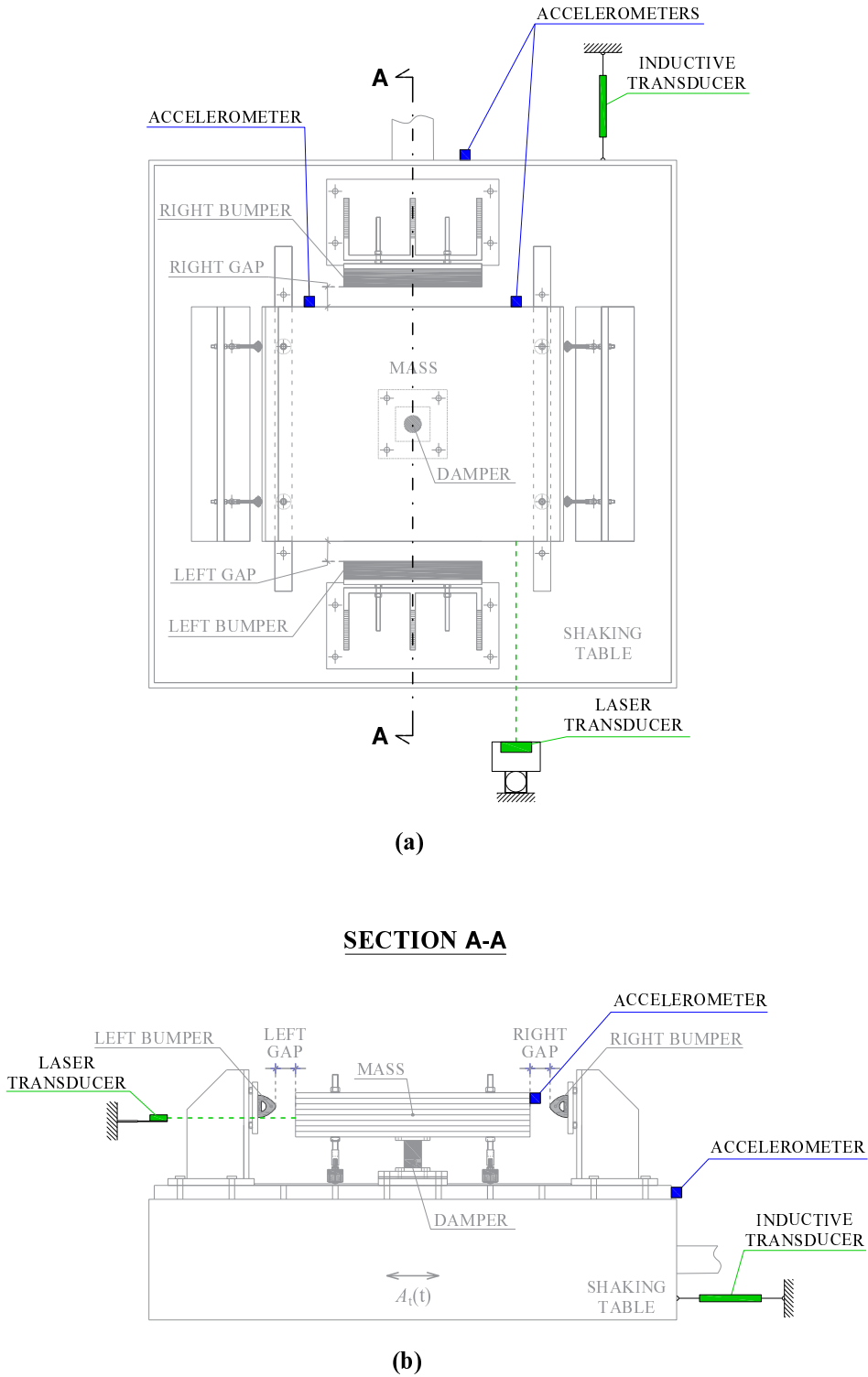
(a)

SECTION A-A

(b)
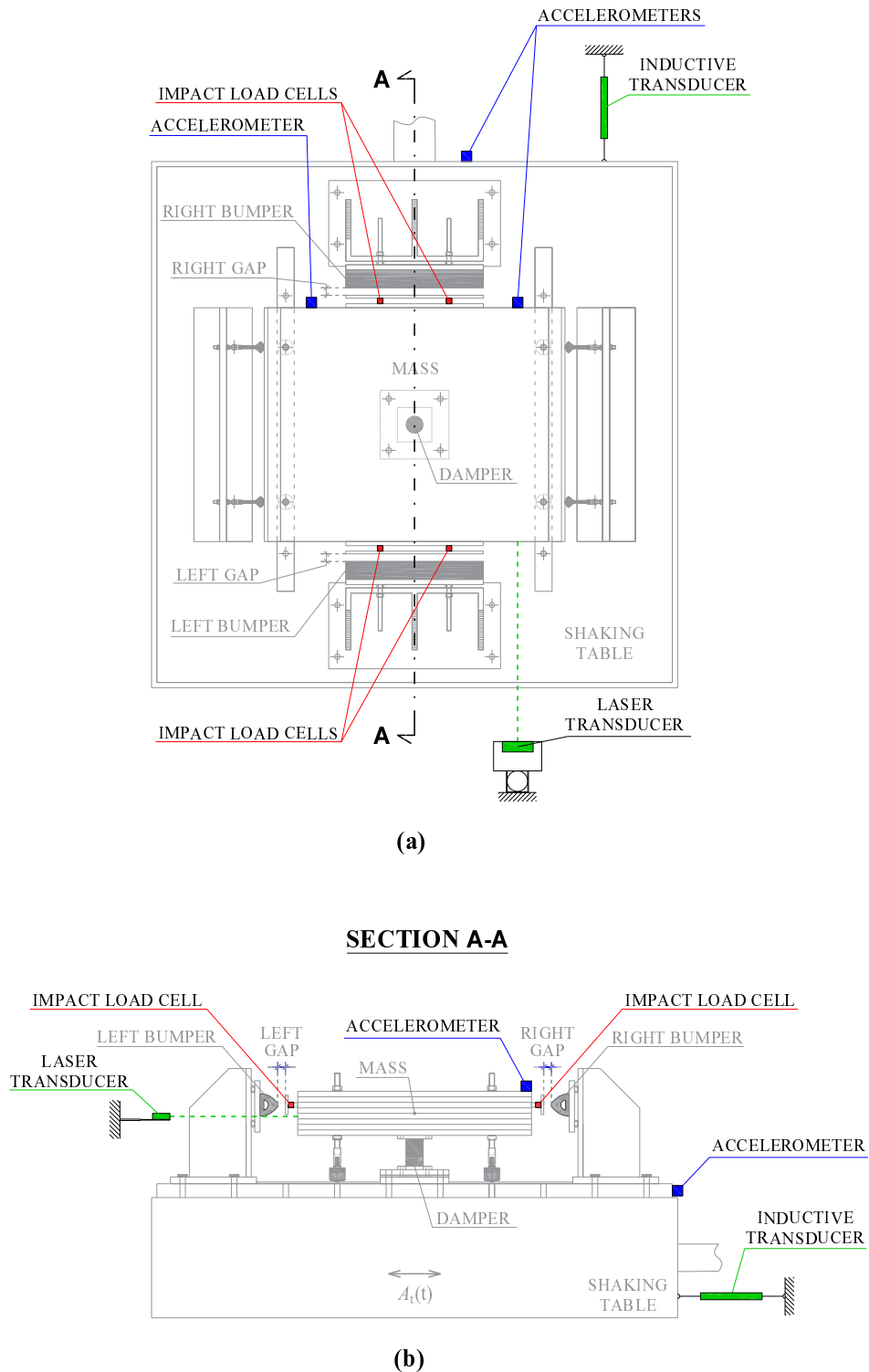
Figure 2.16. Sensors configuration - experimental laboratory campaign 2 (2017).
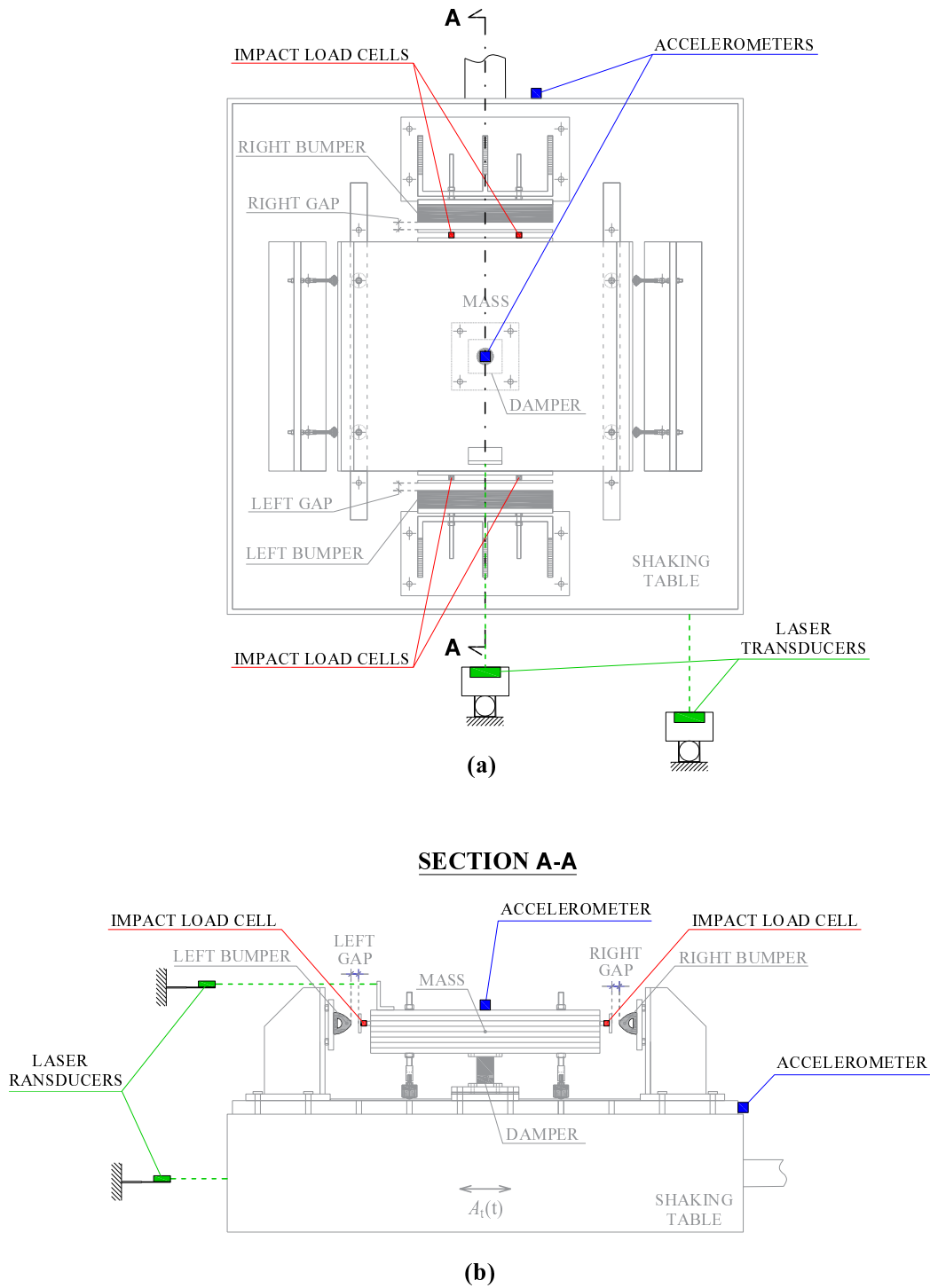
Figure 2.17. Sensors configuration - experimental laboratory campaign 3 (2020).

2.4 Closing remarks

In this chapter, an overview of the numerical and experimental models used to study the considered vibro-impact SDOF system has been provided. These two instruments are of equal importance in the study conducted during the doctoral course since, being intimately linked, they interacted and fed each other constantly.

The choice to study the vibro-impact phenomenon resorting to a simple model, such as a SDOF system in which both the damper and the bumpers are modeled by a viscoelastic model is motivated by the fact that the adoption of an elementary system allows to identify and study, in a simple manner, the fundamental aspects which characterize the nonlinear non-smooth vibro-impact dynamics without resorting to complex models. Simple systems can provide conceptual insights which are fundamental for the study of more complicated systems.

Furthermore, the adoption of a soft impact model, allows to take into account the dynamics of the bumpers and to more accurately describes some phenomena related to the process of collision, otherwise not observable by resorting to the hard impact model.

The inclusion of other sources of nonlinearity, such as those associated with the behavior of the damper, probably will allow to highlight other features. However, already many important aspects have emerged with the simple model, which probably is not able to cover all possible situations which can occur, but it has proven to be satisfactory for the purposes of this study, being able to highlight the peculiarities of the problem.

In the following chapters, the main characteristics of the numerical and/or experimental model will be briefly recalled to help the reader.

Chapter 3

Response scenarios: preliminary experimental and numerical study

Chapter outline In this chapter, possible scenarios within the experimental dynamic response of a vibro-impact Single-Degree-Of-Freedom (SDOF) system, symmetrically constrained by deformable and dissipative bumpers, are identified and described. The different scenarios were obtained varying selected parameters, namely peak table acceleration A, amplitude of the total gap between mass and bumpers G and bumper's stiffness B. Subsequently, using the Simplified Nonlinear Model (SNM) results in good agreement with the experimental outcomes were obtained, although the model includes only the nonlinearities due to clearance existence and impact occurrence. Further numerical analysis highlighted other scenarios that can be obtained for values of the parameters not considered in the experimental laboratory campaign. Finally, to attempt a generalization of the results, suitable dimensionless parameters were introduced.

The contents of this chapter were published in: "Stefani, G., De Angelis, M., Andreaus, U. Scenarios in the experimental response of a vibro-impact single-degree-of-freedom system and numerical simulations, *Nonlinear Dynamics* (2021), [Springer Nature]", [251].

3.1 Introduction

The problem of impact is ubiquitous in many practical (biomedical, mechanical, civil, ...) engineering applications involving mechanical components or structures repeatedly colliding with one another or with obstacles [110]. Impacts occur, for example, in the capsule systems used in clinic endoscopy to inspect the surface lining of the intestine in the human body [87, 165, 166, 293, 294]. Non-smooth dynamics is observed also in the drilling rig used in the oil and gas industry for creation of the wells [57, 65, 158, 159, 161, 267]. In the context of structural pounding, the occurrence of exceptional loads, like severe earthquakes, can produce large

horizontal displacements in base-isolated structures. If these displacements cannot be accommodated through adequate gaps, they can lead to pounding with the surrounding moat walls or adjacent structures, with consequences that can range from local to severe structural damage [140, 187, 190, 191, 194, 221, 222]. Furthermore, the acceleration spikes, produced by the impacts, can damage sensitive equipment housed in the structures [228, 229] and impair their functionality. Pounding is a problem that also affects other systems like strategic facilities [235] and bridges [90, 93, 123]. When it is not possible to guarantee a sufficient seismic gap, the side effects induced by the occurrence of impacts can be mitigated reducing the impact stiffness through the interposition of dissipative and deformable shock absorbers (also known as bumpers) between the colliding systems [6, 223, 224]. Even in the absence of obstacles, there may be a need to limit the displacements, so as to avoid the damage of the isolation system. This objective could be achieved either by inserting suitable obstacles or by using other types of control systems [15, 231].

Several scientific works, of both numerical and experimental nature, dealt with vibro-impact dynamics. In the numerical simulations impact can be modelled using both a steromechanical or a force-based approach [129]. In the first approach, the duration of the contact is neglected and the impact is modelled using the momentum conservation principle and the coefficient of restitution, the latter defined as the ratio between the post- and the pre-impact velocities [82]. In the second approach, the contact force can be modelled in different ways, resorting to more or less sophisticated modelling [77, 78, 186, 200, 232, 241]. The simplest models are represented by the linear spring element and Hertz contact model (nonlinear spring element) [101, 226], which do not account for energy dissipation. In order to overcome the limitations of the pure elastic contact force models, dissipative contact force models were proposed to take into account the energy loss during the contact process, such as the Kelvin-Voigt model which combines a linear spring with a linear damper, arranged in parallel [67, 82, 137] and the Hertzdamp model, proposed by Hunt and Crossley [108], in which the elastic Hertz's law is combined with a nonlinear viscoelastic element.

The types of motion and bifurcations that can occur in the dynamics of vibro-impact systems, with the variation of selected parameters, are the subject of several works. In [271] Wagg and Bishop investigated the dynamics of a two-degree-of-freedom impact oscillator with motion limiting constraint, highlighting differing regimes of impacting motion and studying the bifurcations which occur between them. The dynamics of impact oscillators with multiple degrees of freedom, subject to more than one motion limiting constraint, and the possible impact configurations were investigated by the same authors in [273]. In [176, 181], considering a two-degree-of-freedom system with a clearance subjected to harmonic excitation, the fundamental group of impact motions are defined and the transitions from one motion to the other are studied. Luo and Wang [182] studied the dynamics of a two-degree-of-freedom periodically-forced system with symmetric constraints, with emphasis on the mutual transition characteristics between neighboring regions of fundamental impact motions and designed and realized an electronic circuit for physical implementation of dynamics of the system. A two-sided damping constraint control strategy to improve the performance of the quasi-zero stiffness (QZS) isolator for both low- and high-frequency components simultaneously and to prevent the severity of end-stop impact is proposed by Hao et al. [95]. Wang et al. [274] investigated the dynamical

behavior of a single degree-of-freedom impact oscillator that impacts at one stop and is shocked with impulse excitation at the other stop and established the existing and stability conditions for period-1 motion of the oscillator and its properties. Furthermore, they discussed the effects of system parameters on dynamical response under different initial velocities. The nonlinear dynamic behavior of a one-degree-of-freedom impact oscillator with a single rigid constraint and controlled with an OGY-based state-feedback control law was investigated by Gritli and Belghith [86], through bifurcation diagrams. The experimental response of a cantilever beam with unilateral constraint was studied by de Souza Rebouças et al. [61], considering different gap configurations and levels of excitation. They highlighted different qualitative behaviors and used numerical simulations to reproduce experimental observations.

The practical problem of base-isolated structures impacting against moat-walls inspired several works by the Andreaus et al., of both numerical and experimental nature, in which the response of these structures was simulated using a Single-Degree-Of-Freedom (SDOF) oscillator, consisting of a mass and a damper and impacting against two deformable and dissipative constraints (bumpers), symmetrically arranged on the sides. The theoretical-numerical study presented in [12], allows the authors to outline possible scenarios within the system response and guided subsequent experimental parametric laboratory campaigns [9, 10], conducted on a small-scale physical model of the system using the shaking table. The influence of geometrical and mechanical characteristics of isolation and mitigation devices on the nonlinear non-smooth response of vibro-impact systems was experimentally and numerically investigated in [13]. Suitable choices of pairs of bumpers and gaps, that allows to reach a trade-off between two conflicting objectives, namely, control of excessive displacements and control of excessive accelerations were suggested in [14]. In [249] the author of this thesis with her co-authors focused the attention on the experimental pseudo-resonance curves of maximum absolute acceleration and excursion of the SDOF oscillator and characterized the hysteresis zone between the jumps. Some characteristics of the dynamics with impact, evaluated from the experimental results, namely force and time of contact between mass and bumpers, coefficient of restitution and energy dissipated by the bumpers during the impact were presented and discussed in [247]. In [248], referring to the experimental results relating to one of the considered bumpers, different scenarios that can occur in the system's experimental response, varying the investigated parameters, were highlighted and described. Those scenarios were reproduced also numerically using a Simplified Nonlinear Model (SNM), described in terms of dimensionless parameters.

The present study represents a deepening and an extension of the study presented in [248], the latter limited to one of the considered bumpers. In this chapter the attention is devoted to the identification and characterization of possible scenarios that can occur in the experimental response of the vibro-impact Single-Degree-Of-Freedom (SDOF) system, symmetrically constrained with deformable and dissipative bumpers, varying the peak value of table acceleration A, the amplitude of the total gap between mass and bumpers G and the bumper's stiffness B. Based on the experimental results, the parameters of a Simplified Nonlinear Model (SNM) were identified in order to reproduce the experimental scenarios. In this model both the behaviors of the bumpers and the damper were modelled using a Kelvin-Voigt

model, retaining the other sources of nonlinearity, namely the existence of clearances, the unilaterality of the contact and the occurrence of impact, which causes abrupt changes of stiffness and damping at the contact time. Using the same model, further numerical analyses were carried out in order to integrate the experimental results and highlight the existence of other possible scenarios. Finally, in order to attempt a generalizations of the obtained results, suitable dimensionless parameters were introduced. Despite the limitations of the Kelvin-Voigt model, it is considered satisfactory for the purposes of this study. As emerges from the scientific Literature on this topic, there are not many works that in a such systematic way, resorting both to experimental and numerical investigations, and using different synthetic representations, frame and classify the scenarios that can occur, in the dynamic non-smooth response of a vibro-impact SDOF system.

The chapter is organized as follows. The numerical model of the system and the equations of motion are introduced in Sect. 3.2; the physical model and the experimental tests are described in Sect. 3.3; in Sect. 3.4 some of the experimental results and the identified scenarios are shown and discussed; the identification of the parameters of the Simplified Nonlinear Model (SNM) and the comparison between experimental and numerical results are presented in Sect. 3.5; in Sect. 3.6 further numerical scenarios, obtained for values of the parameters not experimentally investigated, are presented and discussed; suitable dimensionless parameters and a rereading of the results according to these parameters are given in Sect. 3.7; the main conclusions and future developments are drawn in Sect. 3.8.

3.2   Model and equations of motion

The numerical model of the SDOF oscillator is shown in Fig. 3.1. It consists of a mass M, a damper (D) and two bumpers, denoted as right bumper (B_R) and left bumper (B_L) respectively, symmetrically arranged on the two sides of the mass. The system is subject to a base excitation $A_t(t)$.
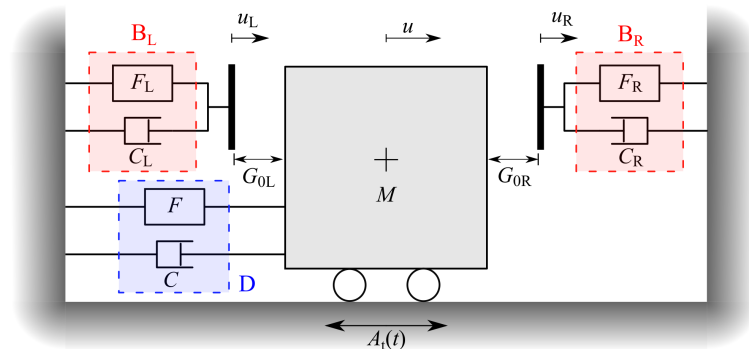

Figure 3.1. Model of the SDOF system.

During the motion, the system can be in three configurations. The corresponding equations of motion are:

- The mass is not in contact with any of the bumpers (flight):

$$M\ddot{u}(t) + C\dot{u}(t) + F(t) = -MA_{\text{t}}(t) \tag{3.1a}$$

$$C_j\dot{u}_j(t) + F_j(t) = 0; \quad G_j(t) > 0 \quad (j = \text{R}, \text{L}) \tag{3.1b}$$

- The mass is in contact with the right bumper:

$$M\ddot{u}(t) + C\dot{u}(t) + F(t) + C_{\text{R}}\dot{u}_{\text{R}}(t) + F_{\text{R}}(t) = -MA_{\text{t}}(t) \tag{3.2a}$$

$$C_{\text{L}}\dot{u}_{\text{L}}(t) + F_{\text{L}}(t) = 0; \quad G_{\text{R}}(t) = 0 \tag{3.2b}$$

- The mass is in contact with the left bumper:

$$M\ddot{u}(t) + C\dot{u}(t) + F(t) + C_{\text{L}}\dot{u}_{\text{L}}(t) + F_{\text{L}}(t) = -MA_{\text{t}}(t) \tag{3.3a}$$

$$C_{\text{R}}\dot{u}_{\text{R}}(t) + F_{\text{R}}(t) = 0; \quad G_{\text{L}}(t) = 0 \tag{3.3b}$$

where $u(t)$ and $u_j(t)$ (j = R, L) are the relative displacements of the mass and of the bumpers respectively with respect to the ground and the dot $(\cdot)$ denotes differentiation with respect to the time t. C and C_j (j = R, L) are the damping coefficients of the damper and the bumpers respectively; $F(t)$ and $F_j(t)$ (j = R, L) are the restoring forces exerted by the damper and the bumpers respectively. $G_j(t)$ (j = R, L) is the clearance function which represents the distance, instant by instant, between the mass and the j-th bumper:

$$G_j(t) = G_{0j} + \Delta u_j(t) \quad (j = \text{R}, \text{L}) \tag{3.4a}$$

$$\Delta u_{\text{R}}(t) = u_{\text{R}}(t) - u(t); \quad \Delta u_{\text{L}}(t) = u(t) - u_{\text{L}}(t) \tag{3.4b}$$

where G_{0j} (j = R, L) is the j-th initial gap, that is the initial distance between the mass and the j-th bumper. When the mass is in contact with the j-th bumper $G_j(t) = 0$, otherwise $G_j(t) > 0$. In this study two equal bumpers symmetrically positioned on the two sides of the mass are considered. Thus, it is $F_{\text{R}} = F_{\text{L}}$, $C_{\text{R}} = C_{\text{L}}$ and $G_{0\text{R}} = G_{0\text{L}}$. The studied physical model is strongly nonlinear. Nonlinearities are due to the behavior of damper and bumpers, the gap, the unilateral constrains and the impact that induces abrupt changes of both stiffness and damping.

3.3 Experimental setup

The physical model of the system consists of a rigid body (mass $M = 550$ kg), an elastomeric High Damping Rubber Bearing (HDRB) isolator (damper), and a couple of symmetrically mounted elastomeric shock absorbers (bumpers placed on steel moat walls), as shown in Fig. 3.2. The system was excited by a step-wise forward ($f = 0.5 - 5$ Hz with $\Delta f = 0.1$ Hz) and backward ($f = 5 - 0.5$ Hz with $\Delta f = 0.1$ Hz) sine sweep in displacement control, in order to impose a given peak acceleration A, with a number of cycles such as to reach the steady state condition. The attainment of the steady state condition was checked by verifying the convergence to the limit cycle in both planes of phase portraits and hysteresis loops. Two configurations, with and without bumpers, under the same base excitation, were considered.

The experimental tests were carried out to investigate the influence on the system response of selected parameters, namely:
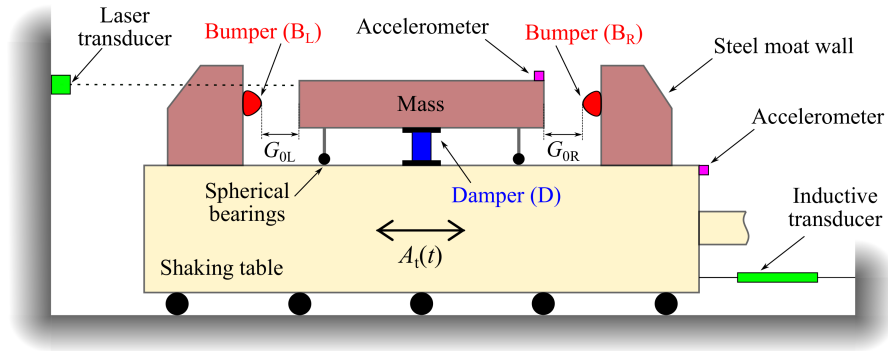
Figure 3.2. Schematic view of the experimental setup.

- peak table acceleration Ai (i = 1, 2, 3); in particular A1 = 0.03g, A2 = 0.04g, A3 = 0.05g, where g is the gravity's acceleration;

- amplitude of the total gap Gj (j = 1, 2, 3, 4 and G∞) between mass and bumpers, defined as the sum of right G_{0R} and left G_{0L} gaps (Fig. 3.2); in particular G1 = 15 mm, G2 = 20 mm, G3 = 25 mm, G4 = 30 mm and G∞ denotes all the situations in which the gap is large enough not to have the impact between the mass and the bumpers; this occurs both in the free flight condition (absence of bumpers) and when the mass just grazes the bumpers; in the latter case, the corresponding value of G∞ depends on A;

- bumper's stiffness Bk (k = 1, 2, 3, 4); the stiffness of the bumper increases as k increases.

In the experimental laboratory campaign, each performed test corresponds to a combination of these three parameters. The measured parameters during the tests were the absolute accelerations and displacements of the mass and of the shaking table. The accelerations were measured by accelerometers and the displacements were measured by a laser transducer, for what concerns the mass, and by an inductive transducer, for what concerns the shaking table (Fig. 3.2). For a more detailed description of the experimental setup see Sect.2.3 and [14].

3.4   Experimental results

In this Section the experimental results, represented in terms of forward and backward Pseudo-Resonance Curves (PRCs) of normalized excursion of absolute acceleration ($\eta_a = E_a/E_{a0}$) and relative displacement ($\eta_d = E_d/E_{d0}$) of the mass, are discussed. The excursion E_i (i = a, d) was calculated as the difference between the maximum and minimum values recorded at steady-state of each sub-frequency range. Subsequently, these excursions E were normalized with respect to the maximum excursion in the backward sweep in free flight condition E_{i0} (i = a, d). Based on this normalization, a value of normalized excursion η_i (i = a, d) greater than 1 means that in presence of bumpers the excursion is larger compared to the free flight condition.

3.4.1   Free flight condition

In the free flight condition, that is when the mass is free to move without obstacles, forward (in the following figures identified with the letter (f) in the legend) and backward (in the following figures indicated with the letter (b) in the legend) PRCs of the excursion of absolute acceleration (E_a) and relative displacement (E_d) of the mass, show a softening behavior, due to the damper, gradually more evident as the excitation amplitude A increases.
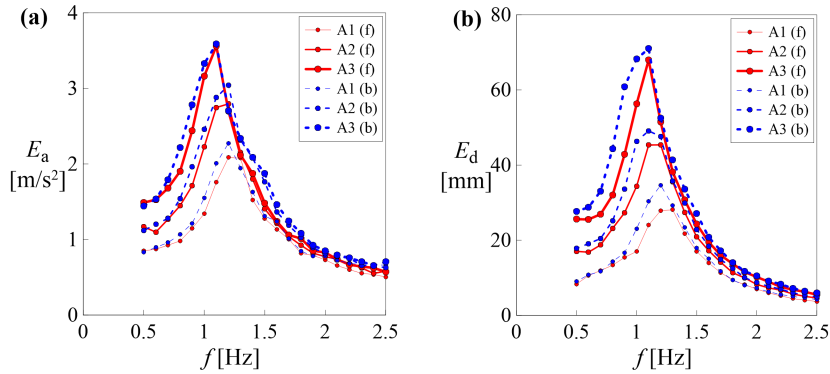
Figure 3.3. Free flight condition: **a** $E_a[\text{m/s}^2]$; **b** $E_d[\text{mm}]$.

As shown in Fig. 3.3, as A increases (increasing thickness of the lines and size of the markers), the maximum values of excursion, of both absolute acceleration and relative displacement, increase and resonance occurs for decreasing values of frequency. As can be seen from the same figures, even in the case of the maximum amplitude of the excitation considered in the laboratory campaign (A3), the extension of the hysteresis is limited.

3.4.2   Contact condition

When impact occurs, the PRCs bend to the right (Figs. 3.4b,c) due to the hardening caused by impact against the bumpers, as it can be seen in Fig. 3.4a, in which the absolute acceleration *vs* relative displacement cycles, in steady-state forward resonance condition, corresponding to the absence (free flight, black curve) and presence of bumper (red curve, corresponding to the combination B4-G4-A3) are compared. In Figs. 3.4b,c the same comparison is made in terms of PRCs of normalized excursion of absolute acceleration η_a (Fig. 3.4b) and relative displacement η_d (Fig. 3.4c). In these figures, the PRCs corresponding to the free flight condition are represented with solid (forward sweep) and dashed (backward sweep) black lines, whereas the PRCs representative of the contact condition (combination B4-G4-A3) are represented with red (forward sweep) and blue (backward sweep) markers. By increasing the excitation frequency (red markers, forward sweep), the amplitude of the response increases, initially overlapping the curve in free flight, until impact occurs; subsequently, the response continues to increase, following a different path until a sudden downward jump (represented with a vertical red arrow pointing downwards) to a smaller amplitude response (associated with the absence of impact) occurs and then continues to decrease slowly, overlapping the curve in free flight. If

Figure 3.4. Comparison between free flight and contact (B4-G4-A3) condition: **a** absolute acceleration *vs* relative displacement cycle; **b** η_a; **c** η_d.
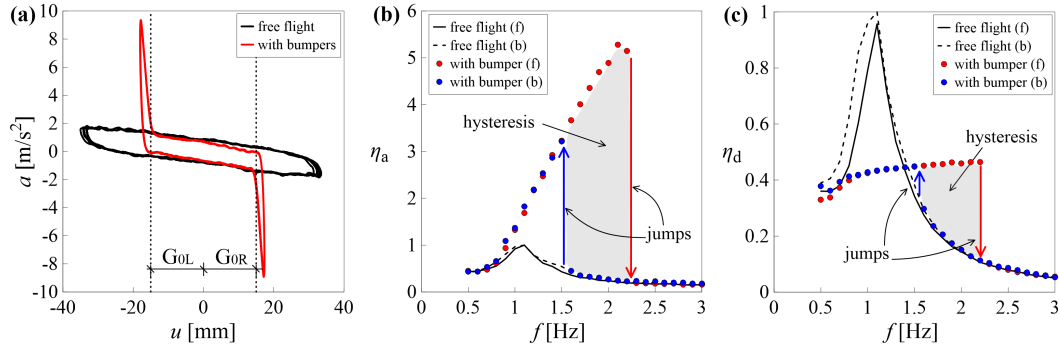
the exciting frequency is decreased (blue markers, backward sweep), the amplitude of the response increases slowly, overlapping the curve in free flight, until a sudden upward jump (represented with a vertical blue arrow pointing upwards) to a larger amplitude response (associated with the occurrence of impact) occurs and then continues to decrease, following the corresponding forward curve. The presence of jumps give rise to an hysteresis in the η_i vs f ($i =$ a, d) plane (*primary resonance with right hysteresis*), highlighted in Figs. 3.4b,c with a light gray shaded area. The attribute "right" refers to the fact that the hysteresis is a consequence of the bending to the right of the frequency response curve at the primary resonance. In the frequency interval between the two jumps, for each value of frequency there are three steady-state solutions, two stable, corresponding respectively to large and small amplitude oscillations, and one unstable and thus not experimentally reproducible.

In the following Figs. 3.5 and 3.6 the forward (solid lines) and backward (dashed lines) PRCs, respectively of normalized excursion of absolute acceleration η_a (Fig. 3.5) and relative displacement η_d (Fig. 3.6) of the mass, are represented for different values of the total gap G (each color corresponds to a gap amplitude). The sub-figures belonging to the same column of the grid are characterized by the same value of peak table acceleration A, while the sub-figures belonging to the same row of the grid correspond to the same bumper B.

From Fig. 3.5 it can be observed that, compared to the free flight condition, the occurrence of impact against the bumpers causes an increase in acceleration; in resonance condition and for the investigated combinations of parameters, η_a is observed to be always greater than 1, both in the forward and in the backward sweeps, with the amplitude of the forward resonance greater than that of the backward resonance. This does not exclude that, for other combinations of the parameters, not investigated, in resonance condition, η_a may be less than 1. For a given pair B-A, which corresponds to a sub-figure in Fig. 3.5 (for example B2-A3), compared to the free flight condition, as the total gap G decreases, the jump frequencies, both in the forward and in the backward sweeps, the latter to a lesser extent, increase. For the selected B-A pair, the maximum values of excursion, both in the forward and in the backward resonance condition, the latter to a lesser extent, show a bell-shaped trend. For other combinations of B and A, it is possible to capture only
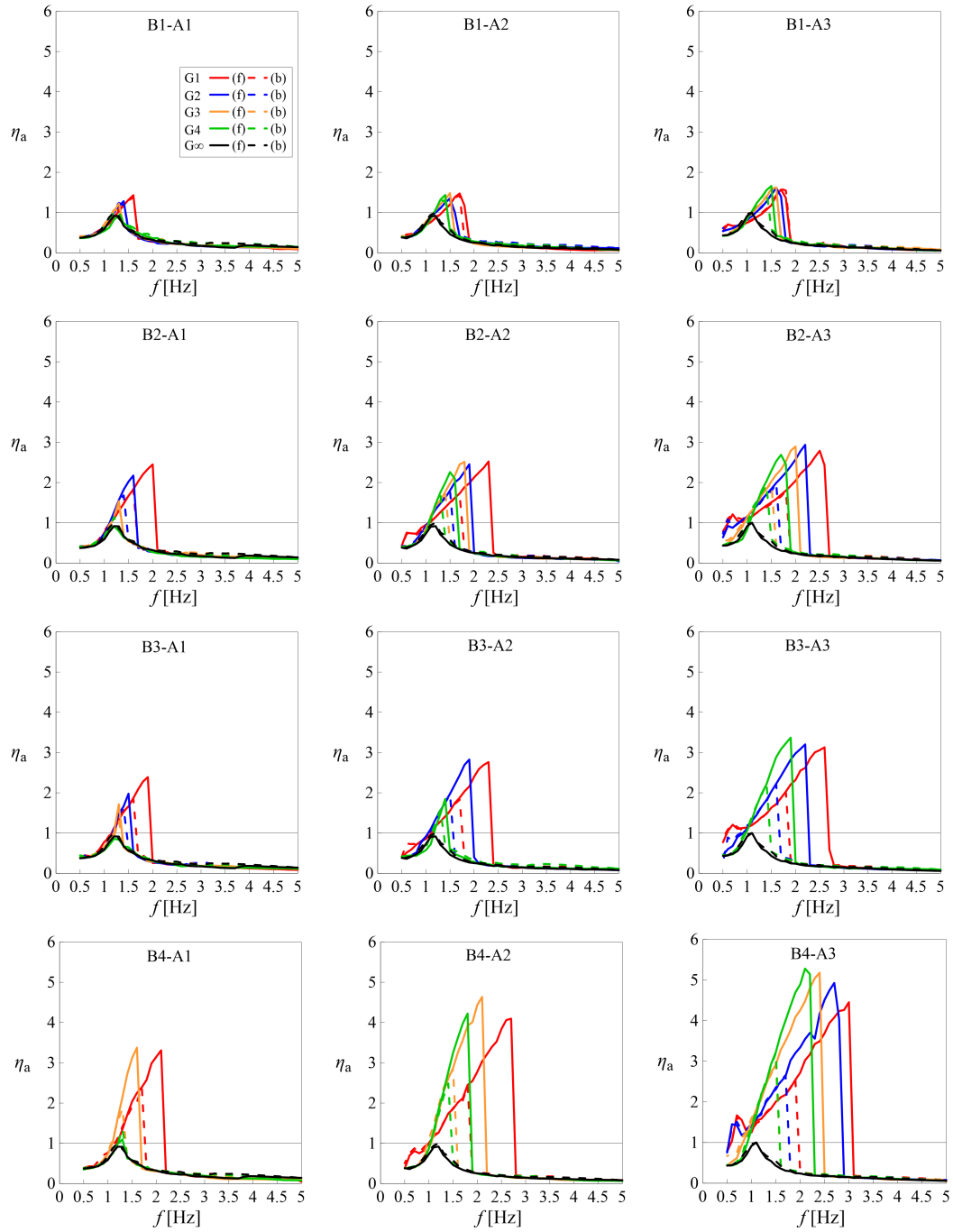
Figure 3.5. Experimental PRCs of η_a.
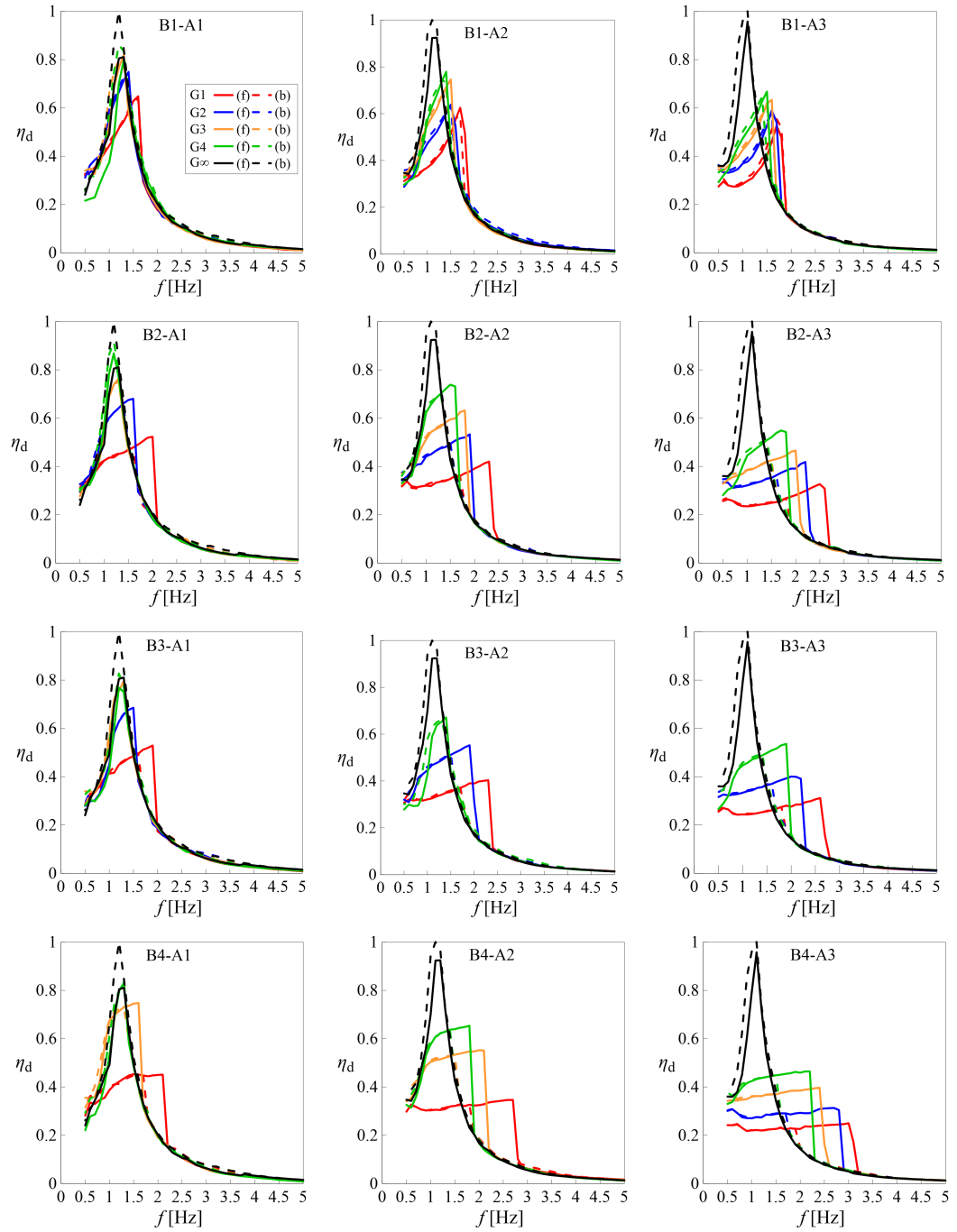
Figure 3.6. Experimental PRCs of η_{d}.

the ascending branch (see for example the sub-figure corresponding to B1-A1) or only the descending branch (see for example the sub-figure corresponding to B4-A3) of the envelope of the maxima. Furthermore, decreasing the total gap, secondary resonances in the low frequency range appear. For a given pair B-G (see for example the second row of sub-figures, associated with the bumper B2 and focus the attention on the curves corresponding for example to the total gap G1), increasing the table acceleration , that is moving from the left column to the right column, it can be observed that the jump frequencies, both in the forward and in the backward sweeps, the latter to a lesser extent, increase. The maximum values of excursion in the forward resonance condition increase, while the maximum values of excursion in the backward resonance condition increase to a lesser extent. Furthermore, increasing the table acceleration, secondary resonances in the low frequency range appear. With the same acceleration A and total gap G (see for example the third column of sub-figures, associated with the acceleration A3 and focus the attention on the curves corresponding to the total gap G1), increasing the bumper stiffness, that is moving from the top row to the bottom row, it can be observed that the jump frequencies, both in the forward and in the backward sweeps, the latter to a lesser extent, increase. The maximum values of excursion both in the forward and in the backward resonance condition increase. Furthermore, increasing the stiffness of the bumper, secondary resonances in the low frequency range appear. It can also be observed that bumpers B2 and B3 behave in a similar way. From Fig. 3.5, it can also be observed that in the case of the combination of the most deformable bumper with the smallest table acceleration (pair B1-A1, top left corner of the figure) PRCs are quite similar to those associated with the free flight condition, while the difference becomes more evident for the pair characterized by the stiffest bumper and the greatest table acceleration (pair B4-A3, lower right corner of the figure). Finally, a fixed point for $f \simeq 1$Hz can be observed, especially for the higher values of B and A.

From Fig. 3.6 it can be observed that, compared to the free flight condition, in presence of bumpers, due to the limitation of the displacement imposed by the constraint, η_d is always lower than 1, both in the forward and in the backward sweeps, with the amplitude of the forward resonance greater then that of the backward resonance. This difference decreases increasing the stiffness of the bumper. It can be observed that, in the absence of impact, PRCs overlap with those relating to the free flight condition. The overlap can occur on both the ascending branch, if impact occurs for frequencies greater that 0.5 Hz, and the descending branch, after the downward jump in the forward sweep and before the upward jump in the backward sweep. The upward jumps, compared to the PRCs of η_a are less evident, especially in the case of large gaps and small accelerations. As regards the variation of the jumps frequencies, and the appearance of secondary resonances, what has already been said for η_a applies. For a given pair B-A, which corresponds to a sub-figure in Fig. 3.6 (for example B2-A2), compared to the free flight condition, as the total gap G decreases the maximum values of excursion, both in the forward and in the backward resonance condition decrease. In the ascending branch, the deviation from the PRCs associated with the free flight condition, occurs for gradually lower frequency values. For a given pair B-G (see for example the second row of sub-figures, associated with the bumper B2 and focus the attention on the curves corresponding to the total gap G1),

increasing the table acceleration, that is moving from the left column to the right column, it can be observed that the maximum values of excursion both in the forward and in the backward resonance condition decrease. With the same acceleration A and total gap G (see for example the third column of sub-figures, associated with the acceleration A3 and focus the attention on the curves corresponding to the total gap G1), increasing the bumper stiffness, that is moving from the top to the bottom, it can be observed that the maximum values of excursion both in the forward and in the backward resonance condition decrease. It can also be observed that bumpers B2 and B3 behave in a similar way. Increasing B, with the same pair G-A, the penetration of the mass into the bumper decreases and becomes progressively independent of the forcing frequency. This branch, characterized by a concavity for the most deformable bumper, becomes gradually more straight and horizontal moving on to the bumper B4, which can be assimilated to a quite rigid obstacle. As already emerged from the Fig. 3.5, also from Fig. 3.6, it can also be observed that in the case of the combination of the most deformable bumper with the smallest table acceleration (pair B1-A1, top left corner of the figure) PRCs are quite similar to those associated with the free flight condition, while the difference becomes more evident for the pair characterized by the stiffest bumper and the greatest table acceleration (pair B4-A3, lower right corner of the figure). Finally, making a comparison, with the same frequency, between the PRCs with and without bumpers, it can be observed that in the presence of the bumpers there are frequency ranges in which, contrary to what one would expect, the excursion of relative displacement of the mass can be greater than what occurs in free flight condition.

Figs. 3.5 and 3.6 provide analogous and dual indications, since they represent two different points of view from which to observe the same problem. In particular, they provide the same indications regarding the evolution of the jumps frequencies and the appearance of secondary resonances. Furthermore, they reflect the dual evolution of the represented quantities, namely accelerations and displacements, that is the introduction of the bumpers causes on the one hand the increase of the accelerations and on the other the decrease of the displacements.

3.4.3   Experimental scenarios

Based on the previous observations, as G decreases, different scenarios can be identified:

- Scenario 0 (S0): free flight condition;

- Scenario 1 (S1): grazing condition;

- Scenario 2 (S2): PRCs with only the primary resonance with right hysteresis;

- Scenario 3 (S3): PRCs with both the primary resonance with right hysteresis and a secondary resonance in the low frequency range, to the left of the primary resonance.

In the following these scenarios will be described, starting from the scenario S3, in more detail. Phase portraits, Fourier spectra and time histories in steady-state

condition will be analysed. In the time histories, the time axis t will be normalized with respect to the period $T = 1/f$ of the harmonic base excitation.

Scenario S3 PRCs belonging to this scenario show both the *primary resonance with right hysteresis*, between the downward and upward jumps, and a *secondary resonance without hysteresis* in the low frequency range. This scenario was experimentally obtained with different combinations of the investigated parameters. For example, the PRCs shown in Fig. 3.7 correspond to the combination B2-G1-A3. The red markers refer to the forward sweep, while the blue ones to the backward sweep. The arrows indicate the two jumps. The three vertical dashed lines represent three values of frequency, corresponding respectively to the secondary resonance ($f_I = 0.7$ Hz), the following valley ($f_{II} = 0.9$ Hz) and the primary resonance ($f_{III} = 2.5$ Hz), that will be investigated in more detail. It is worth noting that, in this case impact occurs already at 0.5 Hz.
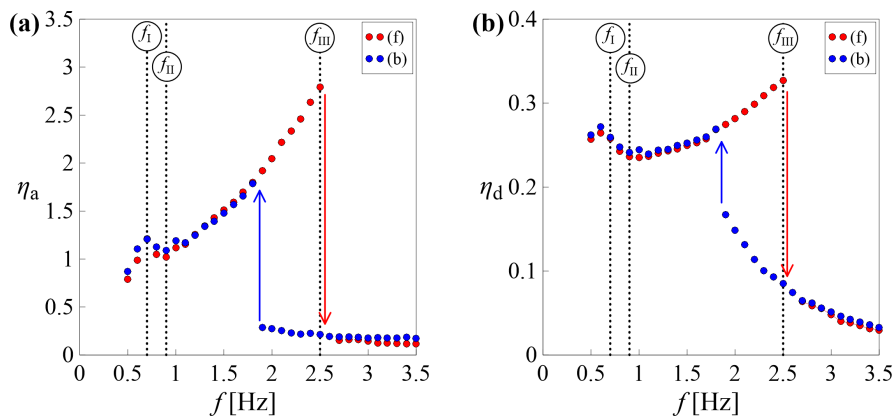
Figure 3.7. Scenario S3 (B2-G1-A3): **a** η_a; **b** η_d.

By focusing the attention on the ridge of the *secondary resonance without hysteresis* (first vertical dashed line on the left in Fig. 3.7, $f = f_I$), from Fig. 3.8a it can be observed that, in the phase plane, the two solutions, corresponding to the forward (red line) and backward (blue line) sweep are approximatively coincident. The red and blue points represent the Poincaré sections and the two vertical dashed lines indicate the gaps. These two coincident solutions are characterized by several harmonic components (as can be seen from Fig. 3.8d), whose amplitude decreases with increasing frequency. At the secondary resonance, in each forcing cycle the mass hits each bumper once, and these impacts are highlighted by peaks in the time history of the absolute acceleration (Fig. 3.8j) and by sudden changes in relative velocity (Fig. 3.8m). The time history of relative displacement is represented in Fig. 3.8g) in which the horizontal dashed lines indicate the gaps. In the same figures, two consecutive impacts, the first one with the right bumper and the second one with the left bumper, were highlighted with vertical yellow bands. The yellow points emphasize the instants of start and end of the contact phase and the corresponding values of displacement, acceleration and velocity, while the acceleration peaks are marked with cyan stars. Moving to the next valley in the PRC (central vertical dashed line in Fig. 3.7, $f = f_{II}$), we still observe, in the phase plane, the presence
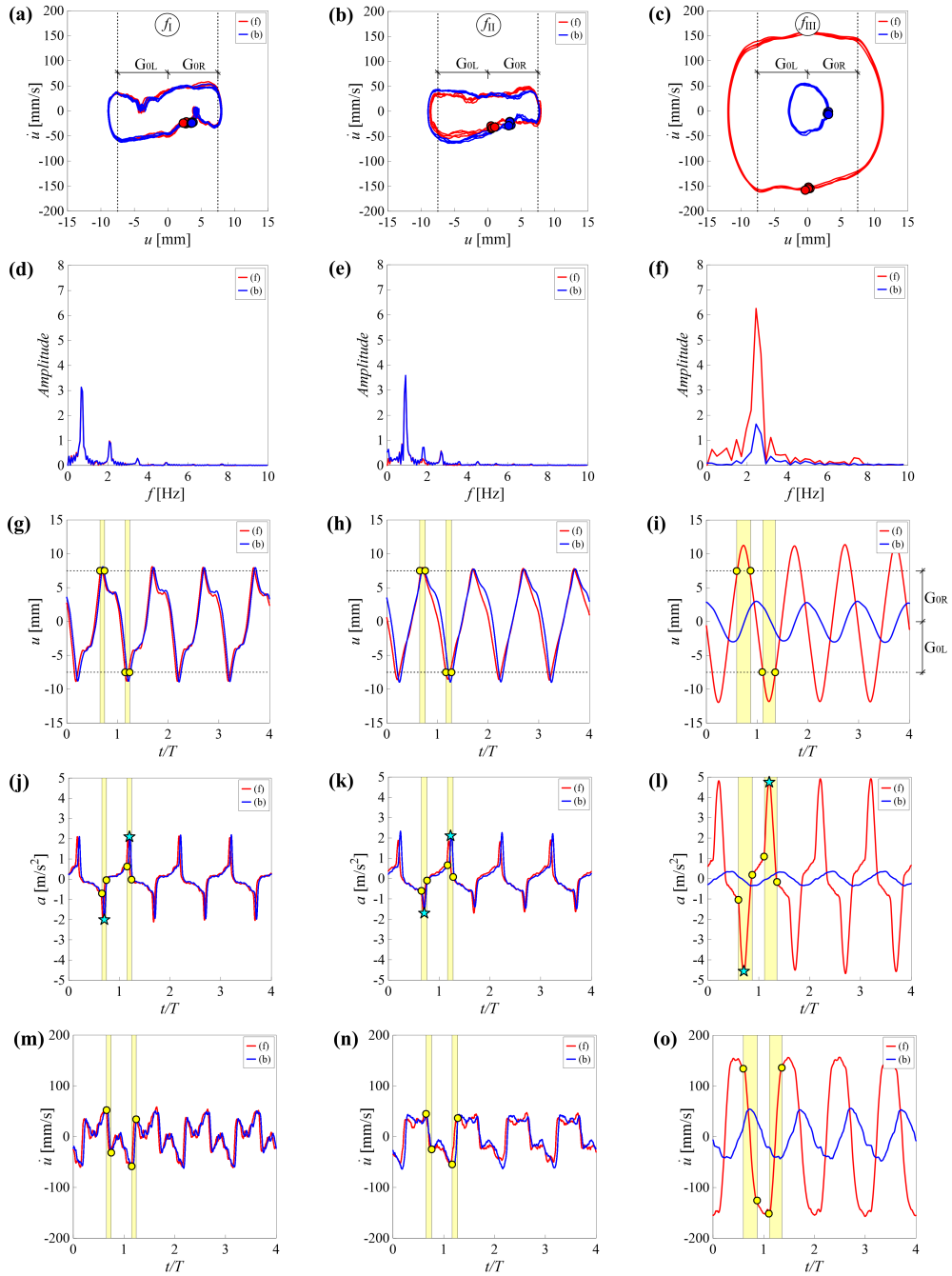
Figure 3.8. Scenario S3 (B2-G1-A3): Phase portrait: **a** $f = f_{\mathrm{I}}$; **b** $f = f_{\mathrm{II}}$; **c** $f = f_{\mathrm{III}}$; Fourier spectrum: **d** $f = f_{\mathrm{I}}$; **e** $f = f_{\mathrm{II}}$; **f** $f = f_{\mathrm{III}}$; Time history of relative displacement: **g** $f = f_{\mathrm{I}}$; **h** $f = f_{\mathrm{II}}$; **i** $f = f_{\mathrm{III}}$; Time history of absolute acceleration: **j** $f = f_{\mathrm{I}}$; **k** $f = f_{\mathrm{II}}$; **l** $f = f_{\mathrm{III}}$; Time history of relative velocity: **m** $f = f_{\mathrm{I}}$; **n** $f = f_{\mathrm{II}}$; **o** $f = f_{\mathrm{III}}$.

of two coincident solutions (Fig. 3.8b). As in the previous case, the two solutions are characterized by several harmonic components (Fig. 3.8e) and, in each forcing cycle, the mass hits each bumper once (Fig. 3.8k). In Figs. 3.8h,k,n two consecutive impacts, the first one with the right bumper and the second one with the left bumper, were highlighted with vertical yellow bands. In the same figures, the yellow points emphasize the instants of start and end of the contact phase and the corresponding values of displacement, acceleration and velocity, while the acceleration peaks are marked with cyan stars. Moving from the valley to the primary hysteresis, the solutions corresponding to the forward and backward sweeps are still coincident and, as the frequency increases, the phase portraits gradually regularize and take on the appearance of an ellipse.

By focusing the attention on the *primary resonance with right hysteresis* (third vertical dashed line in Fig. 3.7, $f = f_{\mathrm{III}}$), just before the downward jump, from Fig. 3.8c it can be observed that, in the phase plane, there are two different steady-state solutions:

- Large-amplitude resonant motion associated with the occurrence of impact (red line);

- Small-amplitude non-resonant motion without impact (blue line).

The two solutions are both periodic with one predominant harmonic component (Fig. 3.8f). Actually, there would be also an unstable solution, that could not be obtained experimentally. By focusing the attention on the large-amplitude motion, it can be observed that, in each forcing cycle, the mass hits each bumper once. In Figs. 3.8i,l,o two consecutive impacts, the first one with the right bumper and the second one with the left bumper, were highlighted with vertical yellow bands. In the same figures, the yellow points emphasize the instants of start and end of the contact phase and the corresponding values of displacement, acceleration and velocity, while the acceleration peaks are marked with cyan stars. Immediately after the downward jump, for greater values of frequency, there is only one solution, the same in the forward and in the backward sweep, characterized by the absence of impact and the corresponding phase portrait takes on the appearance of an ellipse. It is worth noting that the considered setup (B2-G1-A3) is characterized by an accidental geometric dissymmetry, which is reflected in the asymmetry of the phase portraits and of the time histories. This dissymmetry is due to imperfections in the experimental setup, related to the gap, which is not perfectly symmetrical and slightly different from the nominal value. This is particularly evident in Figs. 3.8a,b and less visible in Fig. 3.8c, given the greater penetration of the mass into the bumpers. Furthermore, from Fig. 3.8, it can be observed that the duration of the contact time compared to the period $T = 1/f$ of the harmonic base excitation (width of a single vertical yellow band), increases going from $f = f_{\mathrm{I}}$ to $f = f_{\mathrm{III}}$.

Scenario S2 PRCs belonging to this scenario are characterized only by the presence of the *primary resonance with right hysteresis*, between the downward and upward jumps. This scenario was experimentally obtained with different combinations of the investigated parameters. For example, the PRCs shown in Fig. 3.9 correspond to the combination B2-G2-A2. In the frequency range between the two

jumps, everything goes as described above. Unlike the case examined in the previous paragraph (scenario S3), here, having increased the gap, impact does not occur immediately starting from the smallest frequency value investigated, but in the range between 0.7 and 2 Hz.
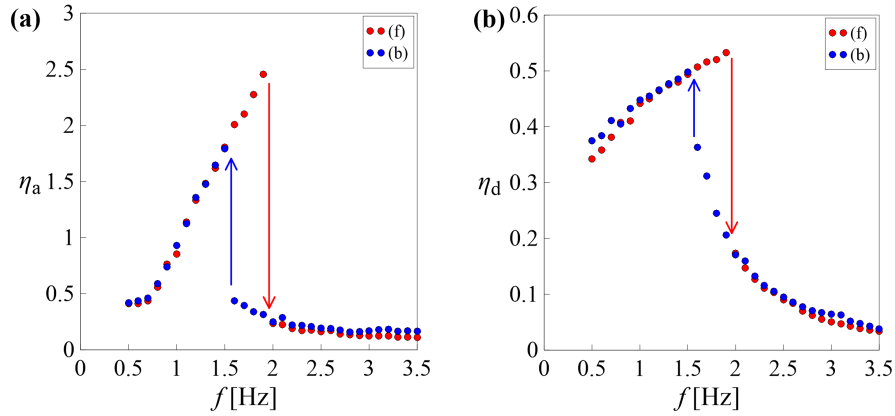
Figure 3.9. Scenario S2 (B2-G2-A2): **a** η_a; **b** η_d.

Scenarios S1   In the grazing condition, the mass just touches the bumpers without deforming them significantly. Consequently, the corresponding PRCs are similar to those occurring in the free flight condition. The grazing condition was experimentally observed in few cases where the combination of the largest gap and the smallest excitation amplitude occurred (Fig. 3.10, corresponding to the combination B2-G4-A1).
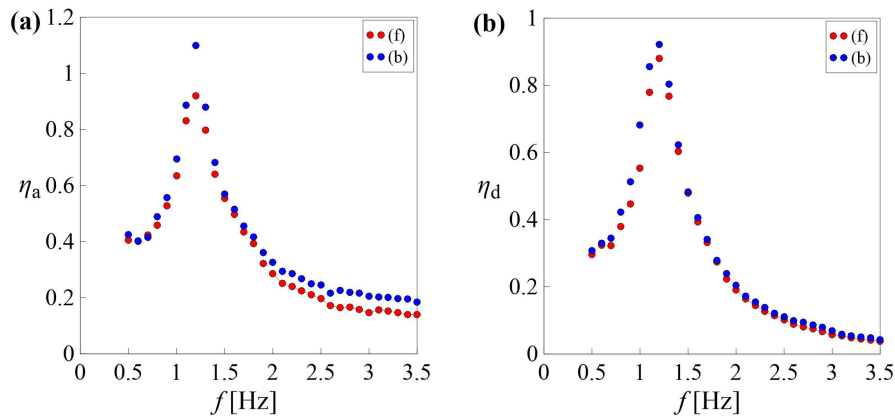
Figure 3.10. Scenario S1 (B2-G4-A1): **a** η_a; **b** η_d.

Scenarios S0   As concerns the free flight condition, what has already been said in Sect. 3.4.1 applies.

3.5 Identification via the Simplified Nonlinear Model (SNM)

The experimental results were compared with those obtained with a numerical model, as described in Section 3.2, in which a linearization of the behaviors of both the bumpers and the damper was made, retaining the other nonlinearities. In particular, the behavior of both damper and bumpers was modelled with a linear elastic spring in parallel with a linear viscous dashpot. Consequently, the restoring forces in Eqs. 3.1, 3.2 and 3.3 assume the expression:

$$F(t) = Ku(t) \tag{3.5a}$$

$$F_j(t) = K_j u_j(t) \quad (j = \mathrm{R, L}) \tag{3.5b}$$

where K and K_j ($j = \mathrm{R, L}$) are the elastic stiffness of the damper and the bumpers respectively. In the case of two equal bumpers symmetrically positioned on the two sides of the mass, it is $K_\mathrm{R} = K_\mathrm{L}$. By virtue of the linearization made, this model was called Simplified Nonlinear Model (SNM). It is worth noting that the other sources of nonlinearities, namely the gap, the unilateral constrains and the impact that induces abrupt changes of both stiffness and damping, are taken into account.
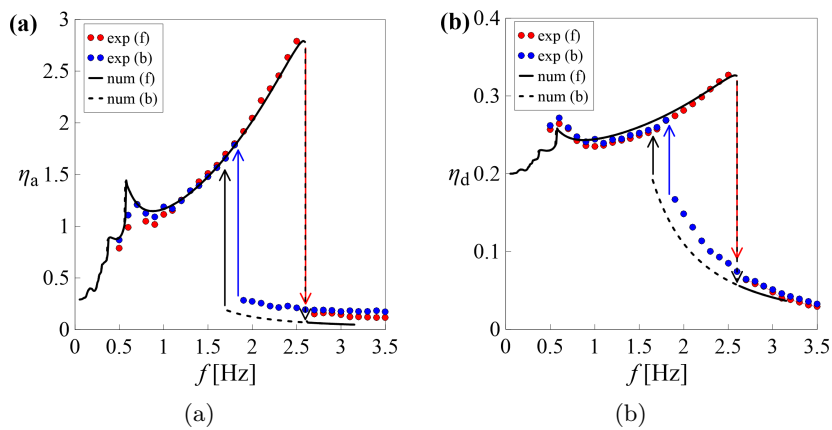
Figure 3.11. Comparison between experimental and numerical PRCs (Scenario S3, combination B2-G1-A3): **a** η_a; **b** η_d.

The visco-elastic model, despite its well-known limitations, particularly when used to model the contact, is considered satisfactory for the purposes of this study. To compare the experimental results with those obtained with the SNM, it was necessary to reduce the nonlinear constitutive law of the damper [9, 202] to a linear elastic one. This was made considering an equivalent stiffness K, estimated in free flight resonance condition, for each value of table acceleration A.

Once the parameters of the numerical model were identified, the scenarios described above were reproduced numerically and a comparison with the experimental data was made in terms of PRCs and phase portraits, as shown in Figs. 3.11, 3.12 and 3.13. In particular, Figs. 3.11 and 3.12 show the PRCs and the phase portraits corresponding to the S3 scenario for the B2-G1-A3 combination; and Fig. 3.13 shows

the PRCs of the S2 scenario for the B2-G2-A2 combination. In these figures, the experimental results were represented with markers in the PRCs (Figs. 3.11 and 3.13) and dotted lines in the phase portraits (Fig. 3.12), while the numerical results were represented with solid and dashed black lines. The identified parameters of the model were: $K_{\mathrm{R}} = K_{\mathrm{L}} = 510$ kN/m, $C_{\mathrm{R}} = C_{\mathrm{L}} = 0.9$ kN s/m for the bumper B2 and, with regards to the damper, $K = 26.8$ kN/m, $C = 1.1$ kN s/m for the scenario S3 and $K = 31.9$ kN/m, $C = 1.1$ kN s/m for the scenario S2.
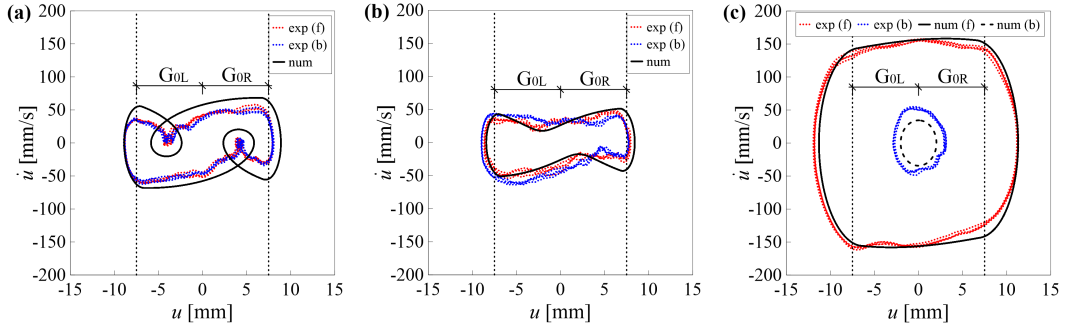
Figure 3.12. Comparison between experimental and numerical phase portraits (Scenario S3, combination B2-G1-A3): **a** $f = f_{\mathrm{I}}$; **b** $f = f_{\mathrm{II}}$; **c** $f = f_{\mathrm{III}}$.

It can be observed that, although the SNM does not include the nonlinearities associated with the behavior of both the damper and the bumpers, there is a good agreement between experimental and numerical results both in terms of PRCs (Fig. 3.11 and 3.13) and in the phase portraits (Fig. 3.12).
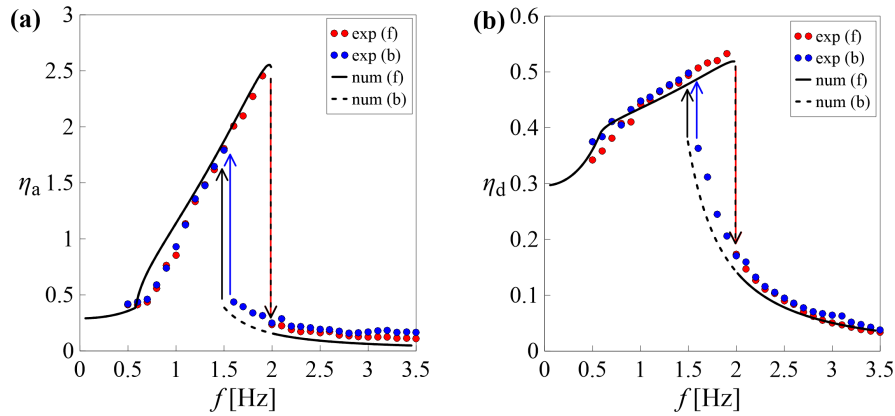
Figure 3.13. Comparison between experimental and numerical PRCs (Scenario S2, combination B2-G2-A2): **a** η_{a}; **b** η_{d}.

The model is able to reproduce both qualitatively and quantitatively the primary resonance and the downward jump, whereas it is not able to precisely capture other phenomena such as the frequency of the upward jump. This is due to the difference between the experimental (nonlinear) and numerical (linear) PRCs in free flight condition which causes that, for a given value of the gap, in the SNM, the upward jump occurs for lower values of the frequency. Furthermore, the position
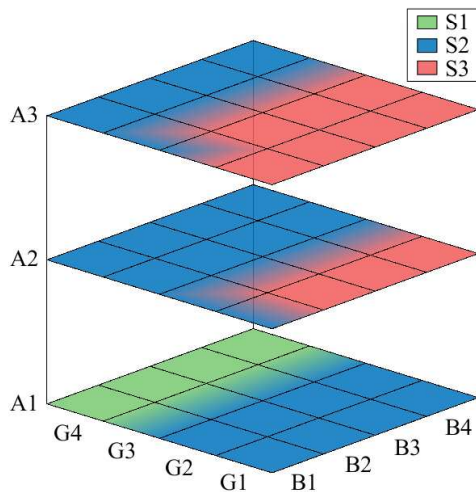
Figure 3.14. Experimental investigated cases and scenarios.

and amplitude of the secondary resonance was reproduced in a sufficiently accurate manner. The numerical model also highlighted the presence of internal loops in the phase portrait, corresponding to the secondary resonance ($f = f_I$, black cycle in Fig. 3.12a) and something similar to small loops can also be recognized in the experimental cycles.

Based on these considerations, the SNM appears to be adequate to simulate the behavior of the system and can give quite satisfying results in good agreement with the experimental outcomes.

3.6 Further numerical scenarios

From the analysis of the experimental results, it was observed that the scenarios become more and more complex decreasing the total gap G, increasing the peak table acceleration A and the bumper's stiffness B (Fig. 3.14). In this figure, each plane corresponds to an investigated value of peak table acceleration A, which grows moving from the lower to the higher plane. In each plane, every single square of the grid correspond to a pair B-G and the corresponding color denotes the associated scenario (S1: green, S2: blue, S3: red). It can be observed that, for the lower value of A (A1), only the scenarios S1 and S2 were observed, the former only for the pair G4-A1; for values of G greater than G4, free flight condition occurs. Increasing A, only the scenarios S2 and S3 were observed and the transition from S2 to S3 occurs decreasing the total gap G and increasing the stiffness of the bumper B; furthermore, the extension of the red region, associated with the scenario S3, increases. The grazing condition was not observed for these values of A, i.e. A2 and A3, because it occurs for values of G∞ greater than G4. Based on these considerations, using the SNM, which has proven to be able to reproduce satisfactorily the experimental results, further numerical simulations were carried out to investigate what happens for combinations of the parameters not accomplished in the experimental tests. Having available for the moment the same bumpers Bk ($k = 1, 2, 3, 4$) used in the experimental campaign, new combinations can be obtained varying the gap amplitude G and the peak table acceleration A. In order to investigate the existence

of more complex scenarios, one choice may be to keep the peak table acceleration A fixed and to reduce the total gap G.

In Fig. 3.15 the numerical PRCs corresponding to the combination B3-A3 with a total gap amplitude G = 10 mm are represented. It can be observed that, compared to the previously defined scenario S3, in this case in the low frequency range different types of secondary resonances arise. In particular, for $f < 0.9$ Hz, several *secondary resonances with left hysteresis* are observed (see the area enclosed by a dotted gray circle). The attribute "left" refers to the fact that the hysteresis is a consequence of the bending to the left of the frequency response curve at the secondary resonance. On the other hand, in the neighbourhood of 1 Hz (rectangular zoomed area), a *secondary non-regular resonance*, with a less regular appearance, is noticed.
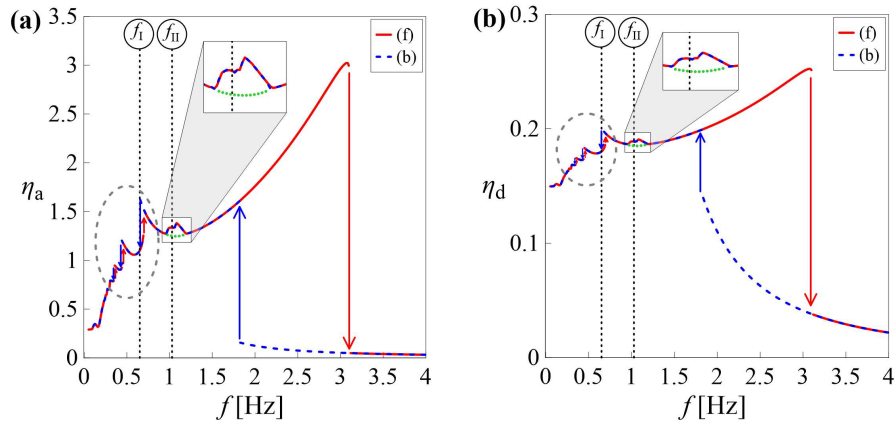
Figure 3.15. Numerical PRCs (B3-A3, G = 10 mm): **a** η_a; **b** η_d.

By focusing the attention on one of the *secondary resonances with left hysteresis* (first vertical dashed line on the left in Fig. 3.15, $f = f_I = 0.651$ Hz), it can be observed that, there are two different steady-state solutions (Fig. 3.16a):

- Large-amplitude motion with impact (blue line);

- Small-amplitude motion with impact (red line).

Each of the two limit cycles in Fig. 3.16a is antisymmetric with respect to the axes. Compared to the primary resonance (Fig. 3.8c), here the large-amplitude motion is associated with the backward sweep. Furthermore, the two solutions are both periodic multi-frequency (Fig. 3.16c) and are characterized by the occurrence of impact, as it can be seen also from Fig. 3.16e,g,i. In particular, in each forcing cycle, the mass hits each bumper twice in the forward sweep (vertical light red bands) and once in the backward sweep (vertical light blue bands). The corresponding acceleration peaks are marked with red (forward sweep) and blue (backward sweep) stars respectively. The number of impacts can also be deduced from the phase portraits (Fig. 3.16a). Both the limit cycles are characterized by the presence of internal loops. In the backward sweep, these loop do not touch the vertical dashed lines that represent the position of the obstacles, whereas in the forward sweep, the loop cross them. As in the primary hysteresis, also here there would be also an unstable solution, that could not be obtained experimentally.
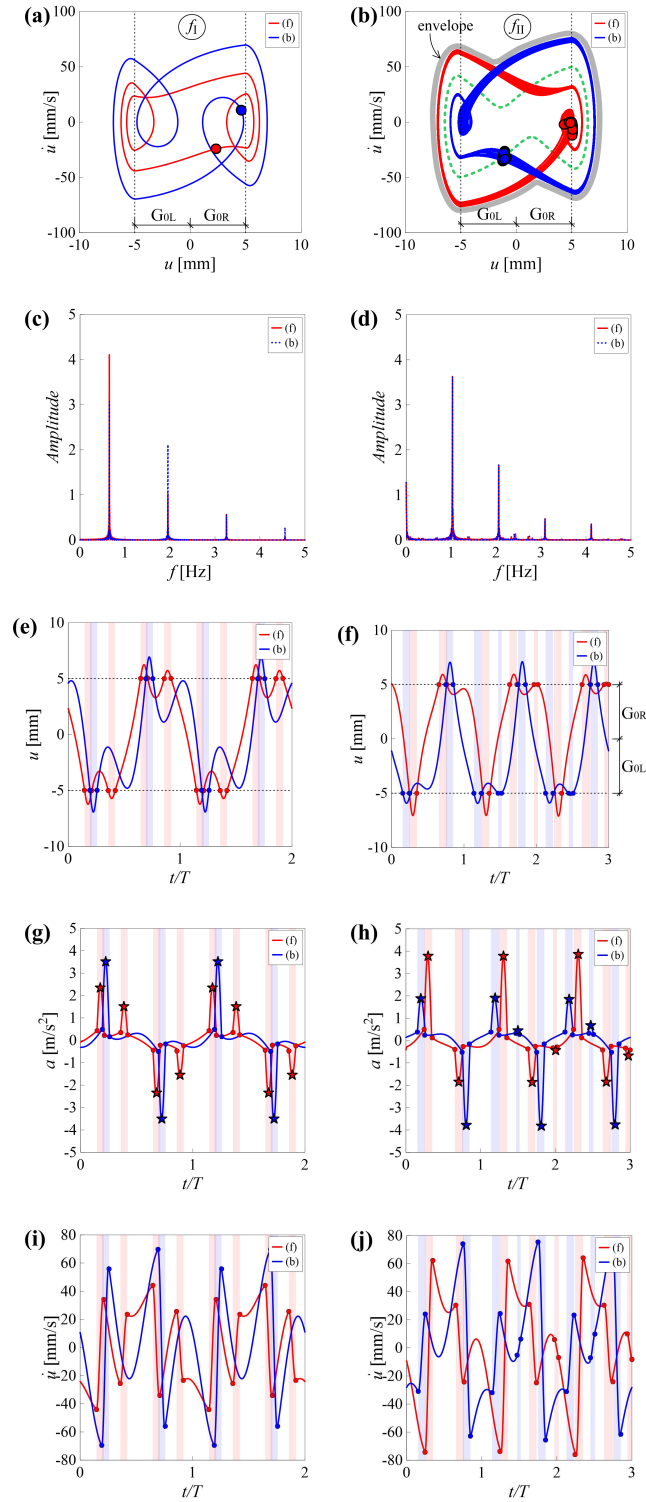
Figure 3.16. Numerical results (B3-A3, G = 10 mm). Phase portrait: **a** $f = f_I$; **b** $f = f_{II}$; Fourier spectrum: **c** $f = f_I$; **d** $f = f_{II}$; Time history of relative displacement: **e** $f = f_I$; **f** $f = f_{II}$; Time history of absolute acceleration: **g** $f = f_I$; **h** $f = f_{II}$; Time history of relative velocity: **i** $f = f_I$; **j** $f = f_{II}$.

Similar considerations apply to the other *secondary resonances with left hysteresis* that occur for smaller frequency values. What changes, in addition to the amplitude of the response, is the number and the position of the internal loops in the phase portraits and, thus, the number of impacts. In particular, decreasing the frequency, the number of impacts per forcing cycle increases, both in the forward and in the backward sweep, with a greater number of impacts always on the forward sweep.

As concerns the *secondary non-regular resonance* (second vertical dashed line in Fig. 3.15, $f = f_{II} = 1.029$ Hz), it can be observed that, in this frequency range, forward and backward PRCs overlap, therefore there is no hysteresis. In the central part of this resonance, characterized by a more or less constant excursion of both absolute acceleration and relative displacement, a *pair of quasi-periodic solutions* is observed (Figs. 3.16b,d). These two limit cycles have the same excursion but are characterized by an eccentricity, calculated as the half-sum of maximum and minimum values at steady state of each sub-frequency range, equal in absolute value but with opposite sign. Consequently, the two solutions are not antisymmetric in themselves, but the antisymmetry is achieved through their envelope, as can be seen from Fig. 3.16b, in which the envelope is highlighted in light gray. Each cycle has an internal loop which, as time goes by, approaches, crosses and then moves away from one of the left vertical dashed lines representing the position of the obstacles. In particular, the internal loop of the red cycle crosses only the right vertical line (right bumper), while the internal loop of the blue cycle crosses only the left vertical line (left bumper). Given the quasi-periodicity of the response, it is not possible to reach a steady-state condition. This results, for each of the two solutions that make up the pair, in a different number of impacts, in each forcing cycle, to the right and left as time goes on (Figs. 3.16f,h,j). In this frequency range, starting from appropriate initial conditions, it is possible to observe, besides the pair of quasi-periodic solutions, also a periodic solution, represented with a dashed green curve in Fig. 3.16b. Compared to the two quasi-periodic solution, this solution is antisymmetric in itself and is characterized by a smaller excursion and zero eccentricity. In the PRCs (Fig. 3.15) the values of excursion associated with these periodic solutions are placed on the dashed green curve, which represents the ideal course of the PRC that would have occurred in the absence of the secondary non-regular resonance.

After passing the range characterized by almost constant excursion, along the following descending branch, the presence of a pair of solutions, with an antisymmetric envelope, is still observed and both the quasi-periodicity and the internal loops gradually disappear increasing the frequency. In the next ascending branch, before the primary hysteresis, we return to having a single periodic solution.

In Fig. 3.17 the numerical PRCs corresponding to the combination B3-A3 with the bumpers initially attached to the mass (G = 0 mm) are represented. It can be observed that the situation returns to be smooth, the forward and backward curves overlap without jumps, hysteresis or secondary resonances and the primary resonance has moved to higher frequencies (about 5.4 Hz). For each frequency value, there is always a single periodic mono-frequency solution (Figs. 3.18a,b), the same on both the forward and backward sweep, and the mass, during its motion, would seem to be always in a contact condition, alternatively with a bumper or the other
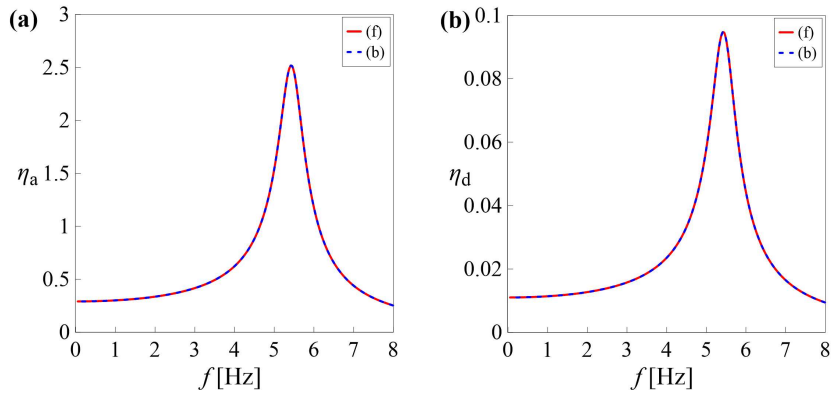
Figure 3.17. Numerical PRCs (B3-A3, G = 0 mm): **a** η_{a}; **b** η_{d}.

(Figs. 3.18c,d,e). In reality, there is also in this case a phase of free flight but it is very short. This is related to the small value of the relaxation time of the bumper, which causes the detachment between the mass and the bumper to take place when the latter has recovered practically all its deformation and immediately afterwards the mass impacts the other bumper, which in the meantime has already recovered its deformation.
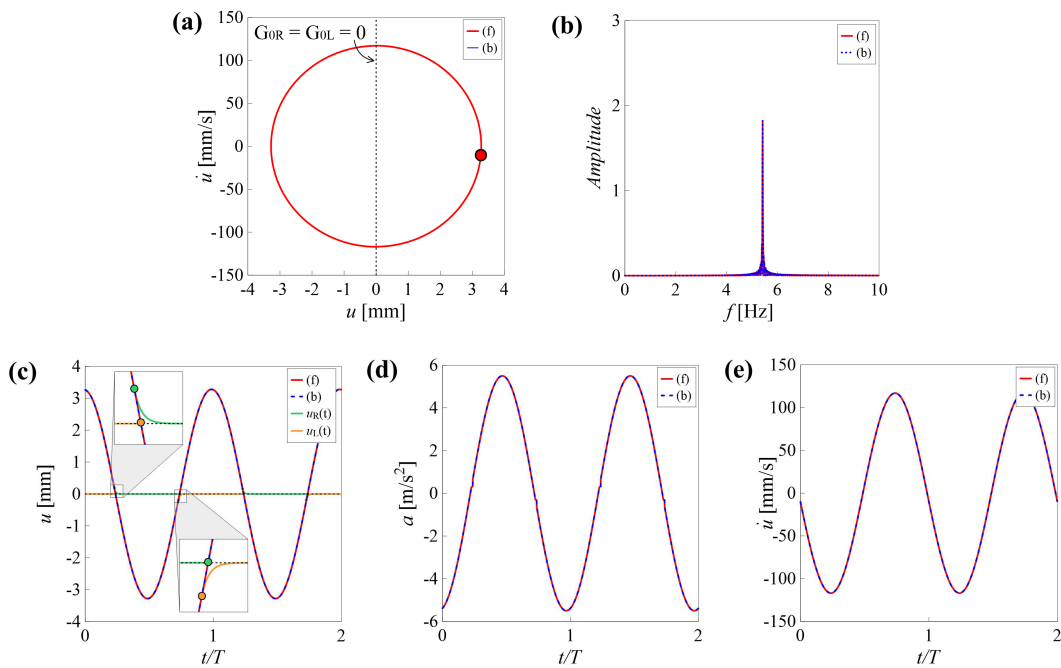
Figure 3.18. Numerical results (B3-A3, G = 0 mm), resonance condition: **a** Phase portrait; **b** Fourier spectrum; **c** Time history of relative displacement; **d** Time history of absolute acceleration; **e** Time history of relative velocity.

This can be seen better by looking at the zoomed areas in Fig. 3.18c, in which, in addition to the relative displacement of the mass, also the displacements of the right (green curve) and left (orange curve) bumpers are represented. Focusing on the zoomed area at the top of the figure, it can be observed that, after the detachment

between the mass and the right bumper, highlighted with a green dot, the right bumper recovers its deformation (green curve) while the mass goes towards the left bumper and the subsequent contact is highlighted with an orange dot.

Repeating the numerical analysis, conducted for the pair B3-A3, for other values of the total gap G and representing all the corresponding PRCs in the same graph, Fig. 3.19 is obtained. In this figure, solid line represent the forward sweep, dashed lines the backward sweep, the vertical arrows indicate the two jumps and each color corresponds to a scenario. Compared to the scenarios observed also experimentally and represented respectively with the colors green (S0 and S1), blue (S2) and red (S3), magenta was used to highlight the PRCs similar to those shown in Fig. 3.15 (the corresponding scenario will be denoted as scenario S4) and light blue for the PRCs (similar to those shown in Fig. 3.17) corresponding to a zero initial gap (the corresponding scenario will be denoted as scenario S5).
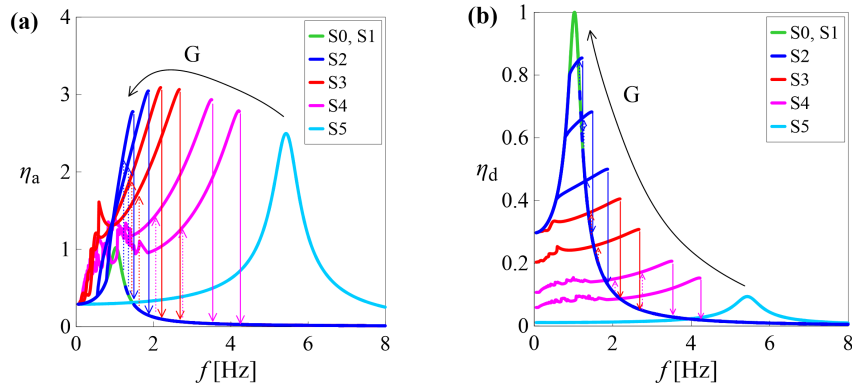
Figure 3.19. Numerical PRCs for the pair B3-A3 and different values of the total gap G: **a** η_a; **b** η_d.

It is worth noting that, using the Simplified Nonlinear Model (SNM), PRCs corresponding to the grazing condition (scenario S1) coincide with those relating to free flight (scenario S0), which are the typical dynamic amplification curves of a visco-elastic system, without jumps and softening.
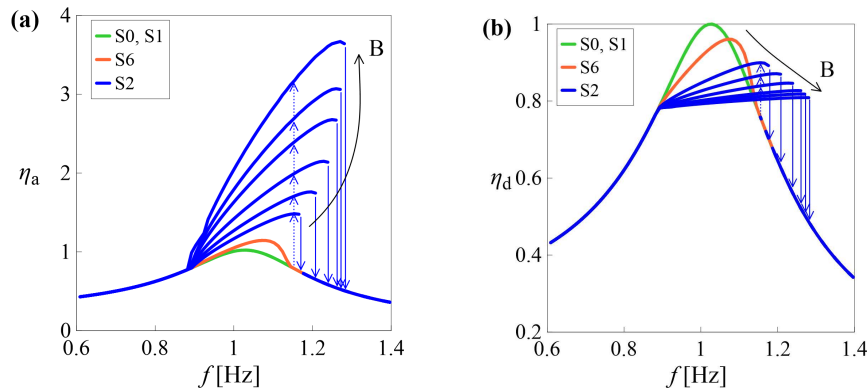
Figure 3.20. Numerical PRCs for the pair G3-A1 and different values of the bumper's stiffness B: **a** η_a; **b** η_d.

In Fig. 3.20 numerical PRCs corresponding to the pair G3-A1 and increasing values of bumper's stiffness B are represented in the same graph. The green PRCs correspond to the free flight condition. It can be observed that, for the selected pair G-A, secondary resonances do not occur even for high values of bumper's stiffness. Most of the PRCs belong to the scenario S2 (color blue), except for very small values of stiffness. In these cases (in the following denoted as scenario S6), forward and backward PRCs (in Fig. 3.20 represented with orange curves) are slightly bent to the right and overlap without jumps and hysteresis; in the frequency range associated with the occurrence of the impact, a single periodic mono-frequency solution is observed. The values of the parameters (G and B) corresponding to the curves shown in Figs. 3.19 and 3.20 have not been indicated because the purpose of the figures is not to make a comparison between numerical and experimental results, which has already been done in Section 3.5, but to give a more complete idea, compared to Figs. 3.5 and 3.6, of how the PRCs evolve with G and B, expanding the range of considered parameters also to values not investigated experimentally.

Based on the numerical results obtained with the SNM which, despite its relative simplicity, has proven to be able to reproduce the experimental scenarios satisfactorily, one of the future developments of this study will be to understand if the further numerical scenarios can be obtained also experimentally.

3.7   Interpretation of the results in terms of dimensionless parameters

The SDOF system response can be described also in terms of the following dimensionless parameters:

- $\lambda_j = K_j/K$ (j = R, L): ratio between the stiffness of the j-th bumper and that of the damper;

- $\tau_{\mathrm{r}j} = \omega C_j/K_j$ (j = R, L): dimensionless relaxation time of the j-th bumper;

- $\delta_{0j} = G_{0j}/u^*$ (j = R, L): dimensionless initial gap, that is the initial distance between the mass and the j-th bumper normalized with respect to the maximum displacement of the SDOF system (mass M and damper D, Fig. 3.1) in the free flight resonance condition. Based on this normalization, a value $\delta_{0j} = 0$ indicates that the j-th bumper is initially attached to the mass; if δ_{0j} takes values between 0 and 1, the mass beats and deforms the j-th bumper; whereas the mass will be in the free flight condition for $\delta_{0j} \geq 1$;

- ξ: damping factor of the SDOF system.

For symmetrically positioned equal bumpers it is $\lambda_{\mathrm{R}} = \lambda_{\mathrm{L}} = \lambda$, $\tau_{\mathrm{rR}} = \tau_{\mathrm{rL}} = \tau_{\mathrm{r}}$ and $\delta_{0\mathrm{R}} = \delta_{0\mathrm{L}} = \delta_0$. Consistently with what has been done in physical terms, in the following we will refer to the dimensionless total gap, denoted simply with δ, without subscript, and defined as the ratio between the total gap ($G_{0\mathrm{R}} + G_{0\mathrm{L}}$) and the maximum excursion of the SDOF system in the free flight resonance condition ($2u^*$). It follows that, for $\delta_{0\mathrm{R}} = \delta_{0\mathrm{L}} = \delta_0$, $\delta = 0.5(\delta_{0\mathrm{R}} + \delta_{0\mathrm{L}}) = \delta_0$.

Table 3.1. Dimensionless parameters

	δ					λ			
	G1	G2	G3	G4	G∞	B1	B2	B3	B4
A1	0.47	0.62	0.78	0.93	≥ 1.00	2.9	15.0	20.0	67.8
A2	0.30	0.40	0.49	0.59	≥ 1.00	3.5	17.8	23.7	80.1
A3	0.22	0.29	0.36	0.43	≥ 1.00	3.8	19.4	25.9	87.5

The estimation of the values of the dimensionless parameters, corresponding to each experimentally investigated combination of bumper's stiffness B, total gap amplitude G and peak table acceleration A, was made assuming a constant value of the damping factor ξ equal to 0.15. In the numerical investigations carried out using the SNM, for each value of peak table acceleration A, an equivalent stiffness K of the damper was considered, evaluated in free flight resonance condition. Consequently, to each bumper B correspond three values of λ, increasing with A (Table 3.1). For the same peak table acceleration A, λ increases with the stiffness of the bumper B. It can be observed that λ, so esteemed, in our case is always greater than 1 and takes on values between about 3 (combination of the most deformable bumper with the smallest table acceleration) and about 90 (combination of the stiffest bumper with the greatest table acceleration). Furthermore, for the types of bumpers considered in the experimental laboratory campaign (Sect. 2.3.1), the relaxation time $\tau_{\rm r}$ does not vary significantly and consequently it was assumed constant and equal to 0.01. As concerns the dimensionless gap δ, since the maximum displacement of the SDOF system u^* depends on the peak table acceleration A, twelve values of δ were considered, each one corresponding to a combination of A and G (Table 3.1). The dimensionless total gap increases with the total gap amplitude G, for a given value of A, and decreases increasing A, for a given value of G. It can be observed that δ in our case takes on values greater than 0.22.

The cases investigated experimentally (corresponding to different combinations B-G-A) are represented in terms of dimensionless parameters, as $\lambda - \delta$ pairs, in Fig. 3.21 for fixed values of ξ and $\tau_{\rm r}$. As in Fig. 3.14, each color corresponds to a scenario; in addition to the scenarios experimentally observed, obtained with different combinations of the parameters (S0: black horizontal line $\delta = 1$ and vertical line $\lambda = 0$, the latter not shown, S1: green region, S2: blue region, S3: red region), also those highlighted by the numerical model (S4: magenta region, S5: light blue horizontal line $\delta = 0$, S6: orange region) are represented. Each symbol corresponds to a bumper (B1: circle, B2: square, B3: triangle, B4: diamond). To each bumper correspond three values of stiffness ratio λ (three vertical dashed lines), one for each value of table acceleration A. For each value of λ (combination B-A) there are four values of δ, one for each value of total gap G. Fig. 3.21 can be seen as the translation in dimensionless terms of Fig. 3.14. The introduction of the dimensionless parameters allowed to summarize both the experimental and numerical results in a single representation (Fig. 3.21). Since the aim of the figure is only to give an idea
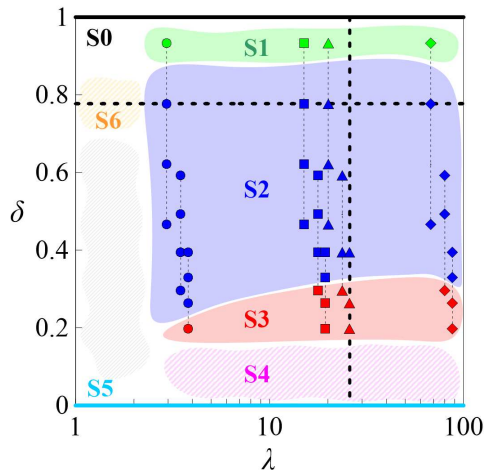
Figure 3.21. Investigated cases in terms of dimensionless parameters ($\xi = 0.15$, $\tau_r = 0.01$). B1: circle, B2: square, B3: triangle, B4: diamond.

of the extension of the regions in which homogeneous behaviors were observed, the author did not deal with defining their boundaries precisely. Consequently, they must be understood as qualitative and must be seen as thick blurred lines, because the transition from one region to another occurs with gradual evolutions.

It is worth noting that, while in physical terms the gap corresponding to grazing $G\infty$ depends on the table acceleration, in dimensionless terms this condition translates into a single value $\delta = 1$. It can be noted that the values of λ associated with the two bumpers B2 and B3 are close to each other. This is due to the fact that these two bumpers have similar stiffness. It can be observed that most of the experimental tests are associated with the scenario S2 (intermediate values of δ), four tests (highest values of δ) can be associated with the scenario S1 and the remainder with the scenario S3 (smallest values of δ). The experimental investigation did not cover a portion of the $\lambda - \delta$ plane. In particular, the vertical band characterized by $\lambda < 2$ and the horizontal band characterized by $\delta < 0.2$ were not explored. Some indications on the scenarios that could arise in these regions have been provided by the SNM (scenarios S4, S5, S6), which has proven to be able to reproduce the experimental results satisfactorily. The unexplored area (light gray shaded area) will be investigated with more detail in future developments of this study, because it is not said that, for example, within the magenta region (scenario S4), there is only the behavior shown in Fig. 3.15.

Once the dimensionless parameters were introduced, Figs. 3.5 and 3.6, represented and described in Sect. 3.4.2 in terms of physical parameters (B, G, A), can be reread also in terms of dimensionless parameters. In particular, each graph of Figs. 3.5 and 3.6, associated with a pair B-A, corresponds to a specific value of λ_{ki} (the subscript k is associated with the bumper Bk, $k = 1, 2, 3, 4$ and the subscript i is associated with the acceleration Ai, $i = 1, 2, 3$) and each curve of the graph corresponds to a specific value of dimensionless gap δ_{ji} (the subscript j is associated with the total gap Gj, $j = 1, 2, 3, 4$ and the subscript i is associated with the acceleration Ai, $i = 1, 2, 3$). Thus, each sub-figure of Figs. 3.5 and 3.6 corresponds to a section $\lambda = constant$ in Fig. 3.21. Fig. 3.19 coincides with one of these section, and it was highlighted with a vertical dashed black line $\lambda = 25.9$. Along each section

$\lambda = constant$, if A is kept fixed and G is reduced, this means reducing δ and thus moving downward. Also Fig. 3.20 can be synthetically represented in Fig. 3.21. It corresponds to the section $\delta = 0.78$, highlighted with an horizontal dashed black line. In fact, each section $\delta = constant$ corresponds to a specific pair G-A along which to increase B means increase λ and therefore move to the right. The introduction of dimensionless parameters allowed to generalize the obtained results, to reduce the number of parameters that influence the response of the system and to highlight how what matters are, not the values assumed by the individual physical parameters, but rather their relationships. This causes that the same result can be obtained with different combinations of the involved physical parameters.

3.8   Closing remarks

In this chapter, some of the scenarios which can occur in the experimental nonlinear nonsmooth response of a vibro-impact SDOF system, symmetrically constrained by deformable and dissipative bumpers under harmonic excitation (forward and backward sine sweep signal), were identified and described. The scenarios were classified by observing the characteristics of the forward and backward Pseudo-Resonance Curves (PRCs) of normalized excursion of absolute acceleration and relative displacement, obtained for different combinations of selected parameters, namely peak table acceleration A, amplitude of the total gap G and bumper's stiffness B.

Four scenarios were identified, specifically: scenario S0 corresponding to the free flight condition; scenario S1 corresponding to the grazing condition; scenario S2 with PRCs characterized by the presence of only the primary resonance with right hysteresis; scenario S3 with PRCs with both the primary resonance with right hysteresis and the secondary resonance. It has been observed that PRCs belonging to the same scenario can be obtained with different combinations of the investigated parameters. The identified scenarios were subsequently investigated in more detail resorting to phase portraits, Fourier spectra and time histories of relative displacement, absolute acceleration and relative velocity of the mass in steady-state condition.

The experimental investigation was followed by a numerical analysis conducted using the Simplified Nonlinear Model (SNM), in which both the bumpers and the damper were modelled with a Kelvin-Voigt model, retaining the other nonlinearities which characterize the problem, namely the existence of clearances, the unilaterality of the contact and the occurrence of impact, which causes abrupt changes of stiffness and damping at the contact time. The use of a linear visco-elastic modeling of both damper and bumpers, despite its limitations, was satisfactory for the purposes of this study. It was observed that the SNM, despite its relative simplicity, can give quite satisfying results in good agreement with the experimental outcomes. For this reason, it was used to extend the range of investigation, considering values of the parameters not investigated experimentally.

The numerical investigations allowed to highlight the existence of more complex response scenarios (characterized by the existence of secondary regular resonances without hysteresis, secondary regular resonances with left hysteresis, secondary non-

regular resonances, these last ones exhibiting pairs of quasi-periodic solutions of large amplitude and -starting by appropriate initial conditions- also periodic solutions of small amplitude), that could be obtained, for example, considering values of the total gap G smaller than those considered in the experimental laboratory campaign.

Finally, suitable dimensionless parameters, namely stiffness ratio, dimensionless relaxation time, dimensionless initial gap and damping ratio of the SDOF system were introduced and the experimental results were framed in terms of these parameters. The transition to the dimensionless parameters allowed to reduce the number of parameters that influence the response of the system and, consequently, to synthesize in a single graph the results of both the experimental and numerical investigations, and to highlight how what matters are, not the values assumed by the individual involved physical parameters, but rather their relationships. This causes that the same scenario can be obtained with different combinations of the involved physical parameters.

Based on the numerical results, as a first future development of this study, there is the intention to investigate the possibility to experimentally regain the more complex scenarios obtained with the SNM. Furthermore, to fully capture, qualitatively and quantitatively, the main aspects of the response of the system, also a more refined nonlinear numerical model, that includes all the nonlinearities will be considered in future analyses.

Chapter 4

Response scenarios: numerical in-depth analysis

Chapter outline In this chapter, some of the scenarios that can occur in the numerical nonlinear non-smooth response of a vibro-impact SDOF system, symmetrically constrained by deformable and dissipative bumpers, are identified and described. The different scenarios, obtained varying selected dimensionless parameters, are investigated identifying homogeneous frequency intervals, characterized by similar features in terms of number and types of limit cycles, and resorting to phase portraits, basins of attraction and Fourier spectra. Despite the relative simplicity of the model, which however takes into account impact, clearance and unilaterality of the constraints, decreasing the dimensionless gap δ_0, from $\delta_0 = 1$ to $\delta_0 = 0$, gradually more complex and varied scenarios, characterized by different types of secondary resonances (with right or left hysteresis or of non-regular type), cascades in the low frequency range, periodic, quasi-periodic or chaotic solutions were observed. The occurrence of primary and secondary grazing was also highlighted.

The contents of this chapter were published in: "Stefani, G., De Angelis, M., Andreaus, U. Numerical study on the response scenarios in a vibro-impact single-degree-of-freedom oscillator with two unilateral dissipative and deformable constraints. *Communications in Nonlinear Science and Numerical Simulation* (2021), [Elsevier]", [250].

4.1 Introduction

In many practical (biomedical, mechanical, civil, ...) engineering applications, mechanical components or structures repeatedly collide with one another or with obstacles [110]. Impacts occur, for example, in the capsule systems used in clinic endoscopy to inspect the surface lining of the intestine in the human body [87, 165, 166, 293, 294], and in the drilling rigs used in the oil and gas industry for creation of wells [57, 65, 158, 159, 161, 267]. In the field of civil engineering, base-isolated systems (building [140, 187, 190, 191, 194, 221, 222], bridges [90, 93, 123], equipment [5, 92, 116, 168, 228, 229], strategic facilities [235]) when subject to exceptional loads,

like severe earthquakes, can undergo large horizontal displacements, concentrated in the isolation system. These displacement can damage the isolation system itself or can lead to pounding between the isolated system and the surrounding moat walls or any adjacent structures, if the available gap is not sufficient. The consequences of pounding can damage the structure or sensitive equipment housed in it, impairing their functionality. When it is not possible to guarantee a sufficient clearance, the side effects of pounding can be mitigated reducing the impact stiffness through the interposition of dissipative and deformable shock absorbers (also known as bumpers) between the colliding systems [223, 224]. In the absence of obstacles near the isolated system, to avoid the excessive deformation or the damage of the isolation system, the displacements can be limited either by inserting end stops or by using other suitable types of control systems [15, 80, 231].

Several scientific works, of both numerical and experimental nature, dealt with vibro-impact dynamics. In the numerical simulations impact can be modeled using both a stereomechanical or a force-based approach [129]. In the first approach, the duration of the contact is neglected and the impact is modeled using the momentum conservation principle and the coefficient of restitution, the latter defined as the ratio between the velocities immediately after impact and immediately before the impact [82]. In the second approach, the contact force can be modeled in different ways, resorting to more or less sophisticated modeling [77, 78, 186, 200, 241], going from pure elastic contact force models, such as the linear spring element and the Hertz contact model (nonlinear spring element [101, 226]), which however do not take into account the energy loss during the impact, to dissipative contact force models, such as the Kelvin-Voigt model [67, 82, 137] and the model proposed by Hunt and Crossley [108], to overcome the drawbacks of the Kelvin-Voigt model, and consisting of an elastic Hertz's law combined with a nonlinear viscoelastic element (Hertzdamp model).

The types of impact motion, and the bifurcations from one motion to the other, that can occur in the dynamics of vibro-impact systems with motion limiting constraints, with the variation of selected parameters are the subject of several studies, of mainly numerical nature [40, 61, 86, 95, 126, 176, 181–183, 271, 273, 274, 299, 304]. The study of the dynamics of a two-degree-of-freedom periodically-forced system with symmetric motion limiting constraints, with emphasis on the transition between fundamental impact motions, together with the design and implementation of an electronic circuit, describing the dynamic characteristics of the non-smooth system, are presented in [182]. The motions of a periodically forced non-smooth Duffing system at the switching boundary and the coexistence of different attractors are investigated in [40] through numerical simulations. Focusing on the switching behaviors on the boundary between two adjacent domains, in a periodically forced modified Duffing-Rayleigh system, the coexistence of attractors, under different initial conditions, is illustrated through basins of attraction and phase planes in [304]. The grazing-induced bifurcations in impact oscillators with one-sided elastic and rigid constraints are investigated and classified in [126] by a path-following method. In [183], pattern types, stability domains and bifurcation characteristics of periodic motions for a two-degree-of-freedom oscillator with a clearance are investigated and attracting domains and Poincaré mapping diagrams of coexisting motions in the neighborhood of grazing bifurcations are discussed. The parameters influence and the

features of the dynamic response of impact oscillators in the vicinity of degenerate grazing points is investigated and characterized in [299], using the GPU computing parallel technology and other numerical methods. Phenomena of coexisting attractors and chaotic transitions, including crisis, are also discussed, considering single and two degree-of-freedom impact oscillators.

The practical problem of base-isolated structures impacting against moat-walls inspired several works of by Andreaus et al., of both numerical and experimental nature, in which the response of these structures was simulated using a Single-Degree-Of-Freedom (SDOF) oscillator, consisting of a mass and a damper, impacting against two deformable and dissipative constraints (bumpers), symmetrically arranged on both sides [9, 10, 12–14, 247–249, 251]. Some of the scenarios that can occur within the system response were first investigated in the theoretical-numerical work presented in [12]. The study of the scenarios was then taken up by the author of this thesis together with her co-authors in [248, 251], in which some scenarios, identified based on the results of an experimental laboratory campaign, were investigated and then reproduced using a suitable numerical model.

Based on the results obtained in [248, 251], the aim of the present work is to deepen the study of the scenarios that can occur in the nonlinear non-smooth response of a vibro-impact SDOF system, from a numerical point of view, extending the range of investigated parameters, compared to the previous studies. The system, symmetrically constrained with deformable and dissipative bumpers, and subject to a sine sweep base excitation, is described in terms of dimensionless parameters and particular attention is devoted in this work to the study of the role played by the damping ratio, due to the adopted normalization. The scenarios are identified based on the characteristics of the Pseudo-Resonance Curves (PRCs) of normalized excursion and eccentricity of absolute acceleration and relative displacement of the mass. The scenarios observed by reducing the dimensionless gap and keeping the values of the other dimensionless parameters fixed, are subsequently investigated by identifying homogeneous frequency ranges and resorting to phase portraits, basins of attraction and Fourier spectra.

The chapter is organized as follows. The numerical model of the nonlinear SDOF system, together with the dimensionless governing equations and the study on the role of damping, are introduced in Sect. 4.2; the identified scenarios are shown and discussed in Sect. 4.3; the conclusions and future developments of the work are finally drawn in Sect. 4.5.

4.2 Numerical model

A suitable numerical model, able to simulate the dynamic behavior of a vibro-impact Single-Degree-Of-Freedom (SDOF) system, impacting against unilateral dissipative and deformable obstacles (bumpers), is shown in Fig. 4.1. The system consists of a mass M and a damper (D), the latter modeled by a linear elastic element, with stiffness K, and a linear viscous damper, with damping coefficient C, arranged in parallel. The two obstacles, denoted as right bumper (B_R) and left bumper (B_L) respectively, are symmetrically positioned on both sides of the mass, at an initial distance (initial gap) G_{0j} ($j = R, L$), are massless and are modeled by a linear elastic

element, with stiffness K_j ($j = $ R, L), and a linear viscous damper, with damping coefficient C_j ($j = $ R, L), arranged in parallel. The system is subject to a harmonic base acceleration $A_t(t) = A_G \sin \Omega t$, with amplitude A_G and circular frequency Ω. In Fig. 4.1, u and u_j ($j = $ R, L) denote the displacements, of the mass and of the two bumpers respectively, relative to the ground.
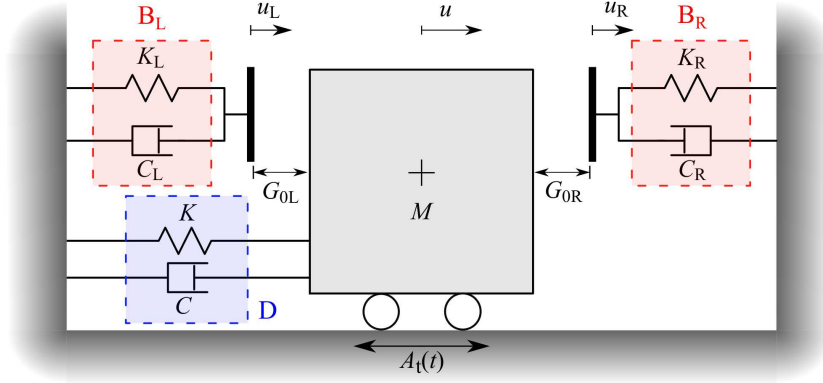
Figure 4.1. Model of the system.

4.2.1 Dimensionless equations of motion

The equations of motion of the system depicted in Fig. 4.1 can be written in the following dimensionless form:

$$\begin{cases} q''(\tau) + 2\xi q'(\tau) + r(\tau) + [2\xi \gamma_j q'(\tau) + r_j(\tau)] \cdot \psi_1 [\delta_j(\tau)] \cdot \psi_2 [f_j(\tau)] = -a_G \sin \beta \tau \\ 2\xi \gamma_i q'(\tau) + r_i(\tau) = 0 \end{cases}$$

(4.1)

In Eq. 4.1, it is assumed that whether $j = $ L then $i = $ R, or whether $j = $ R then $i = $ L. The nondimensionalization of the governing equations was obtained by introducing the following characteristic quantities:

$$\omega = \sqrt{\frac{K}{M}}, \quad u^* = \frac{MA_G}{K} R_{d,max}, \quad F^* = Ku^* = M\omega^2 u^* = MA_G R_{d,max} \quad (4.2)$$

namely the natural circular frequency of the SDOF system ω, the maximum relative displacement u^* and the maximum force F^* in the SDOF system in free flight (that is without obstacles) resonance condition. In Eq. 4.2, $R_{d,max}$ is the maximum value of the dynamic amplification factor R_d, defined as the ratio between the amplitude of the dynamic displacement u to the static displacement MA_G/K, at the resonant frequency, which is function of the damping ratio $\xi = C/(2M\omega)$ of the SDOF system, that is $R_{d,max} = 1/(2\xi\sqrt{1 - \xi^2})$ for $\xi < \sqrt{2}/2$. In Eq. 4.1, $q = u/u^*$ and $q_j = u_j/u^*$ ($j = $ R, L) are the dimensionless relative displacements of the mass and of the right and left bumper respectively, and the apex ($'$) denotes differentiation with respect to the dimensionless time $\tau = \omega t$; $a_G = 2\xi\sqrt{1 - \xi^2}$ is the dimensionless amplitude of the base acceleration $a_t(\tau)$; $\beta = \Omega/\omega$ is the ratio between the circular frequency of the base excitation Ω and the natural circular frequency of the SDOF system

ω; $\gamma_j = C_j/C$ $(j = \text{R}, \text{L})$ is the ratio between the viscous damping coefficients of the j-th bumper and that of the damper and $\delta_j(\tau)$ is the clearance function that represents the distance, instant by instant, between the mass and the j-th bumper and it is defined as follows:

$$\delta_j(\tau) = \delta_{0j} + \Delta q_j(\tau) \quad (j = \text{R}, \text{L}) \tag{4.3a}$$

$$\Delta q_\text{R}(\tau) = q_\text{R}(\tau) - q(\tau), \quad \Delta q_\text{L}(\tau) = q(\tau) - q_\text{L}(\tau) \tag{4.3b}$$

When the mass is in contact with the j-th bumper $\delta_j(\tau) = 0$ $(j = \text{R}, \text{L})$, otherwise $\delta_j(\tau) > 0$. In Eq. 4.3a $\delta_{0j} = G_{0j}/u^*$ $(j = \text{R}, \text{L})$ denotes the initial dimensionless gap between the mass and the j-th bumper. Based on the adopted normalization, $\delta_{0j} = 0$ if the j-th bumper is initially in contact with the mass; for $0 < \delta_{0j} < 1$ the mass beats and deforms the j-th bumper; whereas the mass will be in free flight condition for $\delta_{0j} \geq 1$. In Eq. 4.1, ψ_1 and ψ_2 represent the Heaviside functions, defined as follows:

$$\text{Contact} \quad \psi_1\left[\delta_j(\tau)\right] = \begin{cases} 0, & \delta_j(\tau) > 0 \\ 1, & \delta_j(\tau) = 0 \end{cases} \tag{4.4a}$$

$$\text{Separation} \quad \psi_2\left[f_j(\tau)\right] = \begin{cases} 0, & f_j(\tau) \leq 0 \ (j = \text{R}) \text{ or } f_j(\tau) \geq 0 \ (\text{j} = \text{L}) \\ 1, & f_j(\tau) > 0 \ (j = \text{R}) \text{ or } f_j(\tau) < 0 \ (j = \text{L}) \end{cases} \tag{4.4b}$$

where $f_j(\tau) = 2\xi\gamma_j q'(\tau) + r_j(\tau)$ is the contact force occurring during the contact period with the j-th bumper. The normalized restoring forces, exerted by the damper and the bumpers, were denoted by r and r_j $(j = \text{R}, \text{L})$ respectively, and they have the following expressions:

$$r(\tau) = q(\tau) \tag{4.5a}$$

$$r_\text{R}(\tau) = \lambda_\text{R} q_\text{R}(\tau) = \lambda_\text{R}[q(\tau) - \delta_{0\text{R}}], \quad r_\text{L}(\tau) = \lambda_\text{L} q_\text{L}(\tau) = \lambda_\text{L}[q(\tau) + \delta_{0\text{L}}] \tag{4.5b}$$

where $\lambda_j = K_j/K$ $(j = \text{R}, \text{L})$ is the ratio between the stiffnesses of the j-th bumper and that of the damper.

4.2.2 Parameters

The dimensionless parameters that influence the response of the system are therefore: the frequency ratio β, the damping ratio ξ, the initial dimensionless gap δ_{0j} $(j = \text{R}, \text{L})$, the stiffness ratio λ_j $(j = \text{R}, \text{L})$ and the damping ratio γ_j $(j = \text{R}, \text{L})$. As an alternative to the damping ratio γ_j, the dissipative capacities of the bumpers can also be characterized through the dimensionless relaxation time $\tau_{\text{r}j} = \omega\, t_{\text{r}j}$, where $t_{\text{r}j} = C_j/K_j$ $(j = \text{R}, \text{L})$. In this study we considered two equal bumpers symmetrically arranged on the two sides of the mass. It follows that $\lambda_\text{R} = \lambda_\text{L} = \lambda$, $\gamma_\text{R} = \gamma_\text{L} = \gamma$ (or alternatively $\tau_{\text{rR}} = \tau_{\text{rL}} = \tau_\text{r}$) and $\delta_{0\text{R}} = \delta_{0\text{L}} = \delta_0$.

4.2.3 Nonlinearities

Although both the bumpers and the damper have been modeled with a linear elastic spring in parallel with a linear viscous dashpot, the system is however strongly nonlinear. In particular, the nonlinearities are due to the presence of clearance, the unilateral constrains and the occurrence of impact that causes abrupt changes of stiffness and damping at the contact time.
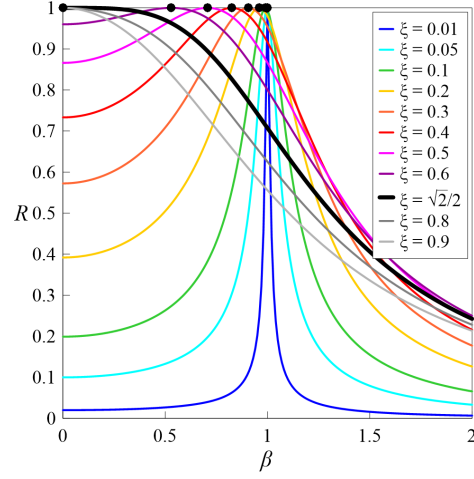
Figure 4.2. Dynamic amplification factor $R(\xi, \beta)$ for different values of the damping ratio ξ.

4.2.4 Role of damping

The damping ratio of the SDOF system ξ affects both the response of the system (it reduces the response amplitude at all excitation frequencies) and, following the adopted normalization, the amplitude of the base acceleration a_G. In the absence of bumpers, by normalizing the amplitude of dynamic displacement u with respect to the maximum displacement in resonance condition u^*, instead of the static displacement, the dynamic amplification factor (denoted as R to distinguish it from R_d, Eq. 2.6), function of both damping ratio ξ and frequency ratio β, for $\xi < \sqrt{2}/2$, is given by:

$$R(\xi, \beta) = \frac{2\xi\sqrt{1 - \xi^2}}{\sqrt{(1 - \beta^2)^2 + (2\xi\beta)^2}} \tag{4.6}$$

In Fig. 4.2, $R(\xi, \beta)$ is plotted for different values of damping ratio ξ. It can be observed that, for $\beta = 0$ (slowly varying excitation), R (Eq. 4.6) attains the value $R(\xi, 0) = 2\xi\sqrt{1 - \xi^2}$ and thus it increases with ξ, as long as $0 < \xi < \sqrt{2}/2$; for $\sqrt{2}/2 \leq \xi < 1$, $R(\xi, 0) = 1$. The variation of the resonant frequency ratio $\beta_{Rd}(\xi) = \sqrt{1 - 2\xi^2}$ with ξ is highlighted with black dots. It can be noted that β_{Rd} decreases as ξ increases and, for $\sqrt{2}/2 \leq \xi < 1$, $\beta_{Rd} = 0$.

In the presence of bumpers, symmetrically placed at an initial distance δ_0, impact can occur. In particular, it is possible to analytically determine the frequency interval in which impact surely will occur, for a given value of δ_0, by imposing:

$$R(\xi, \beta) = \frac{2\xi\sqrt{1 - \xi^2}}{\sqrt{(1 - \beta^2)^2 + (2\xi\beta)^2}} = \delta_0 \tag{4.7}$$

By solving Eq. 4.7, for each (ξ, δ_0) pair in the ranges $0 < \xi < 1$ and $0 \leq \delta_0 \leq 1$, the contour maps of the roots, denoted as β_1 (red) and β_2 (blue) respectively (with $\beta_2 \geq \beta_1$), shown in Fig. 4.3a, were obtained. It can be observed that the $\delta_0 - \xi$ plane is divided in two regions by the thick green curve with equation $\delta_0 = 2\xi\sqrt{1 - \xi^2}$ (for $0 < \xi < \sqrt{2}/2$). Along this curve, $\beta_1 = 0 \; \forall \xi$, whereas β_2 decreases as ξ increases. In the region above this curve, the two contour maps associated with the two roots of Eq. 4.7, β_1 and β_2, overlap. In the region below this curve, there is only the contour map associated with β_2.
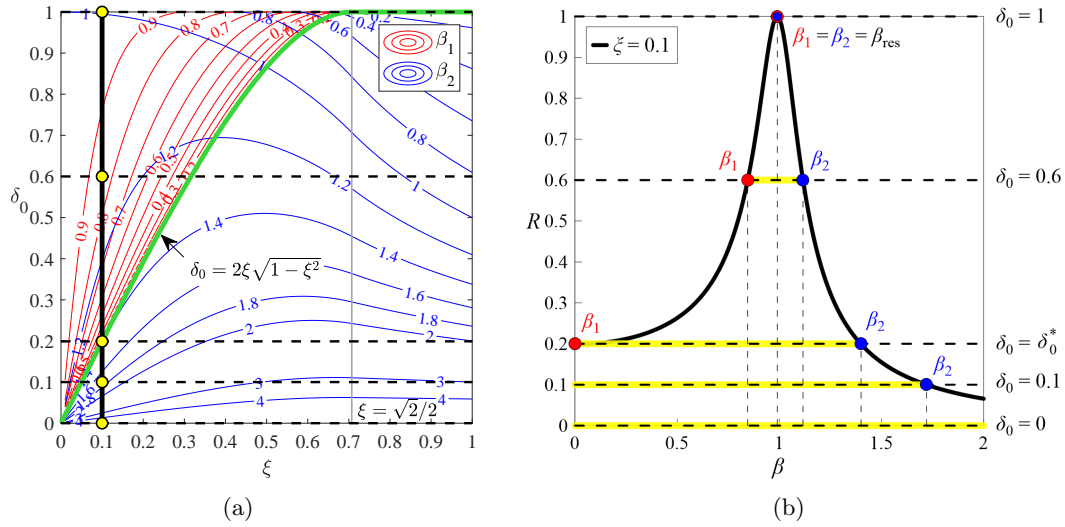
Figure 4.3. **a** Contour maps of the frequency ratios β_1 (red) and β_2 (blue) in the $\xi - \delta_0$ plane; **b** dynamic amplification factor R for $\xi = 0.1$ with the location of β_1 (red) and β_2 (blue) corresponding to the considered δ_0 values (horizontal dashed lines). The frequency interval between β_1 and β_2 (highlighted in yellow) is characterized by the occurrence of impact.

For a given value of damping ratio, for example $\xi = 0.1$ (see the thick black vertical line in Fig. 4.3a and the corresponding dynamic amplification factor $R(0.1, \beta)$ in Fig. 4.3b), different situations can occur depending on the value of δ_0 (yellow dots in Fig. 4.3a). It can be observed that:

- For $\delta_0 = 1$, Eq. 4.7 admits two coincident roots $\beta_1 = \beta_2 = \beta_{\text{Rd}}$; consequently, impact does not occur for any β value;

- For $\delta_0^* = 2\xi\sqrt{1 - \xi^2} < \delta_0 < 1$, e.g. $\delta_0 = 0.6$, Eq. 4.7 admits two non-zero roots, $\beta_1 < \beta_{\text{Rd}}$ and $\beta_2 > \beta_{\text{Rd}}$; these two roots approach as δ_0 increases;

- For $\delta_0 = \delta_0^* = 2\xi\sqrt{1 - \xi^2}$, e.g. $\delta_0 \simeq 0.2$, Eq. 4.7 admits two roots: $\beta_1 = 0$ and $\beta_2 > \beta_{\text{Rd}}$;

- For $0 < \delta_0 < \delta_0^* = 2\xi\sqrt{1 - \xi^2}$, e.g. $\delta_0 = 0.1$, Eq. 4.7 admits a single non-zero root ($\beta_2 > \beta_{\text{Rd}}$), whose value decreases with increasing δ_0;

- For $\delta_0 = 0$, $R(\xi, \beta) > \delta_0 \;\; \forall \beta$; consequently, Eq. 4.7 does not admit roots; this means that impact always occurs independently of β.

In Fig. 4.3b, for each considered δ_0 value, the frequency interval in which impact will surely occur ($\beta_1 \leq \beta \leq \beta_2$) was highlighted with a yellow horizontal line. It can be observed that, this frequency range increases as δ_0 decreases. It is worth noting that impact can also occur for $\beta < \beta_1$ or $\beta > \beta_2$, depending on the nonlinear behavior of the system, the values of the parameters and the initial conditions. The same considerations apply for other values of damping ratio $0 < \xi < \sqrt{2}/2$; what changes is the value of δ_0^* and consequently the amplitudes of δ_0 intervals in which

there is only the root β_2 (below the green curve in Fig. 4.3a) or both roots β_1 and β_2 (above the green curve in Fig. 4.3a). For $\sqrt{2}/2 \leq \xi < 1$, Eq. 4.7 admits a single non-zero root ($\beta_2 > 0$) $\forall \delta_0 \in \,]0;1[$, whereas for $\delta_0 = \delta_0^* = 1$, the two roots are coincident and equal to zero ($\beta_1 = \beta_2 = 0$). As concerns the amplitude of the base excitation, since the system is nonlinear, it can significantly affect the dynamical phenomena exhibited by the system. Due to the adopted normalization, it depends on the damping ratio ξ ($a_G = 2\xi\sqrt{1-\xi^2}$) and varies with the same law shown by the thick green curve in Fig. 4.3a. It can be observed that a_G increases with ξ, as long as $\xi < \sqrt{2}/2$; whereas, for $\sqrt{2}/2 \leq \xi < 1$, it is independent from ξ and it is equal to 1. Consequently, the parameter that describes the input is not what is expected (its amplitude), but rather the damping ratio ξ. The excitation, thus is essentially filtered through the damping ratio. In this study we assumed $\xi = 0.1$, which corresponds to a_G almost equal to 0.2. This study on the role of damping ξ and on the evolution of the roots of Eq. 4.7 with the dimensionless gap δ_0 (Fig. 4.3b) guided the subsequent numerical investigations and, thus, it is functional to what will be said in the following Sections.

4.3 Scenarios

In this Section, some of the scenarios that can occur in the dynamic non-smooth response of the SDOF system, with the variation of selected parameters, will be identified and discussed. In particular, the analyses were conducted by assuming $\xi = 0.1$ and $\gamma = 5$, and by varying λ and δ_0. The author of this thesis do not claim to have exhaustively identified all the possible scenarios that can occur; those shown are just some of situations emerged in this exploratory numerical investigation.

The identification of the scenarios was made on the basis of the characteristics of the Pseudo-Resonance Curves (PRCs) of normalized excursion and eccentricity of relative displacement ($\eta_d = \Delta q/\Delta q_0$ and $e_d = \overline{q}/\Delta q_0$ respectively) and absolute acceleration ($\eta_a = \Delta\alpha/\Delta\alpha_0$ and $e_a = \overline{\alpha}/\Delta\alpha_0$ respectively) of the mass. The PRCs were obtained considering a step-wise forward and backward sine sweep base acceleration, that is a harmonic signal with constant amplitude, in which the forcing frequency is increased (forward sweep) and then decreased (backward sweep) over time, within a specific frequency range and with an appropriate frequency increment, after a certain number of cycles. Subsequently, based on the results obtained with the sine sweep signal, in cases where it was considered necessary, further in-depth analyses on the influence of initial conditions, with the construction of basins of attraction, were carried out. The absolute acceleration of the mass $\alpha(\tau)$ is given by the sum of the acceleration of the ground $a_t(\tau)$ and the relative acceleration between the mass and the ground $q''(\tau)$: $\alpha(\tau) = a_t(\tau) + q''(\tau)$. The excursion ($\Delta q$ and $\Delta\alpha$) was calculated as the difference between the maximum and minimum values recorded at steady-state of each sub-frequency range, that is $\Delta q = q_{max} - q_{min}$ and $\Delta\alpha = \alpha_{max} - \alpha_{min}$, whereas the eccentricity ($\overline{q}$ and $\overline{\alpha}$) was calculated as the half-sum of maximum and minimum values, that is $\overline{q} = (q_{max} + q_{min})/2$ and $\overline{\alpha} = (\alpha_{max} + \alpha_{min})/2$ and thus, it allowed to highlight non symmetric behaviors. Subsequently, both the excursion and the eccentricity, thus calculated, were normalized with respect to the maximum excursion in free flight resonant condition (Δq_0 and $\Delta\alpha_0$ respectively).

Referring to the situation characterized by the presence of the obstacles, initially placed at a distance δ_0 from the mass, in order to classify the scenarios from the characteristics of PRCs, a first distinction was made on the basis of the absence ($\delta_0 \geq 1$) or occurrence ($0 \leq \delta_0 < 1$) of impact. In the latter case, a further differentiation was made based on the absence or existence of the *primary resonance with right hysteresis*, between the jumps in the forward and backward sweeps. Finally, the occurrence and type of *secondary resonances* in the low frequency range, and the existence of frequency ranges characterized by non-zero eccentricity allowed to recognize further scenarios. This procedure made it possible to identify, in the $\lambda - \delta_0$ plane, for $0 \leq \delta_0 \leq 1$ and $0 < \lambda \leq 100$, seven homogeneous regions, identified by Roman numerals enclosed within circles and highlighted with different colors in the map shown in the central part of Fig. 4.4.
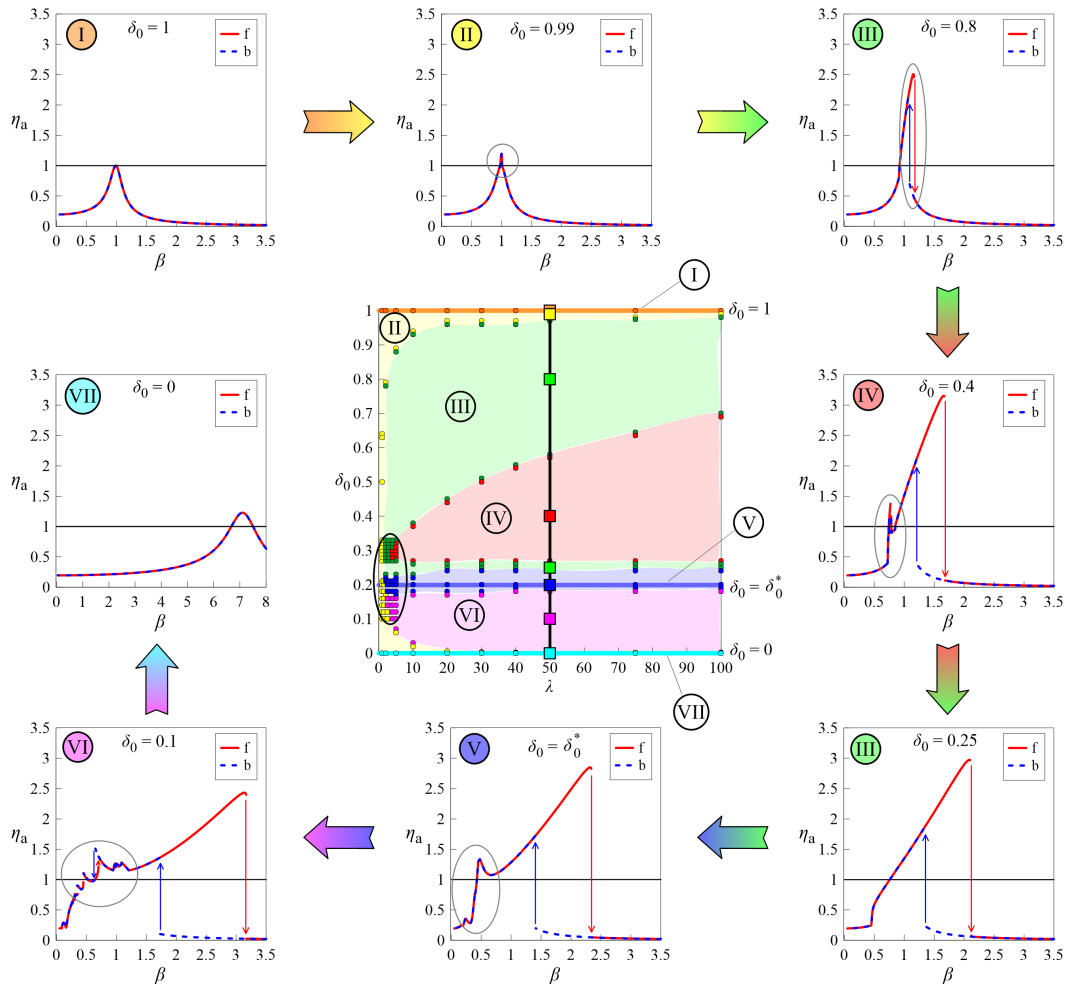
Figure 4.4. Homogeneous regions in the $\lambda - \delta_0$ plane ($\xi = 0.1$, $\gamma = 5$), identified by Roman numerals enclosed within circles and highlighted with different colors. The colored dots represent the $\lambda - \delta_0$ pairs investigated to qualitatively identify the boundaries of the regions. Representative PRCs of η_a for $\lambda = 50$ (vertical black line), corresponding to the colored squares, are arranged clockwise around the map.

The colored dots represent some of the (λ, δ_0) pairs investigated to qualitatively identify, in a discrete way, the boundaries of these regions. These borders should not be seen as well-defined dividing lines, but rather as thick blurred lines, because the transition from one region to another occurs with gradual evolutions. For small values of λ and δ_0 (see the region enclosed by an ellipse), a high density of investigated points is observed. In this zone, which will not be investigated in this work, some of the identified regions converge (high chromatic variety), and thus, small variations in both λ and δ_0 determine the passage from one region to another.

From Fig. 4.4, it can be observed that two of the identified regions are more properly lines, namely $\delta_0 = 1$ (Region I, highlighted with an horizontal orange line), and $\delta_0 = 0$ (Region VII, highlighted with an horizontal cyan line). Furthermore, it can be noted that Region II (yellow colored) follows the three sides of the $\lambda - \delta_0$ domain (δ_0 close to 1, small values of λ and δ_0 close to 0), Region III (highlighted in green) seems to embrace Region IV (highlighted in red) and Region V (highlighted in blue) is placed around $\delta_0 = \delta_0^* \simeq 0.2$ (see Sect. 4.2.4). By focusing the attention on a fixed value of stiffness ratio, e.g. $\lambda = 50$, which corresponds to a quite rigid obstacle (see the black vertical line in the map of Fig. 4.4), the occurrence of one scenario rather than the other depends on the value of the dimensionless gap δ_0. For this value of λ and for each identified region, representative PRCs of normalized excursion of absolute acceleration η_a (which allow to better highlight some behaviors, especially at low frequencies, compared to the PRCs of η_d) and corresponding to the colored squares, are arranged clockwise around the map. In these figures, the solid red curve refers to the forward sweep (indicated with an f in the legend), the dashed blue curve to the backward sweep (indicated with a b in the legend), the vertical arrows represents the jumps and the solid black horizontal line indicates the unit value of η_a.

It can be observed that, starting from $\delta_0 = 1$ (see the figure on the top left), in which the situation is smooth, the encountered scenarios become gradually more complex decreasing δ_0 (move clockwise around the map, following the colored arrows), with the occurrence of the *primary resonance with right hysteresis* and different types of *secondary resonances* (with *right* or *left hysteresis* or of *non-regular* type), while in the limit case $\delta_0 = 0$ (bumpers initially in contact with the mass) the situation returns to be smooth, although the dynamics is different from that corresponding to $\delta_0 = 1$. Based on what was said in Sect. 4.2.4, the horizontal blue line $\delta_0 = \delta_0^*$, at the turn of which lies the Region V, represents the locus of the (λ, δ_0) pairs to which correspond two distinct roots of the Eq. 4.7, one of which (β_1) is equal to zero (Fig. 4.3b), regardless of the λ value. This line represents a watershed that divides the $\lambda - \delta_0$ plane into two parts. Above this line ($\delta_0^* \leq \delta_0 < 1$) there are the (λ, δ_0) pairs to which correspond two distinct roots (β_1 and β_2) of the Eq. 4.7; the two roots become coincident for $\delta_0 = 1$. PRCs do not highlight complex behaviors, except for some values of δ_0 (inside the Region IV); in these cases however, these complex behaviors are observed in small frequency ranges.

More complex and varied scenarios are observed instead for $0 < \delta_0 < \delta_0^*$. In this zone there are the (λ, δ_0) pairs to which corresponds a single non-zero root (β_2) of the Eq. 4.7 and impact occurs immediately starting from $\beta = 0$. It is worth noting that inside Region VI very different behaviors can be observed, slightly varying δ_0, and the figure at the bottom left, corresponding to $\delta_0 = 0.1$, is just one example

of one of these behaviors. From Fig. 4.4 it can be observed how, although the considered model seems apparently simple, by varying the involved parameters, even particularly complex scenarios can be encountered. In the following Subsections, the seven identified scenarios will be described in more detail, starting from the analysis of the PRCs, and resorting to phase portraits in steady-state condition, Poincaré sections, basins of attraction and Fourier spectra.

Region I

For $\delta_0 \geq 1$ (Region I, horizontal orange line in Fig. 4.4), impact does not occur for any β value (Sect. 4.2.4). The corresponding PRCs of normalized excursion of relative displacement η_d, coincide with the thick black curve shown in Fig. 4.3b, in which forward and backward curves overlap, without jumps or hysteresis. As concerns the PRC of excursion of absolute acceleration η_a (see the small figure on the top left corner of Fig. 4.4), it is very close to the PRC of η_d, due to the small value of ξ considered in the analyses. Both for displacement and for acceleration, as a consequence of the normalization adopted for the representation of the PRCs, the maximum value in resonance condition is equal to 1 and occurs for $\beta = \beta_{\mathrm{Rd}} \simeq 0.99$. As concerns the eccentricity (e_d and e_a), it is null for each value of frequency ratio β.

Region II

For values of δ_0 inside Region II (highlighted in yellow in Fig. 4.4), PRCs are analogous to those shown in Fig. 4.5, which corresponds to $\delta_0 = 0.99$. In particular, both the PRCs of normalized excursion η_d (left vertical axis) and eccentricity e_d (right vertical axis) of relative displacement are depicted in Fig. 4.5a, while both the PRCs of normalized excursion η_a (left vertical axis) and eccentricity e_a (right vertical axis) of absolute acceleration are depicted in Fig. 4.5b.

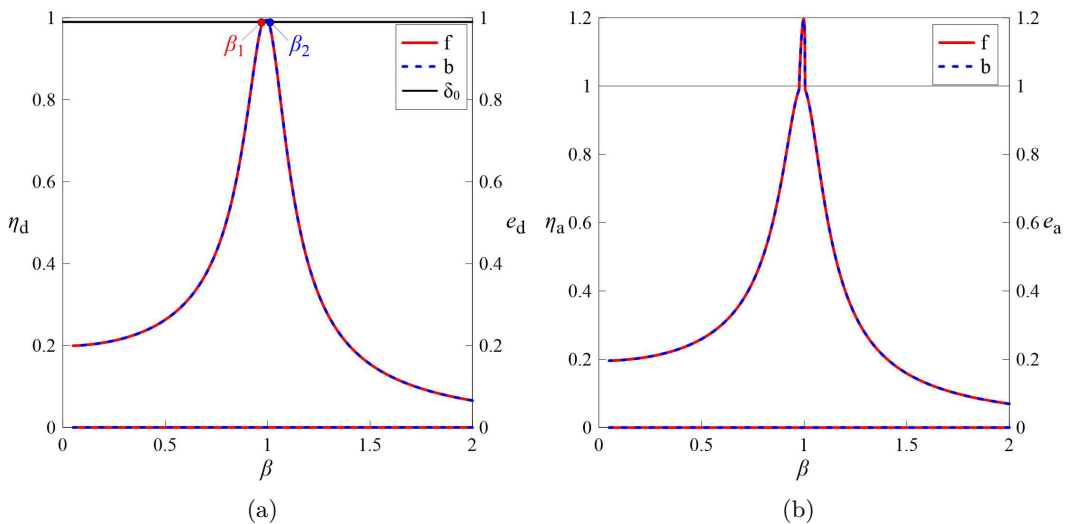(a)   (b)

Figure 4.5. Region II ($\xi = 0.1$, $\gamma = 5$, $\lambda = 50$, $\delta_0 = 0.99$), forward (solid red line) and backward (dashed blue line) PRCs of: **a** η_d and e_d (curves in the lower part of the graph); **b** η_a and e_a (curves in the lower part of the graph).

It can be observed that forward (solid red lines) and backward (dashed blue lines) curves overlap, there are neither jumps nor hysteresis and the eccentricity (see the lower part of each figure) is equal to zero for each β value.

(a)   (b)
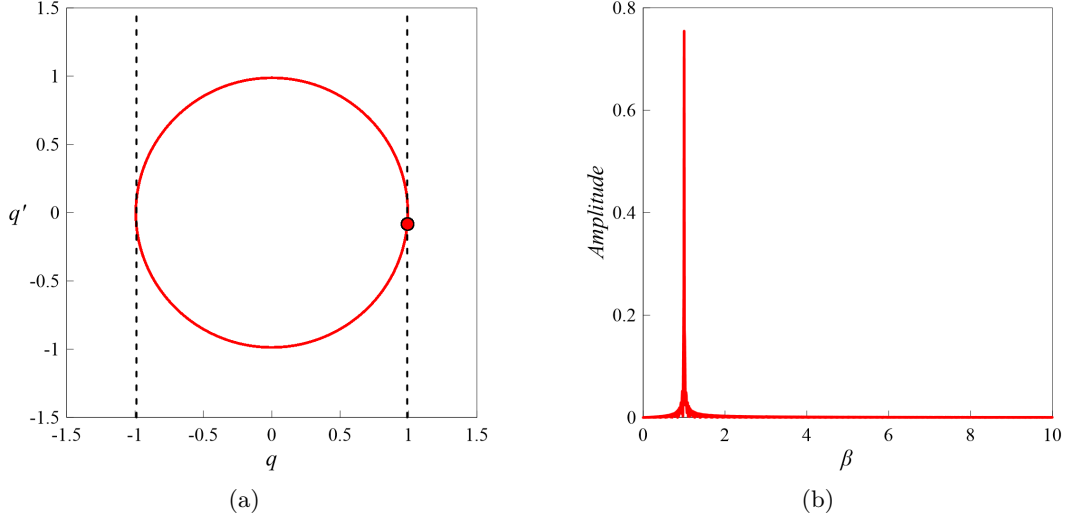
Figure 4.6. Region II ($\xi = 0.1$, $\gamma = 5$, $\lambda = 50$, $\delta_0 = 0.99$): **a** phase portrait with Poincaré section and **b** Fourier spectrum for $\beta = 1$.

Since in this Region $\delta_0^* < \delta_0 < 1$ and, in particular the selected value of δ_0 is very close to 1 (Sect. 4.2.4), impact occurs only in a small frequency range, in the neighbourhood of the resonant frequency, and it is highlighted by the presence of a spike in the PRC of η_a (Fig. 4.5b), while the peak of the PRC of η_d is slightly flattened (Fig. 4.5a), due to the presence of the obstacles, highlighted with an horizontal black line. In the frequency range associated with the occurrence of impact, between β_1 and β_2 (see the red and blue dots in Fig. 4.5a), there is only a periodic steady-state solution (Fig. 4.6a), with the same period of the excitation (thus $n = T_s/T_f = 1$, where T_s is the period of the solution and T_f is the forcing period, as it can be seen from Fig. 4.6b, where only the fundamental harmonic is observed. Consequently, in the Poincaré section, obtained by marking the trajectory at times that are integer multiples of the forcing period T_f, the points coincide with the single point represented by a red dot in Fig. 4.6a. At steady-state, reached with a small number of forcing cycles, the limit cycle in the phase plane is similar to a circle, slightly flattened at the ends, due to the impact and, in each forcing cycle, the mass hits each bumper (two vertical dashed black lines) once.

Region III (upper part)

In the green portion of the $\lambda - \delta_0$ plane (Region III), just below the yellow one (Region II, Fig. 4.4), from Fig. 4.7, which refers to $\delta_0 = 0.8$, it can be observed that, compared to the previous case (Fig. 4.5), the frequency range characterized by the occurrence of impact is greater. Furthermore, the jump phenomena (highlighted with vertical arrows) and the *primary resonance with right hysteresis* are observed. Also in this case, eccentricity is zero for each value of β.

(a)   (b)

Figure 4.7. Region III, upper part ($\xi = 0.1$, $\gamma = 5$, $\lambda = 50$, $\delta_0 = 0.8$), forward (solid red line) and backward (dashed blue line) PRCs of: **a** η_d and e_d (curves in the lower part of the graph); **b** η_a and e_a (curves in the lower part of the graph). The vertical arrows represent the jumps.

In the frequency range between the two jumps (e.g. $\beta = 1.1$), there are two steady-state solutions (Fig. 4.8a):

- Large-amplitude resonant motion with impact (red curve);

- Small-amplitude non-resonant motion without impact (blue curve).

Actually, there would be also an unstable solution, that could not be obtained with the used procedure. Both the observed solutions are periodic, with the same period of the excitation ($n = 1$). Consequently, in both cases, at steady-state (reached with a small number of forcing cycles), the points in the Poincaré sections coincide with a single point, colored red for the large-amplitude motion and colored blue for the small-amplitude motion. In the Fourier spectra (Figs. 4.8c,d), only the fundamental harmonic component is observed. From Fig. 4.8a it can be observed that the small-amplitude limit cycle is similar to a circle, while the limit cycle of the large-amplitude motion is slightly flattened at the ends, due to the occurrence of impact, and in each forcing cycle, the mass hits each bumper once. The basins of attraction of the two solutions are shown in Fig. 4.8b, together with the initial conditions for the sine sweep frequency sub-range that includes the value $\beta = 1.1$, obtained with the continuation technique during the forward (yellow right-pointing triangle) and the backward (yellow left-pointing triangle) sweep. The basins were obtained considering a sufficiently dense mesh of initial conditions (q_0, q'_0), represented with colored dots. Each basin is made up of the set of dots (initial conditions) that lead to the corresponding attractor. In particular, red dots represent the set of initial conditions that lead to the large-amplitude motion, while blue dots represent the set of initial conditions that lead to the small-amplitude motion. It can be observed that the shape of the basins is smooth and regular, due to the periodic behavior of the system.

(a)

(b)

(c)

(d)
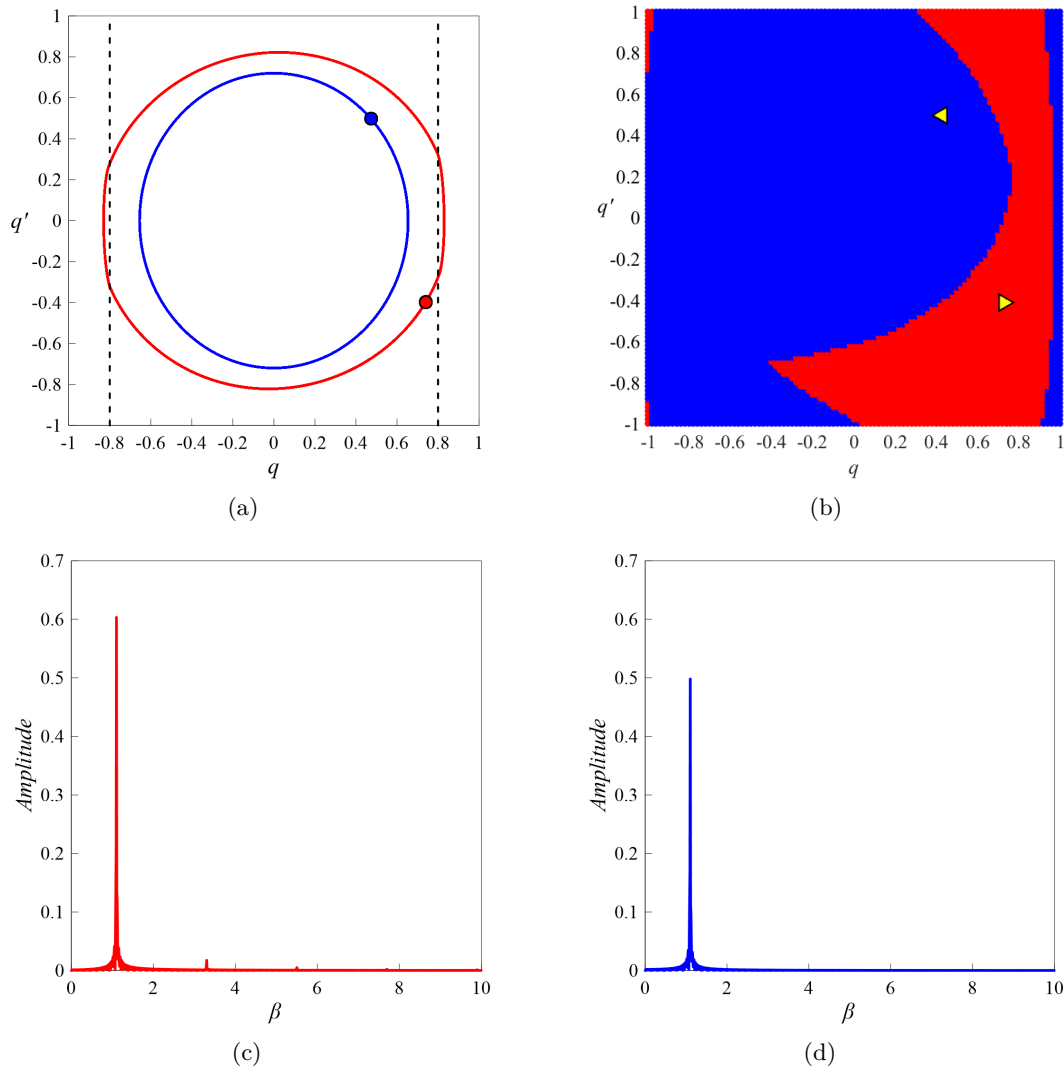
Figure 4.8. Region III, upper part ($\xi = 0.1$, $\gamma = 5$, $\lambda = 50$, $\delta_0 = 0.8$, $\beta = 1.1$): **a** phase portraits with Poincaré sections; **b** basins of attraction; Fourier spectra: **c** ($q_0 = 0.74$, $q_0' = -0.4$), yellow right-pointing triangle; **d** ($q_0 = 0.47$, $q_0' = 0.5$), yellow left-pointing triangle.

Region IV

Decreasing the dimensionless gap δ_0 and entering Region IV, in the PRCs (Fig. 4.9, which corresponds to $\delta_0 = 0.4$), in addition to the *primary resonance with right hysteresis*, the presence of a *secondary resonance* is observed (zoomed rectangular area). This secondary resonance is characterized by the occurrence of a *right hysteresis*, with zero eccentricity, followed by a small frequency range characterized by increasing excursion and zero eccentricity. After an abrupt reduction of excursion, a section, in the neighbourhood of $\beta \simeq 0.8$, with eccentricity other than zero and characterized by an almost constant value of excursion, is observed. The secondary resonance occurs at the frequency value for which, at steady-state, the mass just begins to touch the bumpers with a velocity close to zero ($\beta = \beta_1 \simeq 0.72$, Sect. 4.2.4, highlighted with a red dot in Fig. 4.9a).
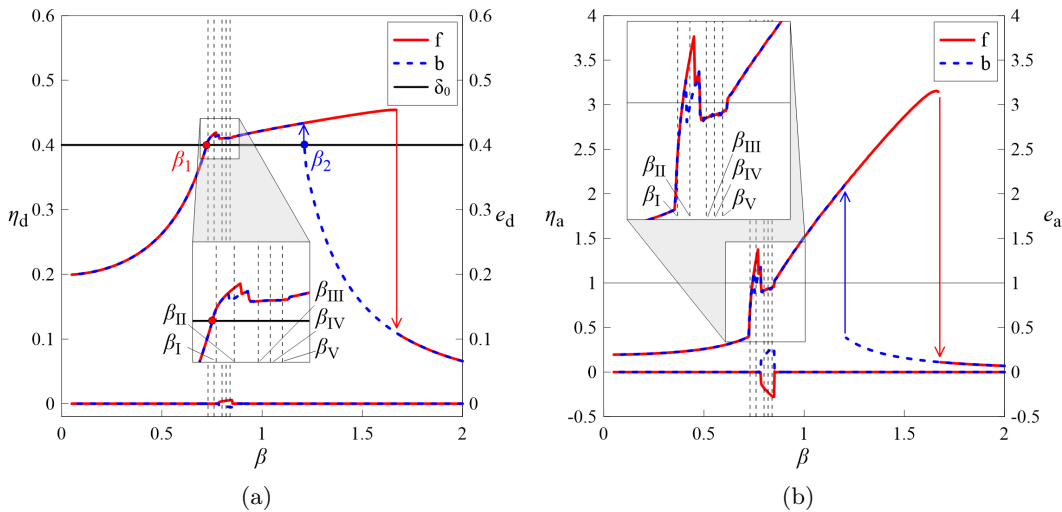
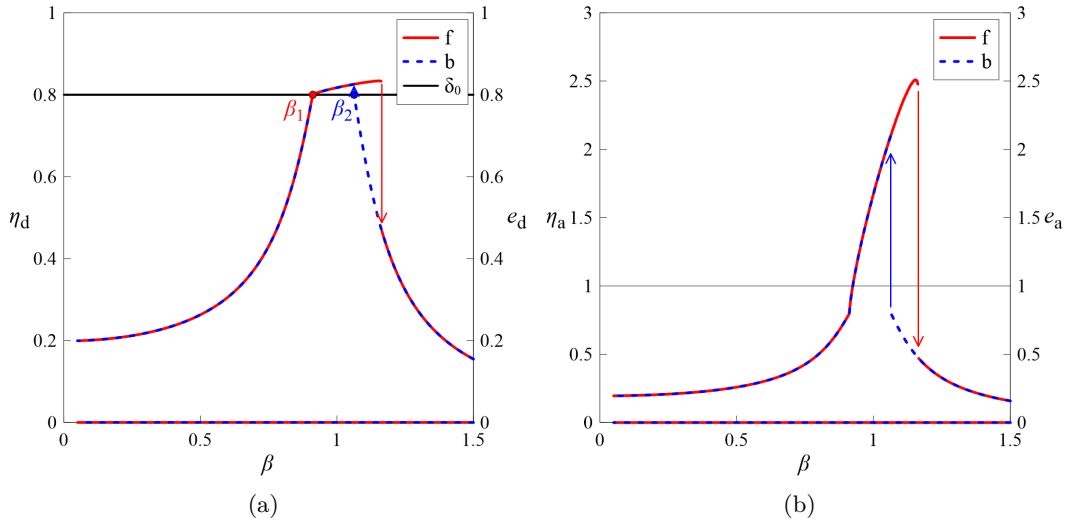**Figure 4.9.** Region IV ($\xi = 0.1$, $\gamma = 5$, $\lambda = 50$, $\delta_0 = 0.4$), forward (solid red line) and backward (dashed blue line) PRCs of: **a** η_d and e_d (curves in the lower part of the graph); **b** η_a and e_a (curves in the lower part of the graph). The vertical arrows represent the jumps. A detail of the secondary resonance is shown in the rectangular zoomed area. The dashed vertical lines represent β values that will be investigated in more detail.

This causes the transition from a single periodic non-impacting steady-state solution, to a single impacting periodic multi-frequency steady-state solution (see Fig. 4.10a, corresponding to $\beta = \beta_I = 0.73$, first vertical dashed line in Fig. 4.9). In the following, this condition will be referred to as *primary grazing*, because it occurs when the periodic non-impacting limit cycle, expanding as β increases, begins to touch the obstacles, with a velocity close to zero.

At steady-state, reached with a quite small number of forcing cycles, the attractor is characterized by interweaving cycles, very close to each other, with antisymmetric envelope (Fig. 4.10a) and has a period that is three times the forcing period ($n = 3$). Consequently, in the Poincaré section, three points were observed. In the Fourier spectrum (Fig. 4.10b), in addition to the fundamental frequency, it is also possible to observe the other commensurate frequencies, characterized by a much smaller amplitude, one of which is equal to one third of the fundamental. At steady-state,
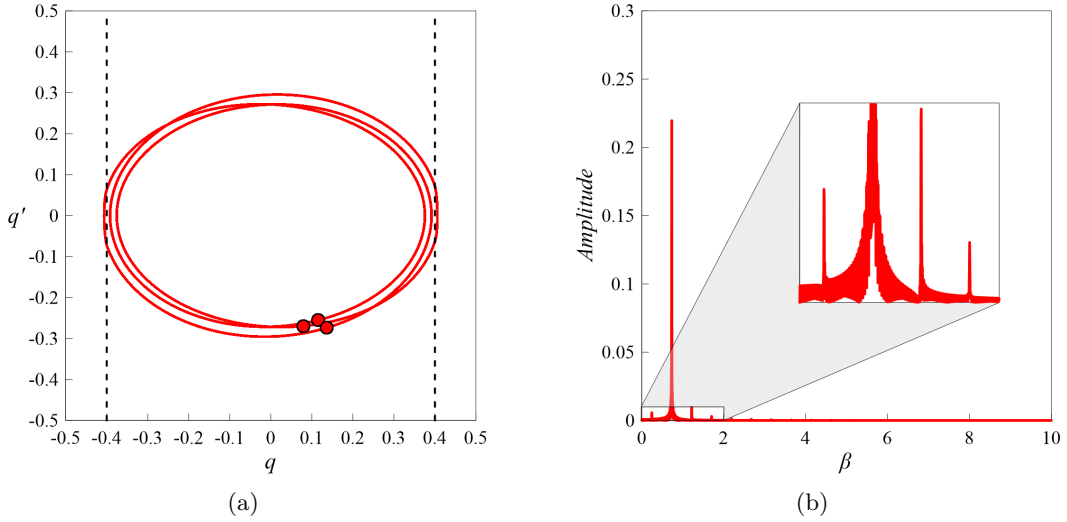
Figure 4.10. Region IV ($\xi = 0.1$, $\gamma = 5$, $\lambda = 50$, $\delta_0 = 0.40$): **a** phase portrait with Poincaré section and **b** Fourier spectrum for $\beta = \beta_{\mathrm{I}}$.

the mass alternatively hits once only one of the two bumpers, then neither, then only the other. In the frequency range characterized by the presence of the *secondary right hysteresis* ($\beta = \beta_{\mathrm{II}} = 0.76$, second vertical dashed line in Fig. 4.9) two coexisting solutions, each with antisymmetric envelope, were observed (Fig. 4.11a):

- A periodic multi-frequency solution (red curve), with $n = 3$, associated with the forward sweep;

- A quasi-periodic solution (blue curve), associated with the backward sweep.

Compared to the *primary right hysteresis* (Fig. 4.8a), both solutions are associated with the occurrence of impact and one of them is quasi-periodic (blue curve). As regards the periodic solution (red curve), which is similar to the limit cycle shown in Fig. 4.10a, the considerations made previously apply. The differences concern the amplitude of the limit cycle, the relative position of the interweaving cycles, which lead to a different distance between the three points in the Poincaré section, and a greater amplitude of the harmonic components in the Fourier spectrum (Fig. 4.11c).

The limit cycle corresponding to the quasi-periodic solution (blue curve) is quite thick and it is characterized by a more complex structure of the Poincaré section. In the Fourier spectrum (Fig. 4.11d), the fundamental frequency stands out significantly compared to the others incommensurate frequencies, which can be seen better in the rectangular zoomed area. Given the quasi-periodic nature of the response, even considering a high number of forcing cycles, it is not possible to reach a real stationary condition; this is reflected in the number of impacts per forcing cycle, which is not constant but changes as time goes by. The basins of attraction of the two coexisting solutions are shown in Fig. 4.11b, together with the initial conditions for the sine sweep frequency sub-range that includes the value $\beta = \beta_{\mathrm{II}}$, obtained with the continuation technique during the forward (yellow right-pointing triangle) and the backward (yellow left-pointing triangle) sweep. Compared to Fig. 4.8b, the

shape of the basins, especially that of the basin of attraction of the quasi-periodic attractor (highlighed in blue), is less regular. The secondary downward jump in the forward sweep occurs when one of the internal interweaving cycles grazes the obstacles. In the following, this condition will be referred to as *secondary grazing*, because it occurs when, in addition to the primary orbit, which impacts the obstacles evidently, one of the internal cycles or loops, expanding, begins to touch them, with a velocity close to zero. This causes the sudden transition, during the forward sweep, to a quasi-periodic attractor, analogous to the blue one shown in Fig. 4.11a. This single quasi-periodic solution was observed in the frequency range, after the jump, characterized by increasing excursion and zero eccentricity, followed by an abrupt reduction of excursion.
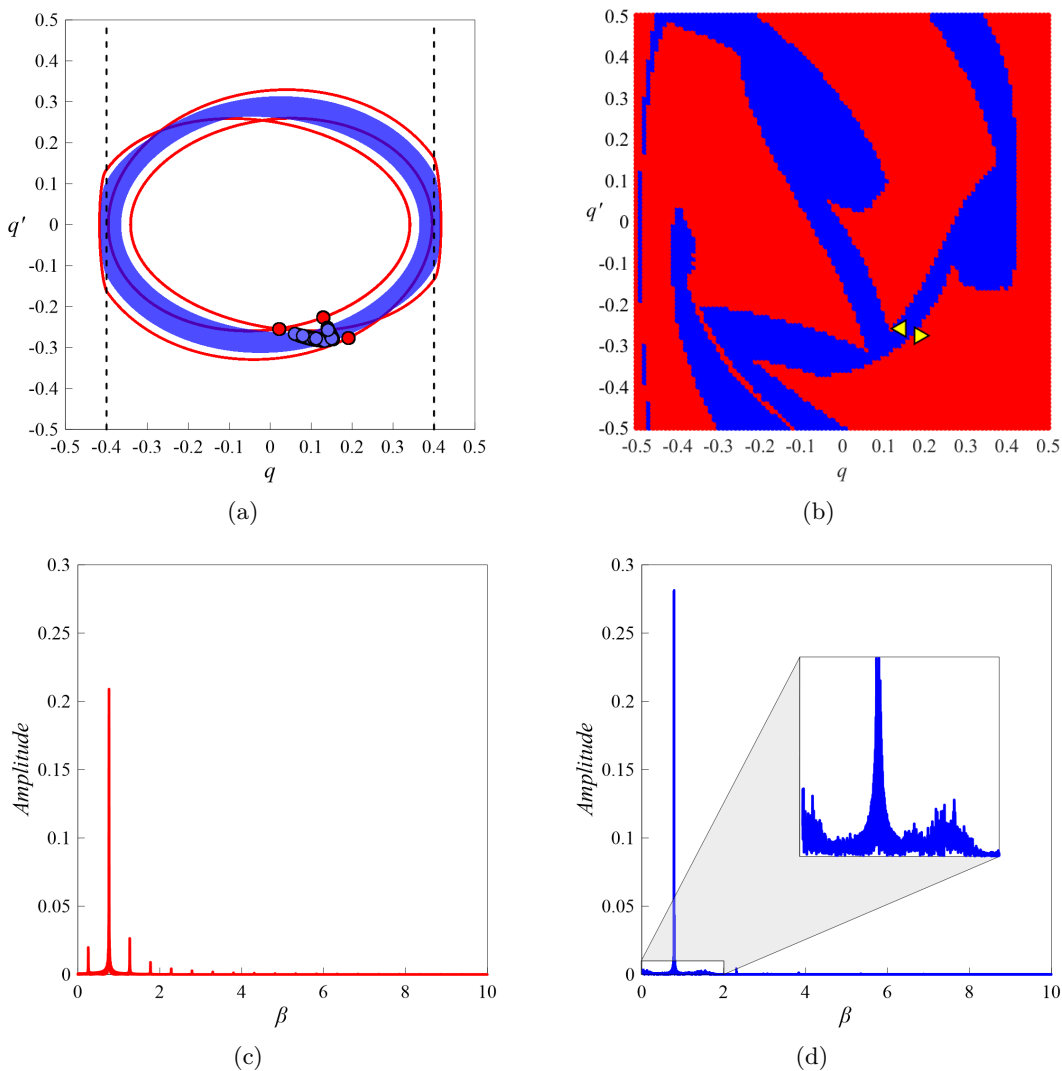
Figure 4.11. Region IV ($\xi = 0.1$, $\gamma = 5$, $\lambda = 50$, $\delta_0 = 0.4$, $\beta = \beta_{\text{II}}$): **a** phase portraits with Poincaré sections; **b** basins of attraction; Fourier spectra: **c** ($q_0 = 0.19$, $q_0' = -0.28$), yellow right-pointing triangle; d) ($q_0 = 0.14$, $q_0' = -0.26$), yellow left-pointing triangle.

In the subsequent frequency range, characterized by eccentricity other than zero and almost constant excursion, the existence of a *pair of quasi-periodic solutions* is observed (Fig. 4.12a, which corresponds to $\beta = \beta_{\mathrm{III}} = 0.80$, third vertical dashed line in Fig. 4.9). These two limit cycles have the same frequency content, the same excursion but are characterized by eccentricities, equal in absolute value but with opposite sign. Consequently, the two solutions are not antisymmetric in themselves, but the antisymmetry is achieved through their envelope.
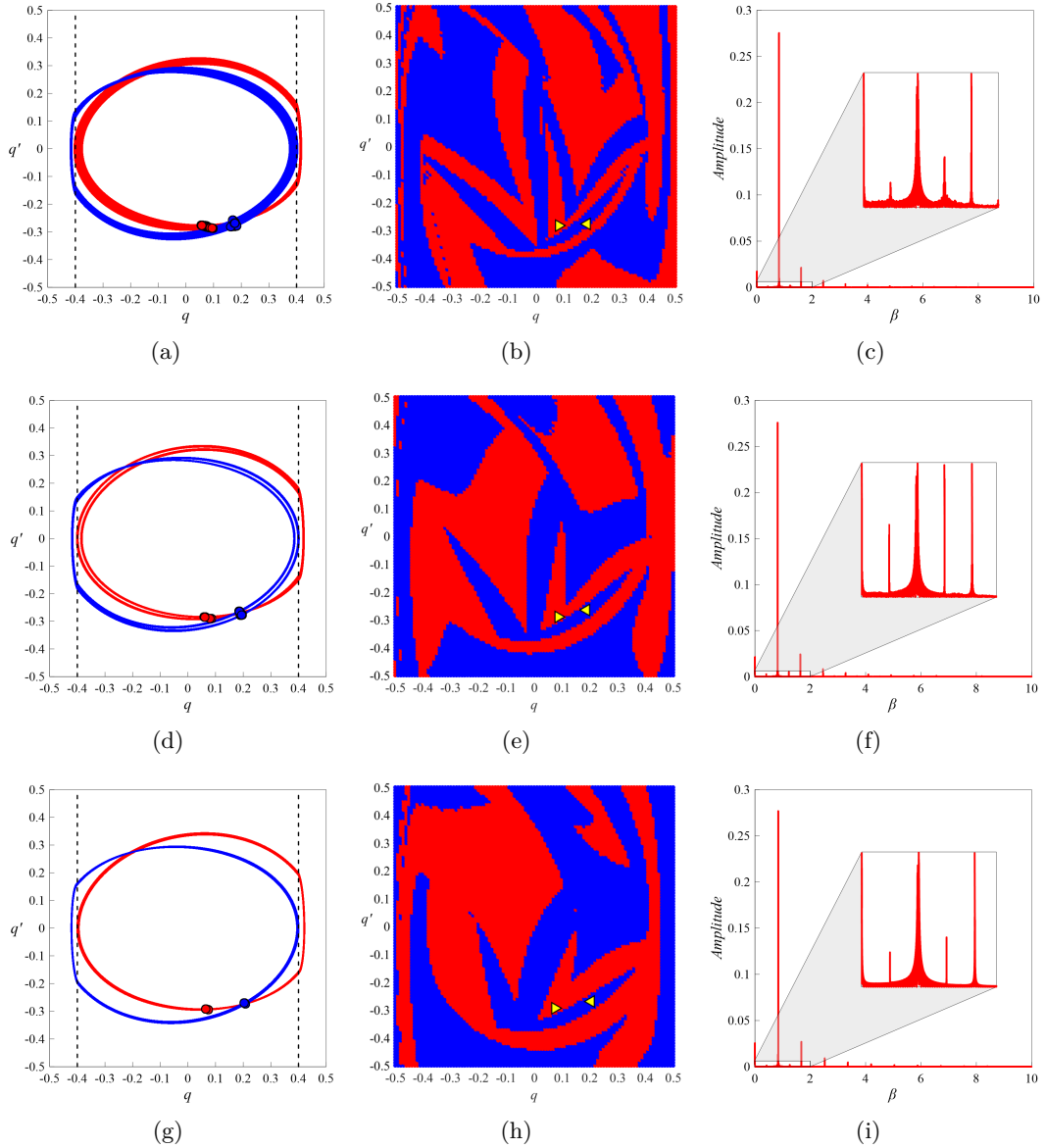
Figure 4.12. Region IV ($\xi = 0.1$, $\gamma = 5$, $\lambda = 50$, $\delta_0 = 0.4$), phase portraits with Poincaré sections for: **a** $\beta = \beta_{\mathrm{III}}$; **d** $\beta = \beta_{\mathrm{IV}}$; **g** $\beta = \beta_{\mathrm{V}}$; basins of attraction for: **b** $\beta = \beta_{\mathrm{III}}$; **e** $\beta = \beta_{\mathrm{IV}}$; **h** $\beta = \beta_{\mathrm{V}}$; Fourier spectra for: **c** $\beta = \beta_{\mathrm{III}}$; **f** $\beta = \beta_{\mathrm{IV}}$; **i** $\beta = \beta_{\mathrm{V}}$.

Compared to the quasi-periodic solution shown in Fig. 4.11a, the limit cycles that make up the pair are weakly quasi-periodic (less thick limit). Consequently,

the incommensurate frequencies are much less obvious (Fig. 4.12c). By focusing the attention on the single cycle that makes up the pair, it can be noted that, the mass impacts one of the two bumpers in an evident manner, while it grazes the other slightly. The basins of attraction of the two solutions are shown in Fig. 4.12b and are characterized by quite irregular boundaries. By increasing β, on the one hand the extent of the impact gradually increases, on the other the grazing reduces (see Fig. 4.11d, corresponding to $\beta = \beta_{\mathrm{IV}} = 0.82$ and Fig. 4.11g, corresponding to $\beta = \beta_{\mathrm{V}} = 0.84$). Consequently, the quasi-periodicity of the solutions, and thus the irregularity of the basins of attraction, decrease. Furthermore, as the quasi-periodicity decreases, the number of forcing cycles required to reach the stationary is also reduced. After this range, characterized by irregular behavior, and before the *primary right hysteresis*, a single periodic steady-state solution with $n = 1$ is observed. As concerns the *primary right hysteresis*, in the frequency range between the two jumps, everything goes as described in Sect. 4.3.

Region III (lower part)

From Fig. 4.4 it was observed that Region III (highlighted in green) embraces Region IV (highlighted in red). Starting from Region IV and moving into the lower green band, by decreasing δ_0, from Fig. 4.13, which refers to $\delta_0 = 0.25$, it can be observed that the PRCs are qualitatively similar to those observed for $\delta_0 = 0.8$ (Fig. 4.7) and are characterized by the presence of only the *primary resonance with right hysteresis* and by a null eccentricity for each β value.

Figure 4.13. Region III, lower part ($\xi = 0.1$, $\gamma = 5$, $\lambda = 50$, $\delta_0 = 0.25$), forward (solid red line) and backward (dashed blue line) PRCs of: **a** η_{d} and e_{d} (curves in the lower part of the graph); **b** η_{a} and e_{a} (curves in the lower part of the graph). The vertical arrows represent the jumps.

Compared to the case $\delta_0 = 0.8$, the frequency range associated with the occurrence of impact is larger, the primary hysteresis is shifted to higher frequency values and its extension is greater. Furthermore, for $\beta = \beta_1 = 0.4575$, highlighted with a red

dot in Fig. 4.13a, it can be observed that, in the PRCs, especially that of η_a, a rather vertical section is observed. When the mass reaches the obstacles, a distortion of the limit cycle occurs, which gradually assumes the appearance of the red one shown in the Fig. 4.14a characterized by an evident antisymmetry.
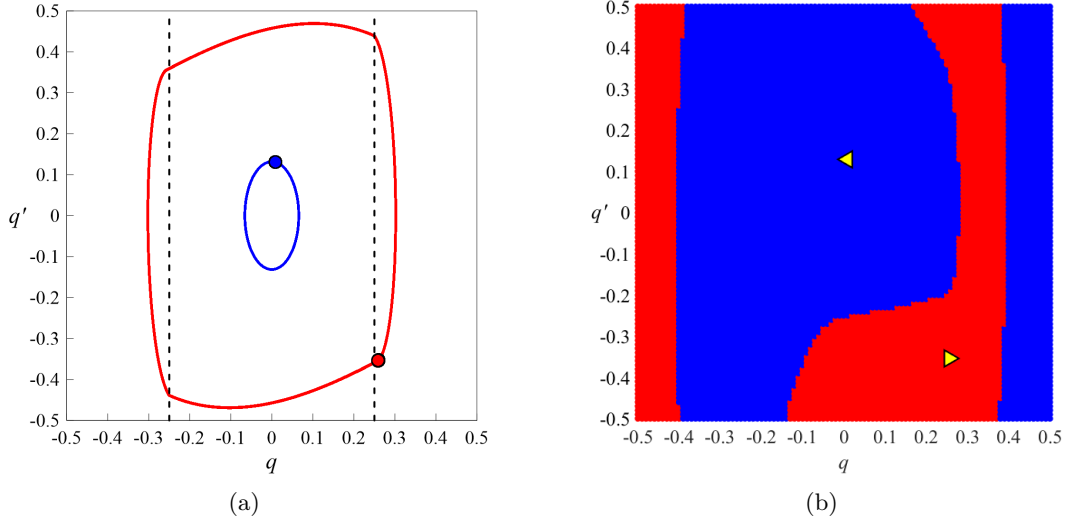
Figure 4.14. Region III, lower part ($\xi = 0.1$, $\gamma = 5$, $\lambda = 50$, $\delta_0 = 0.25$): **a** phase portraits with Poincaré sections and **b** basins of attraction for $\beta = 2$.

As previously said in Sect. 4.3, in the frequency range between the two jumps (e.g. $\beta = 2$), two steady-state solutions (Fig. 4.14a), a large-amplitude resonant motion with impact (red curve) and a small-amplitude non-resonant motion without impact (blue curve), are observed. Both solutions are periodic, with the same period of the excitation ($n = 1$).

Compared to the case $\delta_0 = 0.8$ (Fig. 4.8), as previously said, the large amplitude limit-cycle turns out to be more distorted and in the corresponding Fourier spectrum, in addition to the fundamental harmonic, the presence of another harmonic component, with smaller amplitude, at a frequency that is three times that of the fundamental, is also observed, (Fig. 4.15a) whereas in the Fourier spectrum corresponding to the small-amplitude motion, only the fundamental harmonic component is observed (Fig. 4.15b). Furthermore, since δ_0 is lower, that is the bumpers are closer to the mass, the large-amplitude limit cycle (red curve in Fig. 4.14a) is more squashed at the ends, due to the occurrence of impact, and in each forcing cycle, the mass hits each bumper once. As concerns the small-amplitude limit cycle, it is more like an ellipse.

The basins of attraction of the two solutions are shown in Fig. 4.14b, together with the initial conditions for the sine sweep frequency sub-range including the value $\beta = 2$, obtained with the continuation technique during the forward (yellow right-pointing triangle) and the backward (yellow left-pointing triangle) sweep. As in the case $\delta_0 = 0.8$ (Fig. 4.8b), also in this case the shape of the basins returns to be smooth and regular.
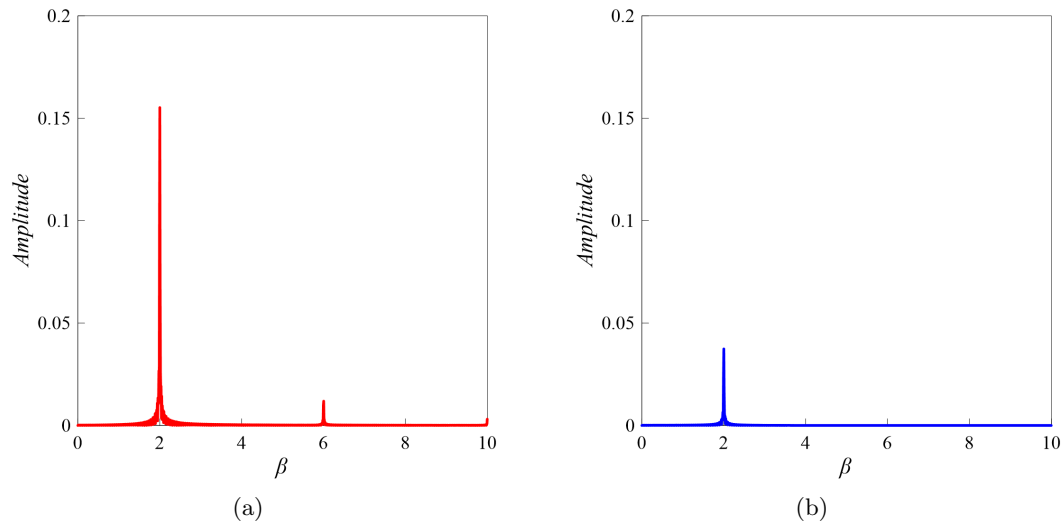
Figure 4.15. Region III, lower part ($\xi = 0.1$, $\gamma = 5$, $\lambda = 50$, $\delta_0 = 0.25$), Fourier spectra for $\beta = 2$ and initial conditions: **a** ($q_0 = 0.26$, $q_0' = -0.35$); **b** ($q_0 = 0.008$, $q_0' = 0.13$).

Region V

The scenarios previously analyzed referred to values of dimensionless gap $\delta_0^* < \delta_0 \le 1$, for which Eq. 4.7 admits two non-zero roots (β_1 and β_2, coincident for $\delta_0 = 1$). Moving into the blue region, which straddles the line $\delta_0 = \delta_0^* \simeq 0.2$, in the forward sweep impact occurs immediately starting from $\beta = \beta_1 = 0$ and the PRCs are characterized by the presence of both the *primary resonance with right hysteresis* and several *secondary resonances without hysteresis* in the low frequency range (enclosed within an ellipse in Fig. 4.16). A detail of the smaller resonances is shown in the rectangular zoomed area. It can be observed that eccentricity is always zero except for a very small frequency range in the neighbourhood of $\beta \simeq 0.4$ (highlighted with a small dashed circle). In the low frequency range, characterized by the alternation of ridges and valleys, a single periodic multi-frequency solution, with $n = 1$ is observed.

In Fig. 4.17, each sub-figure describes the evolution of the phase portraits, at steady-state, moving from one valley to the next ridge (left column, Figs. 4.17a,c,e) and moving from one ridge to the next valley (right column, Figs. 4.17b,d,f). The β values corresponding to the investigated ridges and valleys are indicated with Roman numerals in Fig. 4.16 and the associated phase portraits are represented with thicker lines. From Fig. 4.17 it can be observed that, starting from a valley ($\beta_{\mathrm{I}} = 0.192$, $\beta_{\mathrm{III}} = 0.316$ or $\beta_{\mathrm{V}} = 0.48$) and approaching the next ridge ($\beta_{\mathrm{II}} = 0.24$, Fig. 4.17a, $\beta_{\mathrm{IV}} = 0.43$, Fig. 4.17c, or $\beta_{\mathrm{V}} = 0.67$, Fig. 4.17e), in the phase portrait two internal loops appear. These loops were not observed for $\beta < \beta_{\mathrm{I}}$. As β increases, the internal loops gradually move inward, growing first and then getting smaller. Referring to the two smaller considered ridges (Figs. 4.17a,c), they never touch the obstacles; consequently, in each forcing cycle, the mass hits each bumper once. As regards the larger ridge (Fig. 4.17e) instead, it is observed that the internal loops come to touch the obstacles (*secondary grazing*), more or less in the middle of the
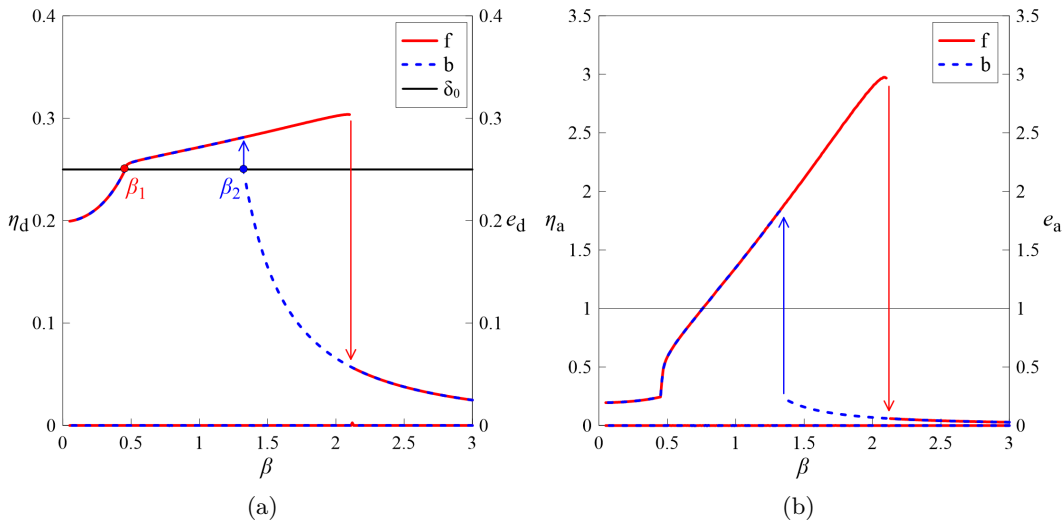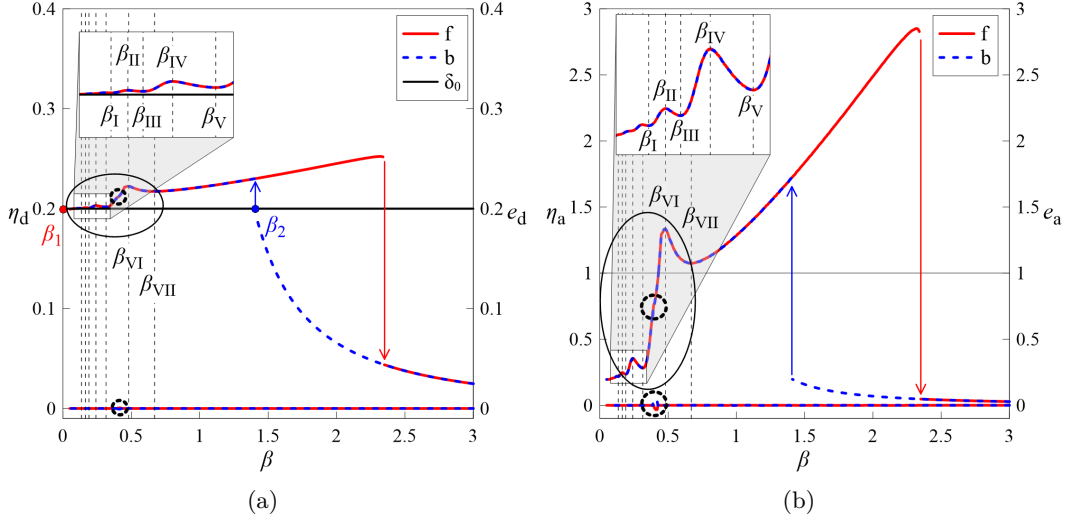
Figure 4.16. Region V ($\xi = 0.1$, $\gamma = 5$, $\lambda = 50$, $\delta_0 = \delta_0^*$, forward (solid red line) and backward (dashed blue line) PRCs of: **a** η_d and e_d (curves in the lower part of the graph); **b** η_a and e_a (curves in the lower part of the graph). The vertical arrows represent the jumps. The secondary resonances are enclosed by the solid black ellipse and a detail of the smaller resonances is shown in the rectangular zoomed area. The small dashed black circles highlight the small frequency interval characterized by non-zero eccentricity. The dashed vertical lines represent β values that will be investigated in more detail.

ascending branch, just before the frequency range with non-zero eccentricity. This will be investigated in more detail later.

Beyond the frequency range with non-zero eccentricity, a single periodic solution with $n = 1$ is observed again. The two internal loops touch the obstacles, causing the mass to impact each bumper twice for each forcing cycle. Subsequently, by further increasing β, the loops begin to move inward, becoming gradually smaller (Fig. 4.17e) and when they no longer intersect the obstacles, the mass returns to hit each bumper once. Conversely, starting from a ridge (β_{II}, β_{IV} or β_{VI}) and approaching the next valley (β_{III}, Fig. 4.17b, β_V, Fig. 4.17d, or β_{VII}, Fig. 4.17f), the two internal loops gradually disappear, taking on the appearance of cusps progressively more rounded and in each forcing cycle, the mass hits each bumper once. Let's now focus the attention on the frequency range enclosed by the small dashed circle, more or less in the middle of the ascending branch, just before the frequency range with non-zero eccentricity. When the internal loops reach the obstacles (*secondary grazing*, indicated by the first green star on the left in Fig. 4.18a), the transition from a periodic impacting steady-state solution with $n = 1$, to a periodic impacting steady-state solution with $n = 3$ is observed (Fig. 4.18b), in a similar way to what was seen for $\delta_0 = 0.4$. At steady-state, reached with a quite small number of forcing cycles, the solution is similar to the one shown in Fig. 4.10a; in addition to the interweaving cycles there are also six internal loops, two of which intersect the obstacles. Consequently, in each forcing cycle, the mass impacts in one cycle once a bumper and two times the other, in the next cycle once both, and so on alternately. As also observed for $\delta_0 = 0.4$ (Fig. 4.11), a small frequency range characterized
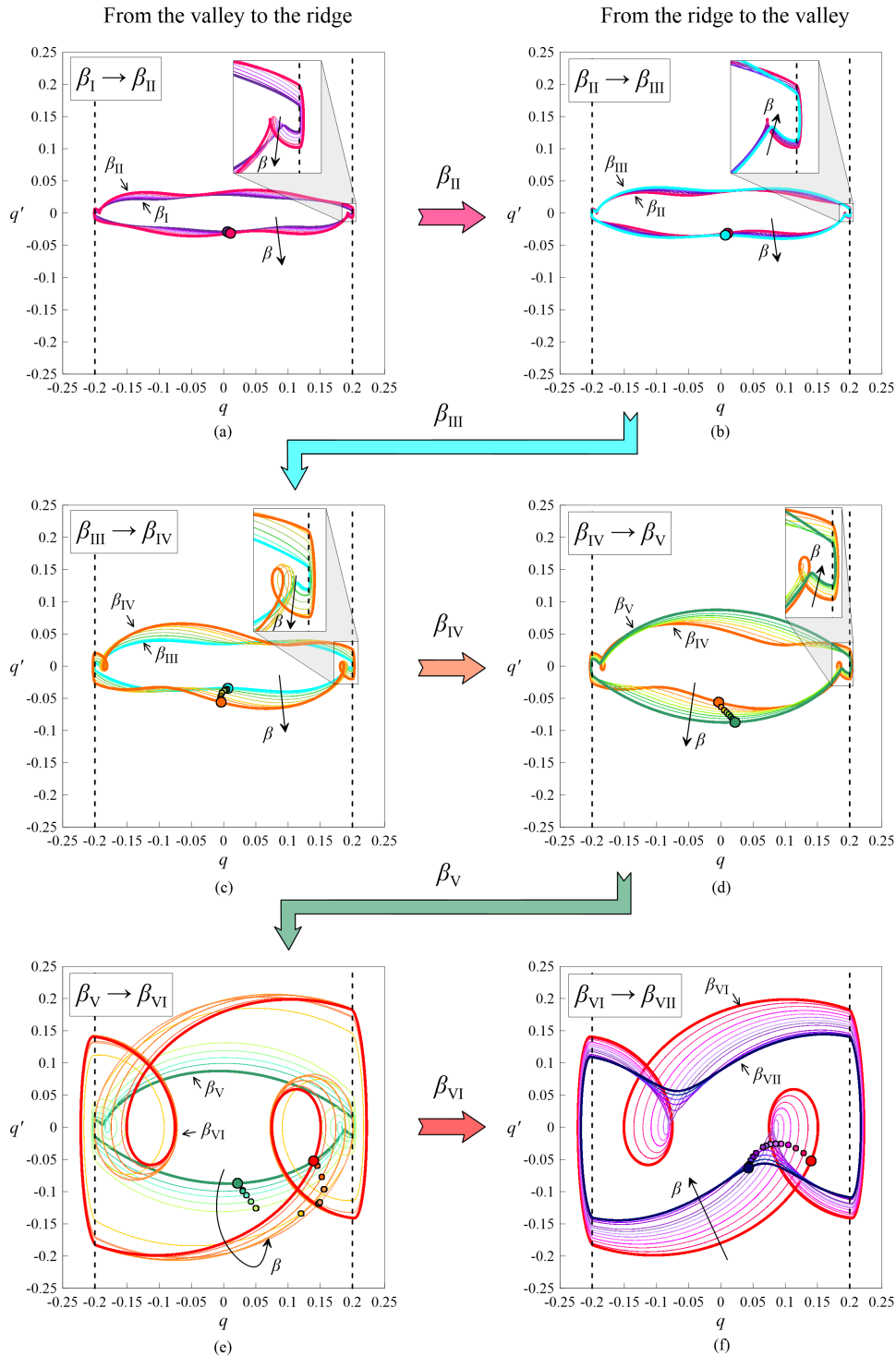
Figure 4.17. Region V ($\xi = 0.1$, $\gamma = 5$, $\lambda = 50$, $\delta_0 = \delta_0^*$), secondary resonances in the low frequency range: evolution of the phase portraits passing from the valley to the ridge (left column) and passing from the ridge to the valley (right column): **a** $\beta_{\mathrm{I}} \to \beta_{\mathrm{II}}$; **b** $\beta_{\mathrm{II}} \to \beta_{\mathrm{III}}$; **c** $\beta_{\mathrm{III}} \to \beta_{\mathrm{IV}}$; **d** $\beta_{\mathrm{IV}} \to \beta_{\mathrm{V}}$; **e** $\beta_{\mathrm{V}} \to \beta_{\mathrm{VI}}$; **f** $\beta_{\mathrm{VI}} \to \beta_{\mathrm{VII}}$. The cycle corresponding to the investigated valleys and ridges are represented with thicker lines. The order of the sub-figures is given by the colored arrows.

by the presence of a *secondary right hysteresis* with zero eccentricity follows (see the zoomed area in Fig. 4.18a). In order to highlight this hysteresis a quite small frequency increment and a higher number of forcing cycles were required. At the hysteresis two coexisting solutions, both associated with the occurrence of impact and each with antisymmetric envelope, were observed (Fig. 4.18c):

- A periodic multi-frequency solution (red curve), with $n = 3$, similar to the limit cycle shown in Fig. 4.18a and associated with the forward sweep;

- A quasi-periodic solution (blue curve), associated with the backward sweep.
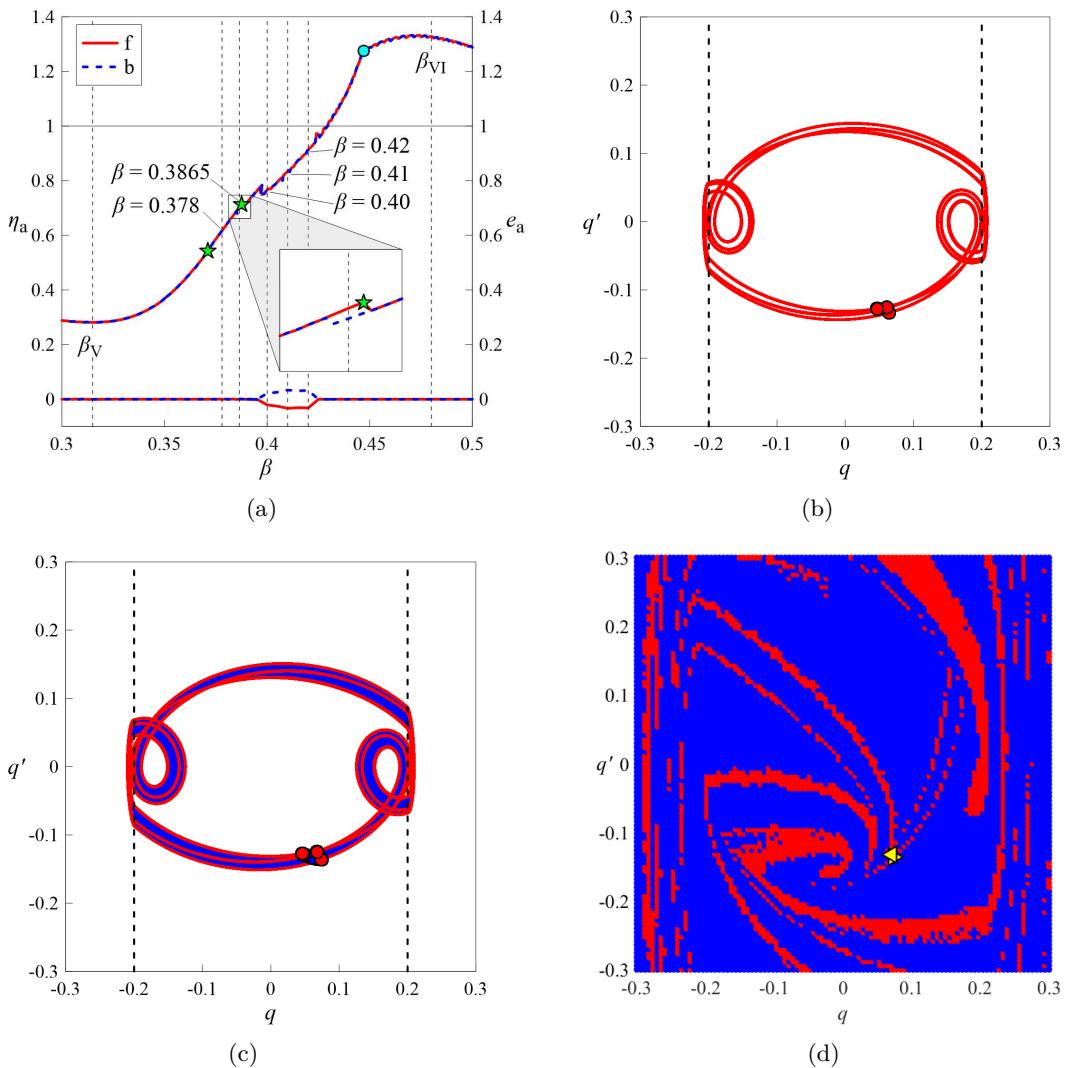
Figure 4.18. Region V ($\xi = 0.1$, $\gamma = 5$, $\lambda = 50$, $\delta_0 = \delta_0^*$): **a** zoom of the PRCs of η_a and e_a in the neighbourhood of the frequency range with non-zero eccentricity; phase portraits with Poincaré sections for: **b** $\beta = 0.378$; **c** $\beta = 0.3865$ (right hysteresis) **d** basins of attraction for $\beta = 0.3865$ (right hysteresis).

The basins of attraction of the two coexisting solutions are shown in Fig. 4.18d. It can be observed that the boundaries of the basins are quite irregular (fractal)

and most of the initial conditions lead to the quasi-periodic solution (blue basin).
In the forward sweep a sudden small downward jump was observed, when two of
the internal loops of the solution (see Fig. 4.18b, or the red curve in Fig. 4.18c)
reach the obstacles (another *secondary grazing*, indicated by the second green star in
Fig. 4.18a)), causing the transition to a quasi-periodic attractor, similar to the blue
one shown in Fig. 4.18c. After another small jump, a small frequency interval, in
the neighbourhood of $\beta \simeq 0.4$, with non-zero eccentricity follows. In this frequency
range, a *pair of quasi-periodic solutions*, whose overall envelope is antisymmetric, is
observed (Fig. 4.19a, which corresponds to $\beta = 0.40$).

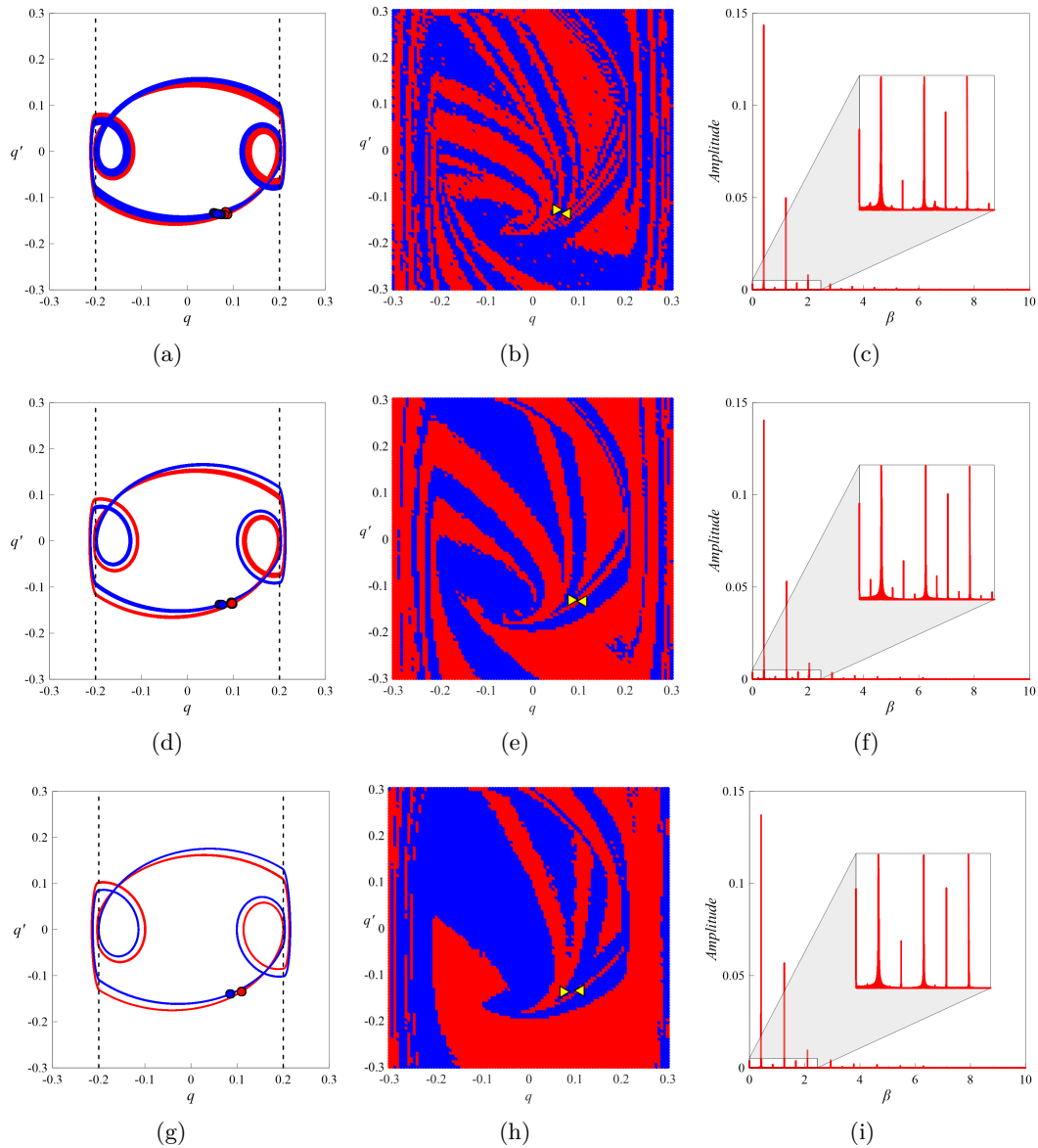**Figure 4.19.** Region V ($\xi = 0.1$, $\gamma = 5$, $\lambda = 50$, $\delta_0 = \delta_0^*$), phase portraits with Poincaré
sections: **a** $\beta = 0.40$; **d** $\beta = 0.41$; **g** $\beta = 0.42$; basins of attraction: **b** $\beta = 0.40$; **e**
$\beta = 0.41$; **h** $\beta = 0.42$; Fourier spectra: **c** $\beta = 0.40$; **f** $\beta = 0.41$; **i** $\beta = 0.42$.

Each of the cycles that make up the pair have internal loops, which, as time goes by, approach, cross and then move away from the vertical dashed lines representing the position of the obstacles. In particular, by focusing the attention on the single cycle that makes up the pair, it can be observed that, one of the internal loop impacts one bumper in an evident manner, while the other only grazes the other bumper. This results, for each of the two solutions, in a different number of impacts, in each forcing cycle, to the right and left as time goes on. It is worth noting that, to reach a stationary condition, a high number of cycles was required. Since the limit cycles that make up the pair are weakly quasi-periodic, the incommensurate frequencies are not very evident in the Fourier spectrum (Fig. 4.19c).

The basins of attraction of the two solutions are shown in Fig. 4.19b and are characterized by quite irregular (fractal) boundaries. By increasing β (Fig. 4.19d, which corresponds to $\beta = 0.41$ and Fig. 4.19i, which corresponds to $\beta = 0.42$), on the one hand the extent of the impact gradually increases, on the other the grazing reduces and therefore also the quasi-periodicity and the complexity of the basins of attraction. As previously said, after the frequency range with non-zero eccentricity and before the ridge (β_{VI}), a single periodic solution, with $n = 1$, is observed again, in which the inner loops, that initially intersect both the obstacles (double impact), progressively become smaller and move inward as β increases. When they no longer intersect the obstacles (cyan dot in Fig. 4.18a), the mass return to hits each bumper once. This sequence of behaviors, similar to that observed for $\delta_0 = 0.4$ and related to the occurrence of consecutive *secondary grazing*, was not observed before the other smaller ridges, where the internal loops do not cause further impacts, but evolve far from the obstacles, as β varies.

Region VI

Further reducing the dimensionless gap δ_0, we move onto Region VI (highlighted in magenta in Fig. 4.4). Since $0 < \delta_0 < \delta_0^*$, Eq. 4.7 admits only a non-zero root (β_2, see Sect. 4.2.4) and impact occurs already starting from $\beta = 0$.

In Fig. 4.20 the PRCs for $\delta_0 = 0.1$ are represented. It can observed that they are characterized by the occurrence of both the *primary resonance with right hysteresis* and different types of secondary resonances in the low frequency range. In particular, for $\beta < 0.9$, a *cascade of secondary resonances with left hysteresis* is observed (in Fig. 4.20 enclosed by an ellipse). Furthermore, in the neighbourhood of $\beta = 1$, a *secondary non-regular resonance* is noticed (rectangular zoomed area) and the eccentricity shows non-zero values. Unlike what was seen in Sect. 4.3 and 4.3, were the irregularity interval (Fig. 4.9 and 4.18) followed a *secondary resonance with right hysteresis*, here the *secondary non-regular resonance* is preceded by a *cascade of secondary resonances with left hysteresis*. In the low frequency range, where the *cascade of secondary resonance with left hysteresis* occurs (see the ellipse in Fig. 4.20), the eccentricity is always zero and the observed solutions, reached with a small number of forcing cycles, have the same period of the excitation ($n = 1$) and are characterized by the occurrence of several internal loops, which is reflected in a high number of impacts, increasing as β decreases. This can be seen better in Fig. 4.21h, where the trend of the number of impacts per forcing cycle, against each bumper, is shown as β changes, both on the forward (increasing β, solid red line) and on the
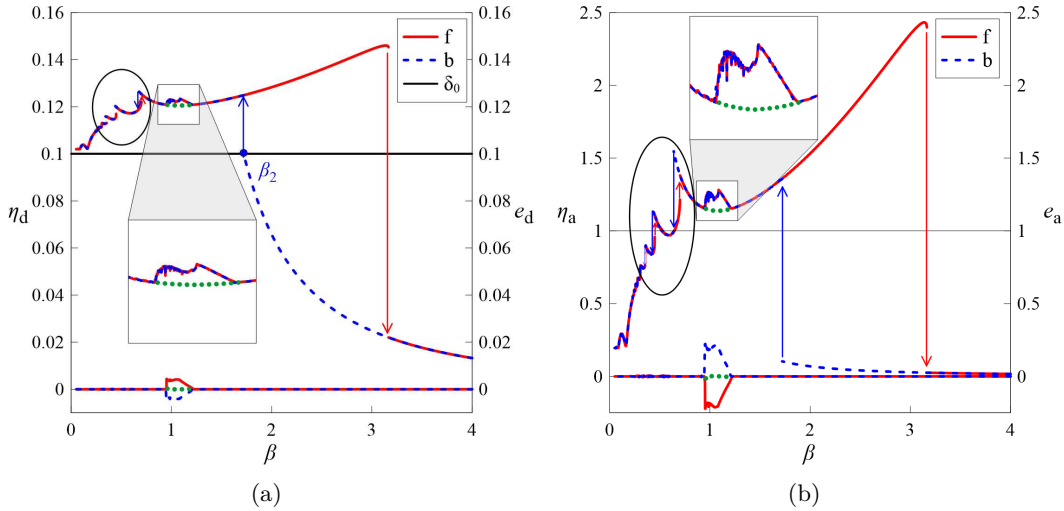
Figure 4.20. Region VI ($\xi = 0.1$, $\gamma = 5$, $\lambda = 50$, $\delta_0 = 0.1$), forward (solid red line) and backward (dashed blue line) PRCs of: **a** η_d and e_d (curves in the lower part of the graph); **b** η_a and e_a (curves in the lower part of the graph). The vertical arrows represent the jumps. The cascade of secondary resonances with left hysteresis is enclosed by the solid black ellipse, whereas a detail of the secondary non-regular resonance is shown in the zoomed square area.

backward (decreasing β, dashed blue line) sweep. Some investigated β values are marked with colored dots and the corresponding phase portraits are represented above and below Fig. 4.21h. In particular, the phase portraits corresponding to the valleys between the secondary resonances are depicted above, in Figs. 4.21a,c,e,g while the solutions observed in the secondary left hysteresis, just before the downward jumps in the backward sweep, denoted as ridges are shown below, in Figs. 4.21b,d,f.

From Fig. 4.21h, it can be noted that, starting from a valley (Fig. 4.21a, for $\beta = 0.935$), in which the limit cycle has no internal loops and the mass hits each bumper once per forcing cycle, and following the backward sweep, that is decreasing β (dashed blue line in Fig. 4.21h, from right to left), a pair of internal loops appears. They grow as β decreases and when they reach the obstacles (blue curve in Fig. 4.21b, for $\beta = 0.64$), a sudden downward jump is observed. This results in an increase of 1 in the number of impacts per forcing cycle against each bumper (Fig. 4.21c, for $\beta = 0.588$). By further decreasing β, another pair of internal loops appears. When even these loops reach the obstacles (blue curve in Fig. 4.21d, for $\beta = 0.43$), another downward jump occurs, after which the numbers of impacts against each bumpers increases again by 1, and so on for the successive ridges and valleys (Figs. 4.21e-g, for $\beta = 0.41$, $\beta = 0.345$ and $\beta = 0.326$ respectively). The limit cycle shown in Fig. 4.21g has six internal loops that intersect the obstacles and the number of impacts against each bumper per forcing cycle is equal to four. Conversely, starting from the valley shown in Fig. 4.21g and following the forward sweep, that is increasing β (solid red line in Fig. 4.21h, from left to right), immediately after the upward jump, the two innermost loops move away from the obstacles (Fig. 4.21f); this results in a 1 drop in the number of impacts against each bumper per forcing cycle.
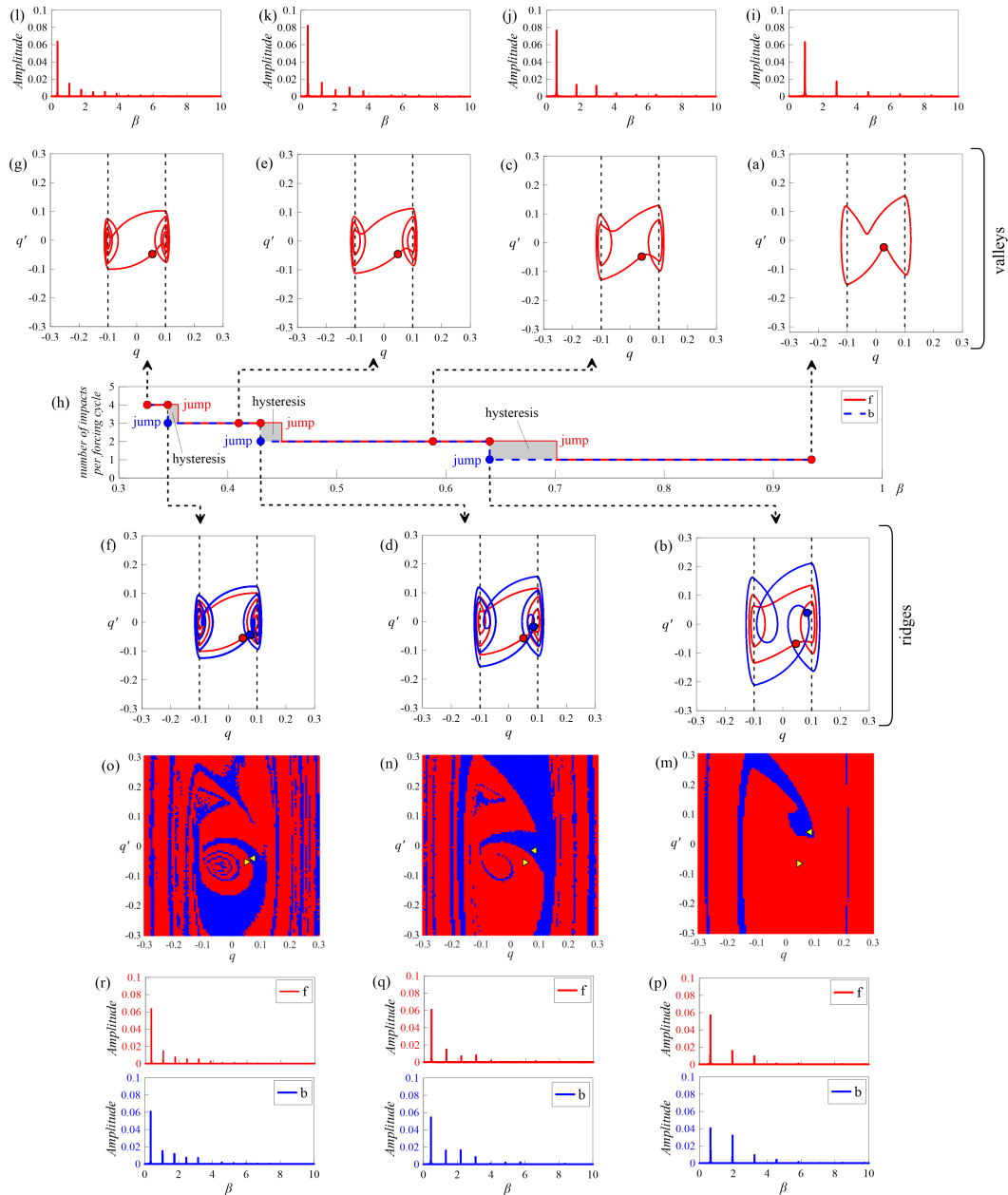
Figure 4.21. Region VI ($\xi = 0.1$, $\gamma = 5$, $\lambda = 50$, $\delta_0 = 0.1$): **h** number of impacts against each bumper per forcing cycle *vs* β and example phase portraits with Poincaré sections, at steady-state, at the valleys (**a**, **c**, **e**, **g**) and at the ridges (secondary left hysteresis, just before the downward jump) (**b**, **d**, **f**). Basins of attraction at the ridges (**m-o**). Fourier spectra at the valleys (**i-l**) and at the ridges (**p-r**).

By further increasing β, this pair of loops progressively disappears. They transform themselves into cusps that gradually blunt, until another jump occurs. This again involves the moving away of the two innermost loops, of those left, from the obstacles (Fig. 4.21e) and the reduction of the number of impacts and so on, until all the inner loops disappear (Figs. 4.21d-a) and the mass returns to hit each bumper once (Fig. 4.21a). The Fourier spectra of the solutions observed at the valleys are shown in Figs. 4.21i-l; they are characterized by the presence of several harmonic components, in addition to the fundamental one, whose number grows as β decreases.

At the *secondary left hysteresis*, colored gray in Fig. 4.21h, there are two steady-state solutions with impact (see Figs. 4.21b,d,f): a large-amplitude motion (blue line) and a small-amplitude motion (red line). As for the primary right hysteresis, the third unstable solution was not obtained. Compared to the *primary resonance with right hysteresis*, here the large-amplitude motion is associated with the backward sweep (blue curve). Both the solutions are periodic, with the same period of the excitation ($n = 1$) and in the corresponding Fourier spectra (Figs. 4.21p-r), several harmonic components, in addition to the fundamental one, are observed.

The basins of attraction are shown in Figs. 4.21m-o and are characterized by gradually more irregular (fractal) boundaries as β decreases. It can be observed that both the solutions have the same number of internal loops; however, while in the small-amplitude solution (red) all the loops intersect the obstacles, in the large-amplitude solution (blue) the innermost loops do not reach them. Consequently, the number of impacts on the forward sweep always exceeds the number of impacts on the backward sweep by 1 (see Fig. 4.21h). Decreasing β, the number of internal loops, and thus, the number of impacts per forcing cycle increases, both in the forward and in the backward sweep, with a greater number of impacts always on the forward sweep. Furthermore, the amplitude of the limit cycles decreases, the number of harmonic components increases and the basins of attraction become less regular, with a gradually decreasing extension of the basin of the smaller cycle (red basin).

In the frequency range in correspondence with the *secondary non-regular resonance*, characterized by almost constant excursion, the same in both the forward and backward curve, and non-zero eccentricity, the existence of a *pair of quasi-periodic solutions*, with antisymmetric envelope, was observed (red and blue curves in Fig. 4.22a, for $\beta = 0.96$). Each cycle that makes up the pair has a thick internal loop which, as time goes by, approaches, grazes, crosses and then moves away from one of the left vertical dashed line representing the position of the obstacle. In particular, the internal loop of the red cycle crosses only the left vertical dashed line (left bumper), while the internal loop of the blue cycle crosses only the right vertical dashed line (right bumper). This results, for each of the two solutions that make up the pair, in a different number of impacts, in each forcing cycle, to the right and left as time goes on. Given the quasi-periodic nature of the response, a high number of forcing cycles was required to reach a fairly stationary condition. By appropriately calibrating the initial conditions, and the number of forcing cycles, it is also possible to observe a periodic multi-frequency solution with $n = 1$, antisymmetric in itself (green curve in Fig. 4.22a), characterized by smaller excursion and zero eccentricity. In the PRCs (Fig. 4.20) the values of excursion and eccentricity, corresponding to

this periodic limit cycle, are represented with green dots. They are placed on the ideal course of the PRC that would have occurred in the absence of the *secondary non-regular resonance.*

(a)

(b)

(c)

(d)
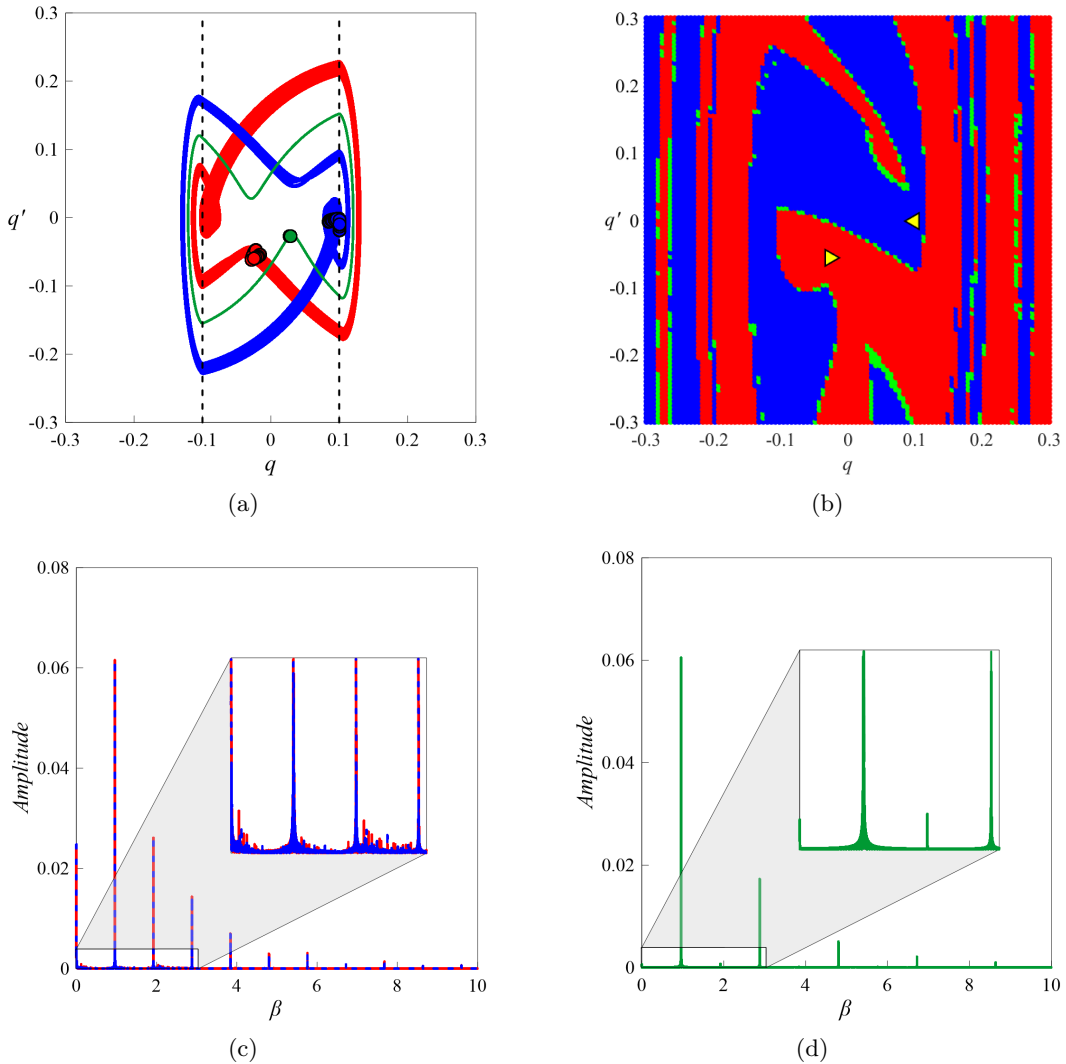
Figure 4.22. Region VI ($\xi = 0.1$, $\gamma = 5$, $\lambda = 50$, $\delta_0 = 0.1$, $\beta = 0.96$), secondary non-regular resonance: **a** phase portraits with Poincaré sections; **b** basins of attraction; Fourier spectra: **c** pair of quasi-periodic solutions, solid red line for ($q_0 = -0.027$, $q'_0 = -0.056$) and dashed blue line for ($q_0 = 0.1$, $q'_0 = -0.002$); d) green solution for ($q_0 = 0.042$, $q'_0 = -0.21$).

The basins of attraction of the solutions are shown in Fig. 4.22b. It can be observed that the initial conditions, corresponding to the periodic solution are located at the boundary between the basins of attraction of the cycles that make up the pair. The Fourier spectra of the two solutions that make up the pair (solid red and dashed blue lines in Fig. 4.22c) coincide and are characterized by several harmonic components. Since the limit cycles are weakly quasi-periodic, the incommensurate frequencies are much less obvious. These can be seen better in the

(a)

(b)

(c)

(d)

(e)

(f)
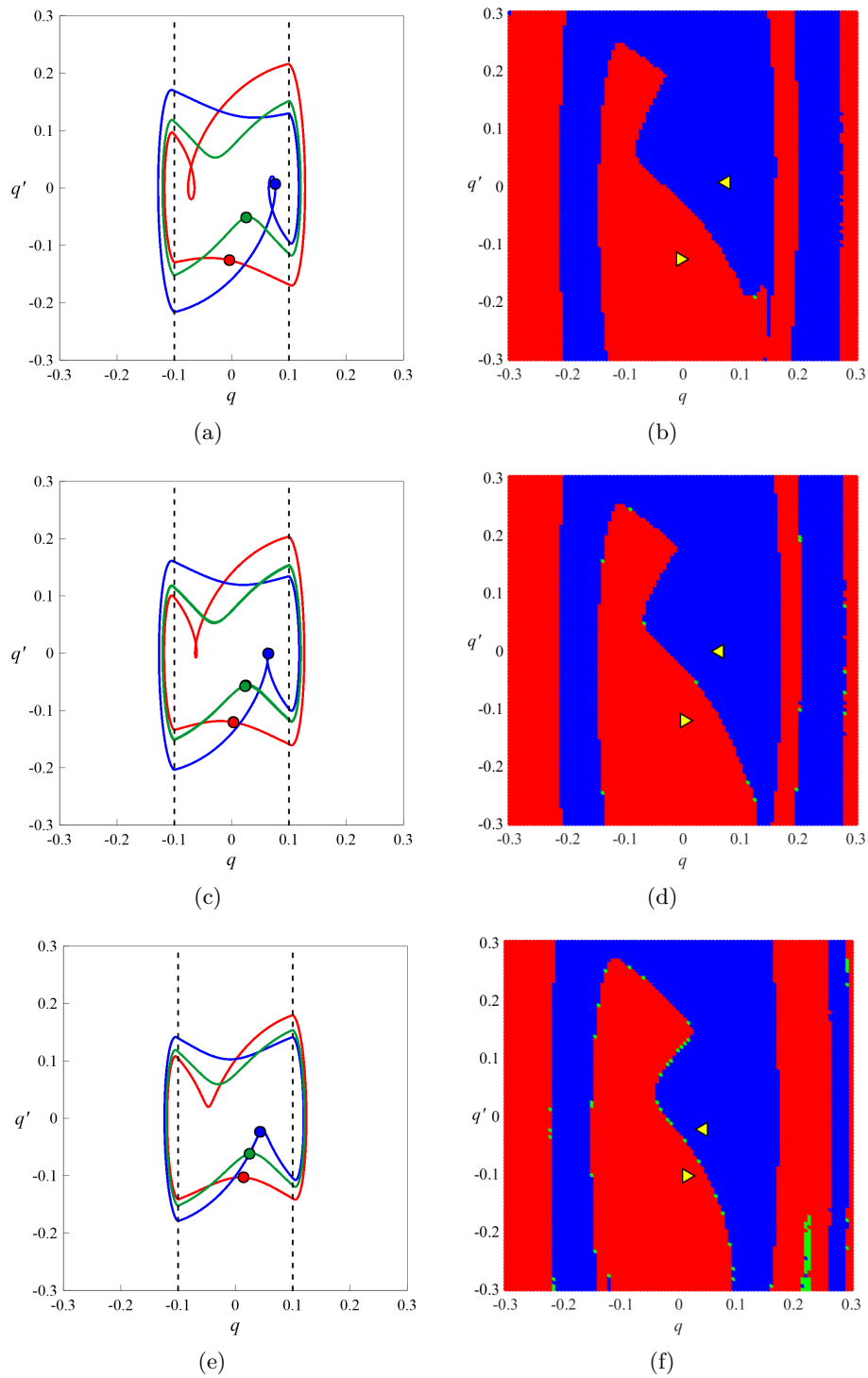
Figure 4.23. Region VI ($\xi = 0.1$, $\gamma = 5$, $\lambda = 50$, $\delta_0 = 0.1$) descending branch of the PRCs, after the secondary non-regular resonance, phase portraits with Poincaré sections: **a** $\beta = 1.12$; **c** $\beta = 1.14$; **e** $\beta = 1.18$; basins of attraction: **b** $\beta = 1.12$; **d** $\beta = 1.14$; **f** $\beta = 1.18$.

rectangular zoomed areas. As concerns the periodic solution, the same commensurate harmonic components are observed (Fig. 4.22d), but some of them have much smaller amplitudes, compared to the two quasi-periodic solutions.

Increasing β, the internal loops of the quasi-periodic solutions gradually move away from the obstacles, reducing the extent of the grazing. Consequently, the quasi-periodicity of the solutions, and thus the irregularity of the basins of attraction, decrease. Also the number of forcing cycles required to reach the stationary reduces.

After passing the range characterized by almost constant excursion, a straight descending branch, along which there is a *pair of periodic solutions* with $n = 1$ (Fig. 4.23), is observed. Also in this frequency range, it is possible to observe a third periodic solution with $n = 1$ (green curve, similar to that shown in Figs. 4.21a and 4.22a), antisymmetric in itself, reachable starting from initial conditions that are placed on the boundaries of the basins of attraction of the other two solutions. The limit cycles that make up the pair initially have internal loops which no longer reach the obstacles (Fig. 4.23a); consequently, in each forcing cycle, the mass hits each bumper once. As β increases, these loops gradually disappear, taking on the appearance of cusps (Fig. 4.23c), progressively more rounded (Fig. 4.23e) and the solutions that make up the pair progressively become more and more similar to each other and to the third (green) solution. The basins of attraction (Figs. 4.23b,d,f) return to have more regular boundaries, compared to Figs. 4.21i-k and 4.22b, and no significant variations are observed with increasing β.

Further scenario inside Region VI

As anticipated in Sect. 4.3, for $0 < \delta_0 < \delta_0^*$, the observed scenarios are more varied and complex than those seen for $\delta_0^* < \delta_0 \leq 1$. An example of the possible situations that can be encountered inside Region VI has been shown in Sect. 4.3, for $\delta_0 = 0.1$. However, by slightly varying δ_0, quite different scenarios can be observed, like the one shown in Fig. 4.24, corresponding to $\delta_0 = 0.05$, which will be described below, without going into too much detail. It can be observed that, as for $\delta_0 = 0.1$ (Fig. 4.20), in the low frequency range, a *cascade* of similar secondary units was observed (enclosed by an ellipse). By analyzing the single unit, for example the largest one, in the range $0.96 \leq \beta \leq 1.71$ (rectangular zoomed area in Fig. 4.24), different homogeneous frequency ranges can be distinguished as β increases:

- Range 1 ($0.963 \leq \beta \leq 1.214$) with a *secondary non-regular resonance*, approximatively zero-eccentricity and almost constant excursion;

- Range 2 ($1.214 < \beta < 1.45$) with a *secondary non-regular resonance*, non-zero-eccentricity and slightly decreasing excursion;

- Range 3 ($1.45 \leq \beta \leq 1.502$) with a *secondary resonance with left hysteresis* and non-zero eccentricity;

- Range 4 ($1.502 < \beta \leq 1.7$) with non-zero-eccentricity and decreasing excursion.

Within Range 1, a single chaotic solution, with antisymmetric envelope is observed (Fig. 4.25a, for $\beta = \beta_I = 1.03$). The corresponding Fourier spectrum is shown in Fig. 4.25b. It can be observed that the trajectory, during its chaotic evolution as

Figure 4.24. Region VI, further scenario ($\xi = 0.1$, $\gamma = 5$, $\lambda = 50$, $\delta_0 = 0.05$), forward (solid red line) and backward (dashed blue line) PRCs of: **a** η_d and e_d (curves in the lower part of the graph); **b** η_a and e_a (curves in the lower part of the graph). The vertical arrows represent the jumps. The cascade in the low frequency range is enclosed by the solid black ellipse, and a detail of one of the units in the cascade is shown in the two zoomed rectangular areas. The two dashed vertical lines represent β values that will be investigated in more detail.
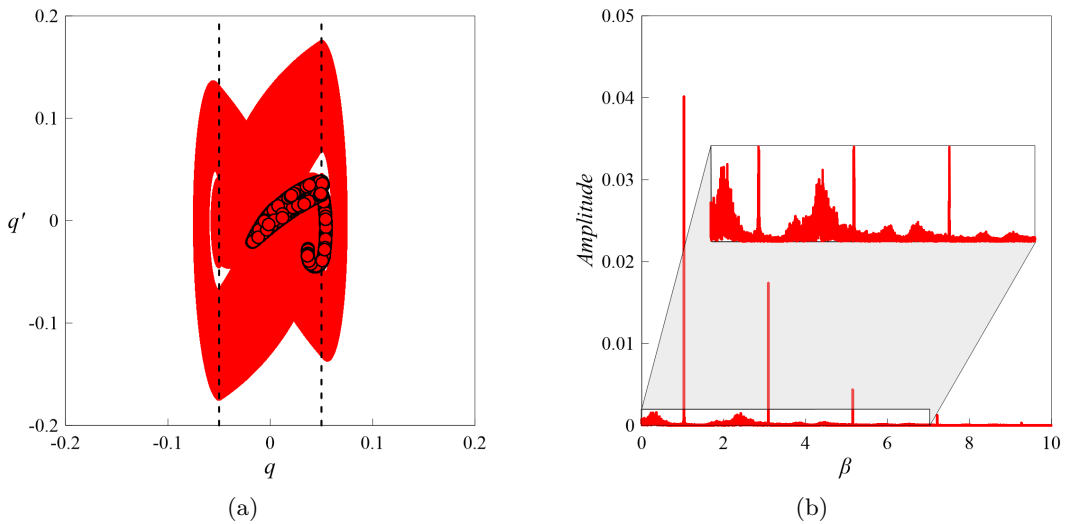
Figure 4.25. Region VI, further scenario ($\xi = 0.1$, $\gamma = 5$, $\lambda = 50$, $\delta_0 = 0.05$), Range 1, chaotic solution for $\beta = \beta_I = 1.03$: **a** phase portrait with Poincaré section; **b** Fourier spectrum.

time goes by, sometimes grazes the obstacles. Within Range 2, a *pair of quasi-periodic solutions*, similar to those shown in Fig. 4.22a, is observed. Within Range 3, characterized by a left hysteresis with non-zero eccentricity, varying the initial conditions, *two pairs of periodic solutions*, (Fig. 4.26a, for $\beta = \beta_{II} = 1.48$), each with $n = 1$, are observed. Each pair is associated with specific values of excursion and eccentricity and the corresponding basins of attraction are shown in Fig. 4.26b. All four solutions have an internal loop. However, while in the pair associated with the forward sweep, the internal loop intersects the obstacle, in the pair associated with the backward sweep the loop does not reach it. Consequently, in each forcing cycle, the number of impacts on the forward sweep always exceeds the number of impact on the backward sweep by 1, as also observed in Sect. 4.3. In the PRCs (Fig. 4.24) the values of excursion and eccentricity, corresponding to the two pairs of periodic limit cycle, are represented with circular markers, and they can be seen better in the two zoomed rectangular areas. By focusing the attention on the eccentricity, it can be observed that, they are placed on four lines, two by two symmetrical with respect to the horizontal axis, respectively $e_d = 0$ and $e_a = 0$. Within Range 4, a *pair of periodic multi-frequency solutions*, with $n = 1$, is observed (similar to that shown in Fig. 4.23). The two solutions evolve with β in a similar way to what was described in the last part of Sect. 4.3.

(a)   (b)
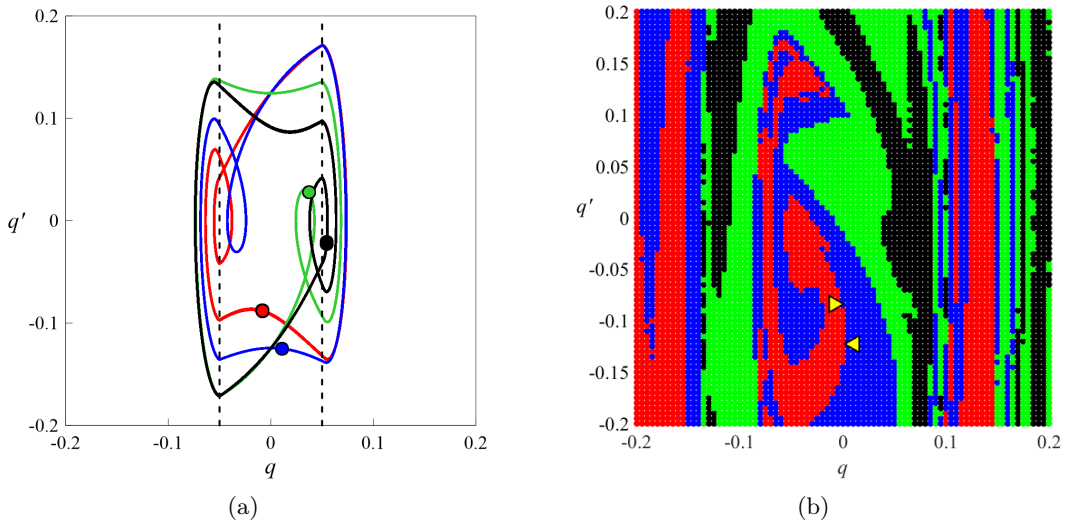
Figure 4.26. Region VI, further scenario ($\xi = 0.1$, $\gamma = 5$, $\lambda = 50$, $\delta_0 = 0.05$), Range 3, two pairs of periodic solutions $\beta = \beta_{II} = 1.48$: **a** phase portraits with Poincaré sections; **b** basins of attraction. The first pair is made up of red and black solutions, the second pair is made up of blue and green solutions.

All the units in the *cascade* are similar to each other and are interspersed with frequency intervals characterized by a single periodic multi-frequency solution with $n = 1$. As observed in Sect. 4.3, decreasing β and moving from one valley to the other, the number of internal loops, and therefore of impacts, increases. By appropriately reducing the frequency increment $\Delta\beta$ of the sine sweep excitation, it is possible to observe, even in the smallest units, the left hysteresis, otherwise not visible. Also in this case, the difference between the left hysteresis belonging to different units lies

in the number of internal loops in the limit cycles, and therefore in the number of impacts. In particular, decreasing β, the number of internal loops and of impacts increases, with a number of impacts on the forward sweep which always exceeds the number of impact on the backward sweep by 1. In addition to the scenarios shown in Fig. 4.20 and 4.24, there may be many others. Given the complexity found within Region VI, it therefore deserves to be further investigated and this will be the aim of our future works.

Region VII

In the limit case $\delta_0 = 0$, that is when the bumpers are initially in contact with the mass, the situation returns to be smooth (Fig. 4.27). Forward and backward

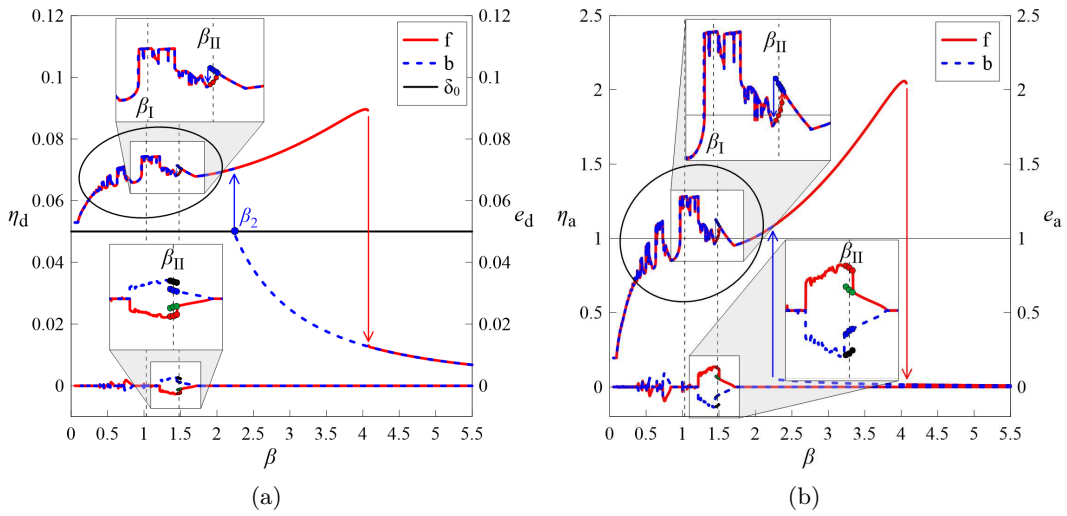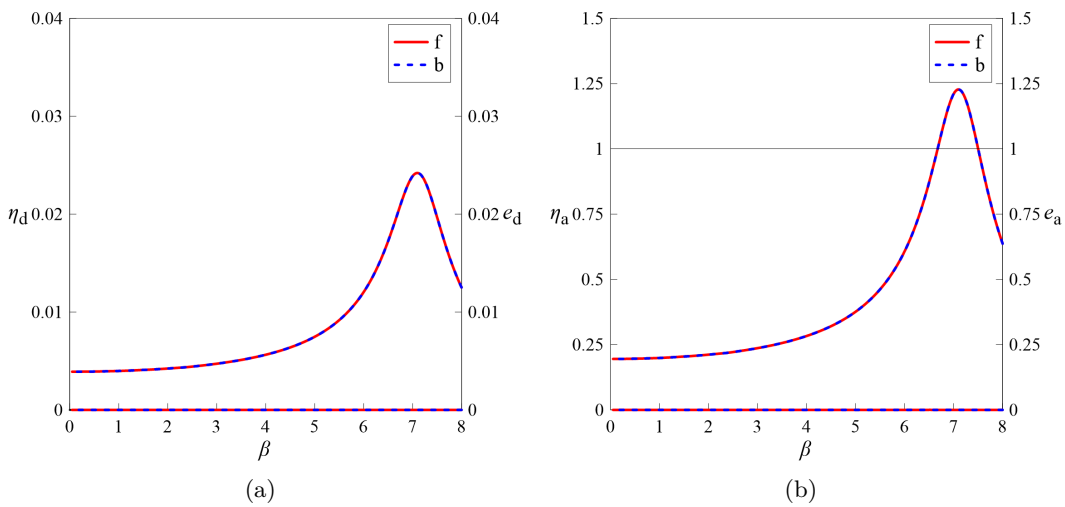**Figure 4.27.** Region VII ($\xi = 0.1$, $\gamma = 5$, $\lambda = 50$, $\delta_0 = 0$), forward (solid red line) and backward (dashed blue line) PRCs of: **a** η_d and e_d (horizontal line in the lower part of the graph); **b** η_a and e_a (horizontal line in the lower part of the graph).

PRCs overlap, without jumps, hysteresis or secondary resonances and the primary resonance has moved to higher frequencies. Furthermore, eccentricity is always zero. However, the dynamic is different from that observed for $\delta_0 = 1$. Based on what was said in Sect. 4.2.4, impact occurs for each β value. It can be observed that the values of excursion of relative displacement η_d are much smaller than those corresponding to the other previously considered values of δ_0.

For each β value a periodic mono-frequency solution, with the same period of the excitation, that is $n = 1$, is observed (Fig. 4.28a). Consequently, at steady-state, reached with a small number of forcing cycles, the points in the Poincaré sections coincide with a single point. The limit cycle takes on the appearance of a very flattened ellipse and in the Fourier spectra (Fig. 4.28b), only the fundamental harmonic component is observed. Given the fairly small value of the relaxation time of the considered bumpers compared to the forcing period ($\tau_r = 0.02$), it is difficult to see the flight phases between consecutive contacts. In fact, the duration of each flight phase is very short, because the detachment between the mass and the single bumper takes place when the latter has recovered practically all its deformation and

(a)   (b)
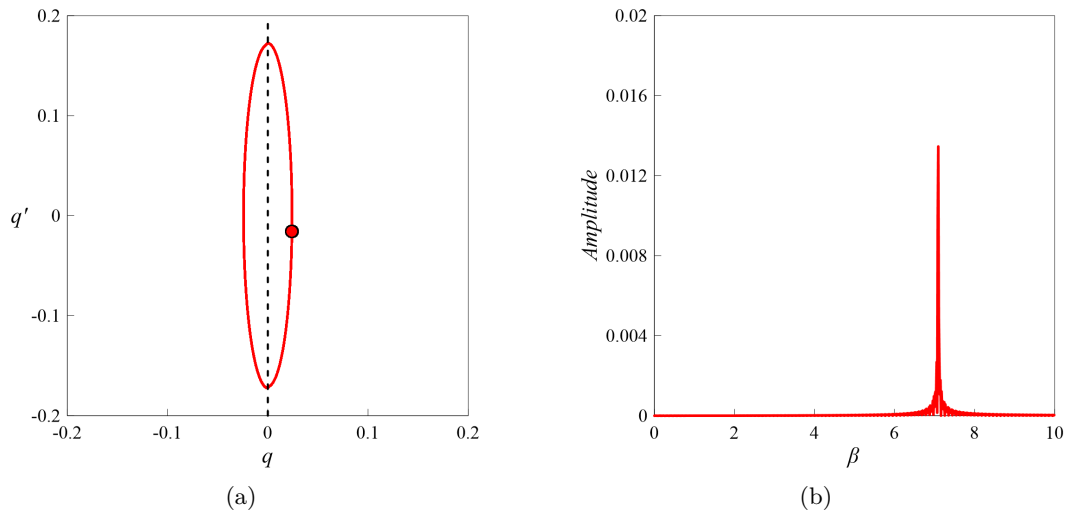
Figure 4.28. Region VII ($\xi = 0.1$, $\gamma = 5$, $\lambda = 50$, $\delta_0 = 0$): **a** phase portrait with Poincaré section and **b** Fourier spectrum for $\beta = 7.1$.

immediately afterwards the mass impacts the other bumper, which in the meantime has already recovered its deformation.

4.4   Summary

In Sect. 4.2.4, it was shown that, once the value of the damping ratio ξ has been set, it is possible to analytically determine, resorting to geometric considerations, the frequency interval in which impact surely will occur ($\beta_1 \leq \beta \leq \beta_2$), for a given value of δ_0 (see the yellow horizontal lines in Fig. 4.3b). Due to the mainly hardening behavior of the considered vibro-impact system, this frequency range, highlighted in yellow in Fig. 4.29a, extends to the right (green region). The green region is bounded by the descending branch of the PRC, after the resonance, which represents the locus of β_2 values, and by the thin dotted black curve which represents the locus of the downward jumps frequencies in the forward sweep (denoted as β_3). While if $\beta_1 \leq \beta \leq \beta_2$ the impact will surely occur for geometric reasons, if $\beta_2 \leq \beta \leq \beta_3$ it will occur, due to the nonlinear behavior of the system, and depending on the values of the parameters and the initial conditions. In the same figure, the horizontal dashed lines represent the investigated δ_0 values and the red and blue dots indicate the corresponding values of β_1 and β_2. Finally, the identified regions are shown on the left, with Roman numerals enclosed within circles.

In the previous Sections, for each considered δ_0 value, and for $\xi = 0.1$, $\gamma = 5$ and $\lambda = 50$, starting from the analysis of the PRCs, homogeneous frequency intervals, characterized by similar features in terms of number and type of observed solutions, presence or absence of hysteresis and eccentricity, were identified. In Fig. 4.29b these frequency ranges are represented with colored horizontal bars. Within the single horizontal bar, every color represents a homogeneous β interval and a brief description of its main characteristics is given in the legend shown at the bottom of Fig. 4.29. The limits of the sub-ranges must be understood as qualitative, especially

in the low frequency range. Furthermore, it is worth noting that these colors have nothing to do with those used in Fig. 4.4 to distinguish the regions in the $\lambda - \delta_0$ plane. By stacking, one below the other, the frequency intervals corresponding to the investigated values of δ_0, and thanks to the use of different colors, it is possible to have an overview of the encountered scenarios and to get an idea of the possible evolution of the different secondary behaviors, as δ_0 decreases, starting from the free flight condition ($\delta_0 = 1$).
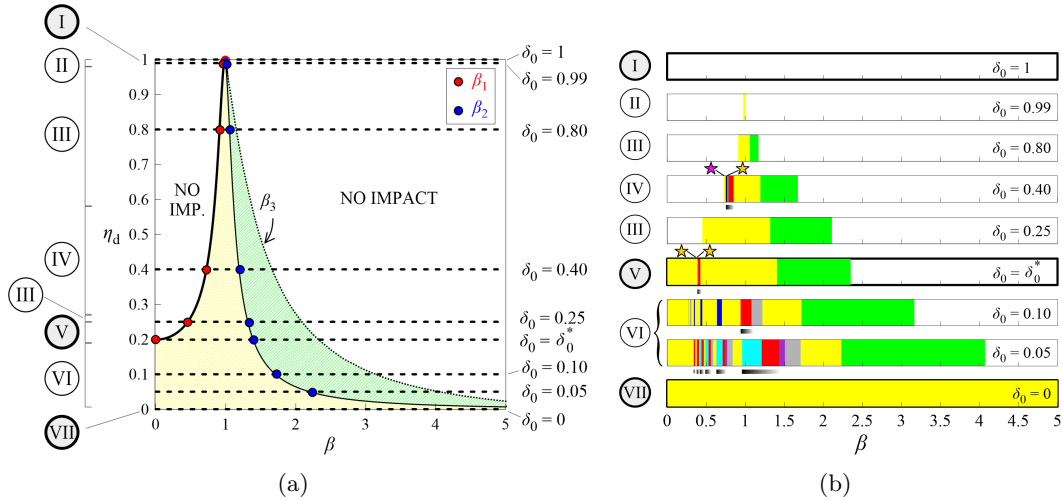
LEGEND

Color	Impact	Eccentricity	Hysteresis	Solutions
(white)	no	$e = 0$	-	a single periodic non-impacting solution ($n = 1$)
(yellow)	yes	$e = 0$	-	a single periodic impacting solution ($n = 1$ or 3)
(green)	yes	$e = 0$	primary right hysteresis	two coexisting periodic solutions ($n = 1$): a large-amplitude impacting motion (forward sweep) and a small-amplitude non-impacting motion (backward sweep)
(black)	yes	$e = 0$	secondary right hysteresis	two coexisting impacting solutions: a periodic solution ($n = 3$) and a quasi-periodic solution
(cyan)	yes	$e = 0$	-	a single quasi-periodic or chaotic impacting solution
(red)	yes	$e \neq 0$	-	a pair of quasi-periodic impacting solutions with antisymmetric envelope, with or without a coexisting periodic impacting solution ($n = 1$)
(blue)	yes	$e = 0$	secondary left hysteresis	two coexisting periodic impacting solutions ($n = 1$): a large-amplitude motion (backward sweep) and a small-amplitude motion (forward sweep)
(gray)	yes	$e \neq 0$	-	a pair of periodic ($n = 1$) impacting solutions with antisymmetric envelope, with or without a coexisting periodic impacting solution ($n = 1$)
(purple)	yes	$e \neq 0$	-	two pairs of periodic impacting solutions ($n = 1$), each with antisymmetric envelope

Figure 4.29. **a** PRC of normalized excursion of relative displacement η_d in free flight condition for $\xi = 0.1$ (thick black curve) with indication of the frequency intervals in which impact surely will occur (yellow) or in which it will occur depending on the initial conditions (green); the dashed horizontal lines represent the investigated δ_0 values and the Roman numerals enclosed within circles indicate the regions. **b** Homogeneous frequency intervals corresponding to the investigated δ_0 values (for $\xi = 0.1$, $\gamma = 5$, $\lambda = 50$). The magenta star denotes the occurrence of primary grazing, whereas the orange stars correspond to the secondary grazing and the shaded black bands highlight the frequency intervals characterized by the occurrence of grazing. A summary of the main features of each frequency interval is given at the bottom of the figure.

It can be observed that in the two limit cases, that is $\delta_0 = 1$ (Region I) and $\delta_0 = 0$ (Region VII), the situation is smooth, although the dynamic is different.

Indeed, in the first case ($\delta_0 = 1$) impact does not occur for any β value, whereas in the second case ($\delta_0 = 0$) impact occurs for each β value.

Leaving out the frequency range characterized by the absence of impact, left white, it can be noted that decreasing δ_0, the amplitude of the frequency range associated with the occurrence of impacting solutions (colored bars) increases. Also the number of used colors, and therefore of encountered behaviors, increases, especially in the low frequency range and for $0 < \delta_0 < \delta_0^*$.

Yellow and green colors appear to prevail over the others. The former represents the frequency range associated with the occurrence of a single periodic impacting solution with $n = 1$ or $n = 3$, while the latter corresponds to the *primary right hysteresis*. It can be observed that, starting from the absence of hysteresis for $\delta_0 = 1$ (forward and backward PRCs overlap), this frequency range increases and finally disappears again for $\delta_0 = 0$ (forward and backward PRCs overlap again). The other colors were used to represent the smaller frequency ranges corresponding to the observed secondary resonances.

As can be seen from Fig. 4.29b, and as already noted in Sect. 4.3, the reference value $\delta_0 = \delta_0^*$ seems to represents the watershed between different types of observed behaviors. Indeed, for $\delta_0^* \leq \delta_0 < 1$, the situation is quite calm, except for very small frequency ranges in which *secondary resonances with right hysteresis*, followed by intervals with non-zero eccentricity, were observed (for $\delta = 0.4$, inside Region IV and for $\delta = \delta_0^*$, inside Region V). Conversely, more complex and varied scenarios (with *secondary resonances with left hysteresis*, *secondary non-regular resonances* and *cascades* of similar behaviors), which reflect in a greater chromatic variety, were observed for $0 < \delta_0 < \delta_0^*$ (inside Region VI). These secondary behaviors affect gradually wider frequency ranges as the δ_0 decreases.

Despite the great variety of identified homogeneous frequency intervals, the use of colors allows to recognize a certain regularity and to highlight the presence of *cascades* of behaviors that are repeated on different scales, keeping a similar shape. In particular, the *cascade of secondary left hysteresis*, for $\delta_0 = 0.1$, highlighted in blue, and the *cascade* of more complex secondary units (formed by the adjacent cyan, red, purple and gray ranges, corresponding to the four ranges defined in Sect. 4.3) observed for $\delta_0 = 0.05$. For values of $0 < \delta_0 \leq \delta_0^*$, internal loops in the phase portraits were also observed. These loops, in the low frequency range, often reach and cross the obstacles, giving rise to number of impacts per forcing cycle, against each bumper, greater than one. As β decreases, these loops gradually increase in number, and thus also the number of impact increases. Therefore, while for $\delta_0^* \leq \delta_0 < 1$ neither *cascades*, nor *secondary resonances with left hysteresis* were observed, but only *secondary resonances with right hysteresis* localized in a small frequency interval, for $0 < \delta_0 < \delta_0^*$ no *secondary right hysteresis* were observed and the secondary resonances affect wider frequency ranges. Furthermore, this study allowed to observe that, in the considered model, the *grazing phenomenon* plays an important role, and it is related to the occurrence of some of the observed scenarios. In particular, in Fig. 4.29b the occurrence of *primary* and *secondary grazing* is highlighted with magenta and orange stars respectively, whereas the shaded black bands represent the frequency intervals in which the trajectories graze the obstacles as time goes by and the extent of grazing decreases as β increases.

4.5   Closing remarks

In this chapter, some of the scenarios that can occur in the numerical nonlinear non-smooth response of a SDOF system, symmetrically constrained by deformable and dissipative bumpers, under a harmonic base excitation, with the variation of selected parameters, were identified and investigated. In the numerical model, both the damper and the bumpers were modeled with the Kelvin-Voigt model. The model is described in terms of dimensionless parameters and, due to the adopted normalization, the damping ratio plays a fundamental role by influencing both the response of the system and the amplitude of the base excitation.

By observing the characteristics of the PRCs of excursion and eccentricity of absolute acceleration and relative displacement of the mass, obtained for fixed values of ξ and γ and considering a sine sweep base excitation, seven homogeneous regions in the $\lambda - \delta_0$ plane, each corresponding to a scenario, were identified. Subsequently, referring to a constant value of the stiffness ratio λ, each scenario, corresponding to a different value of the dimensionless gap δ_0, was investigated resorting to phase portraits and Fourier spectra. In some cases, further analyses varying the initial conditions (basins of attraction) were carried out.

Within each scenario, homogeneous frequency intervals, characterized by similar features in terms of number (single solution, *coexisting solutions* or *pair of solutions*) and types of limit cycles (*periodic*, *quasi-periodic* or *chaotic*), were identified.

Decreasing the dimensionless gap, starting from $\delta_0 = 1$, gradually more complex and varied scenarios, characterized by the presence of the *primary resonance with right hysteresis* and also by the occurrence of different types of *secondary resonances* (with *right* or *left hysteresis* or of *non-regular* type) and *cascades*, affecting gradually wider frequency ranges, were observed. The occurrence of the (*primary* and *secondary*) grazing phenomenon, and its relationship with some of the observed situations, was also highlighted.

A reference value for the dimensionless gap, denoted as δ_0^*, was identified. It allowed to distinguish some δ_0 ranges (namely $\delta_0 = 1$, $\delta_0^* < \delta_0 < 1$, $0 < \delta_0 < \delta_0^*$ and $\delta_0 = 0$) in which different behaviors were observed. In particular, the most complex scenarios were noticed for $0 < \delta_0 < \delta_0^*$. Conversely, for $\delta_0^* \leq \delta_0 < 1$, more calm situations were observed. In the two limit cases ($\delta_0 = 1$ and $\delta_0 = 0$), the situation is instead smooth, although characterized by different dynamics.

Based on the results obtained in this work and in [251], a future development of this study will be to investigate in more detail the part of the $\lambda - \delta_0$ plane where the identified regions converge (enclosed within an ellipse in Fig. 4.4), and to deepen the study of Region VI, which has proven to be particularly complex and rich in behaviors. Furthermore, based on the indications provided by the numerical model, a further experimental laboratory campaign will be carried out to confirm the numerical results, especially for small, null and negative values of the dimensionless gap.

Chapter 5

Experimental study of the transition from positive to negative gaps

Chapter outline In this chapter, the influence of the gap amplitude on the experimental response of a SDOF vibro-impact oscillator, excited by a harmonic base acceleration and symmetrically constrained by two unilateral deformable and dissipative bumpers, is investigated. The parametric investigation considered both positive, null and negative gaps. Particular attention is paid to the study of the effect, on the system response, of the transition from positive to small negative gaps and of excessive negative gaps. Secondary resonances in the low frequency range, associated with the occurrence of multiple impacts, were observed for small positive gaps. Finally, the experimental results were reproduced, in a sufficiently accurate manner, using a suitable numerical model, whose parameters were identified based on the experimental data.

5.1 Introduction

The impact phenomenon is ubiquitous in many (biomedical, mechanical, civil, . . .) engineering applications involving mechanical components or structures repeatedly colliding with one another or with obstacles. Some examples are represented by the capsule systems used in clinic endoscopy to inspect the surface lining of the intestine in the human body [87, 165, 166, 293, 294] and the drilling rig used in the oil and gas industry for creation of the wells [57, 65, 156, 158, 159, 161, 267]. In the context of civil engineering, base isolation represents one of the most applied passive control strategies to mitigate the dynamic response of both new and existing structures [121, 134, 136, 253], bridges [90, 93, 123], strategic facilities [142, 235], nonstructural elements and equipment [5, 116, 168, 228, 229]. The aim of base isolation is to uncouple the motion of the structure from that of the ground by introducing some type of support that isolates it from the shaking ground, thus limiting the energy input into the system and protecting it from damaging. The flexibility introduced by base isolation increases the fundamental vibration period of the structure. The

occurrence of exceptional loads, like strong earthquakes, can produce large horizontal displacements in base-isolated structures, concentrated in the isolation system, which can damage the isolation system itself or can lead to pounding with the surrounding moat walls or adjacent structures [19, 20, 51], if the available seismic gap is not sufficient. A possible mitigation measure consists in the interposition of deformable shock absorbers (bumpers) [6, 223, 224]. On the one hand, the introduction of the bumpers limits the displacement of the structure; on the other, the possible occurrence of the impact with the bumpers can produce acceleration spikes which can be detrimental, not only for the structure itself, but also for any sensitive equipment housed in it. Furthermore, the occurrence of impact can excessively deform the bumpers. In order to limit the response of the base-isolated system, so as to avoid the damage of the isolation system, also other types of control systems can be implemented [15, 21, 80, 231].

The non-smooth dynamics of systems with one-sided or two-sided constraints, the types of impact motion, attractors and bifurcations, have been the subject of several scientific works, of both numerical and experimental nature [29, 47, 50, 85, 86, 112, 113, 126, 181, 183, 213, 256, 265, 274, 286, 299]. The effect of the introduction of the obstacle on the system response depends on several factors, including the mechanical properties of the bumpers and the distance between them and the structure (gap). As concerns the influence of the gap size, few works can be found in Literature, usually dealing with positive gaps. In these works the response is found to decrease as the gap increases [6, 139, 140, 221, 222]. Very small seismic gaps, in combination with strong ground excitation, can lead to relatively milder consequences from pounding, not allowing the structure to develop high velocities before the impact [221, 222]. According to Jankowski et al. [123] the optimal gap size to reduce the response is either a very small one or large enough to avoid collisions. The zero-gap configuration was recommended by Aguiar and Weber [4], since it allows to maximize the impact force in a vibro-impact system without the occurrence of nonlinear jumps. Even less are the works that deal with negative gaps, which cause an initial pre-stress/pre-strain state in the bumpers. Relatively simpler dynamic responses of a two-degree-of-freedom periodically-forced system are found in [182] if the constraints are initially prepressed. The effect of the introduction of a prepressing constraint in a capsule system was highlighted in [293].

The practical problem of excessive displacements in base-isolated structures inspired several works of Andreaus et al., of both numerical and experimental nature, in which a single-degree-of-freedom oscillator, impacting against two deformable and dissipative bumpers, was considered [9, 10, 12–14, 247–249, 251]. Some of the scenarios which can occur in the experimental nonlinear nonsmooth response of the system were identified and described in [251]. These scenarios were also reproduced with a suitable numerical model. Further numerical investigations highlighted the existence of gradually more complex and varied behaviors, that could be observed for values of the gap smaller than those considered in the experimental laboratory campaign [251]. Furthermore, the combination of small gaps with quite deformable bumpers appeared to be a good choice which allows to realize, compared to the free flight condition, a reduction of both accelerations and displacements or a good compromise between reduction of displacements and limited increase in accelerations [14].

Based on these preliminary results, a new laboratory campaign was designed and conducted to investigate, in particular, small positive, null and negative values of the gap and to validate the numerical predictions. The experimental investigation of small positive, null and negative gaps represent an element of novelty of this laboratory campaign. Furthermore, compared to the previous experimental investigations, impact load cells were installed between the mass and the bumpers, to directly measure the contact force during the impact phases.

In this chapter some results of the new laboratory campaign will be presented and discussed. The attention is focused of the influence of the gap amplitude on the system (mass and bumpers) response, especially when passing from small positive to small negative gaps and when the negative gap exceeds a certain threshold value. For small positive gaps, secondary resonances in the low frequency range were observed and the response of the system at these resonances was investigate. Based on the experimental results, the parameters of a relatively simple numerical model were identified in order to reproduce the experimental outcomes. Although several scientific works deal with the problem of impact, there are not many studies that address, in such a systematic way, the study of the influence of the gap on the dynamic response of the system, extending the investigations also to small positive, null and negative gaps.

The chapter is organized as follows. The experimental setup is introduced in Sect. 5.2; some experimental results are presented and discussed in Sect. 5.3; the transition from positive to small negative gaps, the effect of excessive negative gaps and the characteristics of the system's response at the secondary resonances are investigated in Sect. 5.4; the numerical model and the comparison between experimental and numerical results are presented in Sect. 5.5; finally, concluding remarks and future developments of the work are given in Sect. 5.6.

5.2 Experimental setup and performed tests

The experimental setup, shown in Fig. 5.1, consists of a rigid body (mass $M = 550$ kg), an elastomeric High Damping Rubber Bearing (HDRB) isolator (damper), and two elastomeric shock absorbers (bumpers), symmetrically mounted on steel moat walls, denoted as right (B_R) and left (B_L) bumper respectively. The experimental tests investigated two configurations, namely with and without bumpers (the latter will be referred to as free flight condition), under the same base excitation. To study the response of the system in the presence of obstacles, an elastomeric bumper with D-shape hollow section, in the following denoted as B2, was tested (see the photograph in the bottom right corner of Fig. 5.1).

By adjusting the screws behind the plates on which the bumpers are mounted, the distance between the mass and the bumpers (gap) was varied. The gaps considered in the experimental tests were denoted as: G∞, G30, G16, G10, G4, G0, G-1, G-2, G-10, where the number, expressed in mm, represents the nominal amplitude of the total gap G, defined as the sum of the right and left gaps and G∞ indicates the free flight condition. It is worth noting that in the experimental tests, as far as possible, an attempt has been made to achieve a gap equal to the nominal value. The negative gaps (G-1, G-2, G-10) were realized by initially compressing the bumpers against
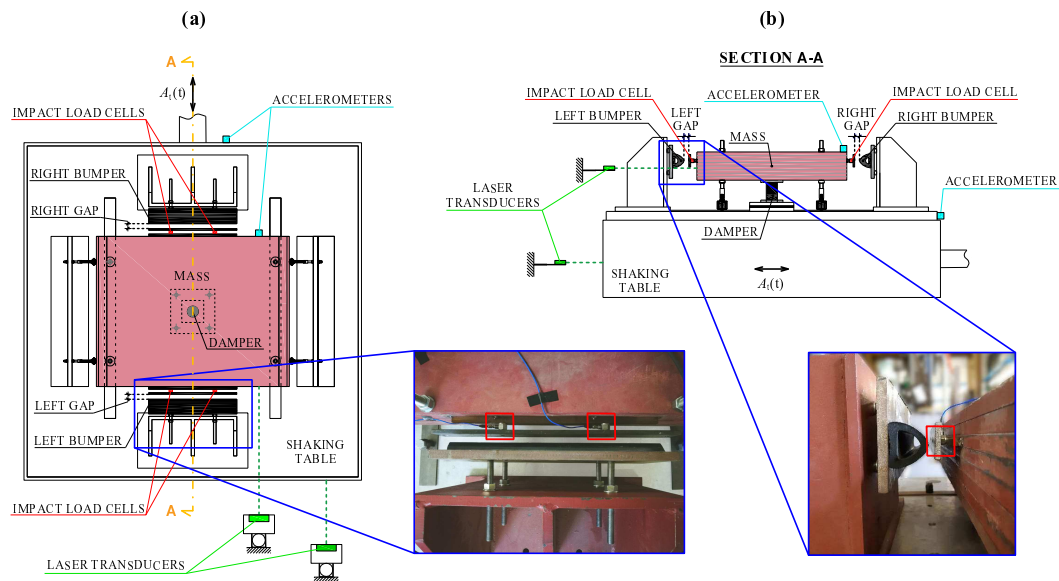
Figure 5.1. Experimental setup: **a** plan view and **b** side view with indication of the main components and sensors. The zoomed areas show two photographs with details of the impact load cells, enclosed by red squares.

the mass, leading to an initial pre-stress/pre-strain state in the bumpers. The investigation of small positive, null and negative gaps represents one of the novelty elements of this laboratory campaign, compared to previous tests and studies.

The experimental tests were carried out in the Materials and Structures Testing Laboratory of the Department of Structural and Geotechnical Engineering of "Sapienza" University of Rome, using a uni-axial shaking table Moog 1.50×1.50 m, managed by Moog Replication Software. The system was excited at the base by a step-wise forward and backward sine sweep in displacement control, in order to impose a given value of peak table acceleration, namely A = 0.05 g, where g is the gravity's acceleration, with a number of cycles n_c, in each sub-frequency range, such as to reach the steady state condition. For positive gaps (G > 0), the investigated frequency range was between 0.5 and 5 Hz, with frequency step $\Delta f = 0.1$ Hz and $n_c = 10$. For G $\leq$ 0, the investigated frequency range was extended from 0.5 to 10 Hz, with frequency step $\Delta f = 0.1$ Hz and $n_c = 10$. In some cases, especially for small positive gaps (G10 and G4), in order to better capture the experimental response of the system in the low frequency range, the frequency step Δf and the number of cycles n_c were varied, depending on the performance of the shaking table, as it will be illustrated in more detail in Sect. 5.4.3.

The measured quantities during the tests were the absolute accelerations and displacements of the mass and of the shaking table and the contact forces between mass and bumpers (Figs. 5.1). The accelerations were measured by accelerometers and the displacements by laser transducers. The forces developed during the contact phases between mass and bumpers were measured by four impact load cells, symmetrically mounted on the mass, two on each side (Sect. 2.3.3). Between the impact load cells and the bumpers, steel plates were mounted to distribute the impact force. The use of impact load cells, in addition to the other sensors, represents

another novelty element of this laboratory campaign, compared to previous tests and studies.

5.3 Experimental results

The total gap amplitude G influences the system response, as shown in Fig. 5.2, in terms of forward (red lines and dots) and backward (blue lines and dots) Pseudo-Resonance Curves (PRCs). Each PRC corresponds to an experimentally tested value of G. The size of the dots and the thickness of the lines decrease as G decreases. In Fig. 5.2a,b the green curves refer to the free flight condition (also referred to as G∞ in the legend).

The represented response quantities are the normalized excursion of the relative displacement of the mass η_d (Fig. 5.2a), the normalized excursion of the absolute acceleration of the mass η_a (Fig. 5.2b), the normalized maximum deformation η_j (Fig. 5.2c) and maximum contact force r_j (Fig. 5.2d) of the right (B_R) and left (B_L) bumpers respectively ($j = $ R, L). These quantities are defined as follows:

$$\eta_\mathrm{d} = \frac{E_\mathrm{d}}{E_\mathrm{d0}} = \frac{u_\mathrm{max} - u_\mathrm{min}}{2u^*} \tag{5.1a}$$

$$\eta_\mathrm{a} = \frac{E_\mathrm{a}}{E_\mathrm{a0}} = \frac{a_\mathrm{max} - a_\mathrm{min}}{2a^*} \tag{5.1b}$$

$$\eta_j = \frac{u_{j,\mathrm{max}}}{u^*} \quad (j = \mathrm{R, L}) \tag{5.1c}$$

$$r_j = \frac{F_{j,\mathrm{max}}}{Mg} \quad (j = \mathrm{R, L}) \tag{5.1d}$$

In the first three cases (Eqs. 5.1a-c), the normalization was made with respect to the free flight resonance condition (u^* and a^* denote the maximum relative displacement and absolute acceleration of the mass in free flight resonance condition). As concerns the contact force F_j ($j = $ R, L), it is normalized with respect to the weight Mg of the impacting mass (Eq. 5.1d).

From Fig. 5.2 it can be observed that, for G > 0, compared to the free flight condition (green curves), the hardening caused by the impact between the mass and the bumpers bends the Pseudo-Resonance Curves (PRCs) to the right, causing the occurrence of jumps (represented with vertical arrows for G4), and thus of a *primary right hysteresis* (highlighted in yellow). Referring to the primary resonance condition, it can be observed that, progressively approaching the bumpers to the mass, that is decreasing G, the movement of the mass is increasingly limited and, consequently, the maximum value of η_d decreases (Fig. 5.2a). On the other hand, the maximum acceleration, after an initial increase, starts to decrease (Fig. 5.2b). Furthermore, as highlighted by previous numerical investigations [251], for quite small gaps (G10 and G4) secondary resonances in the low frequency range were observed, and the number of secondary resonances was found to increase decreasing G. As concerns the two bumpers (Figs. 5.2c,d), it can be observed that the PRCs of the normalized deformation η_j and contact force r_j corresponding to the to bumpers (B_R, above the frequency axis and B_L, below the frequency axis) are qualitative similar to each other, due to the mostly symmetric behavior of the studied system. The trends of

both the deformation (Fig. 5.2c) and the contact force (Fig. 5.2d) for decreasing positive gaps are similar to that of the acceleration of the mass (Fig. 5.2b). The jumps, the right hysteresis and the secondary resonances, are still visible also in these curves. Compared to the PRCs of η_d and η_a, for G > 0, the PRCs of η_j and r_j ($j = $ R, L) are zero at the frequency values for which the impact does not occur.
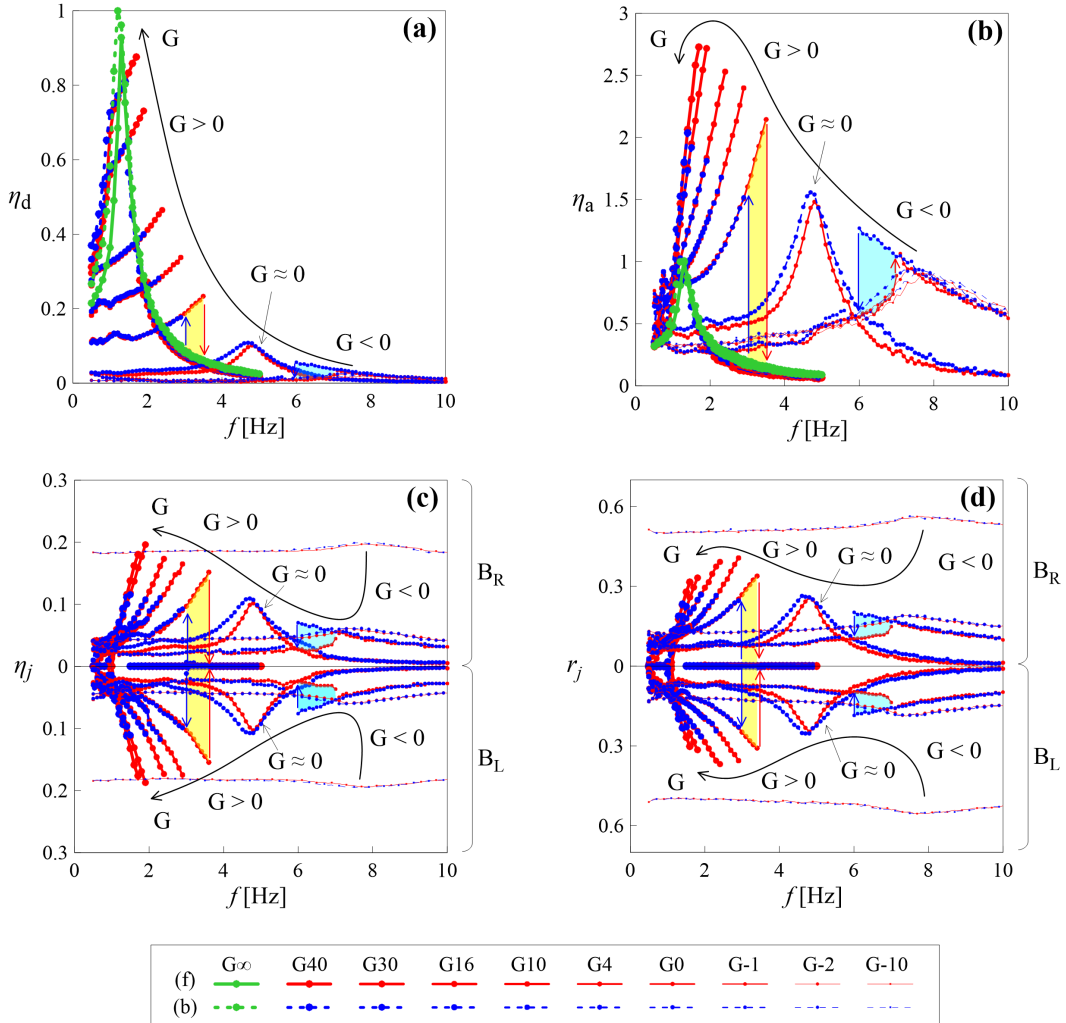
Figure 5.2. Forward (*red*) and backward (*blue*) PRCs of: **a** η_d; **b** η_a; **c** η_j ($j = $ R, L) and **d** r_j ($j = $ R, L) for different values of the total gap amplitude G. In **a** and **b**, the free flight condition (G∞) is represented with green curves.

The situation returns to be smooth for bumpers initially more or less in contact with the mass (G $\simeq$ 0), with the forward and the backward PRCs, of both η_d, η_a, η_j and r_j ($j = $ R, L) substantially overlapped, the resonance shifted to higher frequencies (about 4.8 Hz) and without jumps or hysteresis. As concerns the bumpers, since now impact occurs for each frequency value, the PRCs of η_j and r_j ($j = $ R, L) are always different from zero.

For small negative gaps (G-1), obtained by initially slightly compressing the bumpers against the mass, the PRCs bend to the left, due to a softening-like

behavior, showing jumps (represented with vertical arrows) and a *primary left hysteresis* (highlighted in cyan). The left hysteresis is observed in the PRCs of both $\eta_{\rm d}$, $\eta_{\rm a}$, η_j and r_j ($j =$ R, L). The initial pre-stress/pre-strain state of the bumpers, resulting from the negative gaps, causes an offset of the PRCs of η_j (Fig. 5.2c) and r_j (Fig. 5.2d) ($j =$ R, L) from the frequency axis. Consequently, as in the G$\simeq 0$ case, these curves are always different from zero.

By further compressing the bumpers against the mass (G-2 and G-10), the PRCs are no longer bent, show neither jumps nor hysteresis and the resonance is shifted to higher frequencies (about 7.5 Hz). Furthermore, while the PRCs of $\eta_{\rm d}$ and $\eta_{\rm a}$ corresponding to these two values of the gap are substantially overlapped, those of η_j and r_j ($j =$ R, L) are similar but appear to be shifted with respect to each other, with the extent of the shift related to initial pre-stress/pre-strain state caused by the negative gap.

The effect of the gap amplitude G on the system response can be seen also from Fig. 5.3, in which the force-displacement cycles, in steady-state primary resonance condition, are represented, for both the mass (inertia force $F_{\rm I}$ vs. relative displacement u of the mass, Fig. 5.3a) and the two bumpers (contact force F_j vs. position v_j of the bumper, $j =$ R, L, Fig. 5.3b).
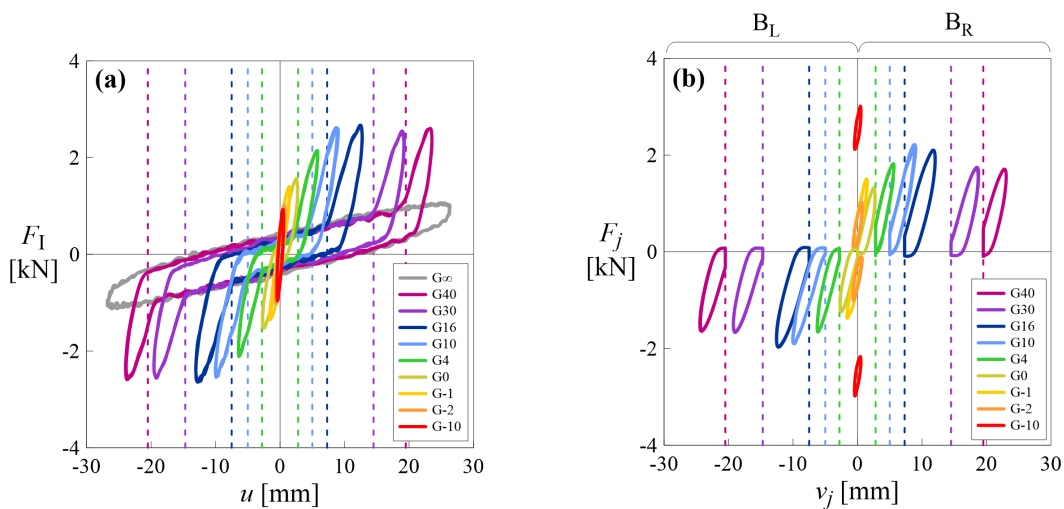
Figure 5.3. Force-displacement cycles in steady-state primary resonance condition corresponding to the investigated values of the total gap G: **a** mass; **b** bumpers.

The position of the extremity of the bumper v_j ($j =$ R, L) is measured from the side of the mass at time $t = 0$ s, as shown in the schematic representations in Fig. 5.4, which refers to the right bumper ($j =$ R). The position v_j is related to the deformation u_j, the latter used for the calculation of η_j, through the expression $v_j = u_j + G_{0j}$, where G_{0j} ($j =$ R, L) represents the initial distance (gap) between the mass and the j-th bumper.

In Fig. 5.3 each color corresponds to a gap amplitude G and the vertical dashed lines represent the initial position of the bumpers for G > 0. Through these representations it is possible to see, in the same figure, the evolution of both the forces and the displacements with the amplitude of the gap. From Fig. 5.3a it is possible to observe both the increment of stiffness (hardening), which occurs when

Figure 5.4. Graphical represen-
tation of the relationship be-
tween bumper's deformation
u_j and position v_j for $j =$
R (right bumper) and consid-
ering **a** positive, **b** null and
c negative initial gaps. The
dashed black lines represent
the initial configuration of the
system.
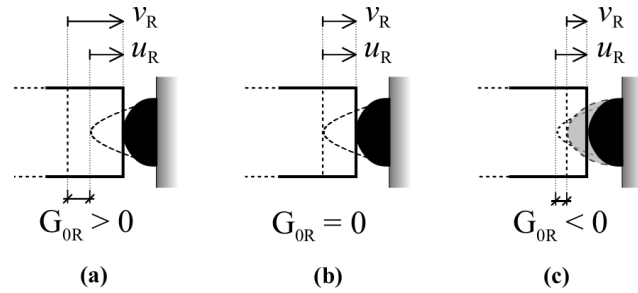
the mass impacts the bumper, for G $\geq$ 0, and the decrease in stiffness (softening) for
small negative gaps (G-1, light orange curve). For negative gaps beyond a certain
value (G-2 and G-10), the response of the mass does not vary significantly and the
F_I-u cycles are substantially overlapped, though they are not quite the same, as it
will be said in the following section. On the contrary, the pre-stress state induced in
the bumpers by the negative gap causes the F_j-v_j ($j =$ R, L) cycles to move away
from the x-axis (Fig. 5.3b). The behavior of the system for small positive, null and
negative values of the gap will be discussed in more detail in the following Sect. 5.4.

5.4 Insights

In this section the attention is focused on the range of small positive, null and
negative gaps. Starting from Fig. 5.5, in which only the PRCs corresponding to
G4 (black lines and dots), G0 (red lines and dots), G-1 (blue lines and dots), G-2
(light green lines and dots) and G-10 (dark green lines and dots) are represented,
three aspects will be further investigated, namely the transition from positive to
negative small gaps (Sect. 5.4.1), the effect of excessive negative gaps on the mass
and the bumpers' responses (Sect. 5.4.2), the characteristics of the system response
for small positive gaps and in the low frequency range, where secondary resonances
were observed (Sect. 5.4.3).

5.4.1 Transition from positive to negative small gaps

From Fig. 5.5 it can be observed that the transition from the hardening-like (black
PRCs with *primary right hysteresis*) to the softening-like (blue PRCs with *primary
left hysteresis*) behavior occurs moving from small positive to small negative values
of the gap, passing through the approximately zero-gap configuration (G$\simeq$0, red
PRCs). The force-displacement cycles in resonance condition, corresponding to the
three gaps in the neighborhood of this transition (namely G4, G0 and G-1), are
represented in Fig. 5.6. The top row refers to the mass (inertia force F_I vs. relative
displacement u of the mass), the bottom row to the bumpers (contact force F_j vs.
position v_j of the bumper, $j =$ R, L).

The first column on the left (Figs. 5.6a,d) corresponds to G4; at the *primary
right hysteresis* (black PRCs in Fig. 5.5) two coexisting stable solutions are observed
(Figs. 5.6a, 5.7a): one corresponding to large-amplitude oscillations with the occur-
rence of impact (forward sweep, solid red cycles) and the other to small-amplitude
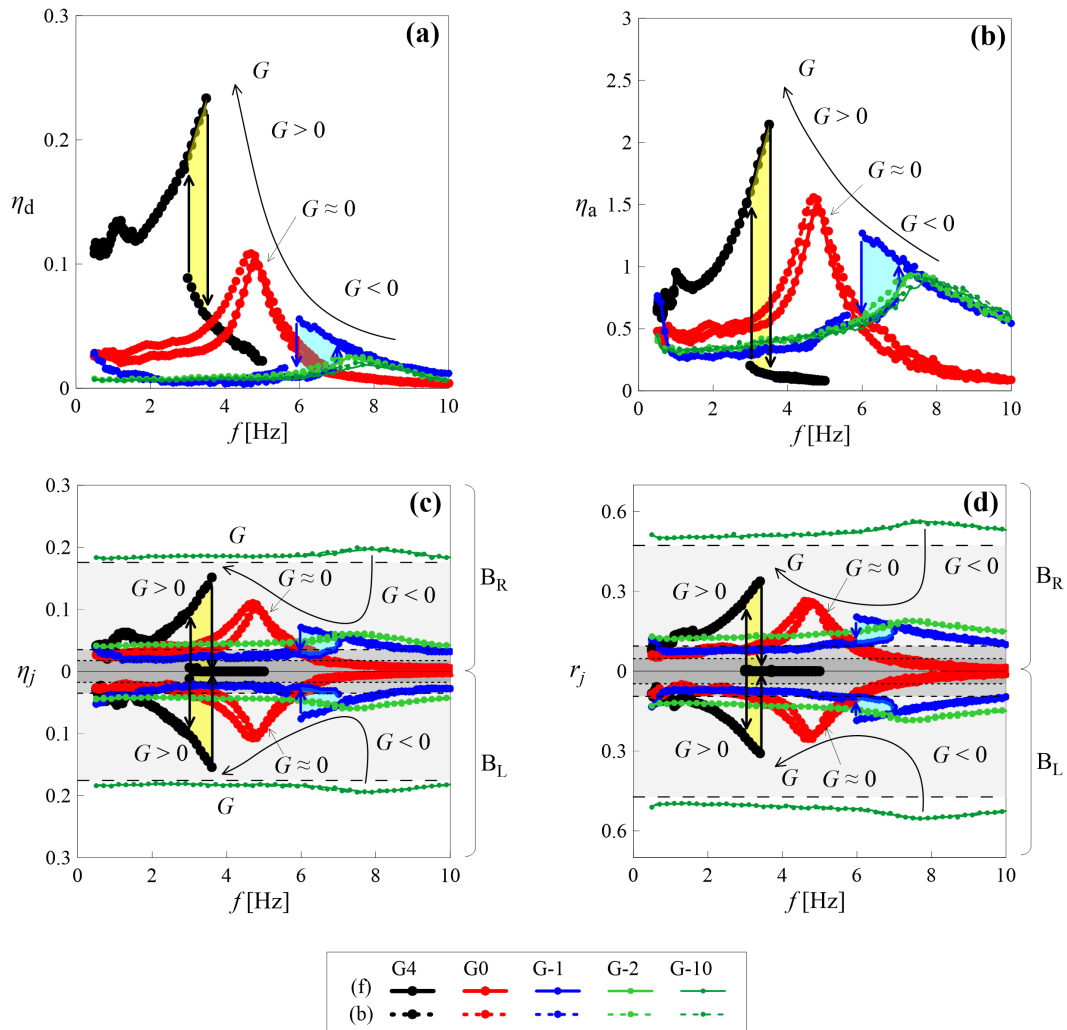
Figure 5.5. Forward (solid line) and backward (dashed line) PRCs of: **a** η_d; **b** η_a; **c** η_j (j = R, L) and **d** r_j (j = R, L) for G4 (black), G0 (red), G-1 (blue), G-2 (light green) and G-10 (dark green). In **a** and **b**, the PRCs corresponding to G-2 and G-10 are almost superimposed on each other. In **c** and **d**, the initial pre-strain/pre-stress states of the bumpers, resulting from the negative gap, are indicated by horizontal dashed lines and also highlighted with gray shaded areas which have, as baseline, the frequency axis.

oscillations without impact (backward sweep, dashed blue cycles). In this frequency range, there would be also a third unstable solution, that could not be obtained experimentally. In Fig. 5.7a, in which the time history of the relative displacement u of the mass is depicted, both in the forward (solid red line) and in the backward (dashed blue line) sweeps, the horizontal dashed lines represent the initial gap and the vertical colored bands highlight the contact phases with each bumper (identified from the time histories of the contact forces). In the time interval between two consecutive colored bands, the mass is not in contact with either bumper (flight). The hardening-like behavior is related to the occurrence of the impact with one of the bumpers, which causes the adding of the resisting force exerted by the bumper to that of the damper.

Figure 5.6. Force-displacement cycles in steady-state resonance condition corresponding to the forward (*red curve*) and the backward sweep (*blue curve*) for: G4, $f = 3.4$ Hz (*hardening*): **a** mass; **d** bumpers. G0, $f = 4.8$ Hz: **b** mass; **e** bumpers. G-1, $f = 6$ Hz (*softening*): **c** mass; **f** bumpers.

For G $\simeq 0$ (second column, Figs. 5.6b,e), the forward and backward cycles are more or less overlapping. In this condition, which is quite difficult to obtain experimentally, although no jumps or hysteresis occur in the PRCs (red PRCs in Fig. 5.5), the behavior of the system is still nonlinear [251]. The dissipative capability of the bumpers means that there is a short time interval in which the mass is not in contact with either bumper (Fig. 5.7b). This phase vanishes for purely elastic bumpers. Due to the small value of the relaxation time of the considered bumper (B2), the mass detaches from one bumper when the latter has recovered practically all its deformation and, right after, it impacts the other bumper, which, in the
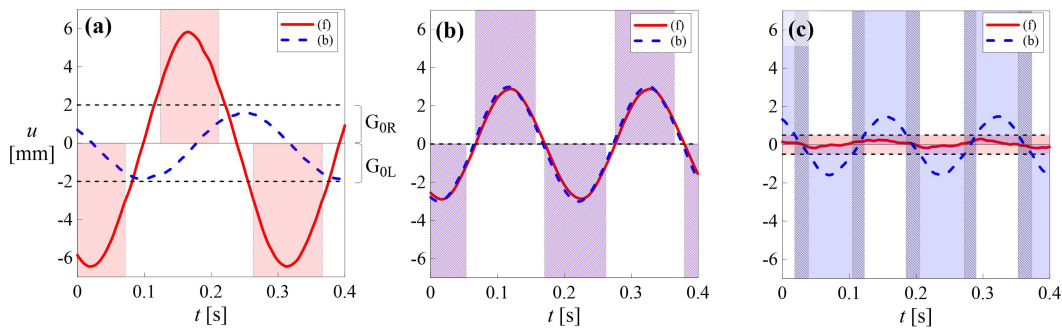
Figure 5.7. Time histories of the relative displacement u of the mass in steady-state condition: **a** G4, $f = 3.4$ Hz (*right hysteresis*); **b** G0, $f = 4.8$ Hz; **c** G-1, $f = 6$ Hz (*left hysteresis*). Red lines refer to the forward sweep, blue lines to the backward sweep. The horizontal dashed lines represent: **a-b** the initial gap; **c** the initial pre-strain of the bumpers. The contact phases with each bumper, identified from the time histories of the contact forces, are highlighted with vertical bands (red for the forward sweep, blue for the backward sweep).

meantime, has already recovered its deformation. Consequently, also in this case, in addition to the nonlinearities associated with the behaviors of the damper and the bumpers, there is still the nonlinear contribution related to the occurrence of impact. By looking at Fig. 5.6b, it is possible to observe the increment of the stiffness associated with the occurrence of impact, while the central part of the cycle refers to the flight condition.

For small negative gaps (third column, Figs. 5.6c,f), a *primary left hysteresys*, associated with a softening-like behavior, was observed (blue PRCs in Fig. 5.5). In correspondence with this hysteresis, two stable solutions can be found (Figs. 5.6c, 5.7c). In particular:

- forward sweep (solid red cycles): the oscillations amplitude is always lower than the absolute value of the negative gap (represented in Fig. 5.7c with horizontal dashed lines). Consequently, the mass, during its motion, is always in contact with both bumpers and the resisting force is given by the sum of the forces exerted by the damper and the two bumpers.

- backward sweep (dashed blue cycles): as long as the amplitude of the displacement u of the mass is lower than the absolute value of the negative gap, the mass is in contact with both bumpers (the corresponding time interval is highlighted in Fig. 5.7c with darker vertical bands), while when u exceeds this value, the mass detaches from one of the bumpers, remaining in contact with the other; this causes a reduction of the stiffness.

The initial pre-stress of the bumpers, resulting from the negative gap, causes an offset of the F_j-v_j ($j =$ R, L) cycles from the x-axis (Fig. 5.6f). From the same figure, it is possible to observe also the increment of the stiffness when the mass is in contact with both bumpers (red cycles). As for the *primary right hysteresis*, also in this case, it was not possible to obtain the third unstable solution.

It is worth noting that the large-amplitude cycles, observed for G4 (forward sweep, Fig. 5.6a) and G-1 (backward sweep, Fig. 5.6c), are both characterized by
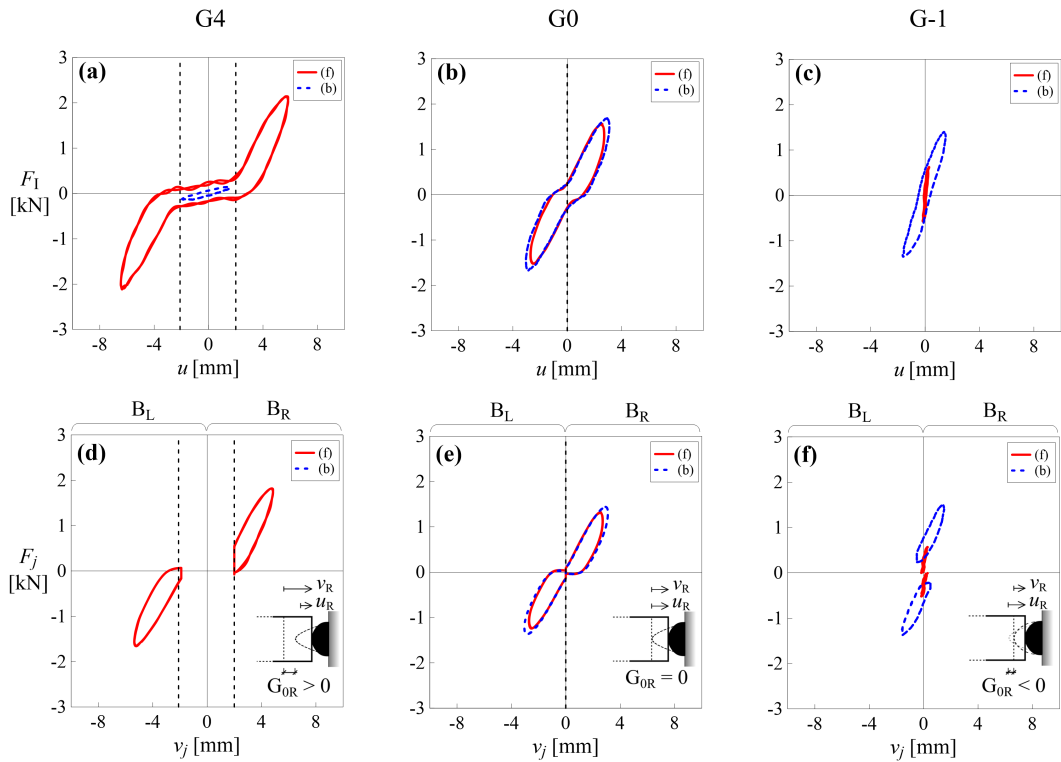
G-2 G-10
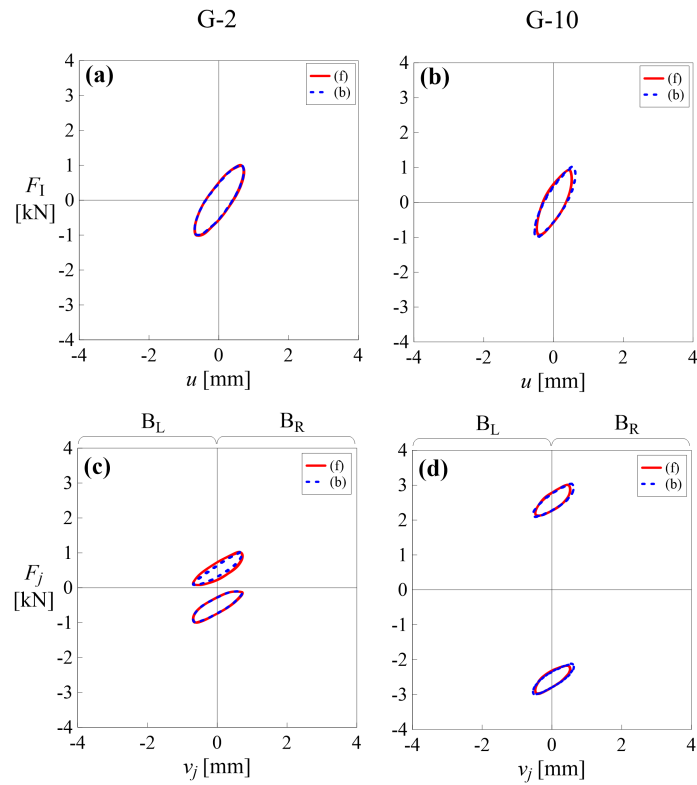
Figure 5.8. Force-displacement cycles in steady-state resonance condition corresponding to the forward (*solid red curve*) and the backward sweep (*dashed blue curve*) for: G-2, $f = 7.3$ Hz: **a** mass; **c** bumpers. G-10, $f = 7.6$ Hz: **b** mass; **d** bumpers.

nonlinearities associated with the unilateral constraint, as well as by the nonlinearities related to the behavior of the damper and the bumpers. The stiffness change is caused in the first case by the occurrence of impact between the mass and one of the two bumpers (*hardening*), and, in a dual manner, by the detachment with one of the bumpers in the second case (*softening*). In the other cases (small-amplitude cycles for G4 and G-1), the behavior of the system is still nonlinear, due to the behavior of the damper and the bumpers.

5.4.2 The effect of excessive negative gaps

From Fig. 5.5 it can also be observed that, for negative gap values greater than G-1 (G-2 and G-10), the PRCs (light green for G-2 and dark green for G-10) are no longer bent and show neither jumps nor hysteresis. For these values of the gap the mass, during its motion is always in contact with both bumpers. The PRCs of η_d (Fig. 5.5a) and η_a (Fig. 5.5b) are substantially superimposed, but they are not exactly the same, due to the nonlinear behavior of the damper and the bumpers. As concerns the bumpers, the PRCs of η_j ($j = $ R, L) (Fig. 5.5c) and r_j ($j = $ R, L) (Fig. 5.5d) have shifted with respect to each other. This shift is caused by the initial pre-stress/pre-strain state resulting from the negative gap, which has been highlighted in Figs. 5.5c,d with horizontal dashed lines and with gray shaded areas which have, as baseline, the frequency axis. Consequently, passing from G-2 to G-10, the PRCs of η_j and r_j ($j = $ R, L) move away from the frequency axis. It is worth noting that, once the initial shift value has been removed, the resulting PRCs are substantially overlapped. Also in this case, these curves are not exactly the same,

due to the nonlinear behavior of the damper and the bumpers. Based on these considerations, it follows that, when the negative gap exceeds a certain value which, for the considered system (mass, damper and bumpers), is between G-1 and G-2, since the mass never detaches from the two bumpers, the resisting force is given by the sum of the forces exerted by the damper and the two bumpers. In this case, further increases in the absolute value of the negative gap, will only increase the initial pre-stress and pre-strain state of the bumpers, without significantly affecting the mass response (Fig. 5.5). This can be seen also from Fig. 5.8, where the force-displacement cycles corresponding to G-2 (first column) and G-10 (second column), in steady-state resonance condition, are represented. As in Fig. 5.6, the top row refers to the mass (inertia force F_I vs. relative displacement u of the mass), and the bottom row to the bumpers (contact force F_j vs. position v_j of the bumper, $j = R$, L). It can be observed that, passing from G-2 to G-10, the F_I-u cycle (Figs. 5.8a,b) does not vary significantly. On the other hand, the consequent increase of the initial pre-stress state in the bumpers causes a gradually increasing distancing of the F_j-v_j ($j = R$, L) cycles (Figs. 5.8c,d).

5.4.3   Secondary resonances

Previous numerical investigations [251] highlighted the existence of gradually more complex response scenarios, as the gap decreases, with the occurrence of the different types of secondary resonances in the low frequency range, not observed in previous experimental laboratory campaigns. The new experimental results, obtained considering smaller gaps compared to the previous tests, confirmed the numerical predictions. In fact, for quite small gaps (G10 and G4) secondary resonances in the low frequency range were observed and the number of resonances was found to increase decreasing the gap. In order to experimentally describe these resonances in a sufficiently accurate manner, it was necessary to properly calibrate the input signal, as previously mentioned in Sect. 5.2.

In particular, as concerns the case G4 (Fig. 5.9), three sine sweep (SSi, $i = 1, 2, 3$) signals were imposed to capture the secondary resonances, compatibly with the shaking table performances, namely:

- SS1 (highlighted with a vertical green band in Fig. 5.9a): sweep frequency range between 0.5 Hz and 0.8 Hz, with frequency step $\Delta f = 0.03$ Hz and $n_c = 20$ cycles in each sub-frequency range;

- SS2 (highlighted with a vertical orange band in Fig. 5.9a): sweep frequency range between 0.8 Hz and 1.6 Hz, with frequency step $\Delta f = 0.05$ Hz and $n_c = 30$ cycles in each sub-frequency range;

- SS3 (highlighted with a vertical light blue band in Fig. 5.9a): sweep frequency range between 0.5 Hz and 5 Hz, with frequency step $\Delta f = 0.1$ Hz and $n_c = 10$ cycles in each sub-frequency range.

By combining the results of these three tests, the PRCs corresponding to the gap G4, shown in Figs. 5.5 and 5.9a, were obtained. Three secondary resonances were observed at frequencies $f_1 = 0.53$ Hz, $f_2 = 0.71$ Hz, $f_3 = 1.1$ Hz (vertical dashed black lines in Fig. 5.9a). In correspondence with these resonances, it can

be observed that forward and backward PRCs are substantially superimposed. The phase portraits, in steady state condition, corresponding to the three resonances, are represented in Figs. 5.9b-d. The inertia force F_I vs. relative displacement u of the mass cycles are instead shown in Figs. 5.9e-g and the contact force F_j vs. position v_j of the bumper cycles ($j = $ R, L) are represented in Figs. 5.9h-j. In the right part of Fig. 5.9, the time histories of the relative displacement u of the mass (Figs. 5.9k-m), the absolute acceleration a of the mass (Figs. 5.9n-p) and the contact forces F_j ($j = $ R, L) (Figs. 5.9q-s), are illustrated. The solid red lines refer to the forward sweep, whereas the dashed blue lines correspond to the backward sweep.
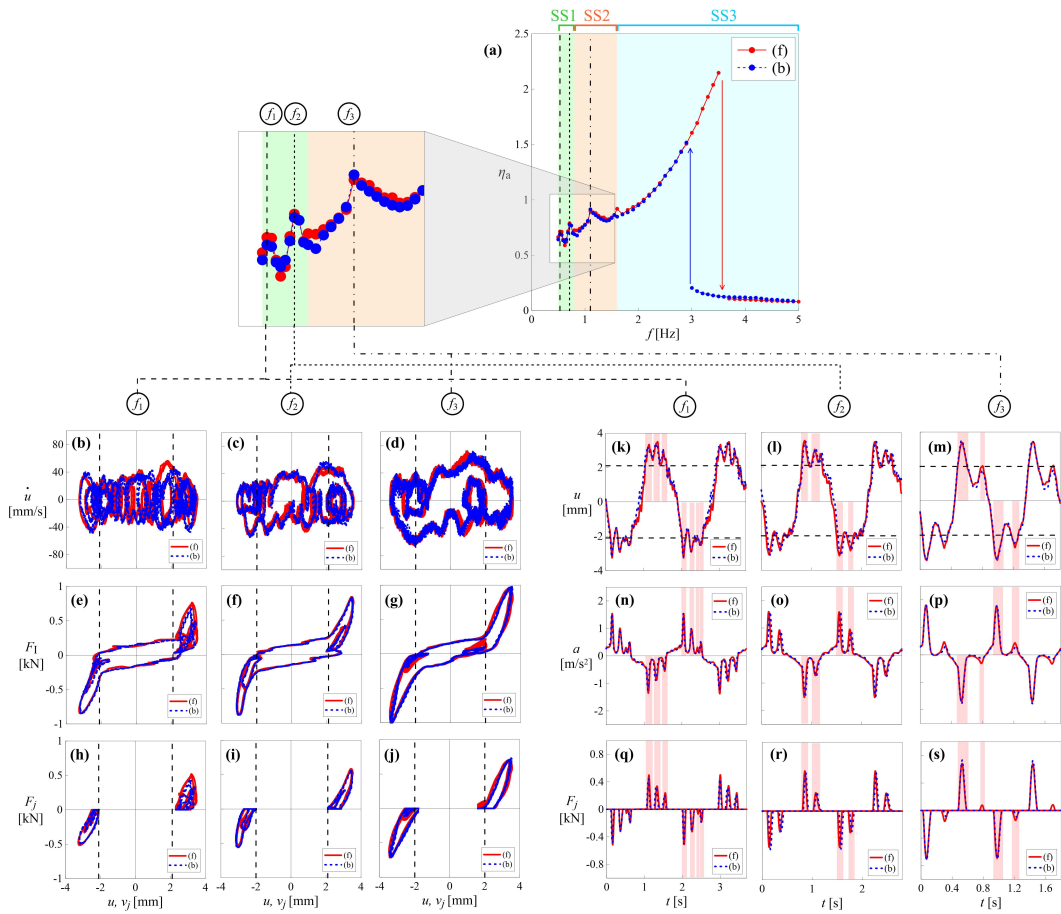
Figure 5.9. Secondary resonances in the low frequency range for G4: **a** PRC of η_a with indication of the different sweep frequency intervals (SSi, $i = 1, 2, 3$). The three vertical lines indicate the values of frequency corresponding to the observed secondary resonances ($f_1 = 0.53$ Hz, $f_2 = 0.71$ Hz, $f_3 = 1.1$ Hz). The other sub-figures represent, at these frequency values: **b-d** trajectories on the phase plane; **e-g** inertia force F_I vs. relative displacement u of the mass cycles; **h-j** contact force F_j vs. position v_j of the bumper cycles ($j = $ R, L); **k-m** time history of the relative displacement u of the mass; **n-p** time history of the absolute acceleration a of the mass; **q-s**: time history of the contact forces F_j ($j = $ R, L). In **b-m** the dashed black lines represent the initial gap. In **h-p** the vertical red bands represent the time intervals corresponding the contact phases with each bumper in one forcing cycle.

The occurrence of internal loops in both the force-displacement cycles, rarely

shown in literature, and the phase portraits, was observed in all three investigated cases. The existence of internal loops for small gap values was already predicted by the numerical model [251] and now confirmed experimentally. It can be observed that, for f_3 (Figs. 5.9d,g) these internal loops barely intersect the vertical dashed lines representing the position of the obstacles. Decreasing the frequency, that is passing from f_3 (Figs. 5.9d,g) to f_1 (Figs. 5.9b,e), these loops move outwards, intersecting the vertical lines in a more evident manner; furthermore, the number of internal loops increases. This is reflected in a number of impacts per forcing cycle, between the mass and each bumper, which increases decreasing the frequency, as shown in Figs. 5.9k-s. In these figures, referring to one forcing cycle, the impacts are highlighted with vertical red bands. It can be observed that for f_3 (Figs. 5.9m,p,s), the mass impact each bumper twice, with both the intensity and duration of the second impact lower than the first one. Passing to f_2 (Figs. 5.9l,o,r), the mass continues to impact each bumper twice, but the second impact is more evident. Actually, also a third slight impact was sometimes observed. Finally, in correspondence to f_1 (Figs. 5.9k,n,q), the mass impacts, in an evident way, each bumper three times, with the intensity of the impact decreasing passing from the first one to the third one. Also in this case, sometimes four impacts were observed. This trend of the number of impacts with decreasing frequency confirms the numerical predictions [251].

5.5 Numerical modeling

The numerical model of the vibro-impact system shown in Fig. 5.1 is illustrated in Fig. 5.10. In this model the behaviors of both the damper (D) and the bumpers (B_j, $j = $ R, L) were linearized. In particular, in both cases, the resisting forces were modeled by a linear spring, with stiffness K and K_j ($j = $ R, L) respectively, in parallel with a linear viscous damper, with damping coefficient C and C_j ($j = $ R, L) respectively. Despite this linearization, the model is still nonlinear, due to the other sources of nonlinearity taken into account, namely the presence of the gap, the unilateral constrains and the occurrence of impact that causes abrupt changes of both stiffness and damping. For this reason, this model was called Simplified Nonlinear Model (SNM) [251]. The authors, aware of the limitations of the linear viscoelastic model, particularly when used to model the contact, consider it satisfactory for their purposes.

During its motion, the mass M can be or not in contact with the bumpers. The two conditions will be referred to as *contact* and *flight* phases respectively. The equations that govern the motion of the system are written as:

$$\begin{cases} M\ddot{u}(t) + C\dot{u}(t) + Ku(t) + F_j(t) \cdot \psi_1\left[G_j(t)\right] \cdot \psi_2\left[F_j(t)\right] = -MA_\text{t}(t) \\ F_i(t) = 0 \end{cases} \tag{5.2}$$

where it is assumed that whether $j = $ L then $i = $ R, or whether $j = $ R then $i = $ L. In Eq. 5.2, $u(t)$ and $u_j(t)$ ($j = $ R, L) represent the relative displacements of the mass and of the bumpers respectively with respect to the ground and the dot ($\cdot$) denotes differentiation with respect to the time t. As previously said, the position of the extremity of the bumper v_j ($j = $ R, L), measured from the side of the mass at time $t = 0$ s (Fig. 5.10), is related to u_j through the expression $v_j = u_j + G_{0j}$, where
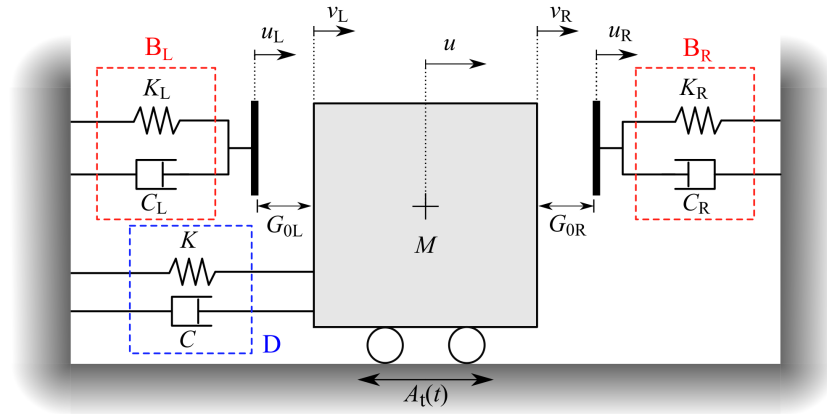
Figure 5.10. Numerical model of the vibro-impact system.

G_{0j} $(j = \mathrm{R}, \mathrm{L})$ is the j-th initial gap, that is the initial distance between the mass and the j-th bumper. $A_\mathrm{t}(t) = A_\mathrm{G} \sin \Omega t$ is the base acceleration, with amplitude A_G and circular frequency Ω. The total (or absolute) acceleration of the mass is therefore given by $a(t) = \ddot{u}(t) + A_\mathrm{t}(t)$. $G_j(t)$ $(j = \mathrm{R}, \mathrm{L})$ is the clearance function which represents the distance, instant by instant, between the mass and the j-th bumper:

$$G_j(t) = G_{0j} + \Delta u_j(t) \quad (j = \mathrm{R}, \mathrm{L}) \tag{5.3}$$

where:

$$\Delta u_\mathrm{R}(t) = u_\mathrm{R}(t) - u(t); \quad \Delta u_\mathrm{L}(t) = u(t) - u_\mathrm{L}(t) \tag{5.4}$$

When the mass is in contact with the j-th bumper $G_j(t) = 0$, otherwise $G_j(t) > 0$. In Eq. 5.2, ψ_1 and ψ_2 represent the Heaviside functions, defined as follows:

$$\text{Contact} \quad \psi_1\left[G_j(t)\right] = \begin{cases} 0, & G_j(t) > 0 \\ 1, & G_j(t) = 0 \end{cases} \tag{5.5a}$$

$$\text{Separation} \quad \psi_2\left[F_j(t)\right] = \begin{cases} 0, & F_j(t) \leq 0 \ (j = \mathrm{R}) \text{ or } F_j(t) \geq 0 \ (j = \mathrm{L}) \\ 1, & F_j(t) > 0 \ (j = \mathrm{R}) \text{ or } F_j(t) < 0 \ (j = \mathrm{L}) \end{cases} \tag{5.5b}$$

where $F_j(t) = C_j \dot{u}_j(t) + K_j u_j(t)$ $(j = \mathrm{R}, \mathrm{L})$ is the contact force occurring during the contact period with the j-th bumper.

The parameters of the model were identified based on the experimental results. In order to make a comparison with the results obtained with the SNM, it was necessary to reduce the nonlinear restoring force exerted by the damper to a linear elastic one. This was made considering an equivalent stiffness K, estimated in free flight resonance condition for a peak table acceleration $A = 0.05$ g. The identified parameters of the model are: $K = 36$ kN/m, $C = 1.1$ kN s/m, for what concerns the damper, and $K_j = 510$ kN/m, $C_j = 0.9$ kN s/m, for what concerns the bumper B2 $(j = \mathrm{R}, \mathrm{L})$.

Considering the gap amplitude G4, some comparisons of the experimental results with the numerical simulations are shown in Fig. 5.11. In the upper part of the figure, the comparison is made in terms of PRCs of both η_a (Fig. 5.11a) and η_d
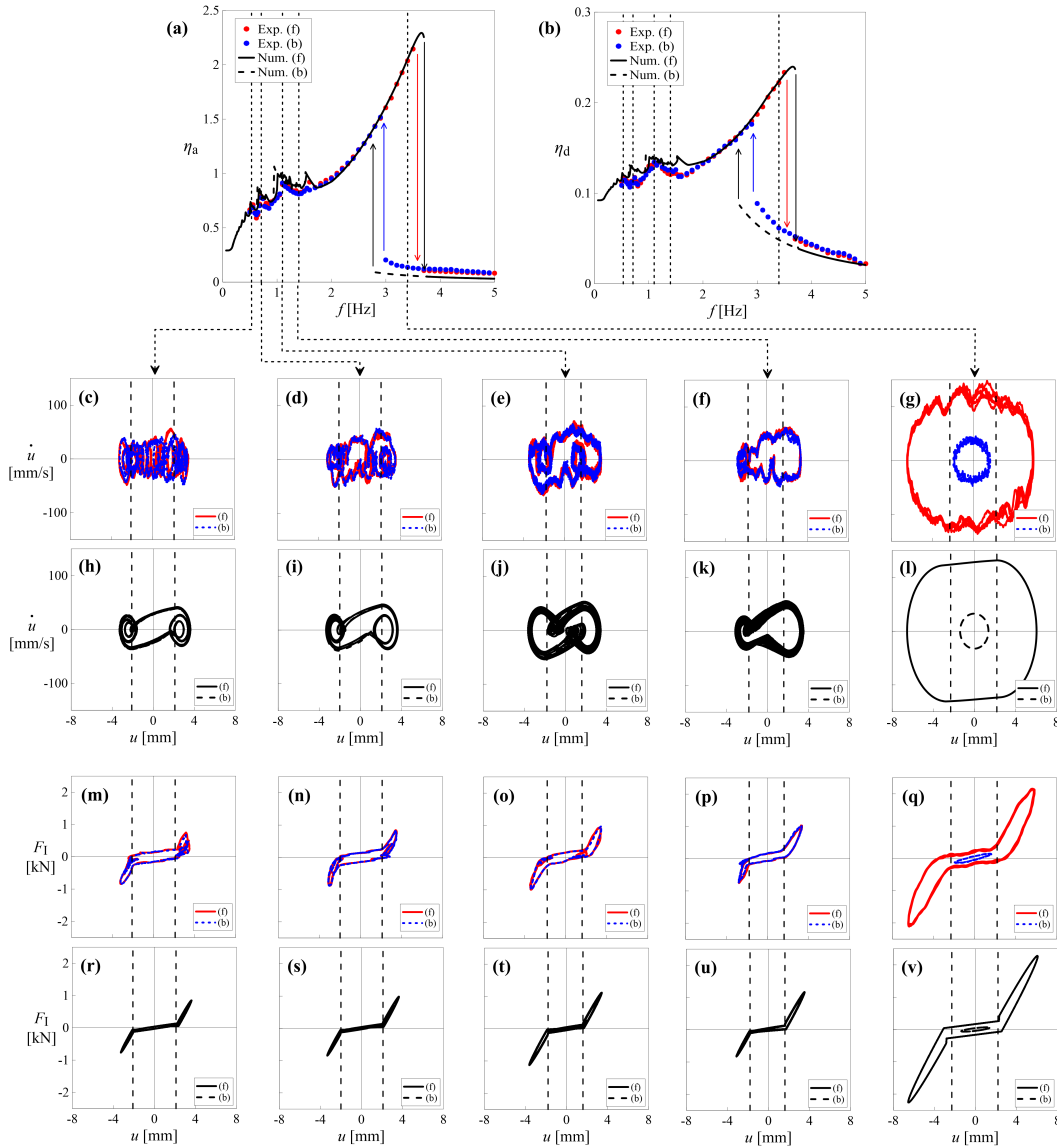
Figure 5.11. PRCs of **a** η_a and **b** η_a obtained experimentally (red and blue dots) and with the numerical model (solid and dashed black lines) for G4. The figures in the lower part show, for five values of frequency, namely $f = 0.53$ Hz, 0.71 Hz, 1.1 Hz, 1.4 Hz and 3.4 Hz, the comparison between experimental (red and blue lines) and numerical results (black lines) in terms of: trajectories on the phase plane (**c-l**); inertia force F_I vs. relative displacement u cycles (**m-v**). In **c-v** the vertical dashed black lines represent the initial gap.

(Fig. 5.11b). The experimental results are represented with red (forward sweep) and blue (backward sweep) dots, while the numerical results are represented with solid (forward sweep) and dashed (backward sweep) black lines. The vertical dashed lines indicates some values of frequency, namely 0.53 Hz, 0.71 Hz, 1.1 Hz, 1.4 Hz and 3.4 Hz, for which the comparison is made, in the lower part of Fig. 5.11, also in terms of phase portraits and hysteresis loops. In particular, each column of sub-figures corresponds to a frequency value. In these sub-figures, the experimental results are represented with solid red (forward sweep) and dashed blue (backward sweep) lines, while the numerical results are represented with solid (forward sweep) and dashed (backward sweep) black lines. The initial gap is represented with vertical dashed lines. As concerns the PRCs (Figs. 5.11a,b), it can be observed that there is a good agreement between experimental and numerical results, although the model does not take into account nonlinearities associated with the behaviors of the damper and the bumpers. The model is able to reproduce satisfactorily the position and amplitude of both the primary resonance and some of the secondary resonances in the low frequency range. Some differences are noted in the branches of the PRCs associated with the absence of impact (after the downward jump in the forward sweep and before the upward jump in the backward sweep) and in the frequency of the upward jump. This is due to the difference between the experimental (nonlinear) and numerical (linear) PRCs in free flight condition; in particular, the numerical curve is below the experimental one. A good agreement is observed also in the trajectories on the phase plane (Figs. 5.11c-l) and in the force-displacement cycles (Figs. 5.11m-v). The presence of internal loops, whose number increases as the frequency decreases, is confirmed also by the model.

The numerical model highlighted the existence of several secondary resonances, of different type (with left hysteresis and of non-regular type), in the low frequency range (Figs. 5.11a,b). The calibration of the characteristics of the sine sweep signal, bound by the limitations of the shaking table, has made it possible to observe also experimentally some secondary resonances (Sect. 5.4.3), but not the left hysteresis, due to the limitations of the shaking table, which didn't allowed to further reduce the frequency step of the sine sweep signal. Thanks to the model it is possible to better describe what was observed with the experimentation. From Figs. 5.11h-j it can be observed that, at the secondary resonances observed experimentally, the numerical response is slightly quasi-periodic, with the extent of the quasi-periodicity increasing with the frequency. Furthermore, the number of internal loops on the left is greater than that of the internal loops on the right. While the larger loops cross the vertical lines representing the obstacles in an evident way, the innermost loops on the left as time goes by, approach, cross and then move away from the left bumper, resulting in a different number of impacts. This behavior was observed also experimentally. The situation returns to be quite symmetric, although with a greater quasi-periodicity, for $f = 1.1$ Hz (third column, Figs. 5.11e,j,o,t). As previously said, the numerical model highlighted also the existence of irregularities between 1 Hz and 1.5 Hz (Figs. 5.11a,b). In this frequency range, an evident asymmetric response was observed experimentally, for example for $f = 1.4$ Hz (fourth column, Figs. 5.11f,k,p,u), and also confirmed by the numerical model. In both the phase portraits (Fig. 5.11f) and the hysteresis loop (Fig. 5.11p) a single internal loop, intersecting the left vertical dashed line (left bumper) was noticed. This results in a

different number of impacts between the mass and the bumpers. In particular, in each forcing cycle, the mass impacts the left bumper twice and the right bumper once.

The asymmetric behavior of the system in this frequency range can be seen also from Fig. 5.12b, in which the time histories of the relative displacement u of the mass, the absolute acceleration a of the mass and the contact forces F_j ($j = R, L$) obtained experimentally (red and blue lines) and with the numerical model (black lines) are compared. In Fig. 5.12a an analogous comparisons is made for $f = 0.53$ Hz, that is in correspondence with the smallest secondary resonance observed experimentally, where the highest number of impact was observed. Finally, in Figs. 5.11g,l,q,v and 5.12c the comparison is made for a value of frequency, $f = 3.4$ Hz, that is in the frequency range between the two jumps (primary right hysteresis). Based on these considerations, the SNM, despite its relative simplicity, has proven to be able to simulate and reproduce satisfactorily the behavior of the system.
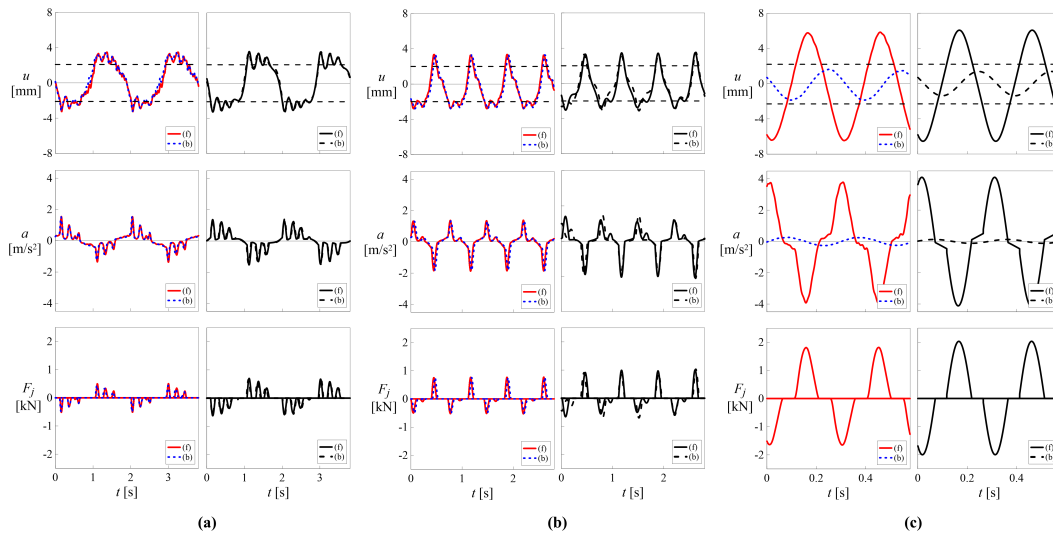
Figure 5.12. Time histories of the relative displacement u of the mass, the absolute acceleration a of the mass and the contact forces F_j ($j = R, L$) obtained experimentally (red and blue lines) and with the numerical model (black lines) for G4 and: **a** $f = 0.53$ Hz, **b** $f = 1.4$ Hz and **c** $f = 3.4$ Hz. The horizontal dashed black lines in the time histories of the relative displacement represent the initial gap.

5.6   Closing remarks

Some of the results of an experimental laboratory campaign, designed based on the results of previous studies, were presented. Compared to previous tests, also small positive, null and negative values of the total gap G between mass and bumpers were investigated. Furthermore, impact load cells were used to directly measure the contact forces between mass and bumpers during the impact phases.

The amplitude of the gap was found to influence the response of both the mass and the bumpers for G > 0, where the occurrence of impact causes a hardening-like behavior, characterized by the presence of jumps and a *primary right hysteresis*

in the PRCs. Referring to the primary resonance condition, the reduction of the gap, causes the reduction of the relative displacement of the mass and an increase, followed by a decrease, of the absolute acceleration. A trend similar to the latter one was observed also in the deformation of the bumpers and in the impact force, which attain zero values in the absence of impact.

By putting the bumpers initially, more or less, in contact with the mass (G $\simeq$ 0) the situation returns to be smooth, without jumps and hysteresis, although the behavior is still nonlinear, due not only to the nonlinear behaviors of the damper and the bumpers but also to the nonlinearity associated with the occurrence of impact, consequent to the existence, also in this case, of a short time interval in which the mass is in contact with either bumper.

For small negative gaps (G-1), obtained experimentally by slightly compressing the bumpers against the mass, both the relative displacement and the absolute acceleration of the mass, the bumpers' deformation and the contact force, in resonance condition, continue to decrease. Compared to G $>$ 0, a softening-like behavior was observed, characterized by the occurrence of jumps and a *primary left hysteresis*. Furthermore, due to the initial pre-stress/pre-strain state resulting from the negative gap, the PRCs of both the bumpers' deformation and the contact forces are always different from zero for each frequency value. The transition from the hardening-like to the softening-like behavior occurs moving from small positive to negative values of the gap, passing through the approximately zero-gap configuration, not easy to realize experimentally. Compared to the case of small positive gaps (hardening) for which the increase in stiffness is caused by the occurrence of impact between the mass and one of the two bumpers, for small negative gaps (softening) the stiffness reduction is due, in a dual manner, to the detachment with one of the bumpers.

For negative gaps exceeding a certain value which, for bumper B2, is between G-1 and G-2, the mass, during its motion, always remains in contact with both bumpers and therefore, the resisting force is given by the sum of the forces exerted by the damper and the two bumpers. Consequently, the PRCs are no longer bent and show neither jumps nor hysteresis. In this case, further increases in the absolute value of the negative gap, will only increase the initial pre-stress and pre-strain state of the bumpers, without affecting the mass response.

Previous numerical investigations highlighted the existence of secondary resonances, of different type (with left hysteresis and of non-regular type), in the low frequency range and for quite small gaps. Some of these resonances were observed also experimentally and the number of secondary resonances was found to increase decreasing G. To experimentally capture, in a sufficiently accurate manner, these resonances, not observed in previous experimental laboratory campaigns, it was necessary to properly calibrate the input signal, compatibly with the shaking table performances. In correspondence with the observed resonances, the occurrence of internal loops, intersecting the obstacles, in both the force-displacement cycles, rarely shown in literature, and the phase portraits, was observed. Decreasing the frequency, the number of internal loops increases, and consequently also the number of impacts per forcing cycle between the mass and the bumpers.

The experimental results were reproduced, in a sufficiently accurate manner, by a suitable numerical model, in which the behavior of both the damper and the bumpers was linearized, retaining the other sources of nonlinearities, namely the presence of

the gap, the unilateral constrains and the occurrence of impact that causes abrupt changes of both stiffness and damping. The identification of the parameters of the model was made based on the experimental data. A good agreement was observed in terms of PRCs, trajectories on the phase plane, force-displacement cycles and time histories.

With regard to the future developments of this work, there is the intention to finish processing the recorded data and to extend the experimental laboratory campaign also considering the earthquake excitation.

Chapter 6

Optimal design of the bumpers based on the response scenarios

Chapter outline In this chapter, the effect of the presence of (existing or newly added) deformable and dissipative obstacles (bumpers) on the nonlinear dynamic response of the SDOF system, is investigated via parametric numerical analyses. Through the study of possible response scenarios, which can occur by varying the bumpers' parameters (i.e., the position, the stiffness, and the damping, respectively), it is observed that the presence of the bumpers is not always unfavorable compared to the free flight condition. By properly selecting the bumpers' parameters it is possible to guide the system's response in order to achieve specific objectives, exploiting the occurrence of impacts with beneficial effects. Furthermore, a relationship between the stiffness and the damping parameters of the bumpers, which allows to minimize the maximum value of the mass acceleration in primary resonance condition, is identified and discussed.

6.1   Introduction

Seismic isolation represents one of the most applied, reliable and effective, passive control strategies to mitigate the dynamic response of both new and existing structures [35, 109, 118, 121, 135], bridges [36, 62, 120, 143, 167, 193, 212, 287], strategic facilities [38, 284], nonstructural components and equipment [5, 44, 73, 80, 92, 116, 168, 228, 229, 255], works of art [37, 49, 245].

Seismically isolated structures, due to the greater flexibility offered by the isolators at the base, are expected to experience large horizontal displacements relative to the ground, especially under near-fault (NF) earthquakes, characterized by long-period pulses [63, 118, 121]. These large displacements, on the one hand, can seriously damage the isolation system by exceeding its limit deformation, on the other, can lead to pounding with surrounding moat walls or adjacent structures if the available seismic gap size is not sufficient. Potential pounding can produce detrimental effects on the effectiveness of seismic isolation and can lead to consequences which range from local slight nonstructural to serious structural damage or even collapse [6, 140, 190, 211, 222]. In particular, the existence of high spikes in the acceleration

response, in correspondence of the floors where pounding occurs, and whose amplitude is influenced by impact rigidity, may affect floor response spectra and thus the response of vulnerable equipment housed in the buildings [52, 224].

In order to prevent the damage of the isolation system and avoid the occurrence of pounding against adjacent structures, the horizontal displacements can be limited by inserting suitable obstacles, which can be placed at a certain distance (gap) from the structure to be protected (*outer pounding*, [14]) or can be incorporated into the isolation system (*inner pounding*, [14]). In this latter case, the built-in buffer (self-braking) mechanism prevents pounding of the isolated structure with the surrounding structures and limits the possible pounding (if any) to be only within the own body of the isolator [18, 75, 96–98, 114, 115, 117, 118, 309].

The occurrence of impact against the obstacles modifies the response of the isolated system, turning it into a nonlinear vibro-impact system. Vibro-impact systems, even the simplest, exhibit complex nonlinear nonsmooth dynamics and a wide variety of phenomena, characterized by different types of resonances, instabilities, bifurcations, periodic and quasi-periodic trajectories and chaotic regimes, that need to be carefully investigated [12, 47, 50, 86, 176, 183, 217, 238, 251, 286, 299].

Some of these behaviors are undesirable as they can cause adverse effects [171]. The study of the behavior of vibro-impact systems, therefore, allowing to highlight possible issues associated with the occurrence of impact, is necessary to identify suitable strategies to mitigate and control the response of such systems. Several authors proposed different strategies for the control of unstable orbits, bifurcation, co-existing orbits and chaos on the basis of the study of practical problem involving collisions [33, 54, 55, 59, 85, 91, 148, 150, 160, 166, 171, 264, 265, 275]. By properly selecting the parameters which characterize the vibro-impact problem, it is possible to guide the behavior of the system, in order to avoid certain scenarios and encourage others, and thus exploit the occurrence of impact with beneficial effects.

Considering two periodically forced oscillators that can interact via soft impacts, Brzeski et al. [34] showed that with properly selection of the systems' parameters, such as the gap between the systems or/and the phase shift of external excitation, it is possible to decrease the number of coexisting solutions via discontinuous coupling. Gritli and Belghith [86] proposed a state-feedback control law in order to control chaos exhibited by a SDOF impact mechanical oscillator with a single rigid obstacle. The results of the analysis carried out by Sun et al. [254] showed that by properly designing the dynamic parameters of viscoelastic end-stops, the nonlinear vibration of a SDOF nonlinear suspension system at primary resonance can be effectively suppressed and the jump phenomena can be eliminated for both hardening and softening primary isolators. Furthermore, the end-stop can effectively attenuate also the absolute acceleration response for a hardening primary isolator, while more damping is needed to attenuate that for a softening primary isolator. Suitable choices of pairs of bumpers and gaps, that allows to reach a trade-off between two conflicting objectives, namely, control of excessive displacements and control of excessive accelerations in a base-isolated SDOF with two-sided deformable constraints, were suggested in [14]. A two-sided damping constraint control strategy was proposed by Hao et al. [95] to improve the performance of the quasi-zero stiffness (QZS) isolator [94]. The proposed control approach can largely lower the isolation frequency while enhancing the effectiveness of isolation in high frequencies and

preventing the severity of end-stop impacts. Based on the analysis of two-parameter bifurcations and basins of attraction, the authors found that the key issue to realize such control objective, is the suppression of period-3 solutions that coexist with the desired period-1 orbits.

The aim of this study is to investigate, through numerical parametric analyses, the effect of the introduction of two deformable and dissipative obstacles on the response of a Single-Degree-Of-Freedom (SDOF) system under harmonic base excitation, compared to the free flight condition (that is without obstacles). The attention is focused both on the resonance condition and on the frequency range of isolation. Through the study of the response scenarios which can occur varying the parameters which characterize the obstacles, that is the position and the mechanical (stiffness and damping) properties, the possibility to exploit the occurrence of impact to reduce both the peak value of the displacement and of the acceleration of the mass, compared to the free flight condition, without possibly reducing the vibration isolation frequency range, is investigated.

The chapter is organized as follows. In Sect. 6.2 the numerical model and the governing equations are presented; in Sect. 6.3 preliminary considerations on control are made; the results of the numerical simulations are shown and discussed in Sect. 6.4; finally, the main conclusions and further development of this study are drawn in Sect. 6.5.

6.2 Model and equations of motion

The study was carried out considering a Single-Degree-Of-Freedom (SDOF) system, composed of a mass M (highlighted in green) and an isolation damper (D, highlighted in blue), with two-sided deformable and dissipative bumpers (highlighted in red), denoted as right bumper (B_R) and left bumper (B_L) respectively, symmetrically positioned on both sides of the mass, at an initial distance (initial gap) G_{0j} ($j = R, L$), as shown in Fig. 6.1.
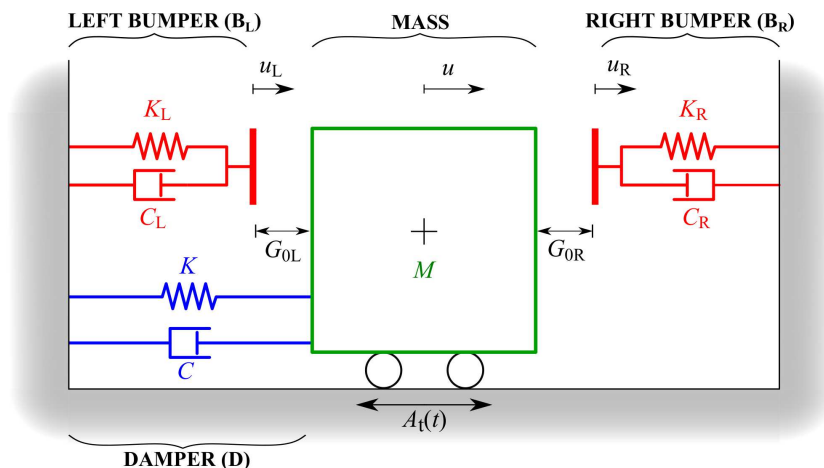
Figure 6.1. Model of the SDOF system with two-sided bumpers.

The damper (D) is modeled by a linear elastic element, with stiffness K, and a linear viscous dashpot, with damping coefficient C, arranged in parallel. The

two bumpers are massless and, as the damper, are modeled by a linear elastic element, with stiffness K_j ($j =$ R, L), and a linear viscous dashpot, with damping coefficient C_j ($j =$ R, L), arranged in parallel. The system is subjected to a harmonic base acceleration $A_t(t) = A_G \sin \Omega t$, characterized by amplitude A_G and circular frequency Ω. The relative displacements of the damper and the bumpers with respect to the ground are denoted as u and u_j ($j =$ R, L) respectively.

To attempt a more general description of the problem, the equations of motion are written in dimensionless form by introducing the following characteristic quantities: the natural circular frequency of the SDOF system $\omega = \sqrt{K/M}$, the maximum relative displacement $u^* = u_{st} R_{d,max}$ and the maximum force $F^* = M\omega^2 u^*$ in the SDOF system in free flight (that is without obstacles) resonance condition. $R_{d,max}(\xi) = 1/(2\xi\sqrt{1-\xi^2})$ is the maximum value of the dynamic amplification factor $R_d(\xi, \beta)$, defined as the ratio between the amplitude of the dynamic displacement to the static displacement $u_{st} = MA_G/K$.

The following dimensionless quantities were subsequently defined: the dimensionless time $\tau = \omega t$, the dimensionless relative displacements of the mass $q = u/u^*$ and of the bumpers $q_j = u_j/u^*$ ($j =$ R, L), the damping ratio of the SDOF system $\xi = C/(2M\omega)$, the dimensionless amplitude of the base excitation $a_G = 2\xi\sqrt{1-\xi^2}$, the frequency ratio $\beta = \Omega/\omega$ and the dimensionless gap $\delta_{0j} = G_{0j}/u^*$ ($j =$ R, L). Based on the adopted normalization, $\delta_{0j} = 0$ if the j-th bumper is initially in contact with the mass; for $0 < \delta_{0j} < 1$ the mass beats and deforms the j-th bumper; whereas the mass will be in free flight condition for $\delta_{0j} \geq 1$. Finally, the generic dimensionless force was denoted as $f = F/F^*$.

By virtue of the above mentioned dimensionless quantities, the equations of motion of the system can be written in the following dimensionless form:

$$\begin{cases} q''(\tau) + 2\xi q'(\tau) + q(\tau) + f_j(\tau) \cdot \psi_1\left[\delta_j(\tau)\right] \cdot \psi_2\left[f_j(\tau)\right] = -a_G \sin \beta\tau \\ f_i(\tau) = 0 \end{cases} \tag{6.1}$$

where it is assumed that whether $j =$ L then $i =$ R, or whether $j =$ R then $i =$ L and the apex ($'$) denotes differentiation with respect to the dimensionless time τ. In Eqs. 6.1, the Heaviside functions ψ_k ($k = 1, 2$) are defined as follows:

$$\text{Contact} \quad \psi_1\left[\delta_j(\tau)\right] = \begin{cases} 0, & \delta_j(\tau) > 0 \\ 1, & \delta_j(\tau) = 0 \end{cases} \tag{6.2a}$$

$$\text{Separation} \quad \psi_2\left[f_j(\tau)\right] = \begin{cases} 0, & f_j(\tau) \leq 0 \ (j = \text{R}) \text{ or } f_j(\tau) \geq 0 \ (\text{j} = \text{L}) \\ 1, & f_j(\tau) > 0 \ (j = \text{R}) \text{ or } f_j(\tau) < 0 \ (j = \text{L}) \end{cases} \tag{6.2b}$$

where $f_j(\tau) = 2\xi\gamma_j q'_j(\tau) + \lambda_j q_j(\tau)$ ($j =$ R, L) is the normalized contact force occurring during the contact period with the j-th bumper, $\gamma_j = C_j/C$ ($j =$ R, L) is the ratio between the viscous damping coefficient of the j-th bumper and that of the damper and $\lambda_j = K_j/K$ ($j =$ R, L) is the ratio between the stiffness of the j-th bumper and that of the damper. $\delta_j(\tau) = \delta_{0j} + \Delta q_j(\tau)$ ($j =$ R, L), where $\Delta q_R(\tau) = q_R(\tau) - q(\tau)$ and $\Delta q_L(\tau) = q(\tau) - q_L(\tau)$, is the clearance function which

represents the distance, at each time instant, between the mass and the j-th bumper. When the mass is in contact with the j-th bumper $\delta_j(\tau) = 0$, otherwise $\delta_j(\tau) > 0$.

Despite the relative simplicity of the model, in which both the bumpers and the damper have been modeled with a Kelvin-Voigt model, the system is however strongly nonlinear, due to the presence of clearance, the unilateral constrains and the occurrence of impact that causes abrupt changes of stiffness and damping at the contact time.

In this study two equal bumpers symmetrically arranged on the two sides of the mass were considered. Consequently, $\lambda_R = \lambda_L = \lambda$, $\gamma_R = \gamma_L = \gamma$ and $\delta_{0R} = \delta_{0L} = \delta_0$.

The equations of motion (Eqs. 6.1) were numerically solved using the central difference method [22], implemented with a numerical code written in Matlab. As concerns the identification of the time period in which impact occurs, this was done as follows. The beginning of the contact phase between the mass and the j-th bumper was identified based on the value of the clearance function $\delta_j(\tau)$ ($j = R, L$), as illustrated in Eq. 6.2a. In particular, impact occurs when $\delta_j(\tau) = 0$. Regarding instead the evaluation of the time instant of detachment, this was made based on the value of the contact force $f_j(\tau)$ ($j = R, L$), as illustrated in Eq. 6.2b. This choice was motivated by the necessity to overcome one of the drawbacks of the Kelvin-Voigt model, when used to model the contact, that is the existence of attracting forces after the restitution phase [77, 78, 186, 241]. Since this does not make sense from a physical point of view, in this study the change of sign of the contact force was assumed as indicator of the end of the contact phase.

6.3 Preliminary considerations

Base-isolated systems, due to the flexibility introduced by the isolation system, can undergo large horizontal displacements, when subjected to exceptional loads like strong earthquakes. These displacements, concentrated in the isolation system, can excessively deform, or even damage, the isolation system itself, or can lead to pounding with the surrounding moat walls or existing adjacent structures or obstacles, if the available seismic gap is not sufficient. The horizontal displacements can be limited by introducing obstacles, with suitable mechanical properties (stiffness and damping) and positioned at a certain distance (gap) from the structure. Due to the occurrence of impact between the system and the obstacles, the introduction of the obstacles modifies the response of the system, in terms of both displacements and accelerations.

Without obstacles

In the absence of obstacles (free flight condition), the response of a viscously damped SDOF system excited by a harmonic base acceleration is influenced by the forcing frequency and the damping, as shown in Fig. 6.2, where the transmissibility $TR_a(\xi, \beta)$ (Fig. 6.2a) and the displacement response factor $R_d(\xi, \beta)$ (Fig. 6.2b) respectively, are represented as a function of the frequency ratio β and for several values of the damping ratio ξ. The transmissibility $TR_a(\xi, \beta)$, defined as the ratio between

the amplitude of the absolute acceleration a_0 transmitted to the mass M and the amplitude of the ground acceleration A_{G}, provides a measure of the rate of the ground acceleration transmitted to the system. The displacement response factor $R_{\mathrm{d}}(\xi, \beta)$, instead, is defined as the ratio between the amplitude of the relative displacement u_0 of the mass M and the amplitude of the static displacement $u_{\mathrm{st},0}$. The analytical expressions of both the transmissibility $\mathrm{TR}_{\mathrm{a}}(\xi, \beta)$ and the displacement response factor $R_{\mathrm{d}}(\xi, \beta)$ are given in Table 6.1.

From Fig. 6.2 it is possible to observe the effect of both the frequency ratio β and the damping ratio ξ on $\mathrm{TR}_{\mathrm{a}}(\xi, \beta)$ and $R_{\mathrm{d}}(\xi, \beta)$.
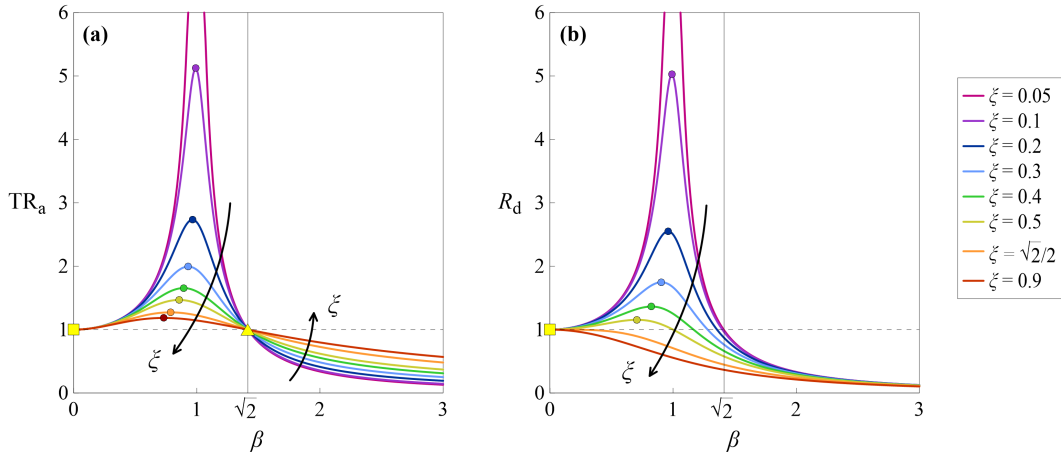
Figure 6.2. **a** Transmissibility TR_{a} and **b** displacement response factor R_{d} for several values of the damping ratio ξ.

Effect of β   As concerns the effect of β, it can be observed that for $\beta = 0$, both $\mathrm{TR}_{\mathrm{a}}(\xi, 0) = 1$ and $R_{\mathrm{d}}(\xi, 0) = 1$ regardless of ξ (yellow square), meaning that, in the case of slowly varying excitation, the maximum absolute acceleration transmitted to the mass is equal to the amplitude of the ground acceleration (and thus the mass moves rigidly with the ground), and the amplitude of the dynamic displacement is equal to the static displacement. Increasing β, also the response of the system increases, until a maximum is reached (resonance), highlighted in Fig. 6.2 with a colored dot, and denoted as $\mathrm{TR}_{\mathrm{a,max}}(\xi)$ and $R_{\mathrm{d,max}}(\xi)$ respectively (Table 6.1). By further increasing the frequency ratio β, beyond the resonant frequency (denoted as $\beta_{\mathrm{Ra}}(\xi)$ and $\beta_{\mathrm{Rd}}(\xi)$ respectively, Table 6.1), the response starts to decrease and tends to zero as $\beta \rightarrow \infty$, meaning that, for rapidly varying excitation, the mass remains still as the ground moves. By looking at Fig. 6.2a it can be noted that the condition $\mathrm{TR}_{\mathrm{a}} = 1$ is attained again, regardless of the value of ξ, for $\beta = \sqrt{2}$ (fixed point for all the curves, highlighted with a yellow triangle). Consequently, referring to the transmissibility, this frequency value ($\beta = \sqrt{2}$) divides the frequency interval in two parts:

- for $\beta < \sqrt{2}$ the amplitude of the absolute acceleration transmitted to the mass is greater than the amplitude of ground acceleration ($\mathrm{TR}_{\mathrm{a}} > 1$).

- for $\beta > \sqrt{2}$ the amplitude of the absolute acceleration transmitted to the mass is lower than the amplitude of ground acceleration ($\mathrm{TR_a} < 1$).

Table 6.1. Analytical expressions related to the transmissibility and the displacement response factor for a viscously damped SDOF system excited by a harmonic force considering both the classical and the new definitions

	Transmissibility	Displacement response factor
Classical definition[a]	$\mathrm{TR_a}(\xi,\beta) = \sqrt{\dfrac{1+(2\xi\beta)^2}{(1-\beta^2)^2+(2\xi\beta)^2}} = \sqrt{1+(2\xi\beta)^2}\,R_\mathrm{d}(\xi,\beta)$	$R_\mathrm{d}(\xi,\beta) = \dfrac{1}{\sqrt{(1-\beta^2)^2+(2\xi\beta)^2}}$
	$\mathrm{TR_a}(\xi,0) = 1 \quad \forall \xi$	$R_\mathrm{d}(\xi,0) = 1 \quad \forall \xi$
	$\mathrm{TR_{a,max}}(\xi) = \dfrac{2\sqrt{2}\xi^2}{\sqrt{-1-4\xi^2+8\xi^4+\sqrt{1+8\xi^2}}}$	$R_\mathrm{d,max}(\xi) = \dfrac{1}{2\xi\sqrt{1-\xi^2}}$
	$\beta_\mathrm{Ra}(\xi) = \dfrac{1}{2\xi}\sqrt{-1+\sqrt{1+8\xi^2}}$	$\beta_\mathrm{Rd}(\xi) = \sqrt{1-2\xi^2}$
New definition[b]	$\mathrm{TR}(\xi,\beta) = \sqrt{\dfrac{1+(2\xi\beta)^2}{(1-\beta^2)^2+(2\xi\beta)^2}}\,\dfrac{\sqrt{-1-4\xi^2+8\xi^4+\sqrt{1+8\xi^2}}}{2\sqrt{2}\xi^2}$	$R(\xi,\beta) = \dfrac{2\xi\sqrt{1-\xi^2}}{\sqrt{(1-\beta^2)^2+(2\xi\beta)^2}}$
	$\mathrm{TR}(\xi,0) = \dfrac{\sqrt{-1-4\xi^2+8\xi^4+\sqrt{1+8\xi^2}}}{2\sqrt{2}\xi^2} = \dfrac{1}{\mathrm{TR_{a,max}}(\xi)}$	$R(\xi,0) = 2\xi\sqrt{1-\xi^2} = \dfrac{1}{R_\mathrm{d,max}(\xi)}$
	$\mathrm{TR_{max}} = 1 \quad \forall \xi$	$R_\mathrm{max} = 1 \quad \forall \xi$

[a] See Fig. 6.2.
[b] See Fig. 6.3.
Note: The given expressions for β_Rd, $R_\mathrm{d,max}$, and R are valid for $0 < \xi < \sqrt{2}/2$. For $\sqrt{2}/2 \le \xi < 1$, no peaks occur for R_d and the maximum response occurs under static conditions ($\beta = 0$) and $R_\mathrm{d,max} = 1$. It follows that, for $\sqrt{2}/2 \le \xi < 1$, $R(\xi,\beta) = 1/\sqrt{(1-\beta^2)^2+(2\xi\beta)^2}$ and $R(\xi,0) = 1$.

Effect of ξ As concerns the effect of the damping ratio ξ, from Fig. 6.2b it can be noted that damping reduces the amplitude of motion at all excitation frequencies [45]. In particular, in the neighborhood of resonance, the response is very sensitive to damping. As ξ increases (for $0 < \xi < \sqrt{2}/2$) both the peak value $R_\mathrm{d,max}(\xi)$ and the resonant frequency $\beta_\mathrm{Rd}(\xi)$ reduce. For $\sqrt{2}/2 \le \xi < 1$, no peak occurs for $R_\mathrm{d}(\xi,\beta)$ and its maximum value is obtained in static conditions, that is for $\beta = 0$ ($R_\mathrm{d,max} = R(\xi,0) = 1$).

Referring to the transmissibility (Fig. 6.2a), damping produces opposite effects depending on whether $\beta < \sqrt{2}$ or $\beta > \sqrt{2}$. In particular, for $\beta < \sqrt{2}$ the increase in the damping ratio ξ reduces both the maximum transmitted acceleration $\mathrm{TR_{a,max}}(\xi)$ and the resonant frequency $\beta_\mathrm{Ra}(\xi)$, whereas for $\beta > \sqrt{2}$ the damping ratio ξ increases the transmitted acceleration.

Comparing Figs. 6.2a and b, it can be observed that for small values of the damping ratio ξ, in the neighborhood of the resonance, the curves of $\mathrm{TR_a}$ and R_d are close, both in terms of maximum values and resonant frequencies.

In this study, consistently with the normalization adopted in the governing equations (Sect. 6.2), both the transmissibility and the displacement response factor were redefined. In both cases, the normalization was made with respect to the maximum response in resonance condition. The analytical expressions of the transmissibility and the displacement response factor so defined, and denoted as $\text{TR}(\xi, \beta)$ and $R(\xi, \beta)$ respectively, are reported in the second part of Table 6.1. The expression of $R(\xi, \beta)$ given in Table 6.1 is valid for $0 < \xi < \sqrt{2}/2$. For $\sqrt{2}/2 \leq \xi < 1$, $R(\xi, \beta) = 1/\sqrt{(1 - \beta^2)^2 + (2\xi\beta)^2} = R_\text{d}(\xi, \beta)$ and $R(\xi, 0) = 1$.

In Fig. 6.3, the trends of both $\text{TR}(\xi, \beta)$ (Fig. 6.3a) and $R(\xi, \beta)$ (Fig. 6.3b) are plotted for different values of damping ratio ξ. As in Fig. 6.2, each color corresponds to a value of ξ. Compared to Fig. 6.2, due to the adopted normalization, the maximum value in resonance condition (highlighted with colored dots) is equal to unity, regardless of damping, and the value assumed for $\beta = 0$ (highlighted with colored squares) increases with ξ (Table 6.1). As concerns R (Fig. 6.3b), it can be observed that $R(\xi, 0) = 1$ for $\sqrt{2}/2 \leq \xi < 1$.
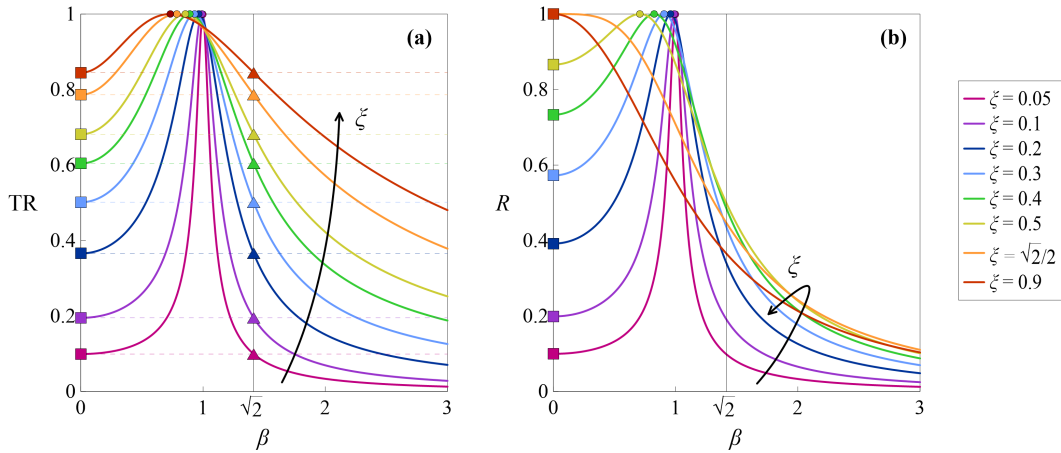
Figure 6.3. **a** Transmissibility TR and **b** displacement response factor R for several values of the damping ratio ξ.

These preliminary considerations give us indications on how, by acting on the damping and frequency ratios (ξ and β), it is possible to mitigate the system response (acceleration and/or displacement) in the absence of obstacles. In particular, the mitigation of the system response can be achieved in two ways: by increasing β for the transmitted acceleration to be less than the ground acceleration (isolation), or by increasing the dissipative capability (increasing ξ) in order to reduce the dynamic amplification in resonance condition. Consequently, in the first case the attention is directed towards the frequency interval $\beta > \sqrt{2}$, in which, theoretically, it would be preferable not to have damping; in the second case, instead, the attention is directed towards the frequency interval $\beta < \sqrt{2}$ in which the effect of damping is beneficial. Even in the case of isolation, however, a certain amount of damping must nevertheless be ensured in order to reduce, on the one hand, the response in resonance condition and, on the other, to lead to acceptable static displacements. Consequently, a compromise must be found.

With obstacles

The presence of obstacles (existing or newly added) increases the number of parameters that influence the system's response. In addition to the frequency ratio β and the damping ratio ξ, also the effect of the gap δ_0 and of the mechanical properties of the obstacles (λ and γ) must be taken into account.

Known the value of the dimensionless gap δ_0, it is possible to preliminary identify the frequency interval in which impact surely will occur, based on geometric considerations. The limits of this frequency interval, denoted as β_1 and β_2 respectively (with $\beta_1 < \beta_2$), can be determined analytically by solving, for each $\xi - \delta_0$ pair, the equation $R(\xi, \beta) = \delta_0$, that is by finding the intersections between the curve representative of the displacement amplification factor $R(\xi, \beta)$, corresponding to the selected ξ value, and the horizontal line $\delta_0 = constant$, as shown in Fig. 6.4 for $\xi = 0.1$. In this figure, β_1 and β_2 are represented with red and blue dots respectively, for some δ_0 values, and the frequency interval $\beta_1 \leq \beta \leq \beta_2$ is highlighted with horizontal yellow lines.

The roots of equation $R(\xi, \beta) = \delta_0$ have the following expressions:

$$
\begin{cases}
\beta_1(\xi, \delta_0) &= \sqrt{1 - 2\xi^2 - \dfrac{2\xi}{\delta_0}\sqrt{(\delta_0^2 - 1)(\xi^2 - 1)}} \\[2ex]
\beta_2(\xi, \delta_0) &= \sqrt{1 - 2\xi^2 + \dfrac{2\xi}{\delta_0}\sqrt{(\delta_0^2 - 1)(\xi^2 - 1)}}
\end{cases}
\quad \text{for } 0 < \xi < \frac{\sqrt{2}}{2} \qquad (6.3a)
$$

$$
\begin{cases}
\beta_1(\xi, \delta_0) &= \sqrt{1 - 2\xi^2 - \dfrac{1}{\delta_0}\sqrt{1 + (2\xi\delta_0)^2(\xi^2 - 1)}} \\[2ex]
\beta_2(\xi, \delta_0) &= \sqrt{1 - 2\xi^2 + \dfrac{1}{\delta_0}\sqrt{1 + (2\xi\delta_0)^2(\xi^2 - 1)}}
\end{cases}
\quad \text{for } \frac{\sqrt{2}}{2} \leq \xi < 1 \qquad (6.3b)
$$
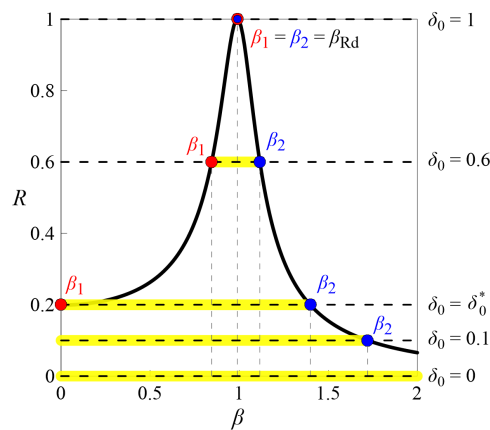
Figure 6.4. Dynamic amplification factor R for $\xi = 0.1$ (*thick black line*) with the location of β_1 (*red dots*) and β_2 (*blue dots*) for some δ_0 values (*horizontal dashed lines*). For $\beta_1 < \beta < \beta_2$ (*horizontal yellow lines*) impact surely occurs for geometric reasons.

From Fig. 6.4 it can be observed that, for a given ξ value (i.e. $\xi = 0.1$), different situations may occur depending on the dimensionless gap δ_0. For $\delta_0 = 1$, that is

in free flight condition, the two roots coincide ($\beta_1 = \beta_2 = \beta_{\text{Rd}}$) and thus impact never occurs for any β value. On the contrary, for $\delta_0 = 0$, that is when the bumpers are initially in contact with the mass, the equation $R(\xi, \beta) = 0$ does not admit roots (Eqs. 6.3a), and consequently impact occurs for each β value. The interval $0 < \delta_0 < 1$ can be divided into two sub-ranges through the value $\delta_0^* = 2\xi\sqrt{1 - \xi^2}$. For $\delta_0^* < \delta_0 < 1$ (for example $\delta_0 = 0.6$) the two roots β_1 and β_2 are both non null and different from each other, with $\beta_1 < \beta_{\text{Rd}}$ and $\beta_2 > \beta_{\text{Rd}}$; furthermore, they diverge as δ_0 decreases, until, for $\delta_0 = \delta_0^*$, β_1 becomes zero, meaning that impact occurs already starting from $\beta = 0$. For $0 < \delta_0 < \delta_0^*$ (for example $\delta_0 = 0.1$), the equation $R(\xi, \beta) = \delta_0$ admits only one solution, that is β_2, which increases as δ_0 decreases and also in this case the impact occurs immediately starting from $\beta = 0$.

It is worth noting that impact can occur also outside the frequency range $\beta_1 \leq \beta \leq \beta_2$, depending on the nonlinear behavior of the system, the values of the parameters and the initial conditions, as it will be shown in the following sections.

The introduction of the obstacles changes the response of the system, which will be influenced not only by ξ and β but also by the parameters which characterize the obstacles (position and mechanical properties). Preliminary considerations can already be made on the basis of geometrical reasoning depending on the position of the obstacle δ_0. The response will be further modified taking into account also the mechanical (stiffness and damping) properties of the obstacles (λ and γ). Based on these preliminary considerations, it is of interest to investigate the effect of obstacles' parameters (δ_0, λ and γ) on the system response, in order to identify possible scenarios and also make some reasoning on control. The study is carried out numerically assuming a fixed value of the damping ratio $\xi = 0.1$, for which $\delta_0^* \simeq 0.199$. The corresponding transmissibility TR and displacement response factor R curves will be taken as a comparison to which reference will be made systematically in the following.

6.4   Results of the numerical investigations

The effect of the introduction of deformable and dissipative obstacles (bumpers), placed at a certain distance, on the dynamic response of a SDOF system, was studied through parametric numerical analyses, considering the model described in Sect. 6.2 (SNM) subjected to a step-wise forward and backward sine sweep base excitation.

The analyses were conducted by assuming $\xi = 0.1$ and initially fixing also the dissipative capability of the bumpers ($\gamma = 5$). To get an idea of how, through the introduction of the obstacles, the response of the system varies, compared to the free flight condition, in this section the evolution with the stiffness ratio λ, of the forward and backward Pseudo-Resonance Curves (PRCs) of selected response quantities, suitably normalized, is presented for fixed values of the dimensionless gap δ_0, going from $\delta_0 = 1$ (free flight condition) to $\delta_0 = 0$ (bumpers initially in contact with the mass).

The selected response quantities are: the normalized excursion of the absolute acceleration of the mass $\eta_{\text{a}} = \Delta\alpha/\Delta\alpha_0$, the normalized excursion of the relative displacement of the mass $\eta_{\text{d}} = \Delta q/\Delta q_0$, the normalized excursion of the contact force

$\eta_{\mathrm{F}} = \Delta f_{\mathrm{B}}/\Delta\alpha_0$ and the normalized excursion of the deformation of the bumpers $\eta_{\mathrm{B}} = \Delta q_{\mathrm{B}}/\Delta q_0$. The absolute acceleration of the mass $\alpha(\tau)$ is given by the sum of the acceleration of the ground $a_{\mathrm{t}}(\tau) = a_{\mathrm{G}}\sin\beta\tau$ and the relative acceleration between the mass and the ground $q''(\tau)$, that is $\alpha(\tau) = a_{\mathrm{t}}(\tau) + q''(\tau)$. The excursion $(\Delta i, \ i = \alpha, \ q, \ f_{\mathrm{B}}, \ q_{\mathrm{B}})$ was calculated as the difference between the maximum and minimum values recorded at steady-state of each sub-frequency range. To calculate the excursion of the contact force (Δf_{B}) and of the bumpers' deformation (Δq_{B}), both the bumpers have been considered. In particular, Δf_{B} and Δq_{B} were calculated as the sum of the maximum absolute values of the contact forces and of the deformations of the two bumpers respectively, recorded at steady-state of each sub-frequency range. The normalization was made with respect to the free flight condition. In particular, $\Delta\alpha_0$ and Δq_0 denote the maximum excursion of the absolute acceleration and of the relative displacement of the mass respectively in free flight resonant condition. In addition to these response quantities, also some considerations regarding the resonant frequency β_{R} and the excursion of the static displacement of the mass $\eta_{\mathrm{d,st}}$ will be made.

Starting from the free flight condition $(\delta_0 = 1)$, the choice of the investigated δ_0 values was made based on the considerations made in Sect. 6.3, involving vibration isolation and the parameters β_1, β_2, δ_0^*, etc. First of all, the gap interval $0 \leq \delta_0 \leq 1$ was divided, through the value $\delta_0^* \simeq 0.199$, into two sub-ranges, namely $\delta_0^* \leq \delta_0 \leq 1$ and $0 \leq \delta_0 < \delta_0^*$, in order to distinguish the situations in which the equation $R(\xi,\beta) = \delta_0$ admits two or one roots. Subsequently, inside these two sub-ranges, some δ_0 values were selected. In particular, referring to the sub-range $\delta_0^* \leq \delta_0 \leq 1$, the following values of the dimensionless gap were selected: $\delta_0 = 1$, $\delta_0 = 0.7$, $\delta_0 = 0.4$ and $\delta_0 = \delta_0^*$. As concerns the sub-range $0 \leq \delta_0 < \delta_0^*$, in addition to the limit value $\delta_0 = 0$, the values of dimensionless gap at which $\beta_2 = \sqrt{2}$ and $\beta_2 = 2$, that is $\delta_0 \simeq 0.1915$ (denoted also as $\delta_{0\mathrm{c}}$) and $\delta_0 \simeq 0.066$ respectively, were considered.

In the following figures (Figs. 6.5-6.10) the thick black curves represent the PRCs of η_{a} and η_{d} in free flight condition (absence of obstacles). The other curves represent the forward (solid lines) and backward (dashed lines) PRCs corresponding to increasing values (increasing thickness of the lines) of λ between 0.1 and 100 (the latter assumed conventionally as representative of the impact against a rigid obstacle and denoted as $\lambda_{\max}$). Only the curves corresponding to some λ values inside this range (namely $\lambda = 0.1, 1, 10, 50, 100$) were represented to make the figures more readable.

As concerns the symbols, the black dots identify the primary resonance condition for all the investigated λ values (even those for which the PRCs are not shown). The yellow squares represent the values of η_{a} and η_{d} for $\beta = 0$. The cyan symbols identify the boundaries of the frequency interval $(\beta_1 \leq \beta \leq \beta_2)$ in which, for the considered value of δ_0, impact will surely occur, based on purely geometric considerations (Sect. 6.3). In particular, the cyan diamond corresponds to β_1 (lower limit of the "geometric" impact range) while the cyan circle corresponds to β_2 (upper limit of the "geometric" impact range). The green triangle was used to represent the β value (denoted as β_{c}) such that, for $\beta > \beta_{\mathrm{c}}$ (this frequency interval is highlighted with an horizontal green line) the maximum absolute acceleration of the mass is lower

than the ground acceleration ($\eta_\text{a} < \eta_\text{a}|_{\beta=0}$). Finally, the vertical arrows identify the jumps.

Free flight ($\delta_0 = 1$)   For $\delta_0 = 1$ impact does not occur for any β value ($\beta_1 = \beta_2 = \beta_\text{Rd} \simeq 0.99$) regardless of λ, since the amplitude of the gap is equal to the maximum displacement of the mass in resonance condition. Since in the adopted model (SNM), both the bumpers and the damper were modeled through a linear spring in parallel with a linear viscous dashpot (Kelvin-Voigt model), the corresponding PRCs of η_a and η_d, represented with thick black curves in Figs. 6.5-6.10, coincide with the curves representative of the transmissibility TR and the displacement response factor R for $\xi = 0.1$ (Fig. 6.3). Due to the considered small value of damping ratio ξ, the PRCs of η_a and η_d in free flight condition are close to each other. Forward and backward curves overlap, without jumps or hysteresis, and the acceleration becomes lower than the ground acceleration for $\beta > \sqrt{2}$.

$\delta_0 = 0.7$ For $\delta_0 = 0.7$ (Fig. 6.5), impact can occur since β_1 (cyan diamond) and β_2 (cyan circle) (Eq. 6.3a) are both different from zero, with $\beta_1 < \beta_\text{Rd}$ and $\beta_2 > \beta_\text{Rd}$. In addition to the frequency range in which impact surely occurs, due to geometric considerations (that is $\beta_1 \leq \beta \leq \beta_2$), the nonlinear behavior of the system causes the occurrence of impact even outside this range.

As it can be seen from Fig. 6.5, due to the hardening caused by the impact, compared to the free flight condition (black curve), the PRCs bend to the right, and the bending becomes more pronounced as the stiffness ratio λ increases. Exceeded a certain value of λ, which will be denoted as λ_H, the system exhibits jump phenomena (highlighted with arrows), leading to the appearance of an hysteresis region between the jumps. The jump phenomena and the hysteresis are observable in the PRCs of both η_a (Fig. 6.5a), η_d (Fig. 6.5b), η_F (Fig. 6.5c) and η_B (Fig. 6.5d). For the selected value of the dimensionless gap $\lambda_\text{H} \simeq 2.2$. As it can be seen from Fig. 6.5, while the frequency value at which the upward jump (blue dashed arrow) occurs, decreasing the forcing frequency (backward sweep), is the same for each λ value and corresponds to β_2, the downward jump (blue solid arrow) occurs, increasing the forcing frequency (forward sweep), at a frequency value, in the following denoted as β_3, which increases with λ. Consequently, β_2 and β_3 give a measure of the extent of the hysteresis region in terms of frequency. As λ increases, this frequency range increases.

In the frequency range corresponding to the hysteresis ($\beta_2 < \beta < \beta_3$), for each β value, and depending on the initial conditions, it is possible to observe two steady-state stable solutions, corresponding respectively to large-amplitude (with impact) and small-amplitude (without impact) oscillations. Actually, there would be also a third unstable solution, that could not be obtained with the used methodology. At the hysteresis region, making a comparison with the free flight condition at the same frequency, depending on the initial conditions, the introduction of the obstacle can be counter-productive (occurrence of impact), leading to an increase not only of accelerations, but also of displacements, or, at best, the response does not change (absence of impact). Therefore, the introduction of the obstacle does not always
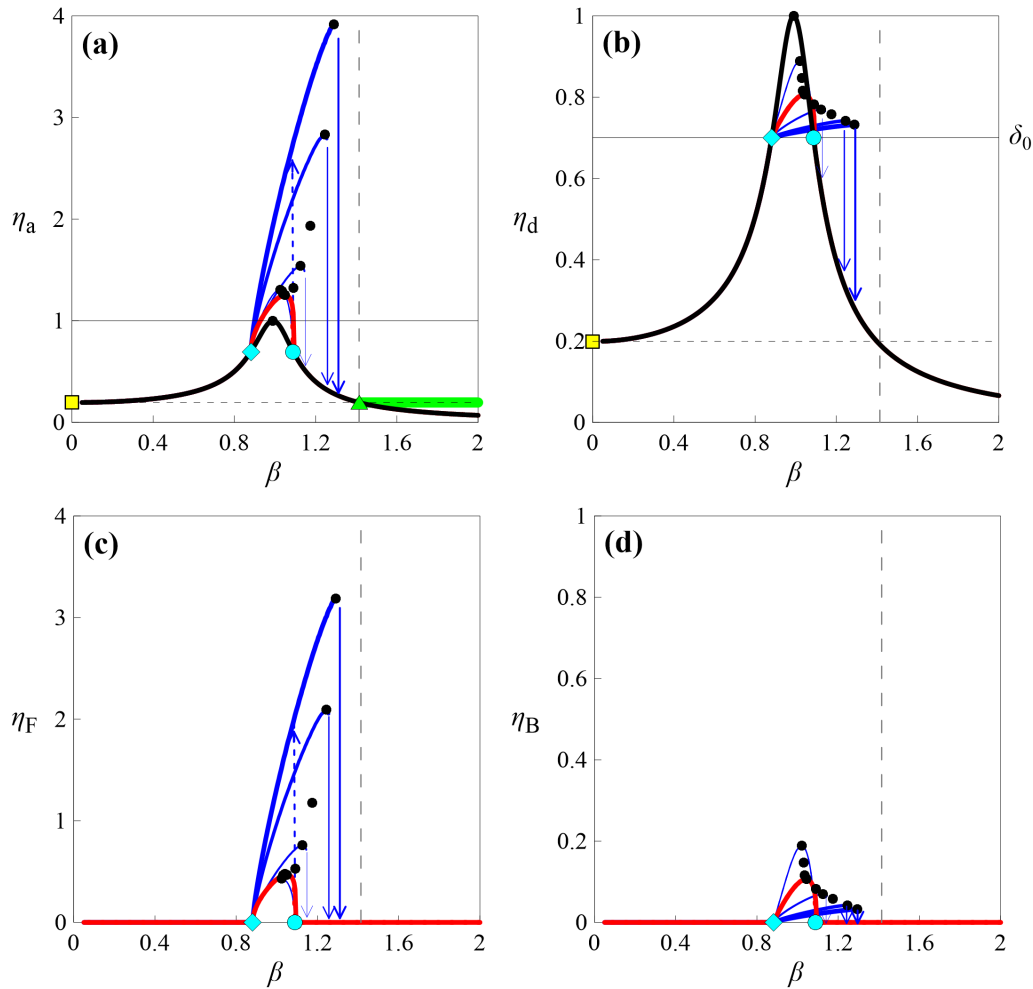
Figure 6.5. Sections of the PRCs for $\xi = 0.1$, $\gamma = 5$, $\delta_0 = 0.7$ and for several values of the stiffness ratio λ ($0.1 \leq \lambda \leq 100$): **a** η_a; **b** η_d; **c** η_F; **d** η_B. The *black curves* (in **a** and **b**) represent the free flight condition, the *red curves* identify the PRCs corresponding to the λ value at which the envelope of the maximum values of the acceleration shows a minimum ($\lambda = \lambda_{\mathrm{opt}}$), while the *blue curves* represent the PRCs corresponding to the other values of λ (the thickness of the line increases with λ). The *black dots* identify the primary resonance condition. In **a** and **b** the *yellow squares* indicate the values of η_a and η_d for $\beta = 0$; the *cyan symbols* represent the location of β_1 (*cyan diamond*) and β_2 (*cyan circle*). Finally, in **a** the *green triangle* identifies the β_c value, for all the considered values of λ, such that $\eta_a < \eta_a|_{\beta=0}$ for $\beta > \beta_c$ (*horizontal green line*).

reduce the displacements compared to the free flight condition, as one would expect. Based on these considerations, the hysteresis, if possible, should be avoided (choosing $\lambda < \lambda_H$).

From Fig. 6.5, it can be observed that the primary resonance (highlighted with black dots) moves to the right, that is it occurs for increasing values of β, as the stiffness ratio λ increases. As concerns the acceleration (Fig. 6.5a) the maximum value in resonance condition (denoted as η_a^*), starting from the free flight condition (black curve) and increasing λ, first increases, then decreases showing a minimum and subsequently starts to grow again, tending to an almost vertical asymptote for large values of stiffness ratio. For each λ value, the maximum value of η_a is always greater than that corresponding to the free flight condition ($\eta_a^* > 1$). The introduction of the obstacle, on the contrary, always reduces the peak value of the excursion of relative displacement ($\eta_d^* < 1$), and the extent of the reduction increases with λ (Fig. 6.5b). No changes in the excursion of the static displacement (highlighted with yellow squares) are observed. As concerns the bumpers, both the contact force and the deformation are null in the absence of impact. When impact occurs, the values of the contact force at resonance (black dots in Fig. 6.5c) show a trend with the stiffness ratio, similar to that of the maximum values of the acceleration, with the occurrence of a minimum, while the deformation of the bumpers (Fig. 6.5d), quite small for the selected δ_0 value, always decreases with λ.

From Fig. 6.5, it can be also noted that, for the considered combination of parameters (ξ, γ and δ_0) and for $0 < \lambda \leq 100$, the occurrence of impact modifies the response of the system only for $\beta < \sqrt{2}$, keeping unaltered the frequency range of interest for the isolation in the linear case, that is $\beta > \sqrt{2}$.

Finally, by looking at the PRCs of η_a (Fig. 6.5a), it is possible to identify a value of stiffness ratio (denoted as λ_{opt}) for which the envelope of the maximum values of η_a shows a minimum ($\min[\eta_a^*]$), although it is, in any case, $\eta_a^* > 1$. For the considered value of δ_0, this occurs for $\lambda_{opt} \simeq 2$ (red curve). In this condition, the resonance occurs for $\beta_R \simeq 1.05$ and since $\lambda_{opt} \simeq 2 < \lambda_H$, no hysteresis occurs. Furthermore, for all the considered values of λ, the acceleration transmitted to the mass becomes smaller than the ground acceleration for $\beta > \sqrt{2}$ ($\beta_c = \sqrt{2}$, green triangle). In Fig. 6.5a this frequency range was highlighted with an horizontal green thick line.

In the condition corresponding to the minimum peak value of η_a ($\lambda = \lambda_{opt}$), also a reduction of the peak value of the relative displacement of the mass, compared to the free flight condition, was noticed (red curve in Fig. 6.5b). On the other hand, no reduction of the static displacement was observed.

By comparing the PRC corresponding to λ_{opt} (red curve) and the PRC in free flight condition (black curve) at the same frequency (for $\beta_1 \leq \beta \leq \beta_2$), it can be noted that, in the condition corresponding to the minimum peak value of the acceleration, while the acceleration is always greater than the free flight condition, the displacement is in general lower, except for frequency values slightly lower than β_2, at which the red curve appears to be above the black one.

$\boldsymbol{\delta_0 = 0.4}$ By reducing the dimensionless gap, always remaining in the range $\delta_0^* < \delta_0 < 1$, the amplitude of the frequency interval in which impact occurs increases (Fig. 6.6, for $\delta_0 = 0.4$). Compared to the previous case ($\delta_0 = 0.7$, Fig. 6.5), it is possible to identify a value of the stiffness ratio (denoted as $\lambda_c < \lambda_{max}$), beyond which the occurrence of impact modifies the response of the system, compared to the free flight condition, not only for $\beta < \sqrt{2}$, but also for $\beta > \sqrt{2}$. For $\delta_0 = 0.4$ this occurs for $\lambda_c \simeq 14$. For $\lambda > \lambda_c$ the transmitted acceleration becomes lower than the ground acceleration after the downward jump, which occurs for increasing values of β as λ increases. Consequently, compared to the linear case, the isolation frequency range decreases.

Compared to the scenarios observed for $\delta_0 = 0.7$ (Fig. 6.5), for $\delta_0 = 0.4$, increasing the stiffness ratio, secondary resonances in the low frequency range appear and become gradually evident, affecting increasingly larger frequency ranges. At these secondary resonances, particularly evident in the PRCs of η_a and η_F, periodic and quasi-periodic responses can be observed, and the acceleration of the mass appear to be always greater compared to the free flight condition.

As concerns the values of the response in resonance condition (black dots), similar considerations apply to those made for $\delta_0 = 0.7$. In particular, also in this case the envelope of the maximum values of the acceleration, in resonance condition, shows a minimum which occurs for $\lambda_{opt} \simeq 1$. Since λ_{opt} is slightly lower than $\lambda_H \simeq 1.2$, no hysteresis occurs. Furthermore, always referring to λ_{opt} (red curve), it can be observed that the maximum value of the acceleration in resonance condition, which occurs for $\beta_R \simeq 1.12$, is close to the value corresponding to the free flight condition ($\eta_a^* \simeq 1$). We can see therefore the possibility of reducing the maximum value of the acceleration compared to the free flight condition, also in the presence of impact, by further reducing the dimensionless gap. Furthermore, since $\lambda_{opt} < \lambda_c$, the response of the system is not altered for $\beta > \sqrt{2}$ ($\beta_c = \sqrt{2}$, green triangle in Fig. 6.6a).

Finally, by comparing the PRC of η_a (Fig. 6.6a) corresponding to λ_{opt} (red curve) and the PRC in free flight condition (black curve) at the same frequency (for $\beta_1 \leq \beta \leq \beta_2$), it can be noted that there is a frequency range (highlighted with a vertical gray band) in which, despite the occurrence of impact, the acceleration is lower than in the free flight condition.

$\boldsymbol{\delta_0 = \delta_0^*}$ Moving to the value of the dimensionless gap $\delta_0 = \delta_0^* = 2\xi\sqrt{1-\xi^2} \simeq 0.199$ (Fig. 6.7), a limit condition is reached in which the impact already occurs for $\beta = 0$ (since $\beta_1 = 0$). In the low frequency range secondary resonances, of different type compared to those observed for $\delta_0 = 0.4$, appear and become gradually evident, affecting increasingly larger frequency ranges as λ increases. In the condition corresponding to the minimum value of the acceleration at resonance ($\min[\eta_a^*]$, red curve), which occurs for $\lambda_{opt} \simeq 1$, no hysteresis is observed ($\lambda < \lambda_H \simeq 1.8$) and since in this condition $\beta_c = \sqrt{2}$ ($\lambda_{opt} < \lambda_c \simeq 2$), the response of the system is not altered for $\beta > \sqrt{2}$, compared to the free flight condition. Furthermore, the maximum value of the acceleration in resonance condition, which occurs for $\beta_R \simeq 1.22$, is lower than the value corresponding to the free flight condition ($\eta_a^* < 1$). Finally, always for $\lambda = \lambda_{opt}$ (red curve), it can be noted that, compared to $\delta_0 = 0.4$ the amplitude of
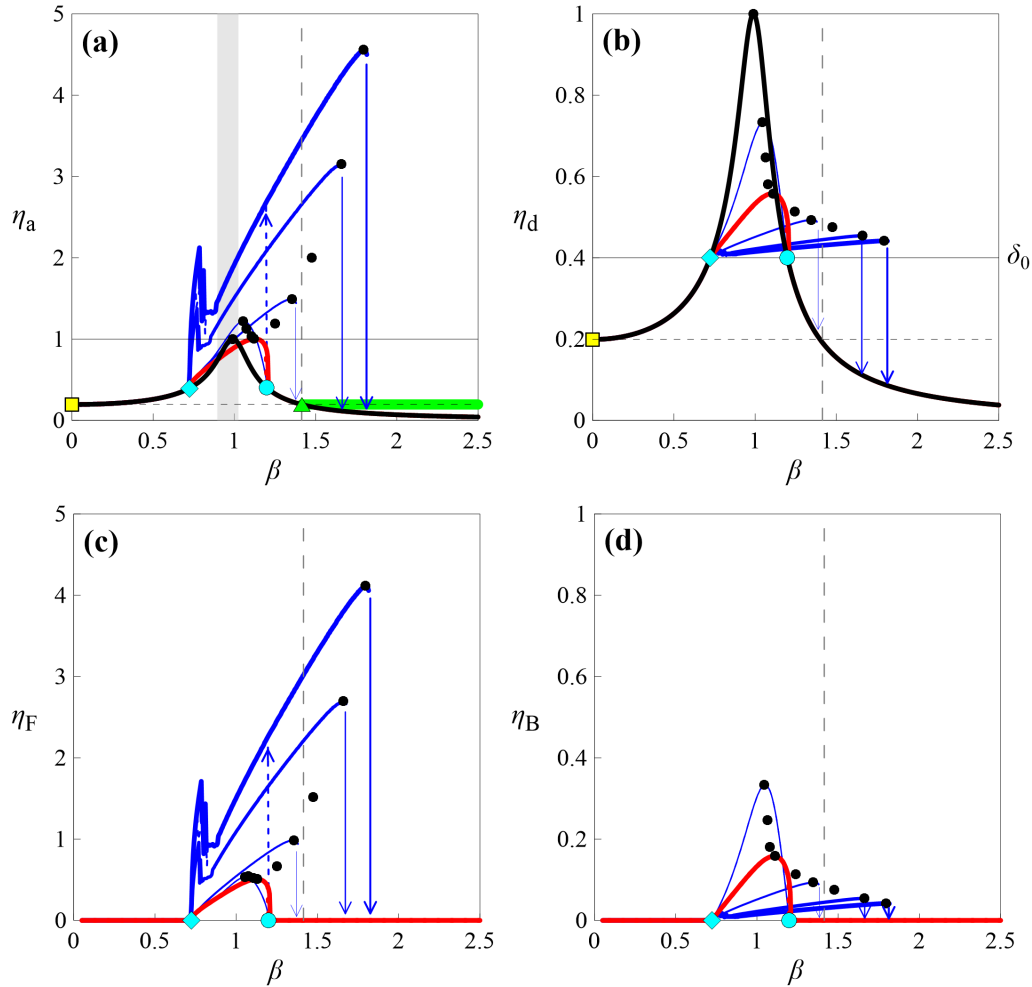
Figure 6.6. Sections of the PRCs for $\xi = 0.1$, $\gamma = 5$, $\delta_0 = 0.4$ and for several values of the stiffness ratio λ ($0.1 \leq \lambda \leq 100$): **a** η_a; **b** η_d; **c** η_F; **d** η_B. The *black curves* (in **a** and **b**) represent the free flight condition, the *red curves* identify the PRCs corresponding to the λ value at which the envelope of the maximum values of the acceleration shows a minimum ($\lambda = \lambda_{opt}$), while the *blue curves* represent the PRCs corresponding to the other values of λ (the thickness of the line increases with λ). The *black dots* identify the primary resonance condition. In **a** and **b** the *yellow squares* indicate the values of η_a and η_d for $\beta = 0$; the *cyan symbols* represent the location of β_1 (*cyan diamond*) and β_2 (*cyan circle*). Finally, in **a** the *green triangle* identifies the β_c value, for $\lambda = \lambda_{opt}$, such that $\eta_a < \eta_a|_{\beta=0}$ for $\beta > \beta_c$ (*horizontal green line*). The *vertical gray band* in **a** highlights the frequency interval in which the PRC of η_a corresponding to $\lambda = \lambda_{opt}$ (*red curve*) is below the PRC corresponding to the free flight condition (*black curve*).

Figure 6.7. Sections of the PRCs for $\xi = 0.1$, $\gamma = 5$, $\delta_0 = \delta_0^* \simeq 0.199$ and for several values of the stiffness ratio λ $(0.1 \leq \lambda \leq 100)$: **a** η_a; **b** η_d; **c** η_F; **d** η_B. The *black curves* (in **a** and **b**) represent the free flight condition, the *red curves* identify the PRCs corresponding to the λ value at which the envelope of the maximum values of the acceleration shows a minimum $(\lambda = \lambda_\mathrm{opt})$, while the *blue curves* represent the PRCs corresponding to the other values of λ (the thickness of the line increases with λ). The *black dots* identify the primary resonance condition. In **a** and **b** the *yellow squares* indicate the values of η_a and η_d for $\beta = 0$; the *cyan symbols* represent the location of β_1 (*cyan diamond*) and β_2 (*cyan circle*). For this value of δ_0 it is $\beta_1 = 0$ and, consequently, the *cyan diamond* is superimposed to the *yellow square*. Finally, in **a** the *green triangle* identifies the β_c value, for $\lambda = \lambda_\mathrm{opt}$, such that $\eta_\mathrm{a} < \eta_\mathrm{a}|_{\beta=0}$ for $\beta > \beta_\mathrm{c}$ (*horizontal green line*). The *vertical gray band* in **a** highlights the frequency interval in which the PRC of η_a corresponding to $\lambda = \lambda_\mathrm{opt}$ (*red curve*) is below the PRC corresponding to the free flight condition (*black curve*).

the frequency range (highlighted with a vertical gray band) in which, despite the occurrence of impact, the acceleration is lower than in the free flight condition, has increased.

$\boldsymbol{\delta_0 = \delta_{0c}}$ By further reducing the gap, the condition in which $\beta_2 = \sqrt{2}$ is reached (Fig. 6.8). Due to the considered damping ratio ξ, the value of dimensionless gap at which this condition occurs, calculated using the second of the Eqs. 6.3a and denoted as δ_{0c}, is slightly lower than δ_0^*, $\delta_{0c} \simeq 0.1915$. Since $0 < \delta_{0c} < \delta_0^*$, the equation $R(\xi, \beta) = \delta_{0c}$ admits only one solution, that is β_2 (cyan circle) and impact occurs already starting from $\beta = 0$. As it can be seen from Fig. 6.8, most of the considerations made for δ_0^* (Fig. 6.7) apply also in this case. However, some differences should be highlighted. Compared to δ_0^*, the increase in λ causes a slight decrease also of the static displacement (yellow squares in Fig. 6.8b). Finally, for this value of the dimensionless gap $\lambda_H \simeq \lambda_c \simeq 1.8$ and the minimum value of the acceleration in resonance occurs again for $\lambda_{opt} \simeq 1$. In this condition $\eta_a^* < 1$, no hysteresis occurs ($\lambda < \lambda_H$) and, since $\beta_c = \beta_2 = \sqrt{2}$ ($\lambda_{opt} < \lambda_c$), the response of the system is not altered for $\beta > \sqrt{2}$, compared to the free flight condition.

$\boldsymbol{\delta_0 \simeq 0.066}$ Let's now consider the value of the dimensionless gap at which $\beta_2 = 2$, that is $\delta_0 \simeq 0.066$. As it can be seen from Fig. 6.9, at this δ_0 value, as λ increases, more complex behaviors appear in the low frequency range. In particular, different types of secondary resonances (with left hysteresis or of non-regular type), of a different nature from those observed for greater values of δ_0, appear and become gradually evident, affecting increasingly larger frequency ranges as λ increases. At these secondary resonances, more evident in the PRCs of η_a (Fig. 6.9a) and η_F (Fig. 6.9c), both periodic, quasi-periodic and even chaotic solutions can be observed. Furthermore, always at the secondary resonances, the number of impact between the mass and each bumper, per forcing cycle, is found to increase as β decreases and, for a given β value, as λ increases.

At this δ_0 value, the reduction of the static displacement with increasing λ, already observed for $\delta_0 = \delta_{0c}$, is more evident (Fig. 6.9b). Compared to δ_{0c}, since in this case $\beta_2 = 2 > \sqrt{2}$, the occurrence of impact modifies, in any case and regardless of λ, the response of the system also for $\beta > \sqrt{2}$, compared to the free flight condition. The extend of the frequency range affected by such changes does not vary as long as $\lambda < \lambda_H \simeq 4.4$ (no hysteresis), whereas it becomes gradually larger as λ increases beyond λ_H.

The minimum value of the acceleration in resonance condition occurs for $\lambda_{opt} \simeq 1$. In this condition, since $\lambda_{opt} < \lambda_H$ no hysteresis occurs and furthermore $\beta_c \simeq 1.9$. At resonance, which occurs for $\beta_R \simeq 1.32$, $\eta_a^* < 1$ and, in addition to a substantial reduction of the peak value of acceleration, a noticeable reduction of both the peak value of the displacement and the static displacement is observed. Compared to the previous considered δ_0 value (Fig. 6.8), the amplitude of the frequency range in which, despite the occurrence of impact, the acceleration is lower than in the free flight condition (vertical gray band in Fig. 6.9a) is increased. However, also the amplitude of the frequency range in which the displacement in presence of impact is
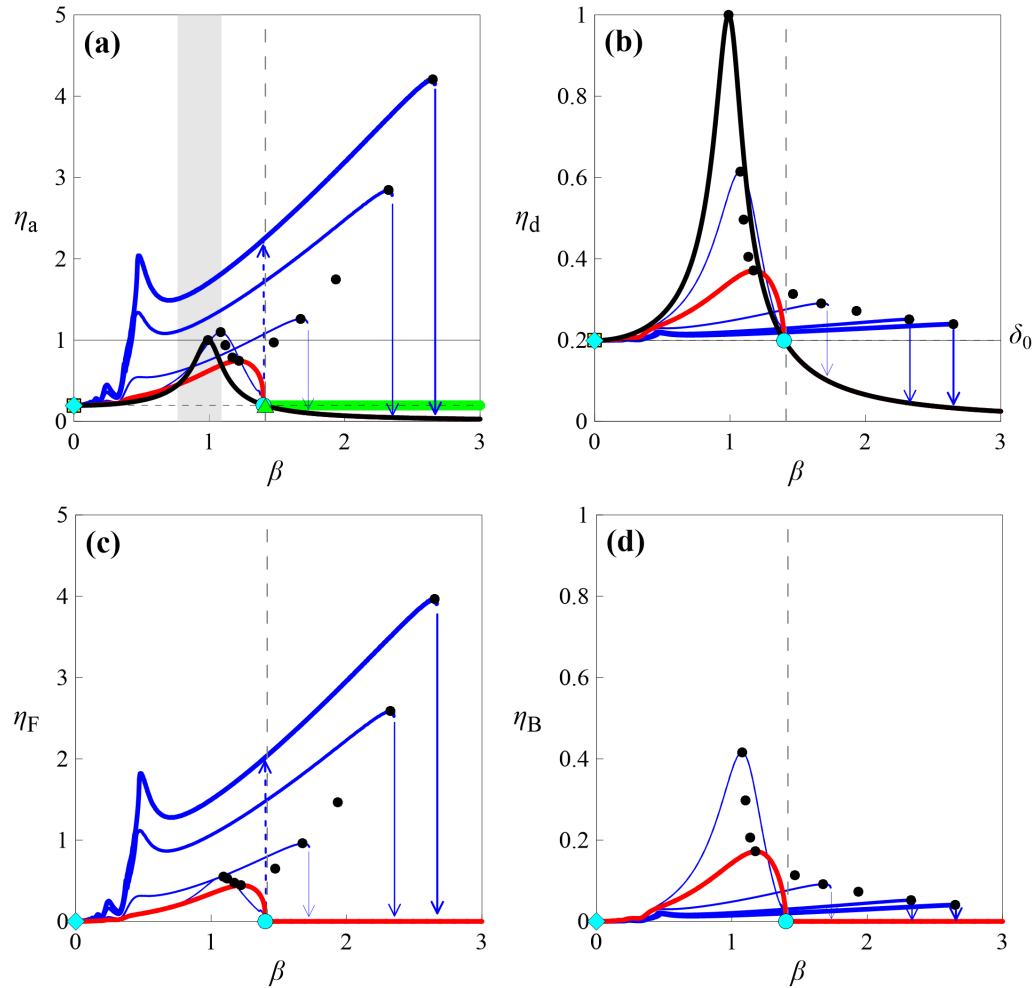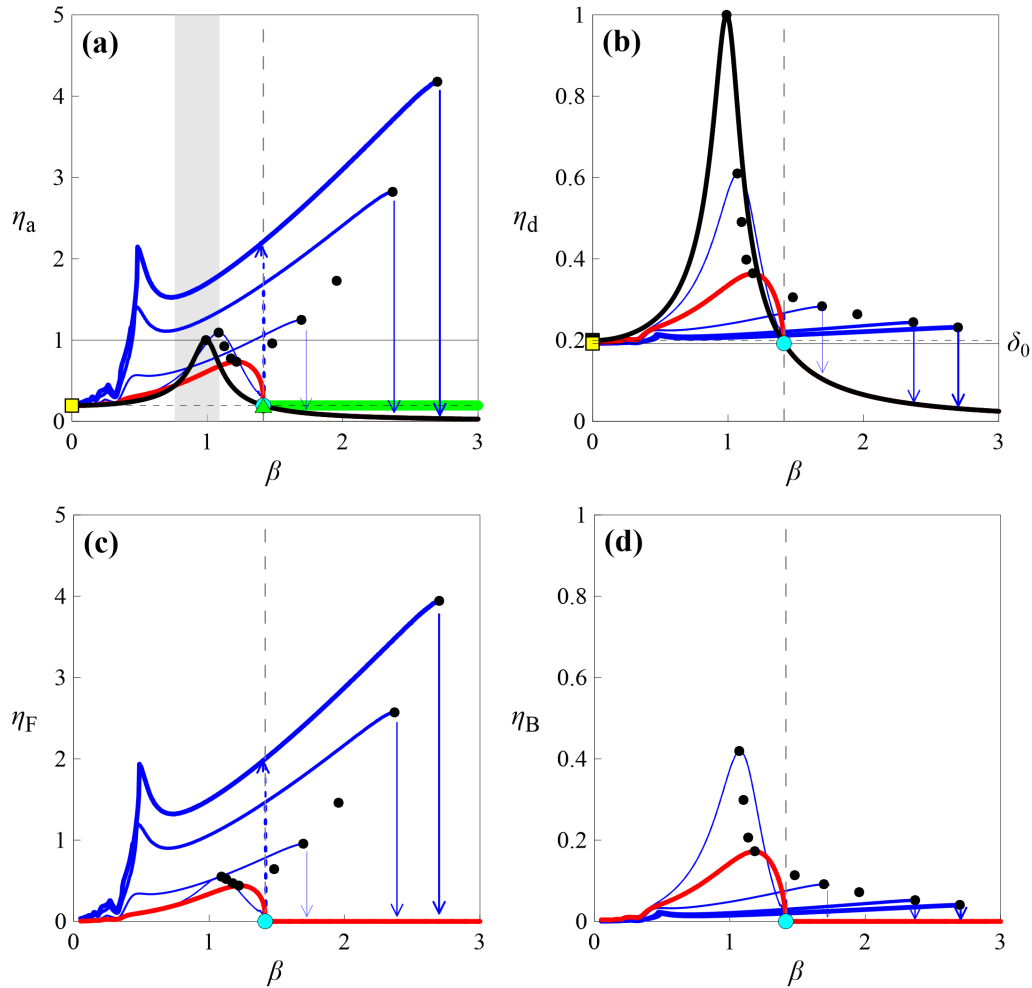
Figure 6.8. Sections of the PRCs for $\xi = 0.1$, $\gamma = 5$, $\delta_0 = \delta_c \simeq 0.1915$ (value of δ_0 so that $\beta_2 = \sqrt{2}$) and for several values of the stiffness ratio λ ($0.1 \leq \lambda \leq 100$): **a** η_a; **b** η_d; **c** η_F; **d** η_B. The *black curves* (in **a** and **b**) represent the free flight condition, the *red curves* identify the PRCs corresponding to the λ value at which the envelope of the maximum values of the acceleration shows a minimum ($\lambda = \lambda_{opt}$), while the *blue curves* represent the PRCs corresponding to the other values of λ (the thickness of the line increases with λ). The *black dots* identify the primary resonance condition. In **a** and **b** the *yellow squares* indicate the values of η_a and η_d for $\beta = 0$. The *cyan circles* represent the location of β_2. Finally, in **a** the *green triangle* identifies the β_c value, for $\lambda = \lambda_{opt}$, such that $\eta_a < \eta_a|_{\beta=0}$ for $\beta > \beta_c$ (*horizontal green line*). For this value of δ_0 and for $\lambda = \lambda_{opt}$, it is $\beta_c = \beta_2$ (the *green triangle* is superimposed to the *cyan circle*). The *vertical gray band* in **a** highlights the frequency interval in which the PRC of η_a corresponding to $\lambda = \lambda_{opt}$ (*red curve*) is below the PRC corresponding to the free flight condition (*black curve*).

Figure 6.9. Sections of the PRCs for $\xi = 0.1$, $\gamma = 5$, $\delta_0 \simeq 0.066$ (value of δ_0 so that $\beta_2 = 2$) and for several values of the stiffness ratio λ ($0.1 \leq \lambda \leq 100$): **a** η_a; **b** η_d; **c** η_F; **d** η_B. The *black curves* (in **a** and **b**) represent the free flight condition, the *red curves* identify the PRCs corresponding to the λ value at which the envelope of the maximum values of the acceleration shows a minimum ($\lambda = \lambda_{\mathrm{opt}}$), while the *blue curves* represent the PRCs corresponding to the other values of λ (the thickness of the line increases with λ). The *black dots* identify the primary resonance condition. In **a** and **b** the *yellow squares* indicate the values of η_a and η_d for $\beta = 0$. The *cyan circles* represent the location of β_2. Finally, in **a** the *green triangle* identifies the β_c value, for $\lambda = \lambda_{\mathrm{opt}}$, such that $\eta_a < \eta_a|_{\beta=0}$ for $\beta > \beta_c$ (*horizontal green line*). The *vertical gray band* in **a** highlights the frequency interval in which the PRC of η_a corresponding to $\lambda = \lambda_{\mathrm{opt}}$ (*red curve*) is below the PRC corresponding to the free flight condition (*black curve*).

greater than in the free flight is increased (Fig. 6.9b).

$\delta_0 = 0$ When the bumpers are initially positioned in contact with the mass, that is when $\delta_0 = 0$, the situation returns to be quite smooth, as shown in Fig. 6.10, although impact occurs for each β value (Sect. 6.3). Due to the occurrence of impact, the behavior of the system is still nonlinear [251], although the PRCs do not show neither jump phenomena nor hysteresis. As λ increases, the primary resonance moves to higher frequency values, up to about 10 for $\lambda = 100$. The occurrence of impact modifies, in any case and regardless of λ, the response of the system for each β value and the PRCs, once exceeded the resonance (black dots), tend to the curve corresponding to the free flight condition (black curve) for $\beta \to \infty$. This happens also in the condition corresponding to the minimum value of the acceleration in resonance, which still occurs for $\lambda_{\mathrm{opt}} \simeq 1$. In this condition, significant reductions of both the peak value of acceleration, the peak value of the displacement and the static displacement of the mass, are observed. For $\lambda = \lambda_{\mathrm{opt}}$ (red curve), the primary resonance occurs for $\beta_{\mathrm{R}} \simeq \sqrt{2}$ and the acceleration of the mass becomes lower than that of the ground for $\beta > \beta_{\mathrm{c}} \simeq 2.3$.

Discussion

The study of the evolution of the PRCs of the selected response quantities with the stiffness ratio λ, for fixed values of both the damping ratios ξ and γ and the dimensionless gap δ_0, allowed to highlight the influence of δ_0, λ and β on the system (mass and bumpers) response. On the basis of the obtained results and the considerations made by looking at fixed values of δ_0, some preliminary conclusions can be drawn.

Scenarios   Starting from the free flight condition ($\delta_0 = 1$) and reducing the gap, gradually more complex scenarios were observed, characterized by the occurrence of primary hysteresis, secondary resonances of different types in the low frequency range, periodic, quasi-periodic and chaotic responses, multiple impacts, to mention a few. Some of these scenarios do not go in the desired direction thinking of control. Consequently, the introduction of the obstacles does not always produce the desired effects. However, by properly selecting the involved parameters, it would be possible to guide the system response to reach specific objectives.

Frequency ranges   Starting from $\delta_0 = 1$ and decreasing δ_0, the amplitude of the frequency interval in which impact will surely occur, due to only geometric considerations ($\beta_1 \leq \beta \leq \beta_2$, under the black curve shown in Fig. 6.11, which is the PRC of η_{d} in free flight condition), increases. For the considered system and parameters, impact does not occur for $\beta < \beta_1$ (on the left of the ascending branch of the black curve in Fig. 6.11), with β_1 becoming zero when δ_0 reaches the value δ_0^*. Furthermore, due to the hardening caused by the impact, when $\lambda > \lambda_{\mathrm{H}}$ (occurrence of hysteresis), where λ_{H} depends on δ_0, impact can occur also for $\beta_2 < \beta < \beta_3$, where β_3 denotes the frequency at which, during the forward sweep (increasing forcing frequency), the downward jump occurs. In Fig. 6.11 the blue curves represent the
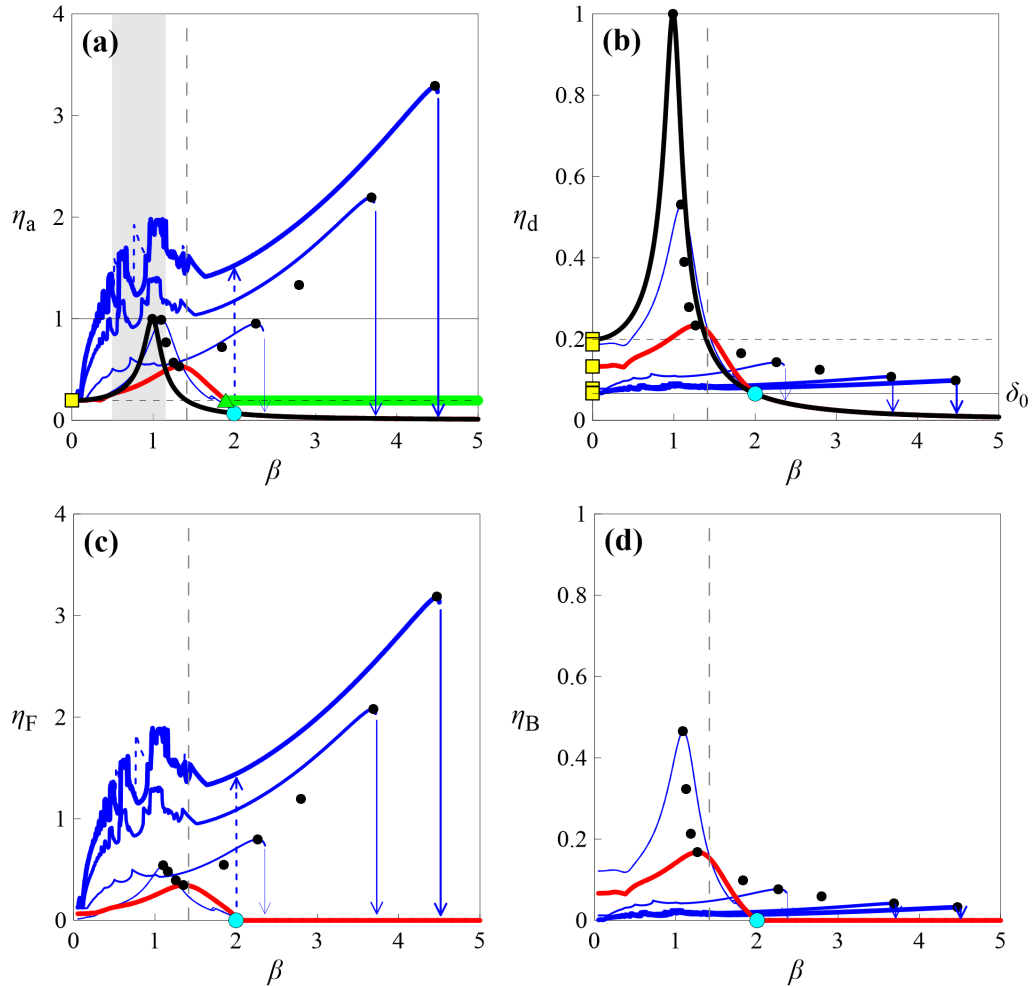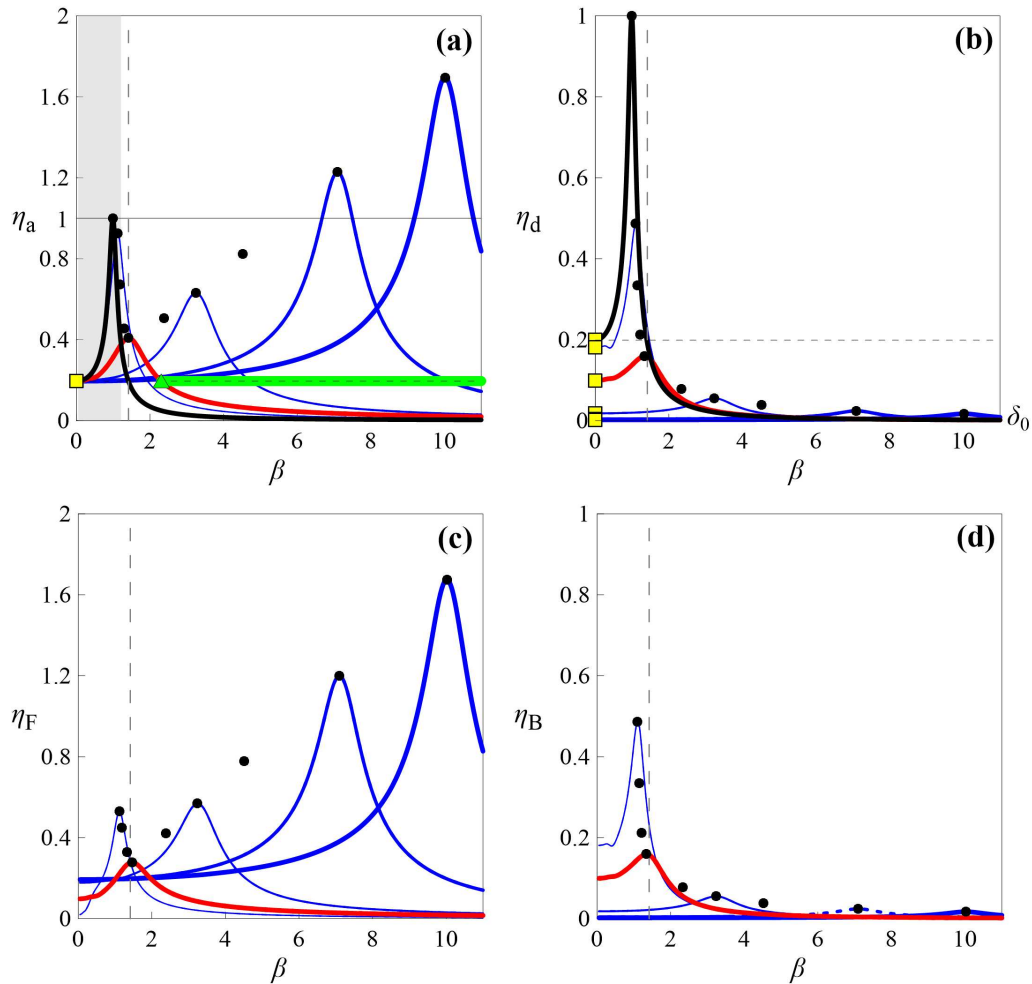
Figure 6.10. Sections of the PRCs for $\xi = 0.1$, $\gamma = 5$, $\delta_0 = 0$ and for several values of the stiffness ratio λ ($0.1 \leq \lambda \leq 100$): **a** η_a; **b** η_d; **c** η_F; **d** η_B. The *black curves* (in **a** and **b**) represent the free flight condition, the *red curves* identify the PRCs corresponding to the λ value at which the envelope of the maximum values of the acceleration shows a minimum ($\lambda = \lambda_\mathrm{opt}$), while the *blue curves* represent the PRCs corresponding to the other values of λ (the thickness of the line increases with λ). The *black dots* identify the primary resonance condition. In **a** and **b** the *yellow squares* indicate the values of η_a and η_d for $\beta = 0$. Finally, in **a** the *green triangle* identifies the β_c value, for $\lambda = \lambda_\mathrm{opt}$, such that $\eta_\mathrm{a} < \eta_\mathrm{a}|_{\beta=0}$ for $\beta > \beta_\mathrm{c}$ (*horizontal green line*). The *vertical gray band* in **a** highlights the frequency interval in which the PRC of η_a corresponding to $\lambda = \lambda_\mathrm{opt}$ (*red curve*) is below the PRC corresponding to the free flight condition (*black curve*).

locus of the β_3 values for different stiffness ratios (the thickness of the lines increases with λ). In the two limit cases, namely $\delta_0 = 1$ (free flight condition, absence of impact) and $\delta_0 = 0$ (bumpers initially in contact with the mass, occurrence of impact for each β value) hysteresis never occurs, regardless of λ. For $0 < \delta_0 < 1$, if the horizontal line $\delta_0 = constant$ intersects one of the blue curves, it means that for that pair $\delta_0 - \lambda$ the jump phenomenon, and thus the hysteresis, will occur. It can be seen that the amplitude of the frequency range associated with the hysteresis (between the descending branch of the black curve and one of the blue curves) increases, for a given δ_0, as λ increases (increasing thickness of the blue line) and, for a given λ, as δ_0 decreases.
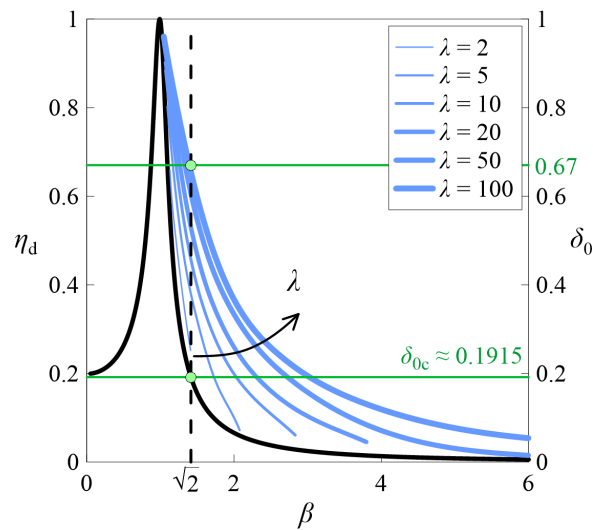
Figure 6.11. PRC of η_{d} in free flight condition (*black curve*) for $\xi = 0.1$ together with the envelopes of the downward jumps frequencies (β_3, *blue lines*) for $\gamma = 5$ and several λ values. The thickness of the line increases with λ.

From the same figure, it is also possible to see if, for the considered values of δ_0 and λ, due to the occurrence of impact, the response of the system will be modified, compared to the free flight condition, also for $\beta > \sqrt{2}$ (vertical dashed line). Three gap ranges can be identified. For $\delta_0 > 0.67$ (above the upper horizontal green line) the occurrence of impact will modify the response of the system only in the frequency range $\beta < \sqrt{2}$, for each considered λ value, with $0 < \lambda \leq 100$, since β_3 is always lower than $\sqrt{2}$ (all the blue curves are to the left of the vertical dotted line $\beta = \sqrt{2}$). It is worth noting that the threshold value of the dimensionless gap $\delta_0 = 0.67$ depends on the maximum value of the stiffness ratio considered in the analysis ($\lambda_{\mathrm{max}} = 100$ in this study) and it increases as λ_{max} increases. For $\delta_0 < \delta_{0c}$ (below the lower horizontal green line), where $\delta_{0c} \simeq 0.1915$ is the value of the dimensionless gap at which $\beta_2 = \sqrt{2}$, the response will be modified in any case, regardless of λ, not only for $0 \leq \beta < \sqrt{2}$, but also for $\beta > \sqrt{2}$. The extend of the frequency range beyond $\sqrt{2}$, affected by the occurrence of impact, becomes gradually larger as λ increases. For $\delta_{0c} \leq \delta_0 \leq 0.67$ (between the two horizontal green lines), the response will be modified also for $\beta > \sqrt{2}$ only if $\lambda > \lambda_c$. For each dimensionless gap within this range, the corresponding λ_c value is that associated with the blue

curve which, for the considered δ_0 value, intersects the vertical dashed line $\beta = \sqrt{2}$. It can be observed that λ_c, starting from $\lambda_c = \lambda_{max} = 100$ for $\delta_0 \simeq 0.67$, decreases as δ_0 decreases.

Resonance condition   For a given δ_0 value, the increase in the stiffness ratio λ causes a gradually more pronounced bending of the PRCs, with the increase in the resonant frequency and the occurrence of the jump phenomena and the hysteresis, for $\lambda > \lambda_H(\delta_0)$. As concerns the values of the selected response quantities in resonance condition (η_i^*, i = a, d, F, B), it was observed that, compared to the free flight condition, the increase in λ causes an increasing reduction of the displacement of the mass and of the deformation of the bumpers, while the acceleration of the mass and the contact force, after a first increase, for very small values of λ, decrease, reach a minimum and then start to grow again. Regarding the static displacement, it decreases, as λ increases, only if $0 \leq \delta_0 < \delta_0^*$.

By extending the range of investigation to other values of the dimensionless gap, for $0 \leq \delta_0 \leq 1$ and $0.05 \leq \lambda \leq 100$, always assuming $\xi = 0.1$ and $\gamma = 5$, the contour maps shown in Fig. 6.12 were obtained. In particular, in Figs. 6.12a-d the contour maps of the maximum values of the excursion of the absolute acceleration of the mass (η_a^*), the relative displacement of the mass (η_d^*), the contact force (η_F^*) and the deformation of the bumpers (η_B^*) respectively, are represented. Fig. 6.12e and Fig. 6.12f, instead, correspond to the resonant frequency β_R and the excursion of the static displacement $\eta_{d,st}$ respectively. The use of logarithmic scale for the λ axis allows to see better the evolution of the selected quantities in the range of small stiffness ratios.

From Fig. 6.12a it can be observed that, in most cases ($\lambda - \delta_0$ pairs), the occurrence of the impact against the obstacles causes an increase of the peak value of the acceleration compared to the free flight condition ($\eta_a^* > 1$). For large values of λ η_a^* can reach values up to 5. However, for small values of λ ($\lambda < 20$) and for $\delta_0 < 0.4$, the peak value of the acceleration, despite the occurrence of impact, can be lower than in free flight condition ($\eta_a^* < 1$. The contour level corresponding to $\eta_a^* = 1$ is highlighted with a thick black line. For each δ_0 value, it is possible to identify the value of λ at which the envelope of the maximum values of the acceleration shows a minimum. The locus of the λ values corresponding to this condition (denoted as λ_{opt}) is represented with a thick red curve. By focusing the attention on the range $0 \leq \delta_0 \leq 0.4$, at which, through the introduction of the obstacles it is possible to obtain a reduction of the acceleration, compared to the free flight condition ($\eta_a^* < 1$), it can be observed that the minimum occurs, regardless of δ_0, for $\lambda_{opt} \simeq 1$.

The thick blue line represents the locus of the values of λ, denoted as λ_H, beyond which, for a given δ_0 value, the jump phenomena, and thus the hysteresis, occur. It can be observed that while in the two limit cases ($\delta_0 = 1$ and $\delta_0 = 0$), the hysteresis never occurs, for $0 < \delta_0 < 1$, λ_H decreases as δ_0 decreases, reaching the lower values ($\lambda_H \simeq 1.4$) for $0.3 < \delta_0 < 0.5$, then it starts to increase again as δ_0 further decreases. It can be noted that, for each δ_0 value, $\lambda_{opt} < \lambda_H$ (the red curve is always to the left of the blue curve), meaning that in the condition corresponding to the minimum peak value of the acceleration of the mass, the hysteresis never occurs.

Finally, the thick green curve represents the locus of the values of λ, denoted as
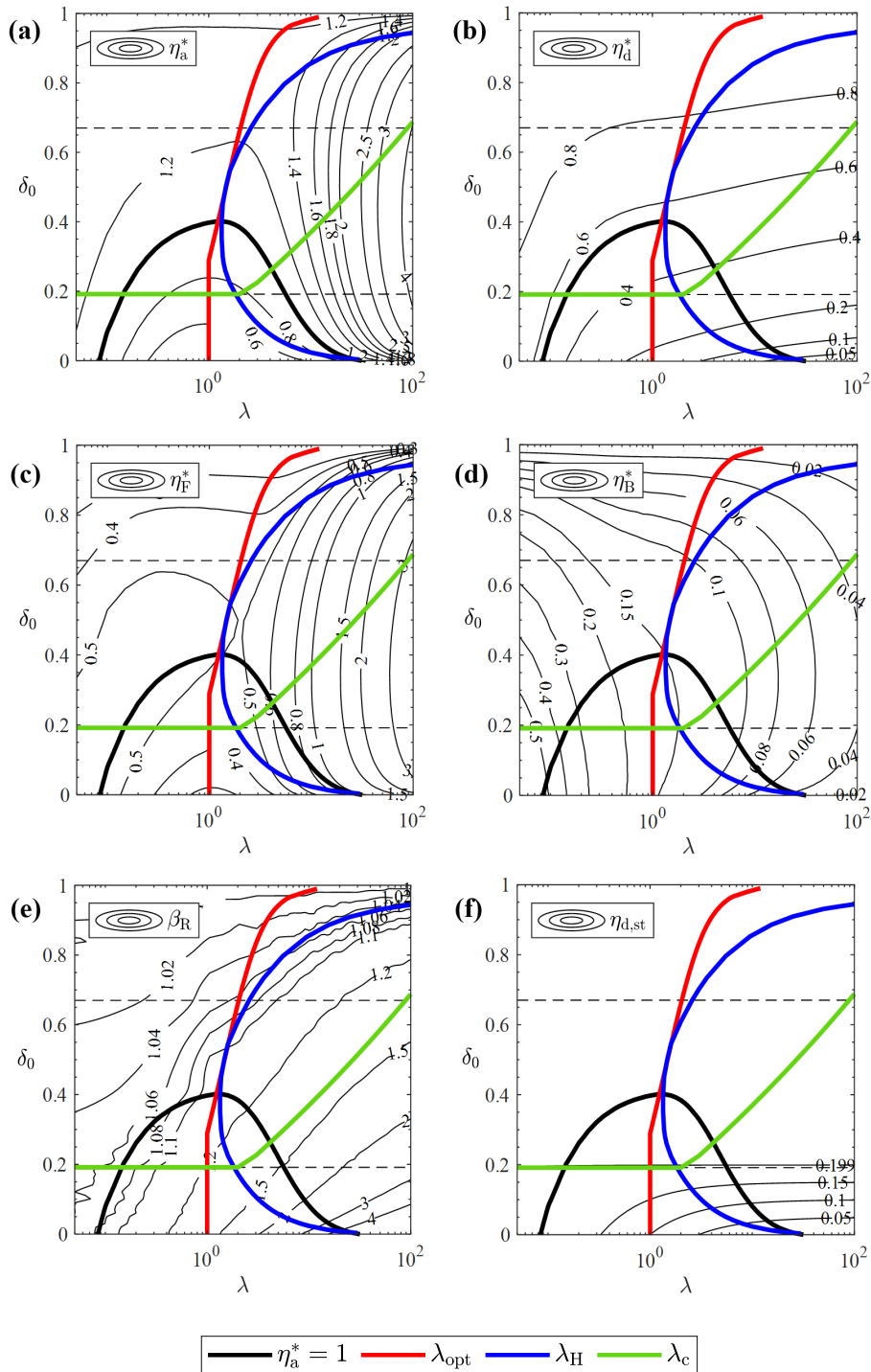
Figure 6.12. Contour maps of: **a** η_a^*; **b** η_d^*; **c** η_F^*; **d** η_B^*; **e** β_R; **f** $\eta_{d,st}$ for $\xi = 0.1$, $\gamma = 5$, $0.05 \le \lambda \le 100$ and $0 \le \delta_0 \le 1$. The *black curve* highlights the contour level corresponding to a unit value of η_a^*. The *red, blue* and *green curves* represent the values of λ_{opt}, λ_H and λ_c respectively, for each δ_0 value.

λ_c, beyond which, for a given δ_0 value, the occurrence of impact causes a modification of the system response, compared to the free flight condition, also for $\beta > \sqrt{2}$. It can be observed this curve tends to an asymptotic value as λ increases. For $\delta_0 \gtrsim 0.67$, since there are no intersections between the green curve and the horizontal line corresponding to a constant gap ($\lambda_c > \lambda_{max} = 100$), the response will be modified, due to the occurrence of impact, only in the frequency range $\beta < \sqrt{2}$. On the contrary, for $\delta_0 < \delta_{0c} \simeq 0.1915$ the response will be modified also for $\beta > \sqrt{2}$ regardless of λ. For $\delta_{0c} \leq \delta_0 \lesssim 0.67$, the isolation frequency range will be modified, compared to the free flight condition, only if $\lambda > \lambda_c$ (on the right of the green curve).

The curves corresponding to $\eta_a^* = 1$ (black curve), λ_{opt} (red curve), λ_H (blue curve) and λ_c (green curve) were reported in all the contour maps in Fig. 6.12.

As concerns the peak value of the excursion of the relative displacement of the mass (Fig. 6.12b) , it is always lower than in the free flight condition ($\eta_d^* < 1$). It decreases as δ_0 decreases, for a given λ value, and decreases as λ increases, for a given δ_0 value. In the latter case, the extent of the reduction decreases as λ increases (the contour lines tend to become horizontal).

The contour map of the peak value of the excursion of the contact force (Fig. 6.12c) is quite similar to that of the acceleration. η_F^* increases with λ, for a given δ_0 value. For a given value of λ, for example $\lambda = 10$, as δ_0 decreases, η_F^* increases, reaches a maximum and then starts to decrease.

As concerns the peak value of the excursion of the deformation of the bumpers (Fig. 6.12d) , it decreases with λ, for a given δ_0 value, becoming particularly small for large values of the stiffness ratio. For a given value of λ, for example $\lambda = 10$, as δ_0 decreases, η_B^* increases, reaches a maximum and then starts to decrease.

As concerns the resonant frequency (Fig. 6.12e) it varies between 0.99 and about 10, and the greater values are reached for quite small dimensionless gaps and large values of the stiffness ratio. It increases with λ, for a given δ_0 value, and it increases as δ_0 decreases, for a given λ value.

Finally, regarding the excursion of the static displacement of the mass, Fig. 6.12f shows that for $\delta_0^* \leq \delta_0 \leq 1$ it remains equal to 0.199 independently of δ_0 and λ, whereas for $0 \leq \delta_0 < \delta_0^*$ the static displacement decreases as δ_0 decreases, for a given λ value, and as λ increases, for a given δ_0 value. In the latter case, the extent of the reduction decreases as λ increases (the contour lines tend to become horizontal).

The case $\lambda = \lambda_{opt}$ Let's now focus the attention on the condition corresponding, for each δ_0 value, to the minimum value of the acceleration of the mass in resonance condition ($\lambda = \lambda_{opt}$, red curve in Fig. 6.12). From Fig. 6.13a it can be observed that, starting from the free flight condition ($\delta_0 = 1$) and decreasing δ_0, the peak value of the normalized excursion of the absolute acceleration of the mass η_a^* (red curve), starting from a unit value for $\delta_0 = 1$ increases, reaches a maximum for $\delta_0 \simeq 0.8$ ($\eta_a^* \simeq 1.27$) and then starts to decrease, becoming again equal to 1 for $\delta_0 \simeq 0.4$ (vertical dashed line) and lower than 1 for $0 \leq \delta_0 < 0.4$. The minimum value is reached for $\delta_0 = 0$, where $\eta_a^* \simeq 0.41$.
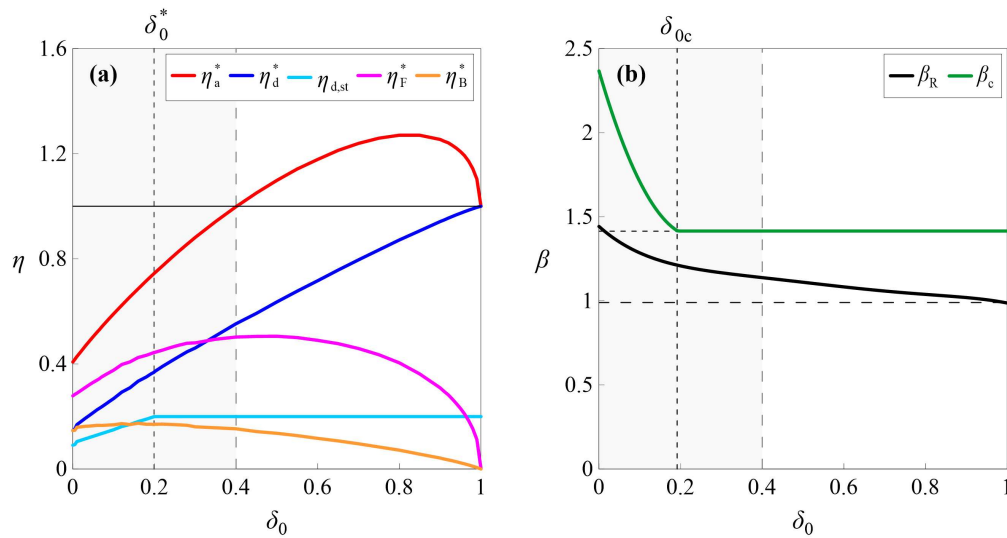
Figure 6.13. Trends with the dimensionless gap δ_0 of: **a** values of the system response at resonance (η_i^*, i = a, d, F, B) and static displacement of the mass ($\eta_{\mathrm{d,st}}$); **b** frequency ratios (β_{R} and β_{c}), for $\xi = 0.1$, $\gamma = 5$ and $\lambda = \lambda_{\mathrm{opt}}(\delta_0)$.

The peak value of the normalized excursion of the relative displacement of the mass η_{d}^* (blue curve), starting from a unit value for $\delta_0 = 1$, decreases as δ_0 decreases, reaching the minimum value for $\delta_0 = 0$, where $\eta_{\mathrm{d}}^* \simeq 0.15$. As concerns the excursion of the static displacement (light blue curve), it does not vary, remaining equal to $2\xi\sqrt{1 - \xi^2} \simeq 0.199$, as long as $\delta_0^* < \delta_0 \leq 1$, whereas for $0 \leq \delta_0 < \delta_0^*$, it starts to decrease as δ_0 decreases, reaching the value $\eta_{\mathrm{d,st}} \simeq 0.09$ for $\delta_0 = 0$.

The peak value of the normalized excursion of the contact force η_{F}^* (magenta curve), starting from zero for $\delta_0 = 1$ (absence of impact), increases, reaches a maximum for $\delta_0 \simeq 0.45$ ($\eta_{\mathrm{F}}^* \simeq 0.5$) and then starts to decrease, reaching the value $\eta_{\mathrm{F}}^* \simeq 0.28$ for $\delta_0 = 0$. In the gap range of interest ($0 \leq \delta_0 \leq 0.4$, highlighted with a light gray band) η_{F}^* decreases as δ_0 decreases.

The peak value of the normalized excursion of the deformation of the bumpers η_{B}^* (orange curve), starting from zero for $\delta_0 = 1$ (absence of impact), increases, reaches a maximum for $\delta_0 \simeq 0.15$ ($\eta_{\mathrm{B}}^* \simeq 0.17$) and then starts to decrease, reaching the value $\eta_{\mathrm{B}}^* \simeq \eta_{\mathrm{d}}^* \simeq 0.15$ (the deformation of the bumpers and the displacement of the mass are comparable) for $\delta_0 = 0$. In the gap range of interest ($0 \leq \delta_0 \leq 0.4$, highlighted with a light gray band) η_{B}^* tends to a more or less constant value as δ_0 decreases.

From Fig. 6.13b it can be observed that, always for $\lambda = \lambda_{\mathrm{opt}}$, the resonant frequency ratio β_{R} (black curve), starting from $\beta_{\mathrm{R}} \simeq 0.99$ (horizontal dashed line) for $\delta_0 = 1$, increases as δ_0 decreases, reaching the value $\beta_{\mathrm{R}} \simeq 1.47$ for $\delta_0 = 0$. As concerns the β value beyond which the absolute acceleration of the mass is lower than the ground acceleration (β_{c}, green curve), it is equal to $\sqrt{2}$ as long as $\delta_{0\mathrm{c}} \leq \delta_0 \leq 1$ (the isolation frequency interval is the same as in the linear case), then it starts to increase, reaching the value $\beta_{\mathrm{c}} \simeq 2.37$ for $\delta_0 = 0$. Consequently, for $0 \leq \delta_0 < \delta_{0\mathrm{c}}$, as δ_0 decreases, the occurrence of impact causes a greater reduction of the interval isolation frequency interval, compared to the linear case.

Based on these considerations, although the reduction of the gap allows to reduce the peak value of the response of the system in resonance condition and, for $0 \leq \delta_0 < \delta_0^*$, also the static displacement, very small values of δ_0 involve an increasing modification of the system response in the frequency range of interest for the isolation in the linear case ($\beta > \sqrt{2}$). Consequently, it would be preferable not to reach too low values of δ_0 in order not to alter, or alter to a limited extent, the system response, accepting higher peak values for acceleration, displacement and static displacement of the mass, contact force and deformation of the bumpers.

Other considerations By comparing, at the same frequency, the PRCs of η_a and η_d for $\lambda = \lambda_{opt}$ with those corresponding to the free flight condition, other interesting considerations have emerged. In general, in the condition corresponding to the minimum value of the acceleration in resonance condition ($\lambda = \lambda_{opt}$), and for $\beta_1 \leq \beta \leq \beta_2$, the displacement is lower compared to the free flight condition, except for a small frequency interval, just before β_2, where the occurrence of impact causes a slight increase of the displacement. As concerns the acceleration, for $0 \leq \delta_0 < 0.4$, there is a frequency range, within $\beta_1 \leq \beta \leq \beta_2$ (highlighted in Figs. 6.6-6.10 with a vertical gray band), in which, the acceleration of the mass, despite the occurrence of impact, is lower compared to the free flight condition. As δ_0 decreases, the amplitude of this frequency range increases. Consequently, if the comparison with the free flight condition is made at the same frequency, and not referring to the resonance condition, contrary to what one would expect, the introduction of the obstacle does not always reduce the displacement and does not always increase the acceleration.

6.4.1   Mechanical justification of the condition corresponding to the minimum peak acceleration

From the results of the parametric analysis it was observed that, for each investigated δ_0 value, and for $\xi = 0.1$ and $\gamma = 5$, as λ increases, while the envelopes of the maximum values of the displacement of the mass η_d^* and of the deformation of the bumpers η_B^* decrease, the envelopes of the peak of the absolute acceleration of the mass η_a^* and of the contact force η_F^* show a minimum. At this condition, in addition to the occurrence of the minimum of η_a^* and η_F^* (although the latter is however greater than in the free flight condition, where impact does not occur), also a reduction of the peak value of both the relative displacement of the mass and of the deformation of the bumpers (although the latter is however greater than in the free flight condition, where impact does not occur) was observed. Furthermore, to this is also added the reduction of the static displacement for $0 \leq \delta_0 < \delta_0^*$.

With reference to the range of δ_0 values of greatest interest in this study, that is $0 \leq \delta_0 \leq 0.4$, at which it is possible to obtain a reduction not only of the displacement, but also of the acceleration of the mass, compared to the free flight condition ($\eta_a^* < 1$), it was found that, regardless of δ_0, the minimum peak value of acceleration occurs at a stiffness value $\lambda_{opt} \simeq 1$. Based on this observation, the aim of this section is to try to give a mechanical justification to why, for $\xi = 0.1$ and $\gamma = 5$, a unit value of the stiffness ratio λ is preferable to the others.

In the following figures, referring to the value of the dimensionless gap corresponding to $\beta_2 = 2$, that is $\delta_0 \simeq 0.066$, a comparison between different values of stiffness ratio λ is carried out, in terms of force-displacement cycles (Fig. 6.14) and time histories (Fig. 6.15) in resonance condition, that is for $\beta = \beta_{\mathrm{R}}(\lambda)$. In particular, in addition to the free flight condition, three values of λ were considered, namely the one that corresponds, for the selected δ_0 value, to the minimum of η_{a}^* ($\lambda = 1$), and two other values of λ, one lower and the other greater than 1, respectively $\lambda = 0.1$ and $\lambda = 5$.

In Fig. 6.14 the comparison between the different λ values is made in terms of force-displacement cycles in resonance condition. In particular, Fig. 6.14a refers to the mass (inertia force f_{I} vs. relative displacement q of the mass), whereas Fig. 6.14b refers to the bumpers (contact force f_j vs. position d_j of the bumper, $j = \mathrm{R, L}$). The position of the extremity of the bumper, measured from the side of the mass at time $\tau = 0$, is related to its deformation q_j through the expression $d_j(\tau) = q_j(\tau) + \delta_{0j}$ ($j = \mathrm{R, L}$). Starting from zero initial condition, the thin lines represent the transient response, while the cycles at steady-state are highlighted with thicker lines. The gray curve refers to the free flight condition, the blue curve to $\lambda = 0.1$, the red curve to $\lambda = 1$ and the black curve to $\lambda = 5$. The two black dashed vertical lines represent the initial position of the bumpers (initial gap δ_0).
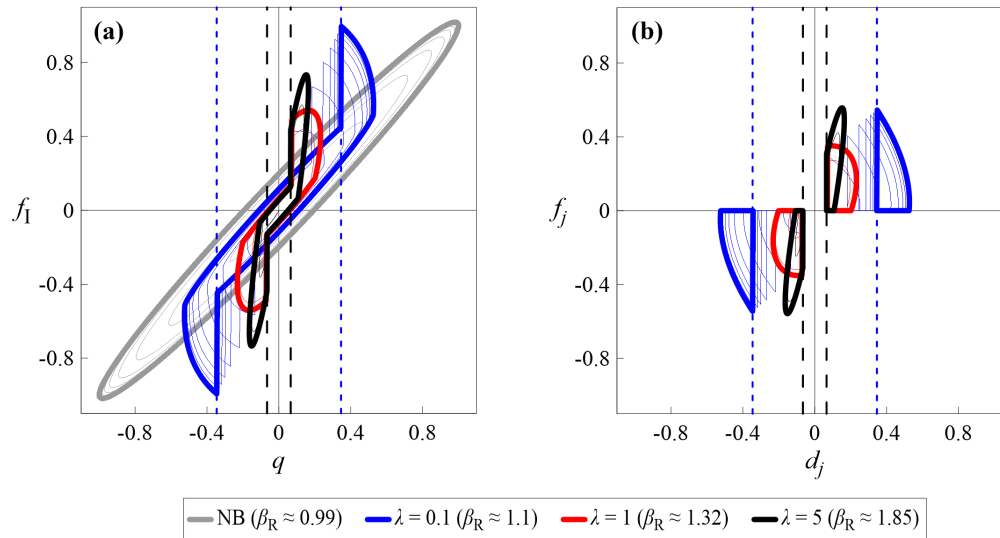
Figure 6.14. Force-displacement cycles ($\xi = 0.1$, $\gamma = 5$, $\delta_0 \simeq 0.066$) in resonance condition ($\beta = \beta_{\mathrm{R}}(\lambda)$), without obstacles (free flight, NB, *gray line*), and for three values of the stiffness ratio, namely $\lambda = 0.1$ (*blue line*), $\lambda = 1$ (*red line*) and $\lambda = 5$ (*black line*): **a** mass; **b** bumpers. Starting from zero initial conditions, the thin lines represent the transient response, while the thick lines highlight the cycle at steady-state.

In Fig. 6.15 the comparison is made in terms of time histories, considering the first 10 cycles and starting from zero initial conditions. The first column (Figs. 6.15a,d,g) refers to $\lambda = 0.1$, the second (Figs. 6.15b,e,h) to $\lambda = 1$ and the third (Figs. 6.15c,f,i) to $\lambda = 5$. In Figs. 6.15a-c the gray line and the black line represent the position $d(\tau)$ of the mass (which is nothing more than its displacement relative to the ground

$d(\tau) = q(\tau))$ in free flight condition (gray line) and after the introduction of the obstacles (black line). The red and blue lines represent the position of the extremity of the right and left bumper respectively, denoted as $d_j(\tau)$ ($j =$ R, L). In Figs. 6.15d-f the gray line and the black line represent the absolute acceleration $\alpha(\tau)$ of the mass in free flight condition (gray line) and after the introduction of the obstacles (black line). Finally, Figs. 6.15g-i show the time histories of the contact forces $f_j(\tau)$ ($j =$ R, L) between the mass and the right (red line) and left (blue line) bumper respectively.

From Fig. 6.14a it can be observed that, compared to the free flight condition (gray curve), the introduction of gradually stiffer obstacles (increasing λ), keeping fixed the gap δ_0, results in gradually increasing reduction of the maximum displacement of the mass, while the peak value of the inertia force (and thus of the absolute acceleration of the mass) shows a minimum for $\lambda = 1$ (red curve) and than starts to increase. As concerns the bumpers (Fig. 6.14b), the increase in λ causes a reduction of the deformation of the bumpers, while the peak value of the contact force shows a minimum for $\lambda = 1$ and than starts to increase. Furthermore, it can be noted that, compared to $\lambda = 1$ (red cycle) and $\lambda = 5$ (black cycle), for $\lambda = 0.1$ (blue cycle), as time goes by, the distance between the mass and the bumpers (gap) gradually increases, reaching, at steady-state, a value greater than the initial one ($\delta_{0,fin} \simeq 0.34 > \delta_0$, represented with blue dotted vertical lines in Figs. 6.14a,b).

■ As it can be seen from Fig. 6.15a, for $\lambda = 0.1$, the mass impacts the bumper before the complete recovery of its deformation, causing the impact to occur, for each forcing cycle, for a value of the gap gradually greater than the initial one (horizontal dashed lines), reaching the final value of about 0.34 at the steady-state. This behavior is due to the relatively large value of the relaxation time of the bumpers, that is the time the bumper needs to completely recover its deformation, which depends on its dissipative capabilities. It is defined as:

$$\tau_{\mathrm{r}j} = \omega \frac{C_j}{K_j} = 2\xi \frac{\gamma_j}{\lambda_j} \quad (j = \mathrm{R, \ L}) \tag{6.4}$$

For a fully elastic material ($\gamma_j = 0$) $\tau_{\mathrm{r}j} = 0$ ($j =$ R, L), and so the recovery is instantaneous, whereas a fully viscous material ($\lambda_j = 0$) $\tau_{\mathrm{r}j} \to \infty$ ($j =$ R, L) remains deformed after the detachment, without recovering its deformation. In presence of both elastic and viscous components, the relaxation time is finite and depends on the dissipative capability of the material.

For $\xi = 0.1$, $\gamma = 5$ and $\lambda = 0.1$ it is $\tau_{\mathrm{r}j} = 10$ ($j =$ R, L). The bumper does not have enough time to completely recover its deformation, and thus to dissipate all the stored energy during the contact, before the mass impacts it again. Consequently, when impact occurs again it has a residual deformation, which cause the actual gap to be greater than the initial one (δ_0).

■ For $\lambda = 5$ (Fig. 6.15c), on the contrary, the bumper quickly recovers the deformation after the detachment from the mass ($\tau_{\mathrm{r}j} = 0.2$, $j =$ R, L) and it remains, for a certain time, in the undeformed configuration until the mass impacts it again.

■ For $\lambda = 1$ (Fig. 6.15b), instead, the mass impacts the bumper practically at the moment when it has finished recovering all its deformation. Consequently, the
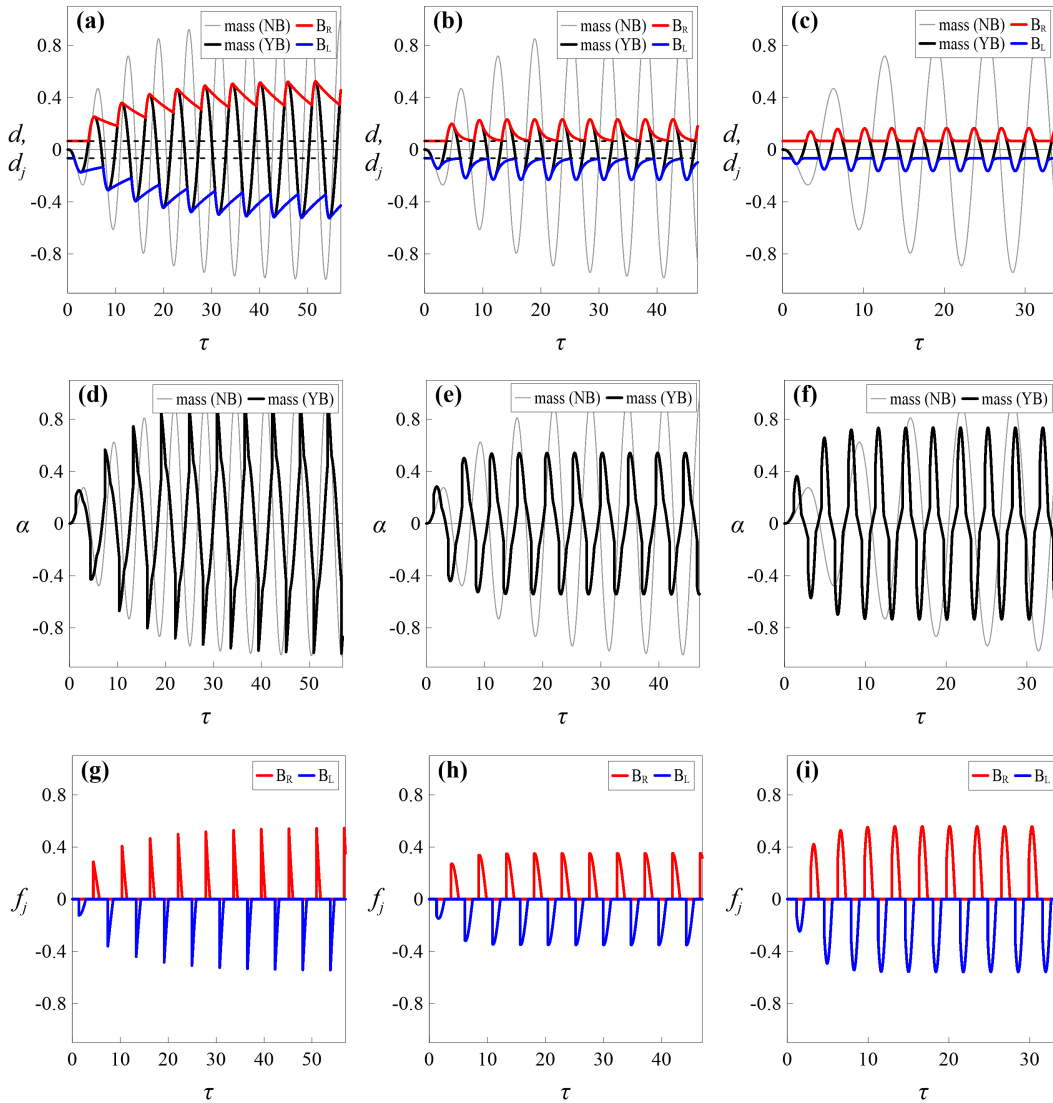
Figure 6.15. Time histories referring to the first ten cycles and starting from zero initial conditions, for $\xi = 0.1$, $\gamma = 5$, $\delta_0 \simeq 0.066$. Position of the mass (*black line*) and the bumpers (*red line* for the right bumper B_R and *blue line* for the left bumper B_L): **a** $\lambda = 0.1$ and $\beta_R \simeq 1.1$; **b** $\lambda = 1$ and $\beta_R \simeq 1.32$; **c** $\lambda = 5$ and $\beta_R \simeq 1.85$. Absolute acceleration of the mass (*black line*): **d** $\lambda = 0.1$ and $\beta_R \simeq 1.1$; **e** $\lambda = 1$ and $\beta_R \simeq 1.32$; **f** $\lambda = 5$ and $\beta_R \simeq 1.85$. Contact force between the mass and the bumpers (*red line* for the right bumper B_R and *blue line* for the left bumper B_L): **g** $\lambda = 0.1$ and $\beta_R \simeq 1.1$; **h** $\lambda = 1$ and $\beta_R \simeq 1.32$; **i** $\lambda = 5$ and $\beta_R \simeq 1.85$. In **a-f** the gray line represents the response (position and absolute acceleration) of the mass in free flight condition (without obstacles).

bumper has enough time to recover and, at the same time, it does not remain inactive. For $\xi = 0.1$ and $\gamma = 5$, this value of λ corresponds to an approximately unit value of the relaxation time ($\tau_{\mathrm{r}j} = 1$, $j = $ R, L).

From the time histories of the absolute acceleration of the mass (Figs. 6.15d-f) it is possible to observe the spikes due to the occurrence of impact. Furthermore, as concerns the amplitude of the acceleration after the introduction of the obstacle (black curve), it can be noted that for $\lambda = 0.1$ (Fig. 6.15d) it is comparable with that corresponding to the free flight condition, while for the other two values of stiffness ratio, it is lower. In particular, for $\lambda = 1$, the reduction is greater, as already observed by looking at the force-displacement cycles (Fig. 6.14a).

At the value of the stiffness ratio corresponding to the minimum of the peak value of the acceleration, also a minimum of the peak value of the contact force corresponds, as shown in Fig. 6.15h.

Based on these considerations, it would seem that, for a given δ_0 value, for $0 \le \delta_0 \le 0.4$, and for $\xi = 0.1$ and $\gamma = 5$, when the stiffness ratio is such that the relaxation time is close to unity ($\tau_{\mathrm{r}j} \simeq 1$, $j = $ R, L), the maximum value of the acceleration of the mass η_{a}^* reaches a minimum. This is probably due to the fact that the bumpers are fully exploited, meaning with this that they have enough time to recover their deformation by dissipating energy and, on the other, they do not remain inactive because impact practically occurs immediately after recovery. Consequently, for $\xi = 0.1$, $\gamma = 5$ and $0 \le \delta_0 \le 0.4$, the condition $\tau_{\mathrm{r}j} \simeq 1$ ($j = $ R, L) can be reasonably assumed as representative of the condition which corresponds to the minimum value of the acceleration of the mass in resonance condition. This allows to reduce the number of parameters which characterize the obstacles (position δ_0, and mechanical properties γ and λ), since two of them (γ and λ) are related to each other through the relationship:

$$\frac{\gamma_j}{\lambda_j} \simeq \frac{1}{2\xi} \quad (j = \mathrm{R, \ L}) \tag{6.5}$$

6.4.2   Further investigations

For each δ_0 value, theoretically there would be infinite λ-γ pairs that satisfy the relationship 6.5. It would therefore be interesting to understand if, among these pairs, there is one preferable to the others. For this purpose, as an example, in Fig. 6.16, is illustrated, assuming $\xi = 0.1$ and $\gamma/\lambda = 5$, the evolution of the PRCs with λ for $\delta_0 \simeq 0.066$, that is the value of the dimensionless gap corresponding to $\beta_2 = 2$. The meaning of colors and symbols is the same as in Figs. 6.5-6.10. The represented PRCs correspond to the free flight condition (black curve) and to the λ-γ pairs: (0.1, 0.5), (1, 5), (2, 10), (5, 25) and (10, 50). It can be observed that, although each PRC shown in Fig. 6.16 corresponds to a λ-γ pair which satisfies the relationship 6.5, the response of the system can vary significantly changing the values of λ and γ (such that $\gamma/\lambda = 5$).
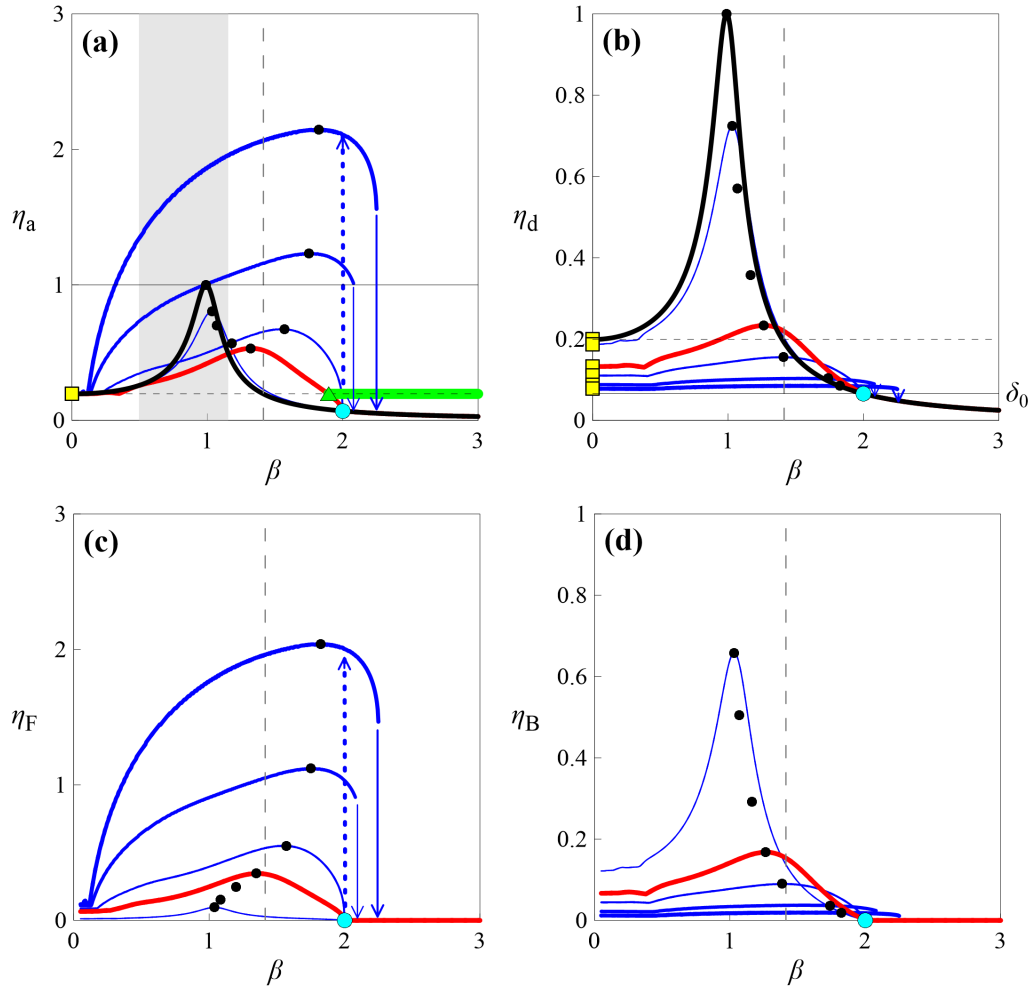
Figure 6.16. Sections of the PRCs for $\xi = 0.1$, $\gamma/\lambda = 5$, $\delta_0 \simeq 0.066$ (value of δ_0 so that $\beta_2 = 2$) and for several values of the stiffness ratio λ ($0.1 \leq \lambda \leq 10$): **a** η_a; **b** η_d; **c** η_F; **d** η_B. The *black curves* (in **a** and **b**) represent the free flight condition, the *red curves* identify the PRCs corresponding to the λ value at which the envelope of the maximum values of the acceleration shows a minimum ($\lambda = \lambda_{opt}$), while the *blue curves* represent the PRCs corresponding to the other values of λ (the thickness of the line increases with λ). The *black dots* identify the primary resonance condition. In **a** and **b** the *yellow squares* indicate the values of η_a and η_d for $\beta = 0$. The *cyan circles* represent the location of β_2. Finally, in **a** the *green triangle* identifies the β_c value, for $\lambda = \lambda_{opt}$, such that $\eta_a < \eta_a|_{\beta=0}$ for $\beta > \beta_c$ (*horizontal green line*). The *vertical gray band* in **a** highlights the frequency interval in which the PRC of η_a corresponding to $\lambda = \lambda_{opt}$ (*red curve*) is below the PRC corresponding to the free flight condition (*black curve*).

As concerns the trend of the maximum values of the response, highlighted with black dots, similar considerations to those made for $\gamma = 5$ (Fig. 6.9) apply. The resonant frequency increases with λ (and thus with γ) and then, for large values of λ and γ, it remains almost constant ($\beta_\mathrm{R} \simeq 1.8$). For small values of λ the peak value of the acceleration of the mass (Fig. 6.16a) first decreases, reaches a minimum (lower than one) and then starts to increase again, reaching values greater than one. The peak values of both the displacement of the mass (Fig. 6.16b) and of the deformation of the bumpers (Fig. 6.16d) decrease as λ (and thus γ) increases. As concerns the peak value of the contact force, it increases with λ (and thus with γ) (Fig. 6.16c). The static displacement of the mass (yellow squares in Fig. 6.16b) decreases with λ (and thus with γ).

Compared to the case where γ is kept fixed (Fig. 6.9), no secondary resonances were observed. As for $\gamma = 5$, also when $\gamma/\lambda = 5$, it is possible to identify a value of λ, beyond which the jump phenomena, and thus the hysteresis, occur. For this δ_0 value it is $\lambda_\mathrm{H} \simeq 2.6$. Furthermore, as already observed for $\gamma = 5$, also in this case, since $\delta_0 < \delta_{0\mathrm{c}}$, the introduction of the obstacles, modifies, regardless of λ, the response of the system also in the frequency range $\beta > \sqrt{2}$ and the reduction of the isolation frequency interval, compared to the linear case, increases as λ increases.

It is worth noting that, although each PRC shown in Fig. 6.16 corresponds to a λ-γ pair which satisfies the relationship 6.5, it is possible to identify a pair which can be considered preferable to the others. This is the λ-γ pair at which the peak value of the acceleration shows a minimum, that is $\lambda_\mathrm{opt} \simeq 1$ and $\gamma_\mathrm{opt} \simeq 5$ (thick red curve in Fig. 6.16a). In this situation, in addition to the reduction of the peak acceleration, which is also lower than the free flight condition ($\eta_\mathrm{a}^* < 1$), also a significant reduction of both the peak value of the displacement of the mass, and of the static displacement, was observed. Furthermore, the acceleration becomes lower than that of the ground for $\beta > \beta_\mathrm{c} \simeq 1.9$ (green triangle in Fig. 6.16a).

In Fig. 6.17 the comparison between three of the considered λ-γ pairs is made in terms of force-displacement cycles at steady-state resonance condition, referring to the mass (Fig. 6.17a) and to the bumpers (Fig. 6.17b) respectively. In particular, in addition to the gray curve, which in Fig. 6.17a represents the free flight condition, the blue, red and black curves refer to the λ-γ pairs $(0.5, 2.5)$, $(1, 5)$ and $(2, 10)$ respectively. This figure is qualitatively similar to Fig. 6.14, in which all the curves are characterized by the same value of γ. The difference is that in Fig. 6.17 each curve corresponds to a λ-γ pair which satisfies the relationship $\gamma/\lambda = 5$ ($\tau_\mathrm{r} = 1$). Despite this, for $\lambda = \lambda_\mathrm{opt} = 1$ and $\gamma = \gamma_\mathrm{opt} = 5$ (red curve), the maximum inertia force (and thus the maximum absolute acceleration of the mass), shows a minimum. Compared to Fig. 6.14b, instead, for this λ-γ pair the maximum contact force does not show a minimum. As concerns the displacement of the mass and the deformation of the bumpers, the considerations made for $\gamma = 5$ apply also in this case.

By repeating the analysis also for other values of δ_0, in the range $0 \leq \delta_0 \leq 1$ and for $0.01 \leq \lambda \leq 10$, always assuming $\xi = 0.1$ and $\gamma/\lambda = 5$, the contour maps shown in Fig. 6.18 were obtained. In particular, in Figs. 6.18a-d the contour maps of the peak values of the absolute acceleration of the mass (η_a^*), the relative displacement
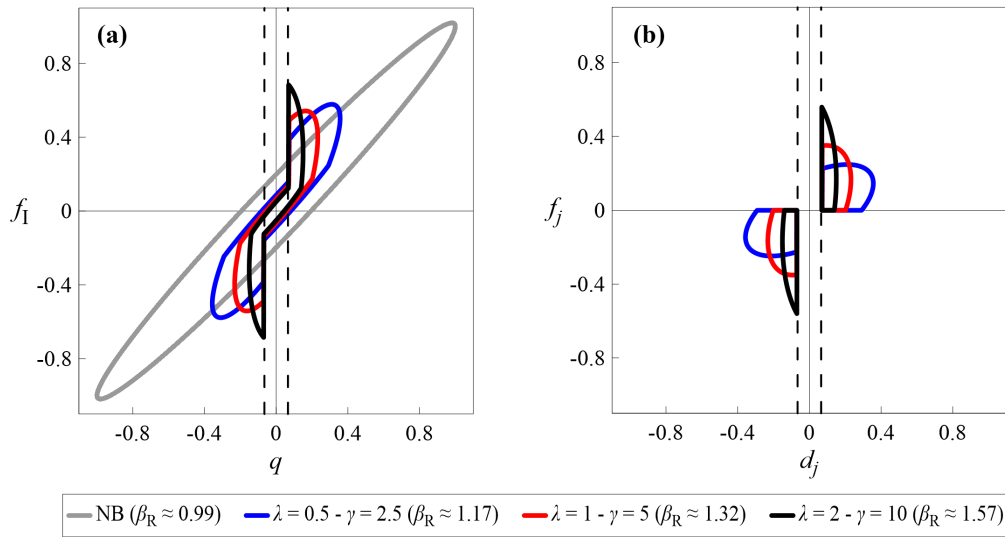
Figure 6.17. Force-displacement cycles ($\xi = 0.1$, $\gamma/\lambda = 5$, $\delta_0 \simeq 0.066$) in steady-state resonance condition ($\beta = \beta_R(\lambda)$), without obstacles (free flight, NB, *gray line*), and for $\lambda = 0.5, \gamma = 2.5$ (*blue line*), $\lambda = 1, \gamma = 5$ (*red line*) and $\lambda = 2, \gamma = 10$ (*black line*): **a** mass; **b** bumpers.

of the mass (η_d^*), the contact force (η_F^*) and the deformation of the bumpers (η_B^*) respectively, are represented. Fig. 6.18e and Fig. 6.18f, instead, show the contour maps of the resonant frequency β_R and of the excursion of the static displacement $\eta_{d,st}$ respectively. The use of logarithmic scale for the λ axis allows to see better the evolution of the selected quantities in the range of small stiffness ratios.

From Fig. 6.18a it can be observed that, in most cases ($\lambda - \delta_0$ pairs), the occurrence of the impact against the obstacle causes an increase of the peak value of the acceleration compared to the free flight condition ($\eta_a^* > 1$). However, for small values of λ ($\lambda < 10$) and for $\delta_0 < 0.8$ the peak value of the acceleration, despite the occurrence of impact, can be lower than in free flight condition ($\eta_a^* < 1$). The contour level corresponding to $\eta_a^* = 1$ is highlighted with a thick black line. For each δ_0 value in the range $0 \leq \delta_0 < 0.8$, it is possible to identify the λ-γ pair corresponding to the minimum peak value of the acceleration. The locus of the λ values corresponding to this condition (λ_{opt}) is represented with a thick red curve. It can be observed that the minimum occurs for gradually smaller values of λ as δ_0 increases. For $\delta_0 \geq 0.8$, instead, the peak value of the acceleration is always greater than in free flight condition ($\eta_a^* > 1$) and it increases with λ.

The thick blue line represents the locus of the values of λ, denoted as λ_H, beyond which, for a given δ_0 value, the jump phenomena, and thus the hysteresis, occur. It can be observed that while in the two limit cases ($\delta_0 = 1$ and $\delta_0 = 0$), the hysteresis never occurs, for $0 < \delta_0 < 1$, λ_H decreases as δ_0 decreases, reaching the lower values ($\lambda_H \simeq 1$) for $0.3 < \delta_0 < 0.5$, then it starts to increase again as δ_0 further decreases. It can be noted that, for each δ_0 value, $\lambda_{opt} < \lambda_H$, meaning that in the condition corresponding to the minimum peak value of the acceleration of the mass the hysteresis never occurs.
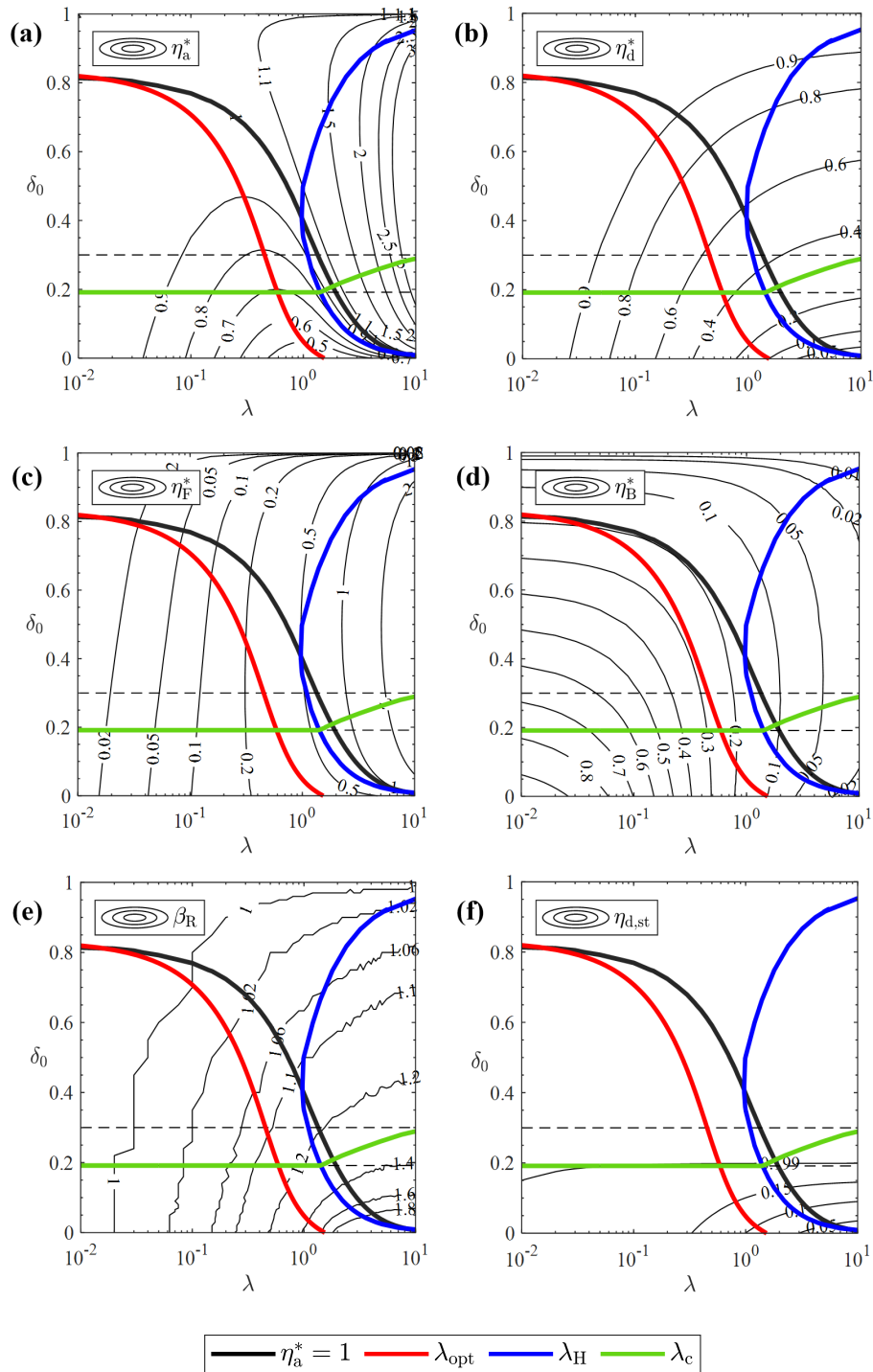
Figure 6.18. Contour maps of: **a** η_a^*; **b** η_d^*; **c** η_F^*; **d** η_B^*; **e** β_R; **f** $\eta_{d,st}$ for $\xi = 0.1$, $\gamma/\lambda = 5$, $0.01 \leq \lambda \leq 10$ and $0 \leq \delta_0 \leq 1$. The *black curve* highlights the contour level corresponding to a unit value of η_a^*. The *red, blue* and *green curves* represent the values of λ_{opt}, λ_H and λ_c respectively, for each δ_0 value.

Finally, the thick green curve represents the locus of the values of λ, denoted as λ_c, beyond which, for a given δ_0 value, the occurrence of impact causes a modification of the system response, compared to the free flight condition, also for $\beta > \sqrt{2}$. It can be observed this curve tends to an asymptotic value as λ increases. For $\delta_0 \gtrsim 0.3$ (above the upper dashed horizontal line), since there are no intersections between the green curve and the horizontal line corresponding to a constant gap ($\lambda_c > 10$), the response will be modified, due to the occurrence of impact, only in the frequency range $\beta < \sqrt{2}$. On the contrary, for $\delta_0 < \delta_{0c} \simeq 0.1915$ (below the lower dashed horizontal line) the response will be modified also for $\beta > \sqrt{2}$ regardless of λ. For $\delta_{0c} \le \delta_0 \lesssim 0.3$ (between the two dashed horizontal lines), the isolation frequency range will be modified, compared to the free flight condition, only if $\lambda > \lambda_c$ (on the right of the green curve). It is worth noting that, compared to the case $\gamma = 5$ (Fig. 6.12), the green curve is much flatter and the threshold value of the gap has been lowered from about 0.67 to about 0.3. Consequently, the gap range in which the isolation frequency interval is not modified, compared to the linear case (absence of intersections between the green curve and the horizontal line $\delta_0 = constant$), has significantly expanded.

The curves corresponding to $\eta_a^* = 1$ (black curve), λ_{opt} (red curve), λ_H (blue curve) and λ_c (green curve) were reported in all the contour maps in Fig. 6.18.

As concerns the peak value of the excursion of the relative displacement of the mass (Fig. 6.18b) , it is always lower than in the free flight condition ($\eta_d^* < 1$). It decreases as δ_0 decreases, for a given λ value, and decreases as λ increases, for a given δ_0 value. In the latter case, the extent of the reduction decreases as λ increases (the contour lines tend to become horizontal).

From Fig. 6.18c it can be observed that the peak value of the excursion of the contact force η_F^* increases with λ, for a given δ_0 value. For a given value of λ, for example $\lambda = 2$, as δ_0 decreases, η_F^* increases, reaches a maximum and then starts to decrease.

As concerns the peak value of the excursion of deformation of the bumpers (Fig. 6.18d) , it decreases with λ, for a given δ_0 value, becoming particularly small for large values of the stiffness ratio. For a given value of λ, for example $\lambda = 2$, as δ_0 decreases, η_B^* increases, reaches a maximum and then starts to decrease.

As concerns the resonant frequency (Fig. 6.18e) it varies between 0.99 and about 4, and the greater values are reached for quite small dimensionless gaps. It increases with λ, for a given δ_0, and it increases as δ_0 decreases, for a given λ value.

Finally, regarding the excursion of the static displacement of the mass, Fig. 6.18f shows that for $\delta_0^* \le \delta_0 \le 1$ it remains equal to 0.199 independently of δ_0 and λ, whereas for $0 \le \delta_0 < \delta_0^*$ the static displacement decreases as δ_0 decreases, for a given λ value, and as λ increases, for a given δ_0 value. In the latter case, the extent of the reduction decreases as λ increases (the contour lines tend to become horizontal).

The case $\lambda = \lambda_{\mathrm{opt}}$

Let's now focus the attention on the condition corresponding to the minimum peak value of the acceleration of the mass ($\lambda = \lambda_{\mathrm{opt}}(\delta_0)$), at which furthermore no hysteresis occurs ($\lambda_{\mathrm{opt}} < \lambda_{\mathrm{H}}$). In this condition, the trends of the characteristic values of β with the dimensionless gap δ_0 are shown in Fig. 6.19a. In particular, the β_1 and β_2 values are represented with a red and a blue line respectively, the black line corresponds to the resonant frequency β_{R}, while the green line refers to β_{c}. While the values of β_1 and β_2 depend only on ξ and δ_0 (Sect. 6.3), β_{R} and β_{c} also depend on λ and γ. This figure allows to highlight some aspects related to the β values, not observable in the contour maps (Fig. 6.18).

From Fig. 6.19a it can be observed that β_{R} (black curve), starting from $\beta_{\mathrm{R}} = \beta_{\mathrm{Rd}} \simeq 0.99$ for $\delta_0 = 1$ (free fight condition), increases as δ_0 decreases, reaching its maximum value ($\beta_{\mathrm{R}} \simeq 1.7$) for $\delta_0 = 0$. This can be seen also from Figs. 6.19b-e, in which, for some selected values of δ_0, the PRCs of η_{a} (upper row) and η_{d} (lower row) are shown, considering both the free flight condition (black curve) and the condition corresponding to the minimum peak value of the acceleration (red curve). In these figures, the resonances are highlighted with black dots.

As concerns β_1 (red curve in Fig. 6.19a) and β_2 (blue curve in Fig. 6.19a), that is the frequencies which delimit the interval in which impact surely occurs due to geometric reasons, they coincide ($\beta_1 = \beta_2 = \beta_{\mathrm{Rd}} \simeq 0.99$) for $\delta_0 = 1$ (free fight condition) and then increasingly diverge as δ_0 decreases, with $\beta_1 < \beta_{\mathrm{Rd}}$ and $\beta_2 > \beta_{\mathrm{Rd}}$. For $\delta_0 \leq \delta_0^* \simeq 0.199$, impact occurs immediately ($\beta_1 = 0$). For $0 \leq \delta_0 < \delta_0^*$ impact still occurs from $\beta = 0$, but, compared to the case $\delta_0 = \delta_0^*$, the equation $R(\xi, \beta) = \delta_0$ admits only one solution (β_2, blue curve). Finally, when the bumpers are initially in contact with the mass ($\delta_0 = 0$), impact occurs for each β value (the equation $R(\xi, \beta) = \delta_0$ does not admit roots). Since $\lambda_{\mathrm{opt}} < \lambda_{\mathrm{H}}$, impact will not occur for $\beta < \beta_1$ nor for $\beta > \beta_2$. In Figs. 6.19b-e these frequency values are represented respectively with a cyan diamond and a cyan circle. These two symbols are both visible for $\delta_0 = 0.3$ (first column, Fig. 6.19b), whereas only β_2 (cyan circle) appears for $\delta_0 = \delta_{0\mathrm{c}} \simeq 0.1915$ (second column, Fig. 6.19c) and for $\delta_0 = 0.03$ (third column, Fig. 6.19d). For $\delta_0 = 0$ (fourth column, Fig. 6.19e), neither is present.

Referring now to the frequency value beyond which, when impact occurs, the amplitude of the acceleration of the mass becomes lower than the amplitude of the ground acceleration, denoted as β_{c} and represented with a green line in Fig. 6.19a (and with a green triangle in the PRCs, Figs. 6.19b-e), it is possible to identify two gap ranges, namely $\delta_{0\mathrm{c}} < \delta_0 \leq 1$ and $0 < \delta_0 < \delta_{0\mathrm{c}}$.

■ For $\delta_{0\mathrm{c}} < \delta_0 \leq 1$ (see also Fig. 6.19b, corresponding to $\delta_0 = 0.3$), $\beta_{\mathrm{c}} = \sqrt{2}$, meaning that, in the presence of obstacles, the frequency interval in which $\eta_{\mathrm{a}} < \eta_{\mathrm{a}}|_{\beta=0}$ (highlighted in green) is the same as in the linear case (free flight condition) and, furthermore, $\beta_2 < \sqrt{2}$. Consequently:

- for $0 \leq \beta < \beta_1$ impact does not occur and thus the system behaves like a linear system; furthermore, $\eta_{\mathrm{a}} > \eta_{\mathrm{a}}|_{\beta=0}$

- for $\beta_1 \leq \beta \leq \beta_2$ impact surely occurs and it is still $\eta_{\mathrm{a}} > \eta_{\mathrm{a}}|_{\beta=0}$
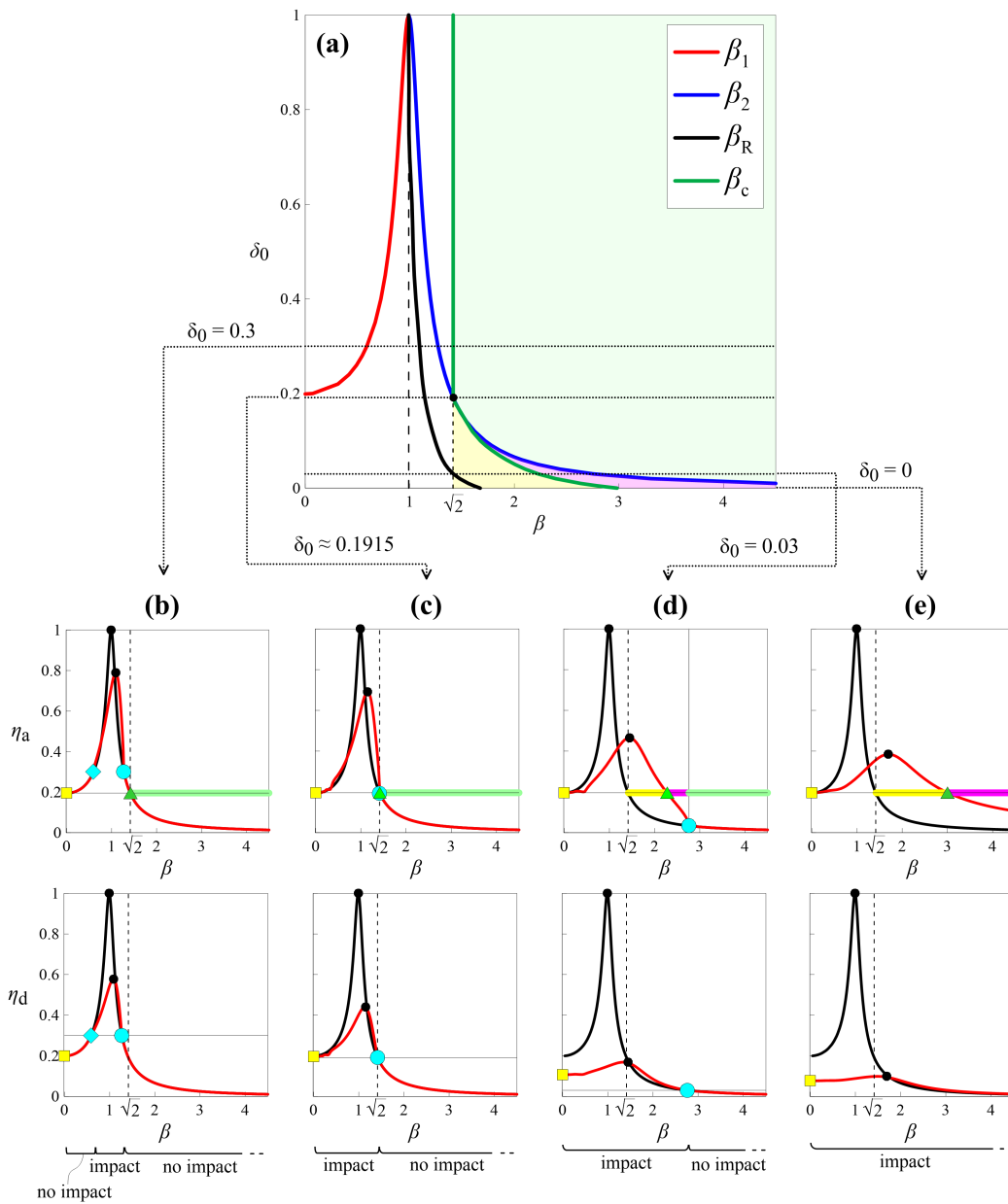
Figure 6.19. **a** Trends of the characteristic β values (β_1: *red line*, β_2: *blue line*, β_R: *black line*, β_c: *green line*) with the dimensionless gap δ_0 in the condition corresponding to the minimum peak value of the acceleration of the mass ($\xi = 0.1$, $\gamma/\lambda = 5$ and $\lambda = \lambda_{\mathrm{opt}}$). The colored areas represent different situations which can occur in the nonlinear system when $\beta > \sqrt{2}$, compared to the free flight condition, as shown also in the lower part of the figure (**b-e**), where for selected values of δ_0, the PRCs of η_a (upper row) and η_d (lower row) referring to both the free flight condition (*black line*) and the condition corresponding to the minimum peak value of the acceleration (*red line*) are represented. The colored symbols represent the location of the characteristic β values (β_1: *cyan diamond*, β_2: *cyan circle*, β_R: *black circles*, β_c: *green triangle*) and the *yellow squares* represent the values of η_a and η_d for $\beta = 0$.

- for $\beta_2 < \beta < \beta_c$ impact does not occur (since $\lambda_{\mathrm{opt}} < \lambda_H$) and thus the system behaves like a linear system; but it is still $\eta_a > \eta_a|_{\beta=0}$

- for $\beta \geq \beta_c$ impact does not occur and thus the system behaves like a linear system; furthermore, $\eta_a < \eta_a|_{\beta=0}$ (this frequency interval is highlighted with a green area in Fig. 6.19a and with an horizontal green line in Fig. 6.19b).

■ For $\delta_0 = \delta_{0c}$ (see also Fig. 6.19c), it is $\beta_2 = \beta_c = \sqrt{2}$ (the blue and the green curves in Fig. 6.19a intersect, and the cyan circle and the green triangle in Fig. 6.19c overlap). Consequently:

- for $0 \leq \beta < \sqrt{2}$ impact surely occurs and it is $\eta_a > \eta_a|_{\beta=0}$

- for $\beta \geq \sqrt{2}$ impact does not occur (since $\lambda_{\mathrm{opt}} < \lambda_H$) and thus the system behaves like a linear system; furthermore, $\eta_a < \eta_a|_{\beta=0}$ (this frequency interval is highlighted with a green area in Fig. 6.19a and with an horizontal green line in Fig. 6.19c).

■ For $0 < \delta_0 < \delta_{0c}$ (see also Fig. 6.19d, corresponding to $\delta_0 = 0.03$), $\beta_c > \sqrt{2}$ and, furthermore, $\beta_2 > \beta_c$. Consequently:

- for $0 \leq \beta < \beta_c$ impact surely occurs. Compared to the linear case (free flight), when impact occurs, for $\sqrt{2} \leq \beta < \beta_c$, it is $\eta_a > \eta_a|_{\beta=0}$. The amplitude of this frequency interval, highlighted with a yellow area in Fig. 6.19a and with an horizontal yellow line in Fig. 6.19d, increases as δ_0 decreases

- for $\beta_c < \beta \leq \beta_2$ impact still occurs but now it is $\eta_a < \eta_a|_{\beta=0}$, meaning that, the amplitude of the acceleration of the mass is lower than the amplitude of the ground acceleration, but it is still greater than the acceleration in free flight condition. The amplitude of this frequency interval, highlighted with a magenta area in Fig. 6.19a and with an horizontal magenta line in Fig. 6.19d, increases as δ_0 decreases

- for $\beta > \beta_2$ impact does not occur (since $\lambda_{\mathrm{opt}} < \lambda_H$) and it is $\eta_a < \eta_a|_{\beta=0}$, and thus the system behaves like a linear system (this frequency interval is highlighted with a green area in Fig. 6.19a and with an horizontal green line in Fig. 6.19d).

■ For $\delta_0 = 0$ (see also Fig. 6.19e), impact occurs for each β value and β_c reaches its maximum value ($\beta_c \simeq 3$). Consequently:

- for $0 \leq \beta < \beta_c$ impact surely occurs. Compared to the linear case (free flight), when impact occurs, for $\sqrt{2} \leq \beta < \beta_c$ (frequency interval highlighted in yellow), it is $\eta_a > \eta_a|_{\beta=0}$

- for $\beta \geq \beta_c$ impact still occurs but now it is $\eta_a < \eta_a|_{\beta=0}$, meaning that, the amplitude of the acceleration of the mass is lower than the amplitude of the ground acceleration, but it is still greater than the acceleration in free flight condition (frequency interval highlighted in magenta).

By comparing the PRCs in free flight condition (black curves) and those associated with the occurrence of impact (red curve) at the same frequency, it can be observed that in some frequency ranges the response (both displacements and accelerations), when impact occurs, is lower then in free flight condition, in other instead is greater.

Based on these considerations, although, at $\delta_0 = 0$ we have the lowest peak values of acceleration, displacement and the lowest values of static displacement (yellow dots), this gap value is characterized by the increased erosion of the frequency range in which isolation occurs in the linear case (the extent of the erosion is highlighted in yellow in Fig. 6.19) and furthermore, for $\beta > \beta_c$, the response is always greater than in the free flight condition.

In order to limit the erosion of the isolation frequency range, compared to the linear case, it would be appropriate to consider higher (but not too much) values of δ_0, accepting higher peaks values of both the acceleration and the displacement of the mass, the contact force, the deformation of the bumpers and the static displacement.

6.5 Closing remarks

In this chapter, the effect of the introduction of deformable and dissipative obstacles (bumpers), to limit the displacement of a base-isolated SDOF system, compared to the free flight condition, was investigated through numerical parametric analyses. The study of the nonlinear dynamic behavior of the system is necessary to get some indications on how to guide the system response in order to reach specific objectives.

The selected response quantities are the absolute acceleration and the relative displacement of the mass, the contact force and the deformation of the bumpers. In addition to these, some considerations regarding the resonant frequency and the static displacement of the mass were also made.

By fixing the damping ratio and the dissipative capabilities of the bumpers, the results showed that the occurrence of the impact against the bumpers can significantly modify the system response, depending on the values of the dimensionless gap and of the stiffness ratio, both for $\beta < \sqrt{2}$ and $\beta > \sqrt{2}$. In particular, while the peak value of the displacement of the mass is always reduced compared to the free flight condition, the peak value of the acceleration in general is increased, except for small values of both the stiffness ratio and the dimensionless gap, for which the peak acceleration can be lower compared to the free flight condition.

Referring to these ranges of parameters, it was observed that, for each value of the dimensionless gap, it is possible to identify a condition preferable to the others at which the envelope of the values of the acceleration in resonance condition shows a minimum. This occurs, regardless of the dimensionless gap, when the stiffness ratio and the damping ratio, which define the mechanical properties of the bumpers, are such that the relaxation time is about 1. In this condition the bumpers, on the one hand, have enough time to recover their deformation, after the detachment from the mass, by dissipating energy and, on the other, they do not remain inactive because impact practically occurs immediately after recovery. In the condition corresponding to the minimum value of the acceleration in resonance neither jumps nor hysteresis occur, and in addition to the minimum value of the acceleration in

resonance condition, also a significant reduction of the displacement was observed. To this is also added the reduction of the static displacement for small gaps.

Furthermore, for a given gap, among all the pairs of stiffness ratio and damping ratio that correspond to a unitary relaxation time, it is possible to identify one at which the maximum acceleration in resonance shows again a minimum.

In general, the results showed that, with reference to the condition corresponding to the minimum value of the acceleration in resonance, the smaller the gap, the greater the reduction of the peak values of both the displacement and the acceleration of the mass and of the static displacement, compared to the free flight condition.

However, it would be preferable not to reach too low values of gap in order not to alter, or alter to a limited extent, the system response for $\beta > \sqrt{2}$, that is in the frequency interval of interest for the isolation in the linear case, accepting higher values in resonance.

In conclusion, the obtained results showed that the occurrence of impact, depending on the values of the parameters, can modify the system response, compared to the free flight condition, both for $\beta < \sqrt{2}$ and $\beta > \sqrt{2}$. By properly selecting the parameters which characterize the obstacles, it is possible to effectively reduce not only the response (displacements and accelerations) in resonance condition, compared to the absence of obstacles, but also the static displacement, maintaining unaltered the frequency interval of interest for the isolation ($\beta > \sqrt{2}$).

With regard to the future developments of this work, there is the intention to extend the study considering other types of excitation (earthquakes, white noise, impulsive force). Furthermore, it would be interesting to confirm the obtained results through experimental tests.

Chapter 7

Conclusions

The subject of this Ph.D. thesis was inspired by the practical problem of large horizontal seismic-induced displacements in base-isolated structures, which, on the one hand, can damage the isolation system itself, and on the other, can lead to pounding with surrounding moat walls or adjacent structures, if the available seismic gap is not sufficient. This thesis starts from the theoretical and experimental exploratory study conducted by Andreaus, De Angelis et al. It aims to investigate in a more targeted and circumscribed way some of the aspects emerged from this exploratory study.

The problem was studied, both experimentally and numerically, considering a Single-Degree-Of-Freedom (SDOF) system with two-sided symmetric deformable and dissipative constraints (bumpers), excited at the base by a step-wise forward and backward sine-sweep signal. With the aim of mitigating the response of the system, thinking both of displacements and accelerations, as a first step, extensive parametric experimental and numerical analyses were carried out to investigate the influence of the fundamental parameters which characterize the problem on the system response. The continuous interaction between experimental and numerical investigations is one of the elements characterizing the study conducted during the doctoral course.

Shaking table tests were carried out on a small-scale physical model, using a rich sensor apparatus (accelerometers, displacement transducers, impact load cells), and considering three values of peak table acceleration A, different gap amplitudes G, and four bumpers B. In particular a number of gap amplitudes, going from large to small positive up to negative, were investigated. Furthermore, the selected bumpers allowed to investigate different types of obstacle, ranging from very soft to quite rigid. Starting from the experimental results, some of the scenarios which can occur in the system response, varying the considered parameters (A, G, B), were identified and described. These scenarios were classified based on the characteristics of the forward and backward Pseudo-Resonance Curves (PRCs) of normalized excursion of absolute acceleration and relative displacement of the mass, assuming as reference case the absence of bumpers (free flight condition). The identified scenarios were subsequently investigated in more detail resorting to phase portraits, Fourier spectra and time histories in steady-state condition.

The experimental investigations have been joined by numerical analyses performed considering a relatively simple model and using a Matlab code, specifically created for this purpose, which made it possible to carry out extensive parametric investigations. In the numerical model, described in terms of dimensionless parameters, both the damper and the bumpers where modeled with a viscoelastic law, retaining the other sources of nonlinearity, namely the existence of clearances, the unilaterality of the contact and the occurrence of impact, which causes abrupt changes of stiffness and damping at the contact time. This model was therefore defined as Simplified Nonlinear Model (SNM) and its parameters were identified based on the experimental data. The adoption of a soft impact model allowed to describe the deformation and the recovery of the bumpers, otherwise not observable by resorting to the coefficient of restitution. The introduction of suitable dimensionless parameters (δ_0, λ and γ) allowed to generalize the results, releasing them from the values assumed by the individual involved physical quantities (A, G, B). Due to the adopted normalization, the effect of the input was taken into account indirectly through the damping ratio and the dimensionless gap. Despite its relative simplicity, the SNM has proven to be able to reproduce satisfactorily the experimental results. For this reason, it was used to deepen the study of the scenarios extending the range of investigation, thus considering values of the parameters not investigated in the experimental tests.

A study on the role played by the damping ratio, which, due to the adopted normalization, influences both the response and the input, allowed to make preliminary considerations that guided further numerical in-depth investigations on the response scenarios. The numerical study, despite the relative simplicity of the model, allowed to highlight the existence of a wide variety of behaviors and phenomena. Decreasing the dimensionless gap, gradually more complex and varied scenarios, characterized by the presence of the *primary resonance with right hysteresis* and also by the occurrence of different types of *secondary resonances* in the low frequency range (with *right* or *left hysteresis* or of *non-regular* type), affecting gradually wider frequency ranges, were observed. Each scenario was investigated resorting to phase portraits and Fourier spectra and, in some cases, further analyses varying the initial conditions, with the construction of basins of attraction, were carried out. Within each scenario, homogeneous frequency intervals, characterized by similar features in terms of number (single solution, *coexisting solutions* or *pair of solutions*) and types of limit cycles (*periodic*, *quasi-periodic* or *chaotic*), were identified. The occurrence of the (*primary* and *secondary*) grazing phenomenon, and its relationship with some of the observed scenarios, was also highlighted.

The most complex scenarios were noticed for values of the gap smaller than those considered in the experimental tests. For this reason, in order to investigate the possibility to experimentally regain these complex scenarios, a new campaign of experimental tests was designed. The new tests investigated in particular small positive, null and negative values of the gap between mass and bumpers. The negative gaps were realized by slightly compressing the bumpers against the mass, causing an initial pre-strain/pre-stress state in the shock absorbers. For positive values of the gap, the experimental results confirmed the numerical predictions, with gradually more complex scenarios, characterized by the occurrence of secondary resonances in the low frequency range, as the gap decreases. At the secondary

resonances, the occurrence of internal loops, intersecting the obstacles, in both the force-displacement cycles and the phase portraits, was observed. Decreasing the frequency ratio, the number of internal loops increases, and consequently also the number of impacts per forcing cycle between the mass and the bumpers. At the approximatively zero-gap configuration the situation returns to be smooth, without jumps and hysteresis, although the behavior is still nonlinear. Moving from positive to small negative gaps, through the zero-gap configuration, a transition from a hardening-like (*primary resonance with right hysteresis*) to a softening-like (*primary resonance with left hysteresis*) behavior was observed. While for positive gaps, the stiffness change is caused by the occurrence of impact between the mass and one of the two bumpers, in a dual manner, for small negative gaps, it is caused by the detachment from one of the bumpers. Further increases in the absolute value of the negative gap, beyond a certain threshold value, since the mass cannot detach from the bumpers during its motion, lead only to an increase in the initial pre-stress and pre-strain state of the bumpers, without significantly affecting the mass (acceleration and displacement) response.

The study of the scenarios enabled to highlight interesting aspects related to the nonlinear non-smooth response of the vibro-impact SDOF system. At the same time, it made it possible to make considerations about vibration control. The intimate link between the study of the nonlinear response and the control problem is another aspect that characterizes this Ph.D. thesis. Numerical parametric analyses, carried out varying the bumpers' parameters (position and mechanical properties), allowed to investigate the effect of the introduction of the obstacles, compared to the free flight condition, and to highlight possible issues associated with the occurrence of impact. The results of the analyses showed that, by properly selecting the parameters which characterize the obstacles (δ_0, λ and γ), it is possible to guide the system's response in order to reach specific objectives, avoiding some scenarios and favouring others, and thus exploiting the occurrence of impact with beneficial effects. It was found that, for a given value of the gap, by choosing the stiffness and damping properties of the bumpers (λ and γ) such that the relaxation time is about 1 (that is $\gamma/\lambda \simeq 1/(2\xi)$), it is possible to minimize the peak value of the absolute acceleration of the mass, compared to other combinations of the obstacles' mechanical properties. Furthermore, this choice allows to avoid the jump phenomena, and thus the hysteresis (multistability). The results also showed that, by decreasing the dimensionless gap, in addition to reducing the mass displacement, it is also possible to mitigate its acceleration, compared to the free flight condition. To this is also added the reduction of the static displacement for small gaps. Gradually smaller gap values however cause a greater reduction of the frequency band of isolation, compared to the linear case. Consequently, in order not to alter, or alter to a limited extent, this frequency range, it would be preferable not to reach too small values of the gap, accepting higher values of the response in resonance.

Future developments   The results obtained in this Ph.D. thesis provide the starting point for possible future developments. First of all the study could be extended, both experimentally and numerically, taking into account also the earthquake excitation. The SNM model has the potential to provide more interesting information, and therefore it can still be used to conduct further insights related to issues arising during the doctoral course. It would be interesting to investigate, for example, the influence of damping. Subsequently, to fully capture, both qualitatively and quantitatively, the response of the system, the numerical model, already satisfactory in this simplified form, could be improved, including also the nonlinearities associated with the behavior of the damper and the bumpers. Finally, starting from the results obtained with the SDOF system, the transition to a Multi-Degree-Of-Freedom (MDOF) system could be addressed, in order to investigate also the effect of the deformation of the structure and of higher modes on the system response when impact occurs.

References

[1] ABDEL RAHEEM, S. E. Pounding mitigation and unseating prevention at expansion joints of isolated multi-span bridges. *Eng. Struct.*, **31** (2009), 2345. `doi:10.1016/j.engstruct.2009.05.010`.

[2] ABDULLAH, M. M., HANIF, J. H., RICHARDSON, A., AND SOBANJO, J. Use of a shared tuned mass damper (STMD) to reduce vibration and pounding in adjacent structures. *Earthq. Eng. Struct. Dyn.*, **30** (2001), 1185. `doi:10.1002/eqe.58`.

[3] AFSHARFARD, A. Suppressing forced vibrations of structures using smart vibro-impact systems. *Nonlinear Dyn.*, **83** (2016), 1643. `doi:10.1007/s11071-015-2437-y`.

[4] AGUIAR, R. R. AND WEBER, H. I. Impact force magnitude analysis of an impact pendulum suspended in a vibrating structure. *Shock Vib.*, **19** (2012), 1359. `doi:10.3233/SAV-2012-0678`.

[5] ALHAN, C. AND GAVIN, H. P. Reliability of base isolation for the protection of critical equipment from earthquake hazards. *Eng. Struct.*, **27** (2005), 1435. `doi:10.1016/j.engstruct.2005.04.007`.

[6] ANAGNOSTOPOULOS, S. A. Pounding of buildings in series during earthquakes. *Earthq. Eng. Struct. Dyn.*, **16** (1988), 443. `doi:10.1002/eqe.4290160311`.

[7] ANAGNOSTOPOULOS, S. A. AND SPILIOPOULOS, K. V. An investigation of earthquake induced pounding between adjacent buildings. *Earthq. Eng. Struct. Dyn.*, **21** (1992), 289. `doi:10.1002/eqe.4290210402`.

[8] ANAJAFI, H. AND MEDINA, R. A. Robust design of a multi-floor isolation system. *Struct. Control Heal. Monit.*, **25** (2018), 1. `doi:10.1002/stc.2130`.

[9] ANDREAUS, U., BARAGATTI, P., DE ANGELIS, M., AND PERNO, S. A Preliminary Experimental Study About Two-Sided Impacting SDOF Oscillator Under Harmonic Excitation. *J. Comput. Nonlinear Dyn.*, **12** (2017), 061010. `doi:10.1115/1.4036816`.

[10] ANDREAUS, U., BARAGATTI, P., DE ANGELIS, M., AND PERNO, S. Shaking table tests and numerical investigation of two-sided damping constraint for end-stop impact protection. *Nonlinear Dyn.*, **90** (2017), 2387. `doi:10.1007/s11071-017-3810-9`.

[11] ANDREAUS, U., BARAGATTI, P., AND PLACIDI, L. Experimental and numerical investigations of the responses of a cantilever beam possibly contacting a deformable and dissipative obstacle under harmonic excitation. *Int. J. Non. Linear. Mech.*, **80** (2016), 96. `doi:10.1016/j.ijnonlinmec.2015.10.007`.

[12] ANDREAUS, U. AND DE ANGELIS, M. Nonlinear dynamic response of a base-excited SDOF oscillator with double-side unilateral constraints. *Nonlinear Dyn.*, **84** (2016), 1447. `doi:10.1007/s11071-015-2581-4`.

[13] ANDREAUS, U. AND DE ANGELIS, M. Experimental and numerical dynamic response of a SDOF vibro-impact system with double gaps and bumpers under harmonic excitation. *Int. J. Dyn. Control*, **7** (2019), 1278. `doi:10.1007/s40435-019-00532-x`.

[14] ANDREAUS, U. AND DE ANGELIS, M. Influence of the characteristics of isolation and mitigation devices on the response of single-degree-of-freedom vibro-impact systems with two-sided bumpers and gaps via shaking table tests. *Struct. Control Heal. Monit.*, **27** (2020), 1. `doi:10.1002/stc.2517`.

[15] ARENA, A., LACARBONARA, W., AND CASALOTTI, A. Payload oscillations control in harbor cranes via semi-active vibration absorbers: Modeling, simulations and experimental results. *Procedia Eng.*, **199** (2017), 501. `doi:10.1016/j.proeng.2017.09.136`.

[16] BANERJEE, A., CHANDA, A., AND DAS, R. Historical Origin and Recent Development on Normal Directional Impact Models for Rigid Body Contact Simulation: A Critical Review. *Arch. Comput. Methods Eng.*, **24** (2017), 397. `doi:10.1007/s11831-016-9164-5`.

[17] BANERJEE, S., ING, J., PAVLOVSKAIA, E., WIERCIGROCH, M., AND REDDY, R. K. Invisible grazings and dangerous bifurcations in impacting systems: The problem of narrow-band chaos. *Phys. Rev. E - Stat. Nonlinear, Soft Matter Phys.*, **79** (2009), 3. `doi:10.1103/PhysRevE.79.037201`.

[18] BAO, Y., BECKER, T. C., SONE, T., AND HAMAGUCHI, H. Experimental study of the effect of restraining rim design on the extreme behavior of pendulum sliding bearings. *Earthq. Eng. Struct. Dyn.*, **47** (2018), 906. `doi:10.1002/eqe.2997`.

[19] BASILI, M. AND DE ANGELIS, M. A reduced order model for optimal design of 2-mdof adjacent structures connected by hysteretic dampers. *J. Sound Vib.*, **306** (2007), 297. `doi:10.1016/j.jsv.2007.05.012`.

[20] BASILI, M. AND DE ANGELIS, M. Optimal passive control of adjacent structures interconnected with nonlinear hysteretic devices. *J. Sound Vib.*, **301** (2007), 106. `doi:10.1016/j.jsv.2006.09.027`.

[21] BASILI, M., DE ANGELIS, M., AND FRARACCIO, G. Shaking table experimentation on adjacent structures controlled by passive and semi-active MR dampers. *J. Sound Vib.*, **332** (2013), 3113. `doi:10.1016/j.jsv.2012.12.040`.

[22] Bathe, K. J. *Finite Element Procedures.* Prentice-Hall, Englewood Cliffs New Jersey, New York (1996). ISBN 0133014584.

[23] Bharti, S. D., Dumne, S. M., and Shrimali, M. K. Seismic response analysis of adjacent buildings connected with MR dampers. *Eng. Struct.*, **32** (2010), 2122. `doi:10.1016/j.engstruct.2010.03.015`.

[24] Bhaskararao, A. V. and Jangid, R. S. Seismic response of adjacent buildings connected with friction dampers. *Bull. Earthq. Eng.*, **4** (2006), 43. `doi:10.1007/s10518-005-5410-1`.

[25] Bi, K. and Hao, H. Numerical simulation of pounding damage to bridge structures under spatially varying ground motions. *Eng. Struct.*, **46** (2013), 62. `doi:10.1016/j.engstruct.2012.07.012`.

[26] Bi, K., Hao, H., and Chouw, N. Required separation distance between decks and at abutments of a bridge crossing a canyon site to avoid seismic pounding. *Earthq. Eng. Struct. Dyn.*, **39** (2010), 303. `doi:10.1002/eqe.943`.

[27] Bishop, S. R. Impact oscillators. *Philos. Trans. R. Soc. London. Ser. A Phys. Eng. Sci.*, **347** (1994), 347. `doi:10.1098/rsta.1994.0047`.

[28] Bishop, S. R., Wagg, D. J., and Xu, D. Use of Control to Maintain Period-1 Motions during Wind-up or Wind-down Operations of an Impacting Driven Beam. *Chaos, Solitons and Fractals*, **9** (1998), 261. `doi:10.1016/S0960-0779(98)90002-9`.

[29] Blazejczyk-Okolewska, B., Czolczynski, K., and Kapitaniak, T. Dynamics of a two-degree-of-freedom cantilever beam with impacts. *Chaos, Solitons and Fractals*, **40** (2009), 1991. `doi:10.1016/j.chaos.2007.09.097`.

[30] Blazejczyk-Okolewska, B., Czolczynski, K., and Kapitaniak, T. Hard versus soft impacts in oscillatory systems modeling. *Commun. Nonlinear Sci. Numer. Simul.*, **15** (2010), 1358. `doi:10.1016/j.cnsns.2009.05.046`.

[31] Blazejczyk-Okolewska, B., Czolczynski, K., and Okolewski, A. Analytical and Numerical Investigations of Stable Periodic Solutions of the Impacting Oscillator with a Moving Base and Two Fenders. *J. Comput. Nonlinear Dyn.*, **12** (2017). `doi:10.1115/1.4036548`.

[32] Blazejczyk-Okolewska, B. and Kapitaniak, T. Co-existing attractors of impact oscillator. *Chaos, Solitons and Fractals*, **9** (1998), 1439. `doi:10.1016/S0960-0779(98)00164-7`.

[33] Bolotnik, N. N. and Melikyan, A. A. Time-optimal control of a vibroimpact system with one degree of freedom. In *Proc. Int. Conf. Control Oscil. Chaos*, 2, pp. 249–252. St. Petersburg, Russia (2000). `doi:10.1109/COC.2000.873964`.

[34] Brzeski, P., Pavlovskaia, E., Kapitaniak, T., and Perlikowski, P. Controlling multistability in coupled systems with soft impacts. *Int. J. Mech. Sci.*, **127** (2017), 118. `doi:10.1016/j.ijmecsci.2016.12.022`.

[35] BUCKLE, I. G. Passive control of structures for seismic loads. In *Proc. 12th World Conf. Earthq. Eng. No. 2834*, pp. 1–13. Auckland, New Zealand (2000). ISBN 0733-9445. `doi:10.1061/(ASCE)0733-9445(2008)134:1(3)`.

[36] BUCKLE, I. G., CONSTANTINOU, M. C., DICELI, M., AND GHASEMI, H. Seismic Isolation of Highway Bridges. Tech. rep., University of Buffalo, New York (2006).

[37] CALIÒ, I. AND MARLETTA, M. Passive control of the seismic rocking response of art objects. *Eng. Struct.*, **25** (2003), 1009. `doi:10.1016/S0141-0296(03)00045-2`.

[38] CASAGRANDE, L., VILLA, E., NESPOLI, A., OCCHIUZZI, A., BONATI, A., AND AURICCHIO, F. Innovative dampers as floor isolation systems for seismically-retrofit multi-storey critical facilities. *Eng. Struct.*, **201** (2019), 109772. `doi:10.1016/j.engstruct.2019.109772`.

[39] CHEHAIBI, K., MRAD, C., AND NASRI, R. Collision modeling of single unit impact absorber for mechanical systems vibration attenuation. *J. Theor. Appl. Mech.*, **57** (2019), 947. `doi:10.15632/jtam-pl/112417`.

[40] CHEN, J., MIN, F., JIN, Q., AND YE, B. Coexistence, bifurcation and chaos of a periodically forced duffing system with absolute nonlinearity. *Eur. Phys. J. Spec. Top.*, **228** (2019), 1405. `doi:10.1140/epjst/e2019-800221-1`.

[41] CHENG, X., JING, W., CHEN, J., AND ZHANG, X. Pounding Dynamic Responses of Sliding Base-Isolated Rectangular Liquid-Storage Structure considering Soil-Structure Interactions. *Shock Vib.*, **2017** (2017). `doi:10.1155/2017/8594051`.

[42] CHENG, X., JING, W., QI, L., AND GONG, L. Pounding Dynamic Responses and Mitigation Measures of Sliding Base-isolated Concrete Rectangular Liquid Storage Structuress. *KSCE J. Civ. Eng.*, **23** (2019), 3146. `doi:10.1007/s12205-019-0082-6`.

[43] CHIN, W., OTT, E., NUSSE, H. E., AND GREBOGI, C. Grazing bifurcations in impact oscillators. *Phys. Rev. E*, **50** (1994), 4427. `doi:10.1103/PhysRevE.50.4427`.

[44] CHIOZZI, A., SIMONI, M., AND TRALLI, A. Base isolation of heavy non-structural monolithic objects at the top of a masonry monumental construction. *Mater. Struct. Constr.*, **49** (2016), 2113. `doi:10.1617/s11527-015-0637-z`.

[45] CHOPRA, A. K. *Dynamic of Structures: Theory and Applications to Earthquake Engineering*. Pearson, Englewood Cliffs, New Jersey, fourth edn. (2012).

[46] CHRISTENSON, R. E., SPENCER, B. F., AND JOHNSON, E. A. Semiactive Connected Control Method for Adjacent Multidegree-of-Freedom Buildings. *J. Eng. Mech.*, **133** (2007), 290. `doi:10.1061/(asce)0733-9399(2007)133:3(290)`.

[47] CHRISTOPHER, P. J., DOBSON, B., AND ALEXANDER, N. A. Exploring the Dynamics of Base-Excited Structures Impacting a Rigid Stop. *Math. Probl. Eng.*, **2020** (2020). `doi:10.1155/2020/6721025`.

[48] COMPARIN, R. AND SINGH, R. Non-linear frequency response characteristics of an impact pair. *J. Sound Vib.*, **134** (1989), 259. `doi:10.1016/0022-460X(89)90652-4`.

[49] CONTENTO, A. AND DI EGIDIO, A. Investigations into the benefits of base isolation for non-symmetric rigid blocks. *Earthq. Eng. Struct. Dyn.*, **38** (2009), 849. `doi:10.1002/eqe.870`.

[50] COSTA, D., VAZIRI, V., KAPITANIAK, M., KOVACS, S., PAVLOVSKAIA, E., SAVI, M. A., AND WIERCIGROCH, M. Chaos in impact oscillators not in vain: Dynamics of new mass excited oscillator. *Nonlinear Dyn.*, (2020). `doi:10.1007/s11071-020-05644-0`.

[51] CROZET, V., POLITOPOULOS, I., AND CHAUDAT, T. Shake table tests of structures subject to pounding. *Earthq. Eng. Struct. Dyn.*, **48** (2019), 1156. `doi:10.1002/eqe.3180`.

[52] CROZET, V., POLITOPOULOS, I., YANG, M., MARTINEZ, J. M., AND ERLICHER, S. Sensitivity analysis of pounding between adjacent structures. *Earthq. Eng. Struct. Dyn.*, **47** (2018), 219. `doi:10.1002/eqe.2949`.

[53] D'ALMEIDA, E. F., AGUIAR, R. R., AND RITTO, T. G. Parametric analysis of a dynamical model of the axial vibration of a vibration-assisted drilling tool, a vibro-impact system with multiple impacts. *Arch. Appl. Mech.*, (2020). `doi:10.1007/s00419-020-01773-5`.

[54] DANKOWICZ, H. AND JERRELIND, J. Control of near-grazing dynamics in impact oscillators. *Proc. R. Soc. A Math. Phys. Eng. Sci.*, **461** (2005), 3365. `doi:10.1098/rspa.2005.1516`.

[55] DANKOWICZ, H. AND SVAHN, F. On the stabilizability of near-grazing dynamics in impact oscillators. *Int. J. Robust Nonlinear Control*, **17** (2007), 1405. `doi:10.1002/rnc.1252On`.

[56] DANKOWICZ, H. AND ZHAO, X. Local analysis of co-dimension-one and co-dimension-two grazing bifurcations in impact microactuators. *Phys. D Nonlinear Phenom.*, **202** (2005), 238. `doi:10.1016/j.physd.2005.02.008`.

[57] DE MORAES, L. P. AND SAVI, M. A. Drill-string vibration analysis considering an axial-torsional-lateral nonsmooth model. *J. Sound Vib.*, **438** (2019), 220. `doi:10.1016/j.jsv.2018.08.054`.

[58] DE SOUZA, S. L. AND CALDAS, I. L. Basins of attraction and transient chaos in a gear-rattling model. *J. Vib. Control*, **7** (2001), 849. `doi:10.1177/107754630100700605`.

[59] DE SOUZA, S. L. AND CALDAS, I. L. Controlling chaotic orbits in mechanical systems with impacts. *Chaos, Solitons and Fractals*, **19** (2004), 171. `doi: 10.1016/S0960-0779(03)00129-2`.

[60] DE SOUZA REBOUÇAS, G. F., SANTOS, I. F., AND THOMSEN, J. J. Validation of vibro-impact force models by numerical simulation, perturbation methods and experiments. *J. Sound Vib.*, **413** (2018), 291. `doi:10.1016/j.jsv.2017.10.028`.

[61] DE SOUZA REBOUÇAS, G. F., SANTOS, I. F., AND THOMSEN, J. J. Unilateral vibro-impact systems - Experimental observations against theoretical predictions based on the coefficient of restitution. *J. Sound Vib.*, **440** (2019), 346. `doi:10.1016/j.jsv.2018.10.037`.

[62] DI SARNO, L. Base Isolation of Railway Bridges. *Int. J. Mech.*, **7** (2013), 302.

[63] DICLELI, M. AND BUDDARAM, S. Equivalent linear analysis of seismic-isolated bridges subjected to near-fault ground motions with forward rupture directivity effect. *Eng. Struct.*, **29** (2007), 21. `doi:10.1016/j.engstruct.2006.04.004`.

[64] DIMITRAKOPOULOS, E. G. Nonsmooth analysis of the impact between successive skew bridge-segments. *Nonlinear Dyn.*, **74** (2013), 911. `doi: 10.1007/s11071-013-1012-7`.

[65] DIVENYI, S., SAVI, M. A., WIERCIGROCH, M., AND PAVLOVSKAIA, E. Drill-string vibration analysis using non-smooth dynamics approach. *Nonlinear Dyn.*, **70** (2012), 1017. `doi:10.1007/s11071-012-0510-3`.

[66] DUBOWSKY, S., DECK, J. F., AND COSTELLO, H. The dynamic modeling of flexible spatial machine systems with clearance connections. *J. Mech. Des. Trans. ASME*, **109** (1987), 87. `doi:10.1115/1.3258790`.

[67] DUBOWSKY, S. AND FREUDENSTEIN, F. Dynamic Analysis of Mechanical Systems With Clearances - Part 1: Formation of Dynamic Model. *J. Eng. Ind.*, **93** (1971), 305. `doi:10.1115/1.3427895`.

[68] DUBOWSKY, S. AND FREUDENSTEIN, F. Dynamic Analysis of Mechanical Systems With Clearances - Part 2: Dynamic Response. *J. Manuf. Sci. Eng. Trans. ASME*, **93** (1971), 310. `doi:10.1115/1.3427896`.

[69] DUBOWSKY, S. AND GARDNER, T. N. Design and analysis of muitilink flexible mechanisms with multiple clearance connections. *J. Manuf. Sci. Eng. Trans. ASME*, **99** (1977), 88. `doi:10.1115/1.3439171`.

[70] EL-SAYAD, M. A., HANNA, S. N., AND IBRAHIM, R. A. Parametric Excitation of Nonlinear Elastic Systems Involving Hydrodynamic Sloshing Impact. *Nonlinear Dyn.*, **18** (1999), 25. `doi:10.1023/A:1008384709906`.

[71] EMANS, J., WIERCIGROCH, M., AND KRIVTSOV, A. M. Cumulative effect of structural nonlinearities: chaotic dynamics of cantilever beam system with impacts. *Chaos, Solitons & Fractals*, **23** (2005), 1661. `doi:10.1016/j.chaos.2004.06.052`.

[72] Ervin, E. K. and Wickert, J. A. Repetitive impact response of a beam structure subjected to harmonic base excitation. *J. Sound Vib.*, **307** (2007), 2. `doi:10.1016/j.jsv.2007.06.038`.

[73] Fan, Y.-C., Loh, C.-H., Yang, J. N., and Lin, P.-Y. Experimental performance evaluation of an equipment isolation using MR dampers. *Earthq. Eng. Struct. Dyn.*, **38** (2009), 285. `doi:10.1002/eqe.844`.

[74] Fegelman, K. J. and Grosh, K. Dynamics of a flexible beam contacting a linear spring at low frequency excitation: Experiment and analysis. *J. Vib. Acoust. Trans. ASME*, **124** (2002), 237. `doi:10.1115/1.1426073`.

[75] Fenz, D. M. and Constantinou, M. C. Behaviour of the double concave Friction Pendulum bearing. *Earthq. Struct.*, **35** (2006), 1403. `doi:10.1002/eqe.589`.

[76] Flores, P., Ambrósio, J., Claro, J. P., and Lankarani, H. M. *Kinematics and Dynamics of Multibody Systems with Imperfect Joints: Models and Case Studies*. 34. Springer, Berlin (2008). ISBN 9783540743613. `doi:10.1007/978-3-540-74361-3`.

[77] Flores, P. and Lankarani, H. M. *Contact Force Models for Multibody Dynamics*. Springer (2016). ISBN 9783319308968.

[78] Flores, P., Machado, M., Silva, M. T., and Martins, J. M. On the continuous contact force models for soft materials in multibody dynamics. *Multibody Syst. Dyn.*, **25** (2011), 357. `doi:10.1007/s11044-010-9237-4`.

[79] Foale, S. and Bishop, S. R. Bifurcations in impact oscillations. *Nonlinear Dyn.*, **6** (1994), 285. `doi:10.1007/BF00053387`.

[80] Gavin, H. P. and Zaicenco, A. Performance and reliability of semi-active equipment isolation. *J. Sound Vib.*, **306** (2007), 74. `doi:10.1016/j.jsv.2007.05.039`.

[81] Gilardi, G. and Sharf, I. Literature survey of contact dynamics modelling. *Mech. Mach. Theory*, **37** (2002), 1213. `doi:10.1016/S0094-114X(02)00045-9`.

[82] Goldsmith, W. *Impact: The Theory and Physical Behavior of Colliding Solids*. Edward Arnold Ltd., London, England (1960).

[83] Grace, I. M., Ibrahim, R. A., and Pilipchuk, V. N. Inelastic impact dynamics of ships with one-sided barriers. Part I: Analytical and numerical investigations. *Nonlinear Dyn.*, **66** (2011), 589. `doi:10.1007/s11071-010-9937-6`.

[84] Grace, I. M., Ibrahim, R. A., and Pilipchuk, V. N. Inelastic impact dynamics of ships with one-sided barriers. Part II: Experimental validation. *Nonlinear Dyn.*, **66** (2011), 609. `doi:10.1007/s11071-010-9934-9`.

[85] GRITLI, H. Robust master-slave synchronization of chaos in a one-sided 1-DoF impact mechanical oscillator subject to parametric uncertainties and disturbances. *Mech. Mach. Theory*, **142** (2019). `doi:10.1016/j.mechmachtheory.2019.103610`.

[86] GRITLI, H. AND BELGHITH, S. Diversity in the nonlinear dynamic behavior of a one-degree-of-freedom impact mechanical oscillator under OGY-based state-feedback control law: Order, chaos and exhibition of the border-collision bifurcation. *Mech. Mach. Theory*, **124** (2018), 1. `doi:10.1016/j.mechmachtheory.2018.02.001`.

[87] GU, X. D. AND DENG, Z. C. Dynamical analysis of vibro-impact capsule system with Hertzian contact model and random perturbation excitations. *Nonlinear Dyn.*, **92** (2018), 1781. `doi:10.1007/s11071-018-4161-x`.

[88] GUNTER, H. E. A mechanical model of vocal-fold collision with high spatial and temporal resolution. *J. Acoust. Soc. Am.*, **113** (2003), 994. `doi:10.1121/1.1534100`.

[89] GUO, A. X. AND LI, H. Pounding reduction of highway bridges with pounding effect by using magnetorheological dampers under earthquake excitations. *Adv. Struct. Eng.*, **11** (2008), 305. `doi:10.1260/136943308785082562`.

[90] GUO, A. X., LI, Z. J., LI, H., AND OU, J. P. Experimental and analytical study on pounding reduction of base isolated highway bridges using MR dampers. *Earthq. Eng. Struct. Dyn.*, **38** (2009), 1307. `doi:10.1002/eqe.903`.

[91] GUTIÉRREZ, E. AND ARROWSMITH, D. K. Control of a double impacting mechanical oscillator using displacement feedback. *Int. J. Bifurcat. Chaos*, **14** (2004), 3095. `doi:10.1142/S021812740401120X`.

[92] HAMIDI, M. AND EL NAGGAR, M. On the performance of SCF in seismic isolation of the interior equipment of buildings. *Earthq. Eng. Struct. Dyn.*, **36** (2007), 1581. `doi:10.1002/eqe.708`.

[93] HAO, H., BI, K., CHOUW, N., AND REN, W. X. State-of-the-art review on seismic induced pounding response of bridge structures. *J. Earthq. Tsunami*, **7** (2013), 1. `doi:10.1142/S179343111350019X`.

[94] HAO, Z. AND CAO, Q. The isolation characteristics of an archetypal dynamical model with stable-quasi-zero-stiffness. *J. Sound Vib.*, **340** (2015), 61. `doi:10.1016/j.jsv.2014.11.038`.

[95] HAO, Z., CAO, Q., AND WIERCIGROCH, M. Two-sided damping constraint control strategy for high-performance vibration isolation and end-stop impact protection. *Nonlinear Dyn.*, **86** (2016), 2129. `doi:10.1007/s11071-016-2685-5`.

[96] HARVEY, P. S. AND GAVIN, H. P. Double rolling isolation systems: A mathematical model and experimental validation. *Int. J. Non. Linear. Mech.*, **61** (2014), 80. `doi:10.1016/j.ijnonlinmec.2014.01.011`.

[97] HARVEY, P. S. AND GAVIN, H. P. Assessment of a rolling isolation system using reduced order structural models. *Eng. Struct.*, **99** (2015), 708. `doi:10.1016/j.engstruct.2015.05.022`.

[98] HARVEY, P. S., ZÉHIL, G.-P., AND GAVIN, H. P. Experimental validation of a simplified model for rolling isolation systems. *Earthq. Eng. Struct. Dyn.*, **43** (2014), 1067. `doi:10.1002/eqe.2387`.

[99] HE, J., JIANG, Y., XUE, Q., ZHANG, C., AND ZHANG, J. Effectiveness of using polymer bumpers to mitigate earthquake-induced pounding between buildings of unequal heights. *Adv. Civ. Eng.*, **2018** (2018). `doi:10.1155/2018/7871404`.

[100] HE, L. X., SHRESTHA, B., HAO, H., BI, K. M., AND REN, W. X. Experimental and three-dimensional finite element method studies on pounding responses of bridge structures subjected to spatially varying ground motions. *Adv. Struct. Eng.*, **20** (2017), 105. `doi:10.1177/1369433216646009`.

[101] HERTZ, H. Über die Berührung fester elastischer Körper. *J. für die reine und Angew. Math.*, **91** (1881), 156.

[102] HINRICHS, N., OESTREICH, M., AND POPP, K. Dynamics of oscillators with impact and friction. *Chaos, Solitons and Fractals*, **8** (1997), 535. `doi:10.1016/s0960-0779(96)00121-x`.

[103] HONG, H. P., WANG, S. S., AND HONG, P. Critical building separation distance in reducing pounding risk under earthquake excitation. *Struct. Saf.*, **25** (2003), 287. `doi:10.1016/S0167-4730(02)00080-2`.

[104] HORÁČEK, J., ŠIDLOF, P., AND ŠVEC, J. G. Numerical simulation of self-oscillations of human vocal folds with Hertz model of impact forces. *J. Fluids Struct.*, **20** (2005), 853. `doi:10.1016/j.jfluidstructs.2005.05.003`.

[105] HOS, C. AND CHAMPNEYS, A. R. Grazing bifurcations and chatter in a pressure relief valve model. *Phys. D Nonlinear Phenom.*, **241** (2012), 2068. `doi:10.1016/j.physd.2011.05.013`.

[106] HOUSNER, G. W., ET AL. Structural Control: Past, Present, and Future. *J. Eng. Mech.*, **123** (1997), 897.

[107] HU, Z., THOULESS, M. D., AND LU, W. Effects of gap size and excitation frequency on the vibrational behavior and wear rate of fuel rods. *Nucl. Eng. Des.*, **308** (2016), 261. `doi:10.1016/j.nucengdes.2016.08.038`.

[108] HUNT, K. AND CROSSLEY, E. Coefficient of restitution interpreted as damping in vibroimpact. *J. Appl. Mech. Am. Soc. Mech. Eng.*, **42** (1975), 440. `doi:10.1115/1.3423596`.

[109] IBRAHIM, R. A. Recent advances in nonlinear passive vibration isolators. *J. Sound Vib.*, **314** (2008), 371. `doi:10.1016/j.jsv.2008.01.014`.

[110] IBRAHIM, R. A. *Vibro-Impact Dynamics: Modeling, Mapping and Applications*, vol. 43. Springer-Verlag Berlin Heidelberg (2009). ISBN 978-3-642-00274-8. `doi:10.1007/978-3-642-00275-5`.

[111] IBRAHIM, R. A. Recent advances in vibro-impact dynamics and collision of ocean vessels. *J. Sound Vib.*, **333** (2014), 5900. `doi:10.1016/j.jsv.2014.02.006`.

[112] ING, J., PAVLOVSKAIA, E., AND WIERCIGROCH, M. Dynamics of a nearly symmetrical piecewise linear oscillator close to grazing incidence: Modelling and experimental verification. *Nonlinear Dyn.*, **46** (2006), 225. `doi:10.1007/s11071-006-9045-9`.

[113] ING, J., PAVLOVSKAIA, E., WIERCIGROCH, M., AND BANERJEE, S. Experimental study of impact oscillator with one-sided elastic constraint. *Philos. Trans. R. Soc. A Math. Phys. Eng. Sci.*, **366** (2008), 679. `doi:10.1098/rsta.2007.2122`.

[114] ISMAIL, M. Inner pounding control of the RNC isolator and its impact on seismic isolation efficiency under near-fault earthquakes. *Eng. Struct.*, **86** (2015), 99. `doi:10.1016/j.engstruct.2014.12.041`.

[115] ISMAIL, M. AND RODELLAR, J. Experimental investigations of a rolling-based seismic isolation system. *J. Vib. Control*, **24** (2018), 323. `doi:10.1177/1077546316640664`.

[116] ISMAIL, M., RODELLAR, J., AND IKHOUANE, F. An innovative isolation bearing for motion-sensitive equipment. *J. Sound Vib.*, **326** (2009), 503. `doi:10.1016/j.jsv.2009.06.022`.

[117] ISMAIL, M., RODELLAR, J., AND IKHOUANE, F. An innovative isolation device for aseismic design. *Eng. Struct.*, **32** (2010), 1168. `doi:10.1016/j.engstruct.2009.12.043`.

[118] ISMAIL, M., RODELLAR, J., AND POZO, F. Passive and hybrid mitigation of potential near-fault inner pounding of a self-braking seismic isolator. *Soil Dyn. Earthq. Eng.*, **69** (2015), 233. `doi:10.1016/j.soildyn.2014.10.019`.

[119] JADHAV, M. B. AND JANGID, R. S. Response of base-isolated liquid storage tanks. *Shock Vib.*, **11** (2004), 33. `doi:10.1155/2004/276030`.

[120] JANGID, R. S. Seismic Response of Isolated Bridges. *J. Bridg. Eng.*, **9** (2004), 156. `doi:10.1061/(asce)1084-0702(2004)9:2(156)`.

[121] JANGID, R. S. AND KELLY, J. M. Base isolation for near-fault motions. *Earthq. Eng. Struct. Dyn.*, **30** (2001), 691. `doi:10.1002/eqe.31`.

[122] JANKOWSKI, R. AND MAHMOUD, S. Linking of adjacent three-storey buildings for mitigation of structural pounding during earthquakes. *Bull. Earthq. Eng.*, **14** (2016), 3075. `doi:10.1007/s10518-016-9946-z`.

[123] JANKOWSKI, R., WILDE, K., AND FUJINO, Y. Reduction of pounding effects in elevated bridges during earthquakes. *Earthq. Eng. Struct. Dyn.*, **29** (2000), 195. `doi:10.1002/(SICI)1096-9845(200002)29:2<195::AID-EQE897>3.0.CO;2-3`.

[124] JIA, G., GIDARIS, I., TAFLANIDIS, A. A., AND MAVROEIDIS, G. P. Reliability-based assessment/design of floor isolation systems. *Eng. Struct.*, **78** (2014), 41. `doi:10.1016/j.engstruct.2014.07.031`.

[125] JIA, H. Y., LAN, X. L., ZHENG, S. X., LI, L. P., AND LIU, C. Q. Assessment on required separation length between adjacent bridge segments to avoid pounding. *Soil Dyn. Earthq. Eng.*, **120** (2019), 398. `doi:10.1016/j.soildyn.2019.01.031`.

[126] JIANG, H., CHONG, A. S., UEDA, Y., AND WIERCIGROCH, M. Grazing-induced bifurcations in impact oscillators with elastic and rigid constraints. *Int. J. Mech. Sci.*, **127** (2017), 204. `doi:10.1016/j.ijmecsci.2017.02.001`.

[127] JIANG, J., ZHANG, P., PATIL, D., LI, H. N., AND SONG, G. Experimental studies on the effectiveness and robustness of a pounding tuned mass damper for vibration suppression of a submerged cylindrical pipe. *Struct. Control Heal. Monit.*, **24** (2017), 1. `doi:10.1002/stc.2027`.

[128] JIANG, J. J. AND ZHANG, Y. Chaotic vibration induced by turbulent noise in a two-mass model of vocal folds. *J. Acoust. Soc. Am.*, **112** (2002), 2127. `doi:10.1121/1.1509430`.

[129] JOHNSON, K. L. *Contact Mechanics.* Cambridge University Press, Cambridge, UK (1985).

[130] JÓNSSON, M. H., BESSASON, B., AND HAFLIDASON, E. Earthquake response of a base-isolated bridge subjected to strong near-fault ground motion. *Soil Dyn. Earthq. Eng.*, **30** (2010), 447. `doi:10.1016/j.soildyn.2010.01.001`.

[131] KAPITANIAK, M., VAZIRI, V., PAÉZ CHÁVEZ, J., AND WIERCIGROCH, M. Numerical Study of Forward and Backward Whirling of Drill-String. *J. Comput. Nonlinear Dyn.*, **12** (2017). `doi:10.1115/1.4037318`.

[132] KAPITANIAK, M., VAZIRI HAMANEH, V., PÁEZ CHÁVEZ, J., NANDAKUMAR, K., AND WIERCIGROCH, M. Unveiling complexity of drill-string vibrations: Experiments and modelling. *Int. J. Mech. Sci.*, **101-102** (2015), 324. `doi:10.1016/j.ijmecsci.2015.07.008`.

[133] KELLY, J. M. Aseismic base isolation: review and bibliography. *Soil Dyn. Earthq. Eng.*, **5** (1986), 202. `doi:10.1016/0267-7261(86)90006-0`.

[134] KELLY, J. M. Base Isolation: Linear Theory and Design. *Earthq. Spectra*, **6** (1990), 223. `doi:10.1193/1.1585566`.

[135] KELLY, J. M. *Earthquake-Resistant Design with Rubber.* Springer London, second edi edn. (1997). ISBN 9781447109716.

[136] KELLY, J. M. The role of damping in seismic isolation. *Earthq. Eng. Struct. Dyn.*, **28** (1999), 3. `doi:10.1002/(SICI)1096-9845(199901)28:1<3::AID-EQE801>3.0.CO;2-D`.

[137] KHULIEF, Y. A. AND SHABANA, A. A. A continuous force model for the impact analysis of flexible multibody systems. *Mech. Mach. Theory*, **22** (1987), 213. `doi:10.1016/0094-114X(87)90004-8`.

[138] KIM, J., RYU, J., AND CHUNG, L. Seismic performance of structures connected by viscoelastic dampers. *Eng. Struct.*, **28** (2006), 183. `doi:10.1016/j.engstruct.2005.05.014`.

[139] KOMODROMOS, P. Simulation of the earthquake-induced pounding of seismically isolated buildings. *Comput. Struct.*, **86** (2008), 618. `doi:10.1016/j.compstruc.2007.08.001`.

[140] KOMODROMOS, P., POLYCARPOU, P. C., PAPALOIZOU, L., AND PHOCAS, M. C. Response of seismically isolated buildings considering poundings. *Earthq. Eng. Struct. Dyn.*, **36** (2007), 1605. `doi:10.1002/eqe.692`.

[141] KONG, L., LI, Y., LV, Y., AND WANG, Q. Numerical investigation on dynamic characteristics of drilling shaft in deep hole drilling influenced by minimal quantity lubrication. *Nonlinear Dyn.*, **74** (2013), 943. `doi:10.1007/s11071-013-1014-5`.

[142] KUMAR, M. AND WHITTAKER, A. S. On the calculation of the clearance to the hard stop for seismically isolated nuclear power plants. In *Trans. 23rd Conf. Struct. Mech. React. Technol.*, vol. 5. Manchester, United Kingdom (2015).

[143] KUNDE, M. AND JANGID, R. Seismic behavior of isolated bridges: A-state-of-the-art review. *Electron. J. Struct. Eng.*, **3** (2003), 140.

[144] KWUIMY, C. A., NATARAJ, C., AND LITAK, G. Melnikov's criteria, parametric control of chaos, and stationary chaos occurrence in systems with asymmetric potential subjected to multiscale type excitation. *Chaos*, **21** (2011), 043113. `doi:10.1063/1.3650699`.

[145] LANDA, P. S. Vocal Folds as a vibro-impacts system. In *Dyn. Vibro-Impact Syst.* (edited by V. Babitsky), pp. 1–10. Springer, Berlin, Heidelberg (1999). `doi:10.1007/978-3-642-60114-9_1`.

[146] LANKARANI, H. M. AND NIKRAVESH, P. E. A contact force model with hysteresis damping for impact analysis of multibody systems. *J. Mech. Des. Trans. ASME*, **112** (1990), 369. `doi:10.1115/1.2912617`.

[147] LANKARANI, H. M. AND NIKRAVESH, P. E. Continuous contact force models for impact analysis in multibody systems. *Nonlinear Dyn.*, **5** (1994), 193. `doi:10.1007/BF00045676`.

[148] LEE, J. Y. AND YAN, J. J. Position control of double-side impact oscillator. *Mech. Syst. Signal Process.*, **21** (2007), 1076. doi:10.1016/j.ymssp.2005.09.008.

[149] LEINE, R. I., GLOCKER, C., AND VAN CAMPEN, D. H. Nonlinear dynamics of the woodpecker toy. In *Proc. ASME Des. Eng. Tech. Conf.*, vol. 6 C, pp. 2629–2637. Pittsburgh, PA (2001).

[150] LENCI, S. AND REGA, G. A Procedure for Reducing the Chaotic Response Region in an Impact Mechanical System. *Nonlinear Dyn.*, **15** (1998), 391. doi:10.1023/A:1008209513877.

[151] LI, B., BI, K., CHOUW, N., BUTTERWORTH, J. W., AND HAO, H. Experimental investigation of spatially varying effect of ground motions on bridge pounding. *Earthq. Eng. Struct. Dyn.*, **41** (2012), 1959. doi:10.1002/eqe.2168.

[152] LI, G. AND DING, W. Global behavior of a vibro-impact system with asymmetric clearances. *J. Sound Vib.*, **423** (2018), 180. doi:10.1016/j.jsv.2018.02.058.

[153] LI, J., PENG, T., AND XU, Y. Damage investigation of girder bridges under the Wenchuan earthquake and corresponding seismic design recommendations. *Earthq. Eng. Eng. Vib.*, **7** (2008), 337. doi:10.1007/s11803-008-1005-6.

[154] LI, K. AND DARBY, A. P. An experimental investigation into the use of a buffered impact damper. *J. Sound Vib.*, **291** (2006), 844. doi:10.1016/j.jsv.2005.06.043.

[155] LIAO, C. M., BALACHANDRAN, B., KARKOUB, M., AND ABDEL-MAGID, Y. L. Drill-string dynamics: Reduced-order models and experimental studies. *J. Vib. Acoust. Trans. ASME*, **133** (2011). doi:10.1115/1.4003406.

[156] LIAO, M., LIU, Y., PÁEZ CHÁVEZ, J., CHONG, A. S., AND WIERCIGROCH, M. Dynamics of vibro-impact drilling with linear and nonlinear rock models. *Int. J. Mech. Sci.*, **146-147** (2018), 200. doi:10.1016/j.ijmecsci.2018.07.039.

[157] LIN, J. H. Separation distance to avoid seismic pounding of adjacent buildings. *Earthq. Eng. Struct. Dyn.*, **26** (1997), 395. doi:10.1002/(SICI)1096-9845(199703)26:3<395::AID-EQE655>3.0.CO;2-F.

[158] LIU, X., VLAJIC, N., LONG, X., MENG, G., AND BALACHANDRAN, B. Nonlinear motions of a flexible rotor with a drill bit: Stick-slip and delay effects. *Nonlinear Dyn.*, **72** (2013), 61. doi:10.1007/s11071-012-0690-x.

[159] LIU, X., VLAJIC, N., LONG, X., MENG, G., AND BALACHANDRAN, B. Coupled axial-torsional dynamics in rotary drilling with state-dependent delay: stability and control. *Nonlinear Dyn.*, **78** (2014), 1891. doi:10.1007/s11071-014-1567-y.

[160] Liu, Y. and Páez Chávez, J. Controlling multistability in a vibro-impact capsule system. *Nonlinear Dyn.*, **88** (2017), 1289. `doi:10.1007/s11071-016-3310-3`.

[161] Liu, Y., Páez Chávez, J., De Sa, R., and Walker, S. Numerical and experimental studies of stick–slip oscillations in drill-strings. *Nonlinear Dyn.*, **90** (2017), 2959. `doi:10.1007/s11071-017-3855-9`.

[162] Liu, Y., Páez Chávez, J., Guo, B., and Birler, R. Bifurcation analysis of a vibro-impact experimental rig with two-sided constraint. *Meccanica*, (2020). `doi:10.1007/s11012-020-01168-4RECENT`.

[163] Liu, Y., Páez Chávez, J., Zhang, J., Tian, J., Guo, B., and Prasad, S. The vibro-impact capsule system in millimetre scale: numerical optimisation and experimental verification. *Meccanica*, **55** (2020), 1885. `doi:10.1007/s11012-020-01237-8`.

[164] Liu, Y., Pavlovskaia, E., Hendry, D., and Wiercigroch, M. Vibro-impact responses of capsule system with various friction models. *Int. J. Mech. Sci.*, **72** (2013), 39. `doi:10.1016/j.ijmecsci.2013.03.009`.

[165] Liu, Y., Pavlovskaia, E., and Wiercigroch, M. Experimental verification of the vibro-impact capsule model. *Nonlinear Dyn.*, **83** (2016), 1029. `doi:10.1007/s11071-015-2385-6`.

[166] Liu, Y., Wiercigroch, M., Pavlovskaia, E., and Peng, Z. Forward and backward motion control of a vibro-impact capsule system. *Int. J. Non. Linear. Mech.*, **70** (2015), 30. `doi:10.1016/j.ijnonlinmec.2014.10.009`.

[167] Lopez Gimenez, J., Himeno, T., Yoshihara, S., and Nuruzzaman, A. S. M. Seismic Isolation of Bridges: Devices, Common Practices in Japan, and Examples of Application. In *4th Int. Conf. Adv. Civ. Eng.*, vol. 2018, p. 6 (2018).

[168] Lu, L. Y. and Lin, G. L. Predictive control of smart isolation system for precision equipment subjected to near-fault earthquakes. *Eng. Struct.*, **30** (2008), 3045. `doi:10.1016/j.engstruct.2008.04.016`.

[169] Luo, A. C. and O'Connor, D. Mechanism of impacting chatter with stick in a gear transmission system. *Int. J. Bifurc. Chaos*, **19** (2009), 2093. `doi:10.1142/S0218127409023937`.

[170] Luo, A. C. and O'Connor, D. Periodic motions and chaos with impacting chatter and stick in a gear transmission system. *Int. J. Bifurcat. Chaos*, **19** (2009), 1975. `doi:10.1142/S0218127409023858`.

[171] Luo, G., Ma, L., and Lv, X. Dynamic analysis and suppressing chaotic impacts of a two-degree-of-freedom oscillator with a clearance. *Nonlinear Anal. Real World Appl.*, **10** (2009), 756. `doi:10.1016/j.nonrwa.2007.11.002`.

[172] LUO, G., XIE, J., ZHU, X., AND ZHANG, J. Periodic motions and bifurcations of a vibro-impact system. *Chaos, Solitons and Fractals*, **36** (2008), 1340. `doi:10.1016/j.chaos.2006.08.009`.

[173] LUO, G. AND ZHANG, Y. Analyses of impact motions of harmonically excited systems having rigid amplitude constraints. *Int. J. Impact Eng.*, **34** (2007), 1883. `doi:10.1016/j.ijimpeng.2006.10.014`.

[174] LUO, G., ZHANG, Y., XIE, J., AND ZHANG, J. Periodic-impact motions and bifurcations of vibro-impact systems near 1:4 strong resonance point. *Commun. Nonlinear Sci. Numer. Simul.*, **13** (2008), 1002. `doi:10.1016/j.cnsns.2006.08.004`.

[175] LUO, G. W. Dynamics of an impact-forming machine. *Int. J. Mech. Sci.*, **48** (2006), 1295. `doi:10.1016/j.ijmecsci.2006.03.017`.

[176] LUO, G. W., LV, X. H., AND SHI, Y. Q. Vibro-impact dynamics of a two-degree-of freedom periodically-forced system with a clearance: Diversity and parameter matching of periodic-impact motions. *Int. J. Non. Linear. Mech.*, **65** (2014), 173. `doi:10.1016/j.ijnonlinmec.2014.04.013`.

[177] LUO, G. W., LV, X. H., AND ZHU, X. F. Dynamics of vibro-impact mechanical systems with large dissipation. *Int. J. Mech. Sci.*, **50** (2008), 214. `doi:10.1016/j.ijmecsci.2007.07.001`.

[178] LUO, G. W. AND YAO, H. M. Dynamics of a small vibro-impact pile driver. *Nonlinear Anal. Real World Appl.*, **9** (2008), 1361. `doi:10.1016/j.nonrwa.2007.03.004`.

[179] LUO, G. W., YU, J. N., AND ZHANG, J. G. Periodic-impact motions and bifurcations of a dual component system. *Nonlinear Anal. Real World Appl.*, **7** (2006), 813. `doi:10.1016/j.nonrwa.2005.03.030`.

[180] LUO, G. W., ZHANG, Y. L., AND ZHANG, J. G. Dynamical behavior of a class of vibratory systems with symmetrical rigid stops near the point of codimension two bifurcation. *J. Sound Vib.*, **297** (2006), 17. `doi:10.1016/j.jsv.2006.02.027`.

[181] LUO, G. W., ZHU, X. F., AND SHI, Y. Q. Dynamics of a two-degree-of freedom periodically-forced system with a rigid stop: Diversity and evolution of periodic-impact motions. *J. Sound Vib.*, **334** (2015), 338. `doi:10.1016/j.jsv.2014.08.029`.

[182] LUO, T. AND WANG, Z. Periodically forced system with symmetric motion limiting constraints: Dynamic characteristics and equivalent electronic circuit realization. *Int. J. Non. Linear. Mech.*, **81** (2016), 283. `doi:10.1016/j.ijnonlinmec.2016.01.021`.

[183] LYU, X., GAO, Q., AND LUO, G. Dynamic characteristics of a mechanical impact oscillator with a clearance. *Int. J. Mech. Sci.*, **178** (2020), 105605. `doi:10.1016/j.ijmecsci.2020.105605`.

[184] MA, Y., AGARWAL, M., AND BANERJEE, S. Border collision bifurcations in a soft impact system. *Phys. Lett. Sect. A Gen. At. Solid State Phys.*, **354** (2006), 281. `doi:10.1016/j.physleta.2006.01.025`.

[185] MA, Y., ING, J., BANERJEE, S., WIERCIGROCH, M., AND PAVLOVSKAIA, E. The nature of the normal form map for soft impacting systems. *Int. J. Non. Linear. Mech.*, **43** (2008), 504. `doi:10.1016/j.ijnonlinmec.2008.04.001`.

[186] MACHADO, M., MOREIRA, P., FLORES, P., AND LANKARANI, H. M. Compliant contact force models in multibody dynamics: Evolution of the Hertz contact theory. *Mech. Mach. Theory*, **53** (2012), 99. `doi:10.1016/j.mechmachtheory.2012.02.010`.

[187] MALHOTRA, P. K. Dynamics of seismic impacts in base-isolated buildings. *Earthq. Eng. Struct. Dyn.*, **26** (1997), 797. `doi:10.1002/(SICI)1096-9845(199708)26:8<797::AID-EQE677>3.0.CO;2-6`.

[188] MALHOTRA, P. K. Method for Seismic Base Isolation of Liquid-Storage Tanks. *J. Struct. Eng.*, **123** (1997), 113. `doi:10.1061/(ASCE)0733-9445(1997)123:1(113)`.

[189] MALHOTRA, P. K. New method for seismic isolation of liquid-storage tanks. *Earthq. Eng. Struct. Dyn.*, **26** (1997), 839. `doi:10.1002/(SICI)1096-9845(199708)26:8<839::AID-EQE679>3.0.CO;2-Y`.

[190] MASROOR, A. AND MOSQUEDA, G. Experimental simulation of base-isolated buildings pounding against moat wall and effects on superstructure response. *Earthq. Eng. Struct. Dyn.*, **41** (2012), 2093. `doi:10.1002/eqe.2177`.

[191] MASROOR, A. AND MOSQUEDA, G. Impact model for simulation of base isolated buildings impacting flexible moat walls. *Earthq. Eng. Struct. Dyn.*, **42** (2013), 357. `doi:10.1002/eqe.2210`.

[192] MATSAGAR, V. A. AND JANGID, R. S. Seismic response of base-isolated structures during impact with adjacent structures. *Eng. Struct.*, **25** (2003), 1311. `doi:10.1016/S0141-0296(03)00081-6`.

[193] MATSAGAR, V. A. AND JANGID, R. S. Seismic response of simply supported base-isolated bridge with different isolators. *Int. J. Appl. Sci. Eng.*, **4** (2006), 53.

[194] MAVRONICOLA, E. A., POLYCARPOU, P. C., AND KOMODROMOS, P. Effect of planar impact modeling on the pounding response of base-isolated buildings. *Front. Built Environ.*, **2** (2016), 1. `doi:10.3389/fbuil.2016.00011`.

[195] MAVRONICOLA, E. A., POLYCARPOU, P. C., AND KOMODROMOS, P. Effect of ground motion directionality on the seismic response of base isolated buildings pounding against adjacent structures. *Eng. Struct.*, **207** (2020), 110202. `doi:10.1016/j.engstruct.2020.110202`.

[196] MIARI, M., CHOONG, K. K., AND JANKOWSKI, R. Seismic pounding between adjacent buildings: Identification of parameters, soil interaction issues and mitigation measures. *Soil Dyn. Earthq. Eng.*, **121** (2019), 135. `doi:10.1016/j.soildyn.2019.02.024`.

[197] MIARI, M., CHOONG, K. K., AND JANKOWSKI, R. Seismic Pounding Between Bridge Segments: A State-of-the-Art Review. *Arch. Comput. Methods Eng.*, (2020). `doi:10.1007/s11831-019-09389-x`.

[198] MIHAJLOVIĆ, N., VAN DE WOUW, N., ROSIELLE, P. C., AND NIJMEIJER, H. Interaction between torsional and lateral vibrations in flexible rotor systems with discontinuous friction. *Nonlinear Dyn.*, **50** (2007), 679. `doi:10.1007/s11071-006-9172-3`.

[199] MOON, F. C. AND SHAW, S. W. Chaotic vibrations of a beam with non-linear boundary conditions. *Int. J. Non. Linear. Mech.*, **18** (1983), 465. `doi:10.1016/0020-7462(83)90033-1`.

[200] MUTHUKUMAR, S. AND DESROCHES, R. A Hertz contact model with non-linear damping for pounding simulation. *Earthq. Eng. Struct. Dyn.*, **35** (2006), 811. `doi:10.1002/eqe.557`.

[201] NADERPOUR, H., BARROS, R. C., KHATAMI, S. M., AND JANKOWSKI, R. Numerical Study on Pounding between Two Adjacent Buildings under Earthquake Excitation. *Shock Vib.*, **2016** (2016). `doi:10.1155/2016/1504783`.

[202] NAEIM, F. AND KELLY, J. M. *Design of Seismic Isolated Structures: From Theory to Practice.* John Wiley, Chichester, U.K. (1999).

[203] NATSIAVAS, S. Analytical Modeling of Discrete Mechanical Systems Involving Contact, Impact, and Friction. *Appl. Mech. Rev.*, **71** (2019), 1. `doi:10.1115/1.4044549`.

[204] NATSIAVAS, S. AND GONZALEZ, H. Vibration of harmonically excited oscillators with asymmetric constraints. *J. Appl. Mech. Trans. ASME*, **59** (1992), S284. `doi:10.1115/1.2899502`.

[205] NAYFEH, A. H. AND BALACHANDRAN, B. *Applied Nonlinear Dynamics and Experimental Methods.* Wiley-VCH Verlag GmbH & Co. KGaA (2004). ISBN 978-0-471-59348-5.

[206] NAYFEH, A. H. AND MOOK, D. T. *Nonlinear oscillations.* Wiley-VCH Verlag GmbH & Co. KGaA (1995).

[207] NORDMARK, A. B. Non-periodic motion caused by grazing incidence in an impact oscillator. *J. Sound Vib.*, **145** (1991), 279. `doi:10.1016/0022-460X(91)90592-8`.

[208] NUCERA, F., VAKAKIS, A. F., McFARLAND, D. M., BERGMAN, L. A., AND KERSCHEN, G. Targeted energy transfers in vibro-impact oscillators for seismic mitigation. *Nonlinear Dyn.*, **50** (2007), 651. `doi:10.1007/s11071-006-9189-7`.

[209] PALACIOS-QUIÑONERO, F., RUBIÓ-MASSEGÚ, J., ROSSELL, J. M., AND KARIMI, H. R. Semiactive-passive structural vibration control strategy for adjacent structures under seismic excitation. *J. Franklin Inst.*, **349** (2012), 3003. `doi:10.1016/j.jfranklin.2012.09.005`.

[210] PANT, D. R. AND WIJEYEWICKREMA, A. C. Structural performance of a base-isolated reinforced concrete building subjected to seismic pounding. *Earthq. Eng. Struct. Dyn.*, **41** (2012), 1709. `doi:10.1002/eqe.2158`.

[211] PAPADRAKAKIS, M. AND MOUZAKIS, H. P. Earthquake simulator testing of pounding between adjacent buildings. *Earthq. Eng. Struct. Dyn.*, **24** (1995), 811. `doi:10.1002/eqe.4290240604`.

[212] PARK, K. S., JUNG, H. J., AND LEE, I. W. A comparative study on aseismic performances of base isolation systems for multi-span continuous bridge. *Eng. Struct.*, **24** (2002), 1001. `doi:10.1016/S0141-0296(02)00020-2`.

[213] PAVLOVSKAIA, E., ING, J., WIERCIGROCH, M., AND BANERJEE, S. Complex dynamics of bilinear oscillator close to grazing. *Int. J. Bifurc. Chaos*, **20** (2010), 3801. `doi:10.1142/S0218127410028069`.

[214] PAVLOVSKAIA, E., WIERCIGROCH, M., WOO, K. C., AND RODGER, A. A. Modelling of ground moling dynamics by an impact oscillator with a frictional slider. *Meccanica*, **38** (2003), 85. `doi:10.1023/A:1022023502199`.

[215] PENZIEN, J. Evaluation of building separation distance required to prevent pounding during strong earthquakes. *Earthq. Eng. Struct. Dyn.*, **26** (1997), 849. `doi:10.1002/(SICI)1096-9845(199708)26:8<849::AID-EQE680>3.0.CO;2-M`.

[216] PERRET-LIAUDET, J. AND RIGAUD, E. Experiments and numerical results on nonlinear vibrations of an impacting Hertzian contact. Part 2: random excitation. *J. Sound Vib.*, **265** (2003), 309. `doi:10.1016/S0022-460X(02)01267-1`.

[217] PETERKA, F. Bifurcations and transition phenomena in an impact oscillator. *Chaos, Solitons and Fractals*, **7** (1996), 1635. `doi:10.1016/S0960-0779(96)00028-8`.

[218] PFEIFFER, F. AND GLOCKER, C. *Multibody Dynamics with Unilateral Contacts*. CISM International Centre for Mechanical Sciences. Springer-Verlag Wien (2000). ISBN 978-3-211-83330-8.

[219] PFEIFFER, F. AND KUNERT, A. Rattling models from deterministic to stochastic processes. *Nonlinear Dyn.*, **1** (1990), 63. `doi:10.1007/BF01857585`.

[220] PILIPCHUK, V. N. AND IBRAHIM, R. A. Dynamics of a two-pendulum model with impact interaction and an elastic support. *Nonlinear Dyn.*, **21** (2000), 221. `doi:10.1023/A:1008333123695`.

[221] POLYCARPOU, P. C. AND KOMODROMOS, P. Earthquake-induced poundings of a seismically isolated building with adjacent structures. *Eng. Struct.*, **32** (2010), 1937. `doi:10.1016/j.engstruct.2010.03.011`.

[222] POLYCARPOU, P. C. AND KOMODROMOS, P. On poundings of a seismically isolated building with adjacent structures during strong earthquakes. *Earthq. Eng. Struct. Dyn.*, **39** (2010), 933. `doi:10.1002/eqe.975`.

[223] POLYCARPOU, P. C. AND KOMODROMOS, P. Numerical investigation of potential mitigation measures for poundings of seismically isolated buildings. *Earthq. Struct.*, **2** (2011), 1. `doi:10.12989/eas.2011.2.1.001`.

[224] POLYCARPOU, P. C., KOMODROMOS, P., AND POLYCARPOU, A. C. A nonlinear impact model for simulating the use of rubber shock absorbers for mitigating the effects of structural pounding during earthquakes. *Earthq. Eng. Struct. Dyn.*, **42** (2013), 81. `doi:10.1002/eqe.2194`.

[225] POLYCARPOU, P. C., PAPALOIZOU, L., AND KOMODROMOS, P. An efficient methodology for simulating earthquake-induced 3D pounding of buildings. *Earthq. Eng. Struct. Dyn.*, **43** (2014), 985. `doi:10.1002/eqe.2383`.

[226] PUST, L. AND PETERKA, F. Impact oscillator with Hertz's model of contact. *Meccanica*, **38** (2003), 99. `doi:10.1023/A:1022075519038`.

[227] RAYEGANI, A. AND NOURI, G. Application of Smart Dampers for Prevention of Seismic Pounding in Isolated Structures Subjected to Near-fault Earthquakes. *J. Earthq. Eng.*, (2020), 1. `doi:10.1080/13632469.2020.1822230`.

[228] REGGIO, A. AND DE ANGELIS, M. Optimal design of an equipment isolation system with nonlinear hysteretic behavior. *Earthq. Eng. Struct. Dyn.*, **42** (2013), 1907. `doi:10.1002/eqe.2304`.

[229] REGGIO, A. AND DE ANGELIS, M. Combined primary-secondary system approach to the design of an equipment isolation system with High-Damping Rubber Bearings. *J. Sound Vib.*, **333** (2014), 2386. `doi:10.1016/j.jsv.2013.12.006`.

[230] REGGIO, A. AND DE ANGELIS, M. Optimal energy-based seismic design of non-conventional Tuned Mass Damper (TMD) implemented via inter-story isolation. *Earthq. Eng. Struct. Dyn. Struct. Dyn.*, **44** (2015), 1623. `doi:10.1002/eqe.2548`.

[231] RENZI, E. AND DE ANGELIS, M. Optimal semi-active control and non-linear dynamic response of variable stiffness structures. *J. Vib. Control*, **11** (2005), 1253. `doi:10.1177/1077546305054597`.

[232] RIGAUD, E. AND PERRET-LIAUDET, J. Experiments and numerical results on nonlinear vibrations of an impacting Hertzian contact. Part 1: Harmonic excitation. *J. Sound Vib.*, **265** (2003), 289. `doi:10.1016/S0022-460X(02)01262-2`.

[233] RIGAUD, E. AND PERRET-LIAUDET, J. Investigation of gear rattle noise including visualization of vibro-impact regimes. *J. Sound Vib.*, **467** (2020). `doi:10.1016/j.jsv.2019.115026`.

[234] RYAN, K. L. AND EARL, C. L. Analysis and design of inter-story isolation systems with nonlinear devices. *J. Earthq. Eng.*, **14** (2010), 1044. `doi:10.1080/13632461003668020`.

[235] SAREBANHA, A., MOSQUEDA, G., KIM, M. K., AND KIM, J. H. Seismic response of base isolated nuclear power plants considering impact to moat walls. *Nucl. Eng. Des.*, **328** (2018), 58. `doi:10.1016/j.nucengdes.2017.12.021`.

[236] SHAW, S. The Dynamics of a Harmonically Excited System having Rigid Amplitude Constraints. Part 1: Subharmonic Motion and Local Bifurcations. *J. Appl. Mech. Trans. ASME*, **52** (1985), 453. `doi:10.1115/1.3169068`.

[237] SHAW, S. AND HOLMES, P. A periodically forced impact oscillaor with large dissipation. *J. Appl. Mech.*, **50** (1983), 849. `doi:10.1115/1.3167156`.

[238] SHAW, S. AND HOLMES, P. A periodically forced piecewise linear oscillator. *J. Sound Vib.*, **90** (1983), 129. `doi:10.1016/0022-460X(83)90407-8`.

[239] SHRESTHA, B., HAO, H., AND BI, K. Effectiveness of using rubber bumper and restrainer on mitigating pounding and unseating damage of bridge structures subjected to spatially varying ground motions. *Eng. Struct.*, **79** (2014), 195. `doi:10.1016/j.engstruct.2014.08.020`.

[240] SHRIMALI, M. K. AND JANGID, R. S. Seismic analysis of base-isolated liquid storage tanks. *J. Sound Vib.*, **275** (2004), 59. `doi:10.1016/S0022-460X(03)00749-1`.

[241] SKRINJAR, L. AND SLAVI, J. A review of continuous contact-force models in multibody dynamics. *Int. J. Mech. Sci.*, **145** (2018), 171. `doi:10.1016/j.ijmecsci.2018.07.010`.

[242] SOŁTYSIK, B., FALBORSKI, T., AND JANKOWSKI, R. Preventing of earthquake-induced pounding between steel structures by using polymer elements-experimental study. *Procedia Eng.*, **199** (2017), 278. `doi:10.1016/j.proeng.2017.09.029`.

[243] SONG, G. B., ZHANG, P., LI, L. Y., SINGLA, M., PATIL, D., LI, H. N., AND MO, Y. L. Vibration Control of a Pipeline Structure Using Pounding Tuned Mass Damper. *J. Eng. Mech.*, **142** (2016), 04016031. `doi:10.1061/(asce)em.1943-7889.0001078`.

[244] SOONG, T. AND DARGUSH, G. *Passive Energy Dissipation Systems in Structural Engineering.* John Wiley and Sons (1997). ISBN 978-0-471-96821-4.

[245] SORACE, S. AND TERENZI, G. Seismic performance assessment and base-isolated floor protection of statues exhibited in museum halls. *Bull. Earthq. Eng.*, **13** (2015), 1873. `doi:10.1007/s10518-014-9680-3`.

[246] SPENCER, B. F. J. AND NAGARAJAIAH, S. State of the Art of Structural Control. *J. Struct. Eng.*, **129** (2003), 845. `doi:10.1061/(ASCE)0733-9445(2003)129:7(845)`.

[247] STEFANI, G., DE ANGELIS, M., AND ANDREAUS, U. Experimental and Numerical Investigation of Base Isolated SDOF System Impact against Bumpers under Harmonic Base Excitation. In *Proc. 7th Int. Conf. Comput. Methods Struct. Dyn. Earthq. Eng. (COMPDYN 2019)* (edited by M. Papadrakakis and M. Fragiadakis), vol. 2, pp. 3333–3343. Institute of Structural Analysis and Antiseismic Research School of Civil Engineering National Technical University of Athens (NTUA) Greece, Athens (2019). ISBN 978-618-82844-5-6. `doi:10.7712/120119.7150.19207`.

[248] STEFANI, G., DE ANGELIS, M., AND ANDREAUS, U. Experimental and Numerical Response Analysis of a Unilaterally Constrained SDOF System Under Harmonic Base Excitation. In *Proc. XXIV AIMETA Conf. 2019. Lect. Notes Mech. Eng.* (edited by A. Carcaterra, A. Paolone, and G. Graziani), pp. 1488–1497. Springer, Cham (2020). `doi:10.1007/978-3-030-41057-5_120`.

[249] STEFANI, G., DE ANGELIS, M., AND ANDREAUS, U. Experimental Dynamic Response of a SDOF Oscillator Constrained by Two Symmetrically Arranged Deformable and Dissipative Bumpers Under Harmonic Base Excitation. In *Nonlinear Dyn. Control* (edited by W. Lacarbonara, B. Balachandran, J. Ma, J. Tenreiro Machado, and G. Stepan), pp. 119–127. Springer International Publishing, Cham (2020). `doi:10.1007/978-3-030-34747-5_12`.

[250] STEFANI, G., DE ANGELIS, M., AND ANDREAUS, U. Numerical study on the response scenarios in a vibro-impact single-degree-of-freedom oscillator with two unilateral dissipative and deformable constraints. *Commun. Nonlinear Sci. Numer. Simul.*, **99** (2021), 105818. `doi:10.1016/j.cnsns.2021.105818`.

[251] STEFANI, G., DE ANGELIS, M., AND ANDREAUS, U. Scenarios in the experimental response of a vibro-impact single-degree-of-freedom system and numerical simulations. *Nonlinear Dyn.*, **103** (2021), 3465. `doi:10.1007/s11071-020-05791-4`.

[252] STRONGE, W. J. *Impact Mechanics*. Cambridge University Press, 2 edn. (2018). ISBN 9781139050227. `doi:10.1017/9781139050227`.

[253] SU, B. L., AHMADI, G., AND TADJBAKHSH, I. G. Comparative study of base isolation systems. *J. Eng. Mech.*, **115** (1989), 1976. `doi:10.1061/(ASCE)0733-9399(1989)115:9(1976)`.

[254] SUN, X., ZHANG, H., MENG, W., ZHANG, R., LI, K., AND PENG, T. Primary resonance analysis and vibration suppression for the harmonically excited nonlinear suspension system using a pair of symmetric viscoelastic buffers. *Nonlinear Dyn.*, **94** (2018), 1243. `doi:10.1007/s11071-018-4421-9`.

[255] TAGHAVI, S. AND MIRANDA, E. *Response Assessment of Nonstructural Building Elements*. PEER Report 2003/05 (2003).

[256] Tao, H. and Gibert, J. Periodic orbits of a conservative 2-DOF vibro-impact system by piecewise continuation: bifurcations and fractals. *Nonlinear Dyn.*, **95** (2019), 2963. `doi:10.1007/s11071-018-04734-4`.

[257] Thompson, J. M. T. and Stewart, H. B. *Nonlinear Dynamics and Chaos.* John Wiley & Sons, Ltd, second edn. (2002).

[258] Tian, L. and Gai, X. Wind-induced vibration control of power transmission tower using pounding tuned mass damper. *J. Vibroengineering*, **17** (2015), 3693.

[259] Tian, L., Rong, K., Zhang, P., and Liu, Y. Vibration Control of a Power Transmission Tower with Pounding Tuned Mass Damper under Multi-Component Seismic Excitations. *Appl. Sci.*, **7** (2017), 1. `doi:10.3390/app7050477`.

[260] Tian, Z., Qian, J., and Zhang, L. Slide roof system for dynamic response reduction. *Earthq. Eng. Struct. Dyn.*, **37** (2008), 647. `doi:10.1002/eqe.780`.

[261] Trung, P. D., Quang, P. T., Toan, N. B., Hoa, H. P., and Phuoc, N. T. The effectiveness of rubber absorber in adjacent planar structures under earthquake-included pounding. *Int. J. Civ. Eng. Technol.*, **9** (2018), 1751.

[262] Tsai, C. S., Chiang, T. C., Chen, B. J., and Lin, S. B. An advanced analytical model for high damping rubber bearings. *Earthq. Eng. Struct. Dyn.*, **32** (2003), 1373. `doi:10.1002/eqe.278`.

[263] Tsai, H. C. Dynamic analysis of base-isolated shear beams bumping against stops. *Earthq. Eng. Struct. Dyn.*, **26** (1997), 515. `doi:10.1002/(SICI)1096-9845(199705)26:5<515::AID-EQE654>3.0.CO;2-C`.

[264] Turki, F., Gritli, H., and Belghith, S. Robust position control of a two-sided 1-dof impacting mechanical oscillator subject to an external persistent disturbance by means of a state-feedback controller. *Complexity*, **2019** (2019), 18. `doi:10.1155/2019/9174284`.

[265] Turki, F., Gritli, H., and Belghith, S. An LMI-based design of a robust state-feedback control for the master-slave tracking of an impact mechanical oscillator with double-side rigid constraints and subject to bounded-parametric uncertainty. *Commun. Nonlinear Sci. Numer. Simul.*, **82** (2020), 1. `doi:10.1016/j.cnsns.2019.105020`.

[266] van Til, J., Alijani, F., Voormeeren, S. N., and Lacarbonara, W. Frequency domain modeling of nonlinear end stop behavior in Tuned Mass Damper systems under single- and multi-harmonic excitations. *J. Sound Vib.*, **438** (2019), 139. `doi:10.1016/j.jsv.2018.09.015`.

[267] Vaziri, V., Kapitaniak, M., and Wiercigroch, M. Suppression of drill-string stick-slip vibration by sliding mode control: Numerical and experimental studies. *Eur. J. Appl. Math.*, **29** (2018), 805. `doi:10.1017/S0956792518000232`.

[268] VILLAVERDE, R. Implementation study of aseismic roof isolation system in 13story building. *J. Seismol. Earthq. Eng.*, **2** (2000), 17.

[269] VILLAVERDE, R., AGUIRRE, M., AND HAMILTON, C. Aseismic roof isolation system built with steel oval elements: Exploratory study. *Earthq. Spectra*, **21** (2005), 225. `doi:10.1193/1.1850528`.

[270] VIRGIN, L. N. AND BEGLEY, C. J. Grazing bifurcations and basins of attraction in an impact-friction oscillator. *Phys. D Nonlinear Phenom.*, **130** (1999), 43. `doi:10.1016/S0167-2789(99)00016-0`.

[271] WAGG, D. J. AND BISHOP, S. R. Chatter, sticking and chaotic impacting motion in a two-degree of freedom impact oscillator. *Int. J. Bifurcat. Chaos*, **11** (2001), 57. `doi:10.1142/S0218127401001943`.

[272] WAGG, D. J. AND BISHOP, S. R. Application of non-smooth modelling techniques to the dynamics of a flexible impacting beam. *J. Sound Vib.*, **256** (2002), 803. `doi:10.1006/jsvi.2002.5020`.

[273] WAGG, D. J. AND BISHOP, S. R. Dynamics of a two degree of freedom vibro-impact system with multiple motion limiting constraints. **14** (2004), 119. `doi:10.1142/S0218127404009223`.

[274] WANG, J., SHEN, Y., AND YANG, S. Dynamical analysis of a single degree-of-freedom impact oscillator with impulse excitation. *Adv. Mech. Eng.*, **9** (2017), 1. `doi:10.1177/1687814017716619`.

[275] WANG, L., XU, W., AND LI, Y. Impulsive control of a class of vibro-impact systems. *Phys. Lett. Sect. A Gen. At. Solid State Phys.*, **372** (2008), 5309. `doi:10.1016/j.physleta.2008.06.027`.

[276] WANG, S.-J., CHANG, K.-C., HWANG, J.-S., HSIAO, J.-Y., LEE, B.-H., AND HUNG, Y.-C. Dynamic behavior of a building structure tested with base and mid-story isolation systems. *Eng. Struct.*, **42** (2012), 420. `doi:10.1016/j.engstruct.2012.04.035`.

[277] WANG, S.-J., CHANG, K. C., HWANG, J.-S., AND LEE, B.-H. Simplified analysis of mid-story seismically isolated buildings. *Earthq. Eng. Struct. Dyn.*, **40** (2011), 119. `doi:10.1002/eqe.1004`.

[278] WANG, S.-J., HWANG, J.-S., CHANG, K.-C., LIN, M.-H., AND LEE, B.-H. Analytical and experimental studies on midstory isolated buildings with modal coupling effect. *Earthq. Eng. Struct. Dyn.*, **42** (2012), 201. `doi:10.1002/eqe.2203`.

[279] WANG, W., HUA, X., CHEN, Z., WANG, X., AND SONG, G. Modeling, simulation, and validation of a pendulum-pounding tuned mass damper for vibration control. *Struct. Control Heal. Monit.*, **26** (2019), 1. `doi:10.1002/stc.2326`.

[280] WANG, W., HUA, X., WANG, X., CHEN, Z., AND SONG, G. Numerical modeling and experimental study on a novel pounding tuned mass damper. *JVC/Journal Vib. Control*, **24** (2018), 4023. `doi:10.1177/1077546317718714`.

[281] WANG, W., WANG, X., HUA, X., SONG, G., AND CHEN, Z. Vibration control of vortex-induced vibrations of a bridge deck by a single-side pounding tuned mass damper. *Eng. Struct.*, **173** (2018), 61. `doi:10.1016/j.engstruct.2018.06.099`.

[282] WEN, G., CHEN, S., AND JIN, Q. A new criterion of period-doubling bifurcation in maps and its application to an inertial impact shaker. *J. Sound Vib.*, **311** (2008), 212. `doi:10.1016/j.jsv.2007.09.003`.

[283] WEN, G., XU, H., AND CHEN, Z. Anti-controlling quasi-periodic impact motion of an inertial impact shaker system. *J. Sound Vib.*, **329** (2010), 4040. `doi:10.1016/j.jsv.2010.03.028`.

[284] WHITTAKER, A. S., KUMAR, M., AND KUMAR, M. Seismic isolation of nuclear power plants. *Nucl. Eng. Technol.*, **46** (2014), 569. `doi:10.5516/NET.09.2014.715`.

[285] WHITTAKER, A. S., SOLLOGOUB, P., AND KIM, M. K. Seismic isolation of nuclear power plants: Past, present and future. *Nucl. Eng. Des.*, **338** (2018), 290. `doi:10.1016/j.nucengdes.2018.07.025`.

[286] WIERCIGROCH, M., KOVACS, S., ZHONG, S., COSTA, D., VAZIRI, V., KAPITANIAK, M., AND PAVLOVSKAIA, E. Versatile mass excited impact oscillator. *Nonlinear Dyn.*, **99** (2020), 323. `doi:10.1007/s11071-019-05368-w`.

[287] WILDE, K., GARDONI, P., AND FUJINO, Y. Base isolation system with shape memory alloy device for elevated highway bridges. *Eng. Struct.*, **22** (2000), 222. `doi:10.1016/S0141-0296(98)00097-2`.

[288] WU, G., WANG, K., LU, G., AND ZHANG, P. An Experimental Investigation of Unbonded Laminated Elastomeric Bearings and the Seismic Evaluations of Highway Bridges with Tested Bearing Components. *Shock Vib.*, **2018** (2018). `doi:10.1155/2018/8439321`.

[289] WU YU, Z., YUN LIU, H., GUO, W., LIU, Q., AND WU YU, Z. A general spectral difference method for calculating the minimum safety distance to avoid the pounding of adjacent structures during earthquakes. *Eng. Struct.*, **150** (2017), 646. `doi:10.1016/j.engstruct.2017.07.068`.

[290] XIE, J. The mathematical model for the impact hammer and global bifurcations. *Acta Mech. Sin.*, **29** (1997), 456.

[291] XU, H. AND JI, J. Analytical-numerical studies on the stability and bifurcations of periodic motion in the vibro-impact systems with clearances. *Int. J. Non. Linear. Mech.*, **109** (2019), 155. `doi:10.1016/j.ijnonlinmec.2018.11.003`.

[292] Xue, Q., Zhang, J., He, J., and Zhang, C. Control performance and robustness of pounding tuned mass damper for vibration reduction in SDOF structure. *Shock Vib.*, **2016** (2016). `doi:10.1155/2016/8021690`.

[293] Yan, Y., Liu, Y., and Liao, M. A comparative study of the vibro-impact capsule systems with one-sided and two-sided constraints. *Nonlinear Dyn.*, **89** (2017), 1063. `doi:10.1007/s11071-017-3500-7`.

[294] Yan, Y., Liu, Y., Manfredi, L., and Prasad, S. Modelling of a vibro-impact self-propelled capsule in the small intestine. *Nonlinear Dyn.*, **96** (2019), 123. `doi:10.1007/s11071-019-04779-z`.

[295] Yang, G., Xu, W., Gu, X., and Huang, D. Response analysis for a vibroimpact Duffing system with bilateral barriers under external and parametric Gaussian white noises. *Chaos, Solitons and Fractals*, **87** (2016), 125. `doi:10.1016/j.chaos.2016.03.017`.

[296] Yang, M., Meng, D., Gao, Q., Zhu, Y., and Hu, S. Experimental study on transverse pounding reduction of a high-speed railway simply-supported girder bridge using rubber bumpers subjected to earthquake excitations. *Eng. Struct.*, **196** (2019), 109290. `doi:10.1016/j.engstruct.2019.109290`.

[297] Yang, Z., Xu, Y. L., and Lu, X. L. Experimental Seismic Study of Adjacent Buildings with Fluid Dampers. *J. Struct. Eng.*, **129** (2003), 197. `doi:10.1061/(asce)0733-9445(2003)129:2(197)`.

[298] Ye, K., Li, L., and Zhu, H. A modified Kelvin impact model for pounding simulation of base-isolated building with adjacent structures. *Earthq. Eng. Eng. Vib.*, **8** (2009), 433. `doi:10.1007/s11803-009-8045-4`.

[299] Yin, S., Wen, G., Ji, J., and Xu, H. Novel two-parameter dynamics of impact oscillators near degenerate grazing points. *Int. J. Non. Linear. Mech.*, **120** (2020), 103403. `doi:10.1016/j.ijnonlinmec.2020.103403`.

[300] Yin, X., Song, G., and Liu, Y. Vibration suppression of wind/traffic/bridge coupled system using multiple pounding tuned mass dampers (MPTMD). *Sensors (Switzerland)*, **19** (2019). `doi:10.3390/s19051133`.

[301] Ying, Z. G., Ni, Y. Q., and Ko, J. M. Stochastic optimal coupling-control of adjacent building structures. *Comput. Struct.*, **81** (2003), 2775. `doi:10.1016/S0045-7949(03)00332-8`.

[302] Yue, L., Kehai, W., and Qiqi, W. Experiment of Ultimate Shear Failure and Friction Sliding Performance of Rubber Bearings of Bridges. *Open Civ. Eng. J.*, **11** (2017), 586. `doi:10.2174/1874149501711010586`.

[303] Zhang, J., Gaidai, O., Gui, B., and Yurchenko, D. Influence of the vibroimpact interaction on sloshing dynamics in a rectangular tank. *Ocean Eng.*, **217** (2020), 107821. `doi:10.1016/j.oceaneng.2020.107821`.

[304] ZHANG, W., MIN, F., CHEN, J., AND DOU, Y. Discontinuous Dynamic Analysis of a Modified Duffing-Rayleigh System with a Piecewise Quadratic Function. *IEEE Access*, **8** (2020), 32312. `doi:10.1109/ACCESS.2020.2973469`.

[305] ZHANG, W. S. AND XU, Y. L. Dynamic characteristics and seismic response of adjacent buildings linked by discrete dampers. *Earthq. Eng. Struct. Dyn.*, **28** (1999), 1163. `doi:10.1002/(SICI)1096-9845(199910)28:10<1163::AID-EQE860>3.0.CO;2-0`.

[306] ZHANG, Y. AND LUO, G. Multistability of a three-degree-of-freedom vibro-impact system. *Commun. Nonlinear Sci. Numer. Simul.*, **57** (2018), 331. `doi:10.1016/j.cnsns.2017.10.007`.

[307] ZHAO, D. AND LIU, Y. Improved Damping Constant of Hertz-Damp Model for Pounding between Structures. *Math. Probl. Eng.*, (2016). `doi:10.1155/2016/9161789`.

[308] ZHAO, N., HUANG, G., LIU, R., ZHANG, P., LU, C., AND SONG, G. Novel Hidden Pounding Tuned Mass Damper for Vibration Control of a Cantilevered Traffic Signal Structure. *J. Eng. Mech.*, **146** (2020), 04020005. `doi:10.1061/(asce)em.1943-7889.0001738`.

[309] ZHOU, X.-Y. AND YANG, L. Study on protection measures for seismic isolation rubber bearings. *ISET J. Earthq. Technol.*, **40** (2003), 137.

[310] ZHU, H. P., GE, D. D., AND HUANG, X. Optimum connecting dampers to reduce the seismic responses of parallel structures. *J. Sound Vib.*, **330** (2011), 1931. `doi:10.1016/j.jsv.2010.11.016`.

[311] ZHU, H. P. AND XU, Y. L. Optimum parameters of Maxwell model-defined dampers used to link adjacent structures. *J. Sound Vib.*, **279** (2005), 253. `doi:10.1016/j.jsv.2003.10.035`.

[312] ZHU, P., ABE, M., AND FUJINO, Y. Modelling three-dimensional non-linear seismic peformance of elevated bridges with emphasis on pounding of girders. *Earthq. Eng. Struct. Dyn.*, **31** (2002), 1891. `doi:10.1002/eqe.194`.

[313] ZIYAEIFAR, M. AND NOGUCHI, H. Partial mass isolation in tall buildings. *Earthq. Eng. Struct. Dyn.*, **27** (1998), 49. `doi:10.1002/(SICI)1096-9845(199801)27:1<49::AID-EQE718>3.0.CO;2-J`.